Pair correlations in strongly interacting Fermi gases

Dissertation

zur Erlangung des akademischen Grades
Doktor der Naturwissenschaften (Dr. rer. nat.)

eingereicht an der
Fakultät für Naturwissenschaften
der
Universität Ulm

von
Manuel Jäger
aus
Mühlacker

Betreuer der Dissertation: Johannes Hecker Denschlag

2024

Amtierender Dekan der Fakultät für Naturwissenschaften: Prof. Dr. Kay-Eberhard Gottschalk
Erstgutachter und Betreuer: Prof. Dr. Johannes Hecker Denschlag
Zweitgutachter: Prof. Dr. Alexander Kubanek
Tag der mündlichen Prüfung:

Die in dieser Dissertation beschriebenen Arbeiten wurden an der

Universität Ulm
Institut für Quantenmaterie
Albert-Einstein-Allee 45
89081 Ulm

durchgeführt.

"Nature has a great simplicity and therefore a great beauty."

- Richard P. Feynman -

Abstract

In this thesis, ultracold, quantum degenerate, strongly interacting Fermi gases are created and studied. The experiments are carried out with a two-component, harmonically trapped Fermi gas of ^{6}Li atoms in the vicinity of a broad magnetic Feshbach resonance at 832.2 Gauss, which allows for precisely tuning the interparticle interactions.

The main focus of this thesis is the experimental investigation of short-range two-body correlations in the Bardeen–Cooper–Schrieffer to Bose-Einstein condensate (BCS-BEC) crossover. In the crossover at low temperatures, the Fermi gas undergoes a transition from a state of weakly bound Cooper pairs to a state of tightly bound molecules. Thereby, the short-range pair correlations change markedly. To probe these correlations, we employ a recently proposed photoexcitation scheme, where fermion pairs are transferred to an excited molecular state. The efficiency of the photoexcitation process yields Tan's contact parameter. This parameter is not only a measure for short-range two-body correlations but also a fundamental quantity for describing various properties of strongly interacting Fermi gases. The experimental results provide a comprehensive map of the contact parameter in the entire phase diagram of the BCS-BEC crossover for various temperatures and interacting strengths. This complements previous work of ours in which we experimentally determined the pair fraction on the BEC side above the critical temperature for superfluidity.

A second topic of this thesis is the test of a new scheme for the holographic detection of single atoms in optical lattices which was recently proposed by us. In the experimental test setup, the atoms are imitated by holes in an opaque mask. Our results indicate that already a small number of scattered photons is sufficient to accurately detect occupied lattice sites. This suggests holographic imaging scheme might be a suitable method for non-destructive single atom imaging. This project was supervised by me and carried out as the master's thesis of Sebastian Kölle.

On the technological side, I present the implementation and major improvements on our robust all-solid-state laser system at 671 nm. This laser system features a stable output power of more than one watt and a narrow linewidth of about 250 kHz. It is therefore well suited for laser cooling of lithium atoms and has been successfully used in our experiments for almost one and a half years.

Zusammenfassung

In dieser Arbeit werden quantenentartete, stark wechselwirkende Fermi-Gase erzeugt und untersucht. Die Experimente werden mit einem ultrakalten atomaren Gas aus fermionischen ^{6}Li-Atomen in zwei Spinzuständen durchgeführt, das sich in einer harmonischen Falle befindet. Dabei arbeiten wir in der Nähe einer breiten magnetischen Feshbach-Resonanz bei 832.2 Gauß, die eine präzise Kontrolle über die Wechselwirkung zwischen den Teilchen ermöglicht.

Der Schwerpunkt dieser Dissertation ist die experimentelle Untersuchung von kurzreichweitigen Zweikörper-Korrelationen im Bardeen-Cooper-Schrieffer-Bose-Einstein-Condensate (BCS-BEC) Übergang. Bei diesem Übergang wechselt das Fermi-Gas bei niedrigen Temperaturen von einem Zustand schwach gebundener Cooper-Paare zu einem Zustand fest gebundener Moleküle. Dabei ändern sich die kurzreichweitigen Paarkorrelationen maßgeblich. Um diese Korrelationen zu untersuchen, verwenden wir ein kürzlich vorgeschlagenes Anregungsschema, bei dem Fermionenpaare durch Photonen in einen angeregten Molekülzustand überführt werden. Aus der Effizienz des Photoanregungsprozesses erhalten wir den Tan Contact Parameter. Diese Größe ist nicht nur ein Maß für Zweikörper-Korrelationen, sondern auch eine grundlegende Größe zur Beschreibung zahlreicher Eigenschaften von stark wechselwirkenden Fermi-Gasen. Unsere Messungen decken einen großen Bereich von Wechselwirkungsstärken und Temperaturen ab, wodurch wir den Tan Contact Parameter im gesamten Phasenraum des BCS-BEC-Übergangs erhalten. Dies ergänzt frühere Arbeiten von uns, in denen wir den Paaranteil auf der BEC-Seite oberhalb der kritischen Temperatur bestimmt haben.

Ein zweites Thema der Arbeit ist der Test eines kürzlich von uns vorgeschlagenen Schemas zur holographischen Abbildung einzelner Atome in optischen Gittern. Im experimentellen Versuchsaufbau werden die Atome von Löchern in einer lichtundurchlässigen Maske nachgeahmt. Unsere Ergebnisse deuten darauf hin, dass bereits eine kleine Anzahl gestreuter Photonen für die Erkennung besetzter Gitterplätze ausreicht. Dies könnte die Methode zu einem geeigneten Werkzeug für die zerstörungsfreie Einzelatomabbildung machen. Dieses Projekt wurde von mir betreut und im Rahmen einer Masterarbeit von Sebastian Kölle durchgeführt.

Auf der technologischen Seite stelle ich die Implementierung und wesentliche Verbesserungen unseres Eigenbau-Festkörperlasersystems bei 671 nm vor. Dieses Lasersystem verfügt über eine stabile Ausgangsleistung von mehr als einem Watt und über eine schmale Linienbreite von etwa 250 kHz. Es ist damit die für die Laserkühlung von Lithiumatomen geeignet und wird seit fast eineinhalb Jahren erfolgreich in unseren Experimenten verwendet.

Contents

Chapter 1

Introduction

Understanding correlations and interactions between elementary particles and complex entities is a cornerstone of scientific progress. Of particular importance are pair correlations in fermionic systems, since fermions - such as electrons, protons and neutrons - form the basis of all matter. At temperatures approaching absolute zero, correlations in these systems become especially pronounced and play a central role in phenomena such as superfluidity and superconductivity [1–5]. In this context, ultracold quantum gases have proven to be a powerful and highly controllable platform for studying such fundamental physics [6–8]. The preparation and investigation of these quantum systems has opened up new avenues of research which has been recognized with three Nobel Prizes over the last years in 1997, 2001 and 2012.
In our experiments in Ulm, we investigate ultracold, quantum degenerate gases of fermionic ^{6}Li atoms in two hyperfine states. These atomic ensembles are brought into the strongly interacting regime by enhancing the scattering between the atoms using a magnetic Feshbach resonance [9]. This has significant effects on the short-range pair correlations which strongly effect the physical properties of the system [10–12]. The investigation of these correlations is the main focus of my thesis. In addition to two first-author publications on this topic [13, 14], I contributed to preliminary work as a third author [15, 16]. Moreover, I have worked on two further topics. The first involves testing a new optical imaging method for atoms in an optical lattice [17]. In the test setup, the atoms are imitated by submicron holes in an opaque mask. This work was conducted within the master's thesis of Sebastian Kölle, which I supervised. The second topic is more technological in nature. I significantly improved and implemented a self-built solid-state laser system into our experimental setup. This system has now been successfully used for laser cooling in our laboratory for almost one and a half years.
In the following, I will briefly discuss the different topics of my thesis and provide additional background information.

Pair correlations in ultracold Fermi gases

Pair correlations are a fundamental concept across all fields of physics, describing the statistical relationships between pairs of particles or complex entities. In nuclear physics, they describe the microscopic behaviour of elementary particles, such as the bonding interactions within the atomic nucleus. In cold chemistry, they are essential for explaining reaction dynamics and molecular

interactions [18] and enable a deeper insight into various physical and chemical processes. Even in astrophysics, at the other end of the length scale, pair correlations characterize the relations between celestial bodies such as planets or stars in solar systems, binary stars or galaxies.
In this context, ultracold quantum gases offer a unique platform to study pair correlations in a highly controllable environment [7, 8, 19]. These atomic or molecular gases are cooled to temperatures near absolute zero, where the wave functions of individual particles start to spatially overlap forming a quantum many-body system [20–22]. This results in phenomena like superfluidity and superconductivity [1–5]. By means of Feshbach resonances, the effective interaction between the particles can be precisely tuned, allowing to investigate a large range of pairing interactions [9]. A particularly interesting type of system in this regard is the Bardeen-Cooper-Schrieffer (BCS) to Bose-Einstein Condensate (BEC) crossover in ultracold Fermi gases. In the crossover, the superfluid state of the Fermi gas smoothly transitions from a state of weakly bound Cooper pairs, as present in superconductors, to a state of tightly bound molecules, characteristic for a Bose-Einstein condensate [23]. In this context, pair correlations describe the relations between fermions of opposite spin, including their spatial and momentum distributions. Spatial correlations thereby quantify the probability of finding interacting pairs of particles at a certain distance from each other.
In the BCS regime, the weak attraction between fermions leads to the formation of Cooper pairs that condense into a coherent superfluid state with pair sizes much larger than the interparticle spacing [2, 3]. Crossing the Feshbach resonance, the nature of the pairs fundamentally changes, as the pairs become more localized and eventually form tightly bound molecules in the BEC regime [9, 20]. This continuous evolution is accompanied by significant changes in the pair correlations [16]. These microscopic correlations also manifest in macroscopic properties of the Fermi gas. This is demonstrated in measurements of the density distribution shown in Figure 1.1. A detailed explanation is given in the figure caption.
In recent years, various groups have used experimental techniques such as radio-frequency spectroscopy [26] and Bragg spectroscopy [27] to probe pairing and pair correlations in ultracold Fermi gases. In addition, theoretical approaches have been employed to study these correlations. These include mean-field theories, quantum Monte Carlo simulations and other advanced computational methods [28–30]. All these efforts have provided insights into the pair correlations in certain regions of the BCS-BEC crossover phase space. What has been missing so far is a comprehensive picture of the pair correlations in the entire crossover at various interaction strengths and temperatures.
With our studies, we contribute to closing this gap by precisely measuring the short-range two-body correlations in BCS-BEC crossover. For this, we work with a spin-balanced, ultracold, harmonically-trapped Fermi gas of ^{6}Li atoms. This atomic species features a broad magnetic Feshbach resonance at 832.2 Gauss, which allows for precisely tuning the interparticle interactions and correlations. We measure the short-range two-body correlations using a novel method based on photoexcitation of atom pairs as recently proposed by Wang *et al.* [31]. In this scheme, two atoms at close range are transferred to an excited, tightly-bound

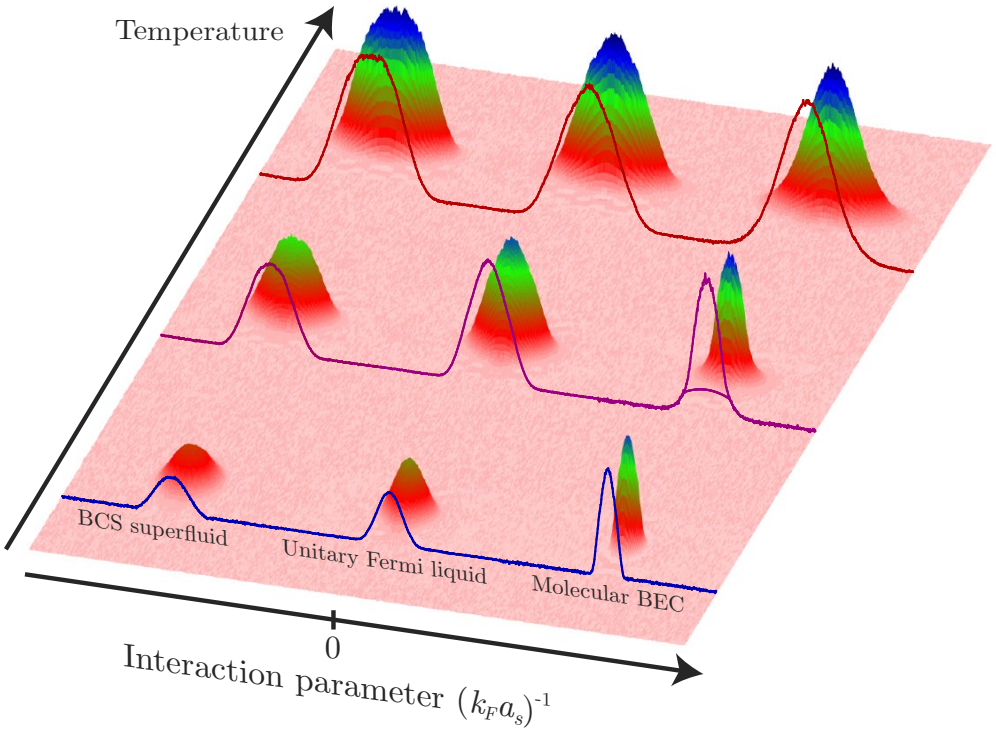

FIGURE 1.1: Density distributions of a harmonically trapped, strongly interacting Fermi gas in the BCS-BEC crossover. The fundamental change of the microscopic pair correlations with temperature and interaction strength is also evident in the density distribution of the macroscopic atom cloud, especially in the superfluid state for $T \to 0$. For an interaction parameter of $(k_F a_s)^{-1} > 0$, corresponding to an effective repulsive interaction, fermions of opposite spin form tightly bound molecules. At low temperatures, these condense into a molecular Bose-Einstein condensate, where the energetic ground state of the gas is macroscopically populated. In a harmonic trapping potential, the corresponding ground state wave function has a small spatial extension. Consequently, the macroscopic atomic cloud is characterized by a small spatial extension and a high density. For effective attractive interactions ($(k_F a_s)^{-1} < 0$) and low temperatures, pairs of fermions form Cooper pairs at the surface of the Fermi sea resulting in a BCS type superfluid. The majority of the atomic cloud however still resembles an almost ideal degenerate Fermi gas. Such a gas has a large spatial extension due to the Fermi pressure, which arises from the Pauli exclusion principle [24, 25]. As the temperature increases, the thermal energy of the atoms becomes larger than the associated binding energies. As a consequence, both Cooper pairs and molecules break up and the density distribution becomes insensitive to the interaction parameter. For more details, see Chapters 2 and 9.

molecular state using photoexcitation. The photon thereby ensures energy conservation. Strong short-range correlations, associated with a scenario in which the atoms are initially already paired closely together, consequently lead to an efficient photoexcitation process. The rate at which we transfer pairs of atoms into the tightly-bound molecular state is therefore a direct measure of the

present short-range two-body correlations. These correlations are quantified by a parameter called *Tan's contact*. This parameter plays a significant role in the description of strongly interacting Fermi gases, as it appears in countless thermodynamic relations that describe such a gas [10–12, 32, 33]. With our measurements, we obtain a continuous map of Tan's contact in the entire BCS-BEC crossover. This complements previous work of ours in which we experimentally determined the fraction of paired fermions on the BEC side above the critical temperature for superfluidity [15].

Single-site detection of atoms in optical lattices

In recent years, the investigation of ultracold atoms in optical lattices has led to numerous breakthroughs in fundamental research [34–36]. Beyond their applications in quantum simulation and information processing [37, 38], atoms in optical lattices provide a versatile platform for studying fundamental aspects of many-body and condensed matter physics, particularly in the examination of tailored solid-state-like systems [39–42]. Fermionic atoms in optical lattices are thereby utilized to mimic the behaviour of electrons in solids, as both are fermions and obey the Pauli exclusion principle [25]. The large lattice constants of optical lattices and the ability to tune the interparticle interactions offer a major advantage over research in solids. Especially the magnetic Feshbach resonance in lithium-6 enables a precise control of the on-site interaction [9, 43]. For all studies, a spin resolved detection of the atomic distribution at the level of individual lattice sites is highly advantageous. However, these imaging techniques are particularly challenging for light elements such as lithium because of the high recoil energy. This energy is inversely proportional to the atomic mass and limits the number of photons that can be scattered before the atoms are heated and ejected from the lattice. Therefore, the aim is to develop detection systems that only require a small number of scattered photons per atom. A great variety of such methods has already been developed. This includes established techniques such as phase contrast imaging [44, 45] and intensity-based defocus-contrast imaging [46, 47], but also more recently developed methods such as dark-field Faraday rotation imaging [48] and shadow-graph imaging [49].
We have recently proposed a novel approach for the detection of atoms in a 2D optical lattice based on off-axis holography [50]. In this scheme, a laser beam of low intensity illuminates the atoms in the lattice and is subsequently scattered. The scattered light is collimated by an objective and superimposed with a coherent reference beam. This beam acts an amplifier for the weak atomic signals. From the resulting interference pattern, one can obtain valuable information about the occupied lattice sites. This has very recently been employed for imaging large atomic clouds of 10^7 sodium atoms [51]. We now test our proposal for the situation of atoms in an optical lattice [17]. In order to create a reproducible and low-noise test environment, the atoms in our setup are imitated by submicron holes in an opaque mask. This enables a precise testing of the proposed scheme under various aspects with well-defined lattice configurations. Our results indicate, that already a few hundred photons scattered per atom could be sufficient to reliably identify occupied lattice sites [17].

Solid state laser sources

The invention of lasers has revolutionized numerous scientific fields and paved the way for the area of ultracold quantum gases [52–55]. Methods of laser cooling and trapping have achieved the necessary reductions of the atomic phase space densities to reach quantum degeneracy [56, 57]. In this context, lasers are used for manipulating the electronic states of the atoms by means of optical transitions. Among various laser types, those using solid-state gain media are particularly powerful and widespread [58]. A notable example are optical fibers and laser crystals doped with neodymium ions (Nd^{3+}) which feature strong optical transitions around $1064\,\mathrm{nm}$ and $1342\,\mathrm{nm}$ [59]. The transition at $1064\,\mathrm{nm}$ is used in commercial lasers and green laser pointers, where the green light at $532\,\mathrm{nm}$ is generated via subsequent second harmonic generation. However, the optical transition at $1342\,\mathrm{nm}$ is also of great importance, especially for the preparation of ultracold lithium gases. By second harmonic generation, this wavelength can be converted to $671\,\mathrm{nm}$ which coincidentally matches the lithium D-line transitions, making it suitable for laser cooling and imaging of lithium atoms [60–63].
In contrast to laser diodes at $660\,\mathrm{nm}$, $780\,\mathrm{nm}$ or $405\,\mathrm{nm}$, which are commercially used for reading from and writing to CD, DVD and BluRay discs [64], the particular wavelength of $671\,\mathrm{nm}$ is known for the difficulties to manufacture high power long-lived laser diodes because of the fragile semiconductor material systems [60]. Therefore, solid-state lasers at $671\,\mathrm{nm}$ increase the longevity of the experimental apparatuses and the achievable optical powers required for cooling lithium atoms to quantum degeneracy.
Over the course of the last years, we set up an all solid-state laser system capable of generating more than one watt of optical power at $671\,\mathrm{nm}$ [65, 66]. The system is based on a model of the Salomon group in Paris [61–63]. Within this thesis, I significantly improved the stability and linewidth of our laser system and integrated it into the experimental setup. For this, I also carried out extensive numerical simulations of the laser system, which were crucial for understanding and solving the existing problems. The system now reliably provides the necessary optical power for laser cooling and forms the basis for all our experiments.

Outline

This thesis is organized as follows.

In Chapter 2, I give an introduction to the most important theoretical aspects relevant for this thesis. Initially, the statistical properties of Fermi, Bose and composite Bose gases are introduced. Subsequently, I present the basic principles of scattering theory and magnetic Feshbach resonances as a tool to manipulate the scattering process. A focus is put on the properties of ^{6}Li, especially in the high magnetic field near the broad Feshbach resonance. Following this, I describe the BCS-BEC crossover of a strongly interacting Fermi gas. The chapter concludes with the introduction of Tan's contact, which is a measure for short-range two-body correlations.

In Chapter 3, the technical realization of the experimental apparatus is detailed. This includes the vacuum system, the experimental control unit, the coil systems, laser sources, and all other devices needed for preparing, manipulating and probing the degenerate Fermi gases. This includes our realization of a repulsive optical ring potential, which we aim to use in the future to create and study homogeneous Fermi gases.

In Chapter 4, I explain the experimental steps required to produce a degenerate Fermi gas, putting the focus on the physics behind the atom gas preparation. This includes standard cooling methods such as laser cooling, molasses cooling as well as evaporative cooling. Additionally, the experimental methods for imaging the atoms and exciting atom pairs are detailed.

In Chapter 5, I present our realization of a high power solid-state laser system at $671\,\mathrm{nm}$. This system provides the light for laser cooling and thereby sets the basis for all our measurements.

In Chapter 6, our experimental work on measuring Tan's contact in our strongly interacting Fermi gas is presented. Within this work, short-range two-body correlations are quite precisely measured using a novel photoexcitation scheme.

In Chapter 7, I present our experimental methods and theoretical approaches for studying Tan's contact in the BCS-BEC crossover. This extends the work presented in Chapter 6 and gives further details on the experimental methods and calibration techniques as well as an overview over theoretical calculation for Tan's contact using various approaches.

In Chapter 8, I report on our work on holographic imaging of submicron light scatterers. This work extends our recently proposed imaging scheme for atoms in optical lattices and suggests that atoms can be imaged with high fidelity with only a few photons scattered per atom.

In Chapter 9, I introduce different approaches for theoretically describing a strongly interacting Fermi gas in the BCS-BEC crossover. These approaches have been implemented and used as a theoretical extension of our measurements and for deepening our understanding of the physics in the crossover.

In Chapter 10, the work conducted within this thesis is briefly summarized. In addition, an outlook on possible future experiments and suggestions for the extension of ongoing work is presented.

Chapter 2

Ultracold quantum gases

In the experiments described in this thesis, a strongly interacting two-component Fermi gas of lithium-6 atoms is created and studied. Using forced evaporative cooling and a broad magnetic Feshbach resonance, we can control both the temperature and the interparticle interaction of the fermions. This allows for experimentally realizing and studying all kinds of different normal and superfluid gas phases, including a BCS type superfluid, a resonantly interacting Fermi gas and a Bose-Einstein condensate of diatomic molecules. Across the phase space of the Fermi gas, its short-range particle correlations change fundamentally. These correlations can be described by a quantity called *Tan's contact*.
The following chapter provides an overview of the properties of strongly interacting Fermi gases. This includes the underlying particle statistics of fermions and bosons, their scattering properties at ultracold temperatures and the exceptionally broad Feshbach resonance of lithium-6. In addition, the phase space of a strongly interacting Fermi gas, the so-called BCS-BEC crossover, is introduced and an overview about the pair correlations and Tan's contact is given. The information presented is taken from several textbooks, reviews, and research articles.

2.1 Particle statistics and distribution functions

All particles can be classified as either fermions or bosons, distinguished by the symmetry of their wave functions upon particle exchange and their spin. Fermions have anti-symmetric wave functions and half-integer spin, while bosons have symmetric wave functions and integer spin. Unlike bosons, which can occupy the same quantum state without restriction, two identical fermions cannot occupy the same quantum state [19, 21]. This fundamental difference gives rise to distinct distribution functions for fermions and bosons, which particularly differ at low temperatures.
Fermions follow the Fermi-Dirac distribution where the mean occupation number of a given quantum state with energy ϵ_i at temperature T is given by [43]

$$n_{i,F} = \frac{1}{e^{(\epsilon_i - \mu)/k_B T} + 1} \tag{2.1}$$

where μ is the chemical potential and k_B the Boltzmann constant. One directly sees, that $n_{i,F}$ cannot exceed 1. This is also expressed in the Pauli principle which states that two (identical) fermions cannot occupy the same quantum state [25].

In contrast, bosons obey the Bose-Einstein distribution

$$n_{i,B} = \frac{1}{e^{(\epsilon_i - \mu)/k_B T} - 1} \tag{2.2}$$

which can be larger than one and even diverge at small temperatures, when the chemical potential μ approaches the energy of the ground state ϵ_0 [21, 67]. This essentially leads to the phenomenon of Bose-Einstein condensation, the macroscopic occupation of the ground state (see Section 2.1.2 for more details) [67]. The chemical potential is usually fixed by the constraint, that the sum over the occupation numbers of all states must equal the total particle number N, i.e. $\sum_i n_{i,F/B} = N$ [21]. As an example for illustrating the different occupation probabilities, figure 2.1 shows the occupation of the energy levels of a one-dimensional harmonic oscillator potential by fermions and bosons, respectively.

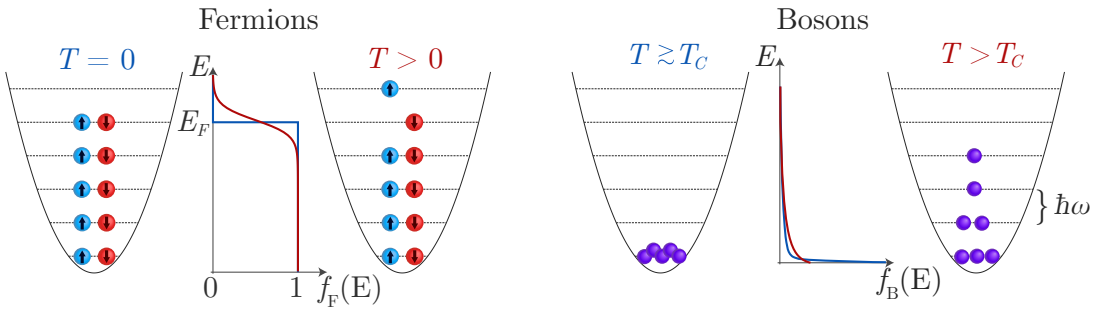

FIGURE 2.1: Occupation of the energy levels of a (1D) quantum harmonic oscillator potential by fermions of two spin components (left) and indistinguishable bosons (right). The blue line in the distribution functions indicates the occupation at $T = 0$ for fermions and $T \gtrsim T_C$ for bosons, while the red line illustrates the situation $T > 0$ for fermions and $T > T_C$ for bosons. Here, T_C indicates the critical temperature for Bose-Einstein condensation, for more details see Section 2.1.2

In the following, we consider fermions and bosons with kinetic energies $E_{kin} = \frac{p^2}{2m}$ in an external trapping potential $V(\mathbf{r})$. Here $\mathbf{p}$ is their momentum, $\mathbf{r}$ their position and m their mass. In the framework of the local density approximation (LDA), the atomic gas can be considered to consist of locally homogeneous clusters. The LDA is valid, when the density varies smoothly compared to the characteristic length scales of the system, such as the Fermi wavelength [21, 68, 69]. Within this semi-classical approximation, the probability of finding a fermion/boson with momentum $\mathbf{p}$ at position $\mathbf{r}$ is then given by

$$f_F(\mathbf{p},\mathbf{r}) = \frac{1}{e^{(\frac{p^2}{2m} + V(\mathbf{r}) - \mu)/k_B T} + 1} \qquad f_B(\mathbf{p},\mathbf{r}) = \frac{1}{e^{(\frac{p^2}{2m} + V(\mathbf{r}) - \mu)/k_B T} - 1}. \tag{2.3}$$

In the experiments presented in this thesis, the trapping potentials for the atoms are harmonic to a good approximation in all three spatial directions with trap

frequencies ω_i. In this case the trapping potential is

$$V(\mathbf{r}) = V(x,y,z) = \frac{1}{2}m\left(\omega_x^2 x^2 + \omega_y^2 y^2 + \omega_z^2 z^2\right). \tag{2.4}$$

In this thesis, the LDA in which the gas is assumed to be locally homogeneous is often used to describe atomic gases in any external trapping potentials. Moreover, I also realized an optical box-like potential which can provide a homogeneous confinement for the atoms in future studies (see Section 3.6.2). For this reason, the following sections are devoted to fermions and bosons in both harmonic and homogeneous potentials.

2.1.1 Fermions

In the following section, we consider fermions of only one spin component. This represents an ideal Fermi gas, where the individual fermions do not interact with each other at ultracold temperatures due to the Pauli principle [43].

Fermi energy, Fermi temperature and Fermi momentum

At zero temperature, each state of the harmonic trapping potential up to the Fermi energy E_F is occupied by a single fermion. Above the energy E_F no states are occupied. In this limit, the chemical potential is equal to the Fermi energy and $f_F(\mathbf{p},\mathbf{r})$ can written as a step function [21]

$$f_{\mathrm{F}}(\mathbf{p},\mathbf{r}) = \begin{cases} 0 & \text{for} \quad \frac{\mathrm{p}^2}{2\mathrm{m}} + \mathrm{V}(\mathbf{r}) > \mathrm{E_F} \\ 1 & \text{for} \quad \frac{\mathrm{p}^2}{2\mathrm{m}} + \mathrm{V}(\mathbf{r}) < \mathrm{E_F} \end{cases}. \tag{2.5}$$

The total number of fermions N is then

$$N = \frac{1}{h^3}\int\int \mathrm{d}\mathbf{p}\,\mathrm{d}\mathbf{r}\, f_{\mathrm{F}}(\mathbf{p},\mathbf{r}) = \frac{E_F^3}{6(\hbar\bar{\omega})^3} \leftrightarrow E_F = \hbar\bar{\omega}(6N)^{1/3} \tag{2.6}$$

where $\bar{\omega} = (\omega_x\omega_y\omega_z)^{1/3}$ is the geometric mean of the trap frequencies and $h = 2\pi \times \hbar$ is the Planck constant. With the Fermi energy E_F one can associate a corresponding Fermi temperature

$$T_F = E_F/k_B = \hbar\bar{\omega}(6N)^{1/3}/k_B \tag{2.7}$$

and a Fermi (angular) momentum k_F which is given by

$$k_F = \sqrt{2mE_F}/\hbar = \sqrt{2m\bar{\omega}/\hbar}(6N)^{1/6} \tag{2.8}$$

and refers to the peak Fermi momentum in the center of the harmonic trap.
In the experiments carried out in this thesis, typical atom numbers and trap frequencies are $N = 10^5 - 10^6$ and $\omega_i \approx 2\pi \times 100$ Hz. Therefore, the Fermi temperature is on the order of one micro kelvin and the corresponding Fermi momentum is $\approx 3\mu\mathrm{m}^{-1}$.
In a homogeneous Fermi gas, the density $n = N/V$ is uniform in the volume V

that the gas occupies. Here, the total number of fermions at zero temperature is

$$N = \frac{1}{h^3}\int\int \mathrm{d}\mathbf{p}\,\mathrm{d}\mathbf{r}\, f_{\mathrm{F}}(\mathbf{p},\mathbf{r}) = \frac{V}{6\pi^2}\left(\frac{2mE_F^{\mathrm{hom}}}{\hbar^2}\right)^{3/2}. \tag{2.9}$$

The local Fermi energy E_F^{hom}, Fermi temperature T_F^{hom} and Fermi momentum k_F^{hom} are then

$$E_F^{\mathrm{hom}} = \frac{\hbar^2}{2m}(6\pi^2 n)^{2/3}, \tag{2.10}$$

$$T_F^{\mathrm{hom}} = \frac{\hbar^2}{2mk_B}(6\pi^2 n)^{2/3} \tag{2.11}$$

and

$$k_F^{\mathrm{hom}} = (6\pi^2 n)^{1/3}. \tag{2.12}$$

Density distributions

In our experiments, we obtain valuable information about the Fermi gas by measuring its real-space density distribution. For non-interacting fermions the distribution within the LDA is obtained by integrating $f_F(\mathbf{p},\mathbf{r})$ over momentum space

$$n_F(\mathbf{r}) = \frac{1}{h^3}\int \mathrm{d}\mathbf{p}\, f_F(\mathbf{p},\mathbf{r}) = \frac{1}{h^3}\int \mathrm{d}\mathbf{p}\,\frac{1}{\exp\left[(\frac{p^2}{2m}+V(\mathbf{r})-\mu)/k_BT\right]+1}. \tag{2.13}$$

We can experimentally realize atom clouds at various temperatures, from (quasi) degenerate Fermi gases at $0 \lesssim T \lesssim 1T_F$ to thermal classical gases for $T \gg T_F$. They differ fundamentally in their thermodynamical properties and pair correlations. This also reflects in the respective density distributions.

At zero temperature, where $\mu = E_F$, the integration in Equation (2.13) yields

$$n_{F,T=0}(\mathbf{r}) = \frac{8N}{\pi^2 R_{TF,x}R_{TF,y}R_{TF,z}}\left(1-\frac{x^2}{R_{TF,x}^2}-\frac{y^2}{R_{TF,y}^2}-\frac{z^2}{R_{TF,z}^2}\right)^{3/2} \tag{2.14}$$

which holds for $x_i^2 < R_{TF,i}^2$ where $R_{TF,i} = \sqrt{\frac{2E_F}{m\omega_i^2}}$ are the Thomas-Fermi radii. Outside the Thomas-Fermi radii, the density is zero.

At finite temperatures, the integration in (2.13) yields

$$n_{F,T}(\mathbf{r}) = -\frac{1}{\lambda_{dB}^3}\mathrm{Li}_{3/2}\left(-e^{(\mu-V(\mathbf{r}))/k_BT}\right) \tag{2.15}$$

where $\lambda_{dB} = \frac{h}{\sqrt{2\pi m k_B T}}$ is the thermal de Broglie wavelength and $\mathrm{Li}_s(z)$ is the polylogarithm of order s and argument z. It results from the integration of the Fermi-Dirac/Bose-Einstein distribution function and is defined by a series

expansion as

$$\mathrm{Li}_s(z) = \sum_{k=1}^{\infty} \frac{z^k}{k^s} \tag{2.16}$$

or by an integral representation as $\mathrm{Li}_s(z) = \Gamma(s)^{-1} \int_0^\infty \mathrm{d}t\, t^{s-1}(e^t/z - 1)^{-1}$ for $s > 0$ and $z \leq 1$, where $\Gamma(s)$ is the Gamma function [21]. A plot of the polylogarithm functions $\mathrm{Li}_{3/2}(z)$ and $\mathrm{Li}_3(z)$ is shown in Figure 2.2.

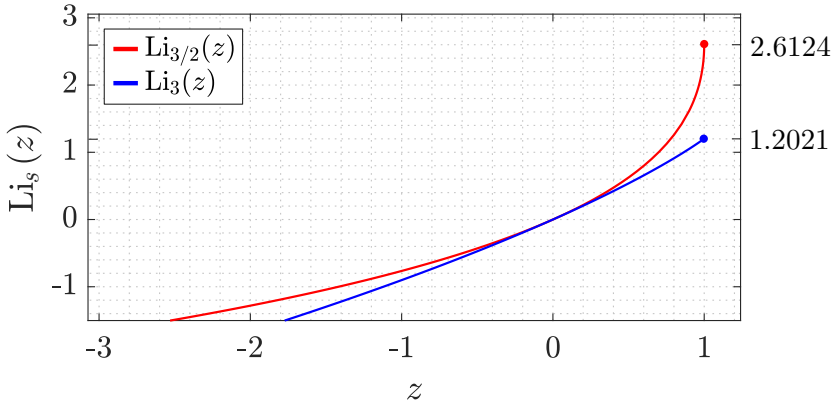

FIGURE 2.2: Polylogarithm functions $\mathrm{Li}_{3/2}(z)$ and $\mathrm{Li}_3(z)$. The functions arise from the integration of the Fermi-Dirac and Bose-Einstein distribution function and are therefore closely related to the density and momentum distributions of fermions and bosons.

In the limit of high temperatures, where $T \gg T_F$, the, argument of the polylogarithm in Equation (2.15), the so-called fugacity $z = e^{(\mu - V(\mathbf{r}))/k_B T}$, becomes a small quantity $0 < z \ll 1$ [70]. In this limit, the polylogarithm is linear in its argument $\mathrm{Li}_{3/2}(-z) \approx -z$. Therefore, the density distribution $n_{F,T}(\mathbf{r})$ becomes a classical Boltzmann distribution

$$n_{F,T}(\mathbf{r}) \approx \frac{1}{\lambda_{dB}^3} e^{(\mu - V(\mathbf{r}))/k_B T} \tag{2.17}$$

$$= \frac{1}{\lambda_{dB}^3} e^{(\mu/k_B T)} e^{-\frac{x^2}{\sigma_x^2} - \frac{y^2}{\sigma_y^2} - \frac{z^2}{\sigma_z^2}} \tag{2.18}$$

which, for a harmonic trapping potential, results in a Gaussian distribution of the density with widths $\sigma_i = \sqrt{\frac{2k_B T}{m\omega_i^2}}$.

Figure 2.3 shows calculated density distributions of a harmonically trapped Fermi gas at various temperatures. The calculations are based on equations (2.13), (2.15) and (2.18). For $T/T_F > 1$, the classical and quantum statistical calculations yield almost identical results. Notably, the calculations based on Fermi statistics (solid lines) show a slightly lower peak density and a broader width compared to the classical calculations (dashed lines) at the same temperatures. This is a consequence of the Pauli exclusion principle, which prevents two fermions from occupying the same quantum state. Consequently, the same number of fermions must occupy more and higher energy levels. As higher energy levels in a harmonic oscillator have spatially more extended wave functions,

the resulting density distribution for a fixed particle number extends further and becomes more dilute. This phenomenon is also known as Fermi pressure [24].

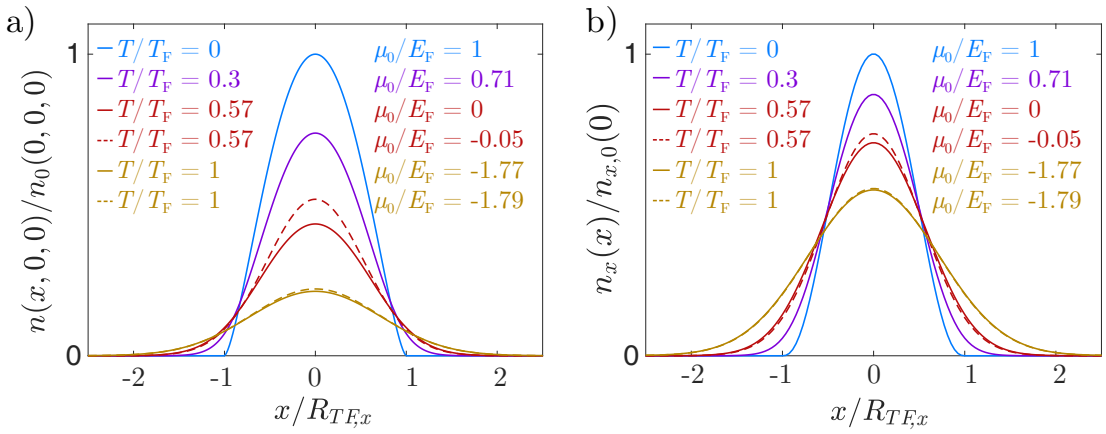

FIGURE 2.3: Calculated density distributions and central chemical potentials μ_0 of a harmonically trapped Fermi gas at various temperatures. The solid lines are calculations based on Equation (2.15), which accounts for Fermi statistics, while the dashed lines correspond to calculations based on classical Maxwell-Boltzmann statistics which result in a Gaussian distribution given by Equation (2.18). a) Shows the central (3D) densities along the x-axis at $y = z = 0$ normalized to the central density $n(0,0,0)$ at $T = 0$. b) Shows the (1D) line densities along the x-axis, calculated from the 3D density by integration over y and z: $n_x(x) = \int\int \mathrm{d}y\,\mathrm{d}z\, n(x,y,z)$. These distributions are also normalized by the central line density $n_{x,0}(0)$ at $T = 0$.

The relations discussed above only truly hold for non-interacting Fermi gases, e.g. spin-polarized Fermi gases where only one spin component is present. Most of our experiments are carried out with two-component Fermi gas, where fermions of opposite spin can interact with each other via elastic scattering (see 2.2). In this scenario weak interactions can be treated by a so-called mean-field approach. More details on this are given in Chapter 9.

2.1.2 Bosons

In our two-component Fermi gas, we can produce Feshbach molecules in the vicinity of the Feshbach resonance. These molecules are composed of two fermions of opposite spin and show Bose statistics, when their binding energy is larger than the thermal energy and the interaction energy. For this reason, the following section provides an overview over bosons and their thermodynamical properties.

Density distributions

As bosons obey the Bose-Einstein statistics, the probability of finding a boson with momentum $\mathbf{p}$ at position $\mathbf{r}$ is given by the Bose-Einstein distribution function $f_B(\mathbf{p},\mathbf{r})$ in Equation (2.3). As in the previous section, the real space density distribution $n_B(\mathbf{r})$ is acquired by integrating $f_B(\mathbf{p},\mathbf{r})$ in momentum space.

At finite temperatures, one finds within the LDA

$$n_B(\mathbf{r}) = \frac{1}{h^3}\int \mathrm{d}\mathbf{p}\, f_B(\mathbf{p},\mathbf{r}) = +\frac{1}{\lambda_{dB}^3}\mathrm{Li}_{3/2}\left(+e^{(\mu-V(\mathbf{r}))/k_BT}\right). \tag{2.19}$$

In the high temperature limit, the fugacity $z = e^{(\mu-V(\mathbf{r}))/k_BT}$ is again a small parameter, such that the density distribution

$$n_{B,T}(\mathbf{r}) \approx \frac{1}{\lambda_{dB}^3}e^{(\mu-V(\mathbf{r}))/k_BT} \tag{2.20}$$

$$= \frac{1}{\lambda_{dB}^3}e^{(\mu/k_BT)}e^{-\frac{x^2}{\sigma_x^2}-\frac{y^2}{\sigma_y^2}-\frac{z^2}{\sigma_z^2}} \tag{2.21}$$

again turns into a classical Gaussian distribution for bosons in a harmonic trapping potential. Again, these relations for the density distributions only hold for non-interacting bosons. In presence of interparticle interactions, they have to be modified. One approach for this is described in Chapter 9.

Bose-Einstein condensation

From (2.19) one can find the total atom number $N = \int \mathrm{d}\mathbf{r}\, n_B(\mathbf{r})$ by integration. For a harmonic trapping potential, the result is

$$N = \left(\frac{k_BT}{\hbar\bar{\omega}}\right)^3 \mathrm{Li}_3\left(e^{\mu/k_BT}\right). \tag{2.22}$$

At a fixed temperature T and trap frequencies ω_i, this number has an upper limit of

$$N_{th} = \left(\frac{k_BT}{\hbar\bar{\omega}}\right)^3 \mathrm{Li}_3\left(1\right) = \left(\frac{k_BT}{\hbar\bar{\omega}}\right)^3 \zeta(3) \approx \left(\frac{k_BT}{\hbar\bar{\omega}}\right)^3 \times 1.2021 \tag{2.23}$$

where $\zeta(\dots)$ is the Riemann zeta function. Adding more atoms or further reducing the temperature below

$$T_C = \frac{\hbar\bar{\omega}}{k_B}\left(\frac{N}{\zeta(3)}\right)^{1/3} \approx 0.94\frac{\hbar\bar{\omega}}{k_B}(N)^{1/3} \tag{2.24}$$

leads to Bose-Einstein condensation, where the bosons start to macroscopically occupy the ground state of the harmonic trapping potential [21]. The total atom number N is then the sum of the atom number in the ground state N_0 and the thermal, non-condensed atom number N_{th}. For a non-interacting Bose-Einstein condensate, the condensate fraction in the harmonic trapping potential is given by

$$\frac{N_0}{N} = \frac{N-N_{th}}{N} = 1 - \frac{N_{th}}{N} = 1 - \left(\frac{T}{T_C}\right)^3. \tag{2.25}$$

Bose-Einstein condensation first happens in the center of the harmonic trap, when locally the critical density

$$n_C = \frac{1}{\lambda_{dB}^3}\mathrm{Li}_{3/2}(1) = \frac{1}{\lambda_{dB}^3}\zeta(3/2) \approx \frac{2.61}{\lambda_{dB}^3} = 2.61\frac{(2\pi m k_B T)^{2/3}}{h^3} \tag{2.26}$$

is reached (see Eq. (2.19)). The total density $n = n_0 + n_C$ is then the sum of the condensate density n_0 and the (limited) thermal density n_C. Locally the condensate fraction n_0/n is then given by

$$\frac{n_0}{n} = 1 - \left(\frac{T}{T_C^{\mathrm{hom}}}\right)^{2/3}. \tag{2.27}$$

The density distribution of the condensate in the case of non-interacting bosons is given by the square of the ground state wave function of the harmonic trapping potential times the number of condensed atoms $n_0 \sim N_0|\Psi_0|^2$. At small (repulsive) interactions, as present in our experiments, the Bose-Einstein condensate can be described by the time-independent Gross-Pitaevskii equation (GPE)

$$\mu\Psi(\mathbf{r}) = \left(-\frac{\hbar^2}{2m}\nabla^2 + V(\mathbf{r}) + g|\Psi(\mathbf{r})|^2\right)\Psi(\mathbf{r}). \tag{2.28}$$

where $g = \frac{4\pi\hbar^2}{m}a_B$ is the coupling constant and a_B the scattering length of the bosons. The nonlinear term $|\Psi(\mathbf{r})|^2$ in the GPE is essentially the density n_0 of the condensate. The particle interaction $g|\Psi(\mathbf{r})|^2 = gn_0$ is therefore treated in the mean-field approximation. Equation (2.28) can be further simplified by the Thomas-Fermi approximation, where the small kinetic term $-\frac{\hbar^2}{2m}\nabla^2\Psi(\mathbf{r})$ is neglected.
The density distribution therefore simply becomes a flipped version of the external trapping potential

$$n_0(\mathbf{r}) = \frac{\mu - V(\mathbf{r})}{g} \quad \text{for} \quad \mu - V(\mathbf{r}) > 0, \qquad \text{and} \qquad n_0 = 0 \quad \text{else.} \tag{2.29}$$

This can be understood in such a way that the condensed bosons push themselves into the external potential through their repulsive interaction and thus simply take on its form. By introducing the Thomas-Fermi radii for condensed bosons $R_{TB,i} = \sqrt{\frac{2\mu}{m\omega_i^2}}$, the condensate density distribution in the harmonic trapping potential is given by

$$n_0(\mathbf{r}) = \frac{15N_0}{8\pi R_{TB,x}R_{TB,y}R_{TB,z}}\left(1 - \frac{x^2}{R_{TB,x}^2} - \frac{y^2}{R_{TB,y}^2} - \frac{z^2}{R_{TB,z}^2}\right) \tag{2.30}$$

for $x_i^2 < R_{TB,i}^2$.

For temperatures $0 < T < T_C$**,** a Bose gas consists of a condensed and a non-condensed, normal phase. As their densities follow different distribution functions (see equations (2.19) and (2.30) respectively), the total density distribution

of the atom cloud shows a characteristic bimodal feature, as also shown in figure 1.1. It clearly indicates that the condensed atoms with high density accumulate in the center of the trap while the thermal atoms ones surround them. However, the bimodal feature is only strongly pronounced for non-interacting bosons. For strong repulsive interactions, it can become almost invisible. Further details on this can be found in Chapter 9.

2.1.3 Composite Bosons

As mentioned in the previous sections, we are able to produce Feshbach molecules in the vicinity of the Feshbach resonance. These are composite bosons and consist of two fermions with opposite spin.
In the BEC regime of weak interactions, large binding energies and small temperatures, these molecules essentially behave as bosons and can therefore condense as a molecular Bose-Einstein condensate (mBEC) below a certain critical temperature T_C. For a harmonic trapping potential, the critical temperature from Equation (2.24) can be expressed in terms of the (trap) Fermi temperature defined in (2.7) as

$$\frac{T_C}{T_F} = \frac{\frac{\hbar\bar{\omega}}{k_B}\left(\frac{N}{\zeta(3)}\right)^{1/3}}{\frac{\hbar\bar{\omega}}{k_B}(6N)^{1/3}} \approx 0.5176. \tag{2.31}$$

For a homogeneous gas, one can combine equations (2.26) and (2.11) to find the homogeneous critical temperature

$$\frac{T_C^{\mathrm{hom}}}{T_F^{\mathrm{hom}}} = \left(\frac{(2\pi)^{3/2}}{6\pi^2 \times \zeta(3/2)}\right)^{2/3} \approx 0.218. \tag{2.32}$$

This is also the local critical temperature expressed in the local Fermi temperature at which the condensation in the center of the harmonic trap starts. It should be noted that the thermal de Broglie wavelength of dimers is by a factor $\sqrt{2}$ smaller than that of atoms they consist of, as their mass is twice as large. These critical temperatures for harmonically trapped and homogeneous Fermi gases only hold in the true BEC limit of very weak to no (repulsive) interactions. For stronger repulsive interactions (closer to the Feshbach resonance, see 2.4.3) the critical temperature is lowered [71]. This can be understood simply by the fact that the repulsive interaction prevents the gas from reaching the critical density. A detailed quantitative analysis can be found in Section 9.2.

2.2 Elastic scattering

The interaction between two atoms at distance r can be described by a central scattering potential $V_{sc}(r)$. At distances of a few ten Bohr radii a_0, the atoms interact with the van der Waals potential $-C_6/r^6$ which arises from temporary fluctuations in the electron distribution around the two atoms [72]. These fluctuations create temporary dipoles resulting in a weak attraction. Here C_6 is a coefficient, which depends on the atomic species. At shorter distances of a few

Bohr radii a_0, the electron distributions around the atoms strongly repel each other [72].
The resulting interatomic potentials can become quite complex (see Figure 4.13) and including these potentials into the description of an atom cloud of $\approx 10^6$ atoms would be quite challenging. However, in our experiments the atom clouds are dilute and ultracold which significantly simplifies the problem. While the interatomic potential for ^{6}Li has a range of $r_0 = (mC_6/\hbar^2)^{1/4} \approx 62.5\,a_0$ with $C_6 = 1.333 \times 10^{-76}\,\mathrm{Jm}^6$ [73], the interparticle distance at typical densities of $n \sim 10^{19}/\mathrm{m}^3$ is approximately $n^{-1/3} \sim 10\,000\,a_0$. Secondly, the thermal de Broglie wavelength of our ultracold atoms is on the order of $\lambda_{dB} = h/\sqrt{2\pi m k_B T} \sim 1\mu\mathrm{m}$ for $T \sim 100\,\mathrm{nK}$. As a consequence, the scattering atoms do not feel the details of the short-range interaction potential and the entire collision can be effectively described by a single parameter, the scattering length.

To derive this quantity, we consider a two-body scattering process of two atoms at positions $\mathbf{r_1}$ and $\mathbf{r_2}$ with an interaction potential $V_{sc}(|\mathbf{r_1} - \mathbf{r_2}|)$ only depending on their distance. This problem can be separated into the center of mass ($\mathbf{R} = (\mathbf{r_1} + \mathbf{r_2})/2$) and the relative coordinate frame ($\mathbf{r} = \mathbf{r_1} - \mathbf{r_2}$) of the two atoms. In relative coordinates, the problem becomes a simple one-body problem. The solution of the corresponding Schrödinger equation

$$\left(-\frac{\hbar^2}{2m_r}\nabla^2 + V_{sc}(\mathbf{r})\right)\Psi_{\mathbf{k}}(\mathbf{r}) = E_{\mathbf{k}}\Psi_{\mathbf{k}}(\mathbf{r}) \tag{2.33}$$

far outside the range r_0 of the scattering potential can be expressed as the sum of the incident plane wave and the scattered wave function

$$\Psi_{\mathbf{k}}(\mathbf{r}) \sim e^{i\mathbf{kr}} + f(k,\Theta)\frac{e^{i\mathbf{kr}}}{r} \tag{2.34}$$

where $m_r = m/2$ is the reduced mass and $f(\mathbf{k},\Theta)$ the scattering amplitude. $f(\mathbf{k},\Theta)$ depends on the angle of the collision θ and on the wave number $\mathbf{k}$. The wave number $\mathbf{k}$ does not change in magnitude in the collision process due to the collision being elastic.
The total scattering cross section $\sigma(k)$ is obtained by integrating $f(k,\Theta)$ over the solid angle Ω

$$\sigma(k) = \int_\Omega \mathrm{d}\Omega\,|f(k,\Theta)|^2. \tag{2.35}$$

In the scattering process, different partial waves scatter differently and therefore acquire different scattering phase shifts δ_l. Here, $l = 0, 1, 2, ...$ denote the different angular momenta. Using a partial wave expansion of the scattering wave function, the scattering amplitude $f(k,\Theta)$ and thus the cross section $\sigma(k)$ for distinguishable particles are given by

$$f(k,\Theta) = \frac{1}{2ik}\sum_{l=0}^{\infty}(2l+1)(e^{2i\delta_l} - 1)P_l(\cos\Theta) \tag{2.36}$$

and

$$\sigma(k) = \sum_{l=0}^{\infty} \sigma_l(k) = \frac{4\pi}{k^2} \sum_{l=0}^{\infty} (2l+1) \sin^2(\delta_l). \tag{2.37}$$

For small collision energies ($k \to 0$) scattering in higher partial waves is suppressed by the repulsive centrifugal barrier[1] $\sim \hbar^2 l(l+1)/(2m_r r^2)$. One can show that $\delta_l \sim k^{2l+1}$ [75], so $\sigma_l(k)$ drops as k^{4l} for $k \to 0$. For this reason, only s-wave scattering (where $l = 0$) becomes relevant at low temperatures.
By defining the s-wave scattering length

$$a_s = -\lim_{k \ll 1/r_0} \frac{\tan \delta_0(k)}{k^2}, \tag{2.38}$$

the scattering cross section for s-wave scattering is given by

$$\sigma_0 = 4\pi a_s^2 \tag{2.39}$$

for non-identical particles. For identical bosons, one obtains $\sigma_0 = 8\pi a_s^2$ while for identical fermions $\sigma_0 = 0$ in agreement with the Pauli principle.
The relation (2.39) only holds for finite scattering lengths $a_s \ll 1/k$. For large scattering lengths $a_s \gtrsim k$ one finds the result [19, 21]

$$\sigma_0(k) = \frac{4\pi a_s^2}{1 + k^2 a_s^2} \tag{2.40}$$

which recovers $\sigma_0 = 4\pi a_s^2$ for $a_s^2 \ll 1/k^2$ and $\sigma_u = 4\pi/k^2$ for $a_s^2 \gg 1/k^2$. For s-wave collisions $\sigma_u = 4\pi/k^2$ is the largest possible cross section, which is obtained when $\sin^2(\delta_0) = 1$. This is the so-called unitary limit.

2.3 Feshbach resonances

In the previous chapter, the s-wave scattering length was essentially a constant determined by the interaction potential $V_{sc}(\mathbf{r})$. Unfortunately, the scattering potential cannot be manipulated easily to tune the scattering properties. For this purpose, magnetic Feshbach resonances have proven to be powerful instrument to manipulate particle interactions during collisions.
The principle of a magnetic Feshbach resonance can be well described by a two-channel model [9]. For this, we consider the interaction potential $V_{sc}(\mathbf{r})$ (the open channel) of the two colliding atoms colliding in an s-wave with collision energy $E_c \lesssim 0$ and a second interaction potential belonging to a different internal quantum state. The second interaction potential represents a so-called closed channel if its energetic asymptote[2] lies above the collision energy E_c (see figure 2.4 a)). A magnetic Feshbach resonance can occur, when a bound-state of the closed channel is energetically tuned into degeneracy with the collision energy E_c of the two colliding particles. This can be achieved, when the open and closed channel potentials have different magnetic moments $\mu_{m,1}$ and $\mu_{m,2}$. Their

[1] For ^{6}Li the barrier for $l = 1$ has a height of $\approx k_B \times 7$ mK [74].
[2] The asymptote refers to the potential energy of a scattering potential $V_{sc}(r)$ for $r \to \infty$

relative energy ΔE then shifts by $\Delta E = (\mu_{m,2} - \mu_{m,1}) \times B = \Delta\mu_m \times B$. If there is a coupling (e.g. hyperfine coupling) between the closed and open channel, the scattering wave function is affected by the bound state of the closed channel potential which leads to a change of the scattering phase shift and thus the scattering length a_s. When the bound state is energetically above the scattering state, $a_s < 0$ and the interaction is considered attractive. If it lies below, $a_s > 0$ and the interaction is repulsive. In the magnetic vicinity of the Feshbach resonance, the s-wave scattering length can be written as

$$a_s(B) = a_{bg}\left(1 - \frac{\Delta B}{B - B_0}\right). \tag{2.41}$$

Here, a_{bg} is the background scattering length, ΔB is the width and B_0 the position of the Feshbach resonance (see figure 2.4 b)). The width of the resonance is determined by the strength of the coupling between the bound state and the scattering state and depends on the internal states of the closed and open channel. At the position of the Feshbach resonance B_0 the scattering length diverges and changes sign. For repulsive interaction, when the bound state of the closed channel is energetically below the scattering state, Feshbach dimers of binding energy

$$E_b = \frac{\hbar^2}{m a_s^2} \tag{2.42}$$

can form.

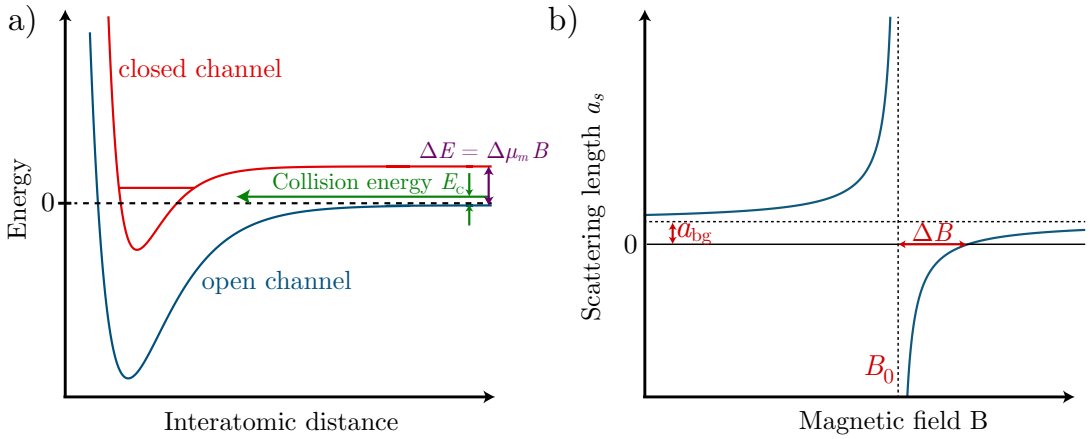

FIGURE 2.4: a) Two-channel model of a magnetic Feshbach resonance. Two atoms with collision energy $E_c > 0$ collide in an open-channel potential. A magnetic Feshbach resonance occurs, when a bound state of a closed channel is magnetically tuned to degeneracy with the collision energy, thereby strongly modifying the phase shift and scattering length. b) Scattering length a_s as a function of the magnetic field B in the vicinity of a magnetic Feshbach resonance at a field of B_0. a_{bg} is the background scattering length and ΔB the width of the resonance. The relation between a_s and B is given by Equation (2.41).

2.4 Lithium-6 and its broad Feshbach resonance

In our experiments, we cool, trap, manipulate and image clouds of neutral lithium-6 atoms. Most of these steps rely on electronically exciting the atoms, while manipulating their electronic states and scattering properties with external magnetic fields. For this reason, the following sections provide an overview of the electronic structure of lithium-6, its response to external magnetic fields and the origin of its exceptionally broad Feshbach resonance, which essentially enables us to precisely study the different interaction regimes.

2.4.1 Atomic structure

Like all Alkali metals, ^{6}Li has a single unpaired valence electron in its outer shell, the 2S orbital. Therefore, it has a total electron spin of $\mathrm{S} = 1/2$. Its nucleus consists of three neutrons and three protons that combine to a total nuclear spin of $\mathrm{I} = 1$. As a consequence, the total spin of a ^{6}Li atom is half-integer valued, which makes it a fermion[3].
For the electronic ground state, the orbital angular momentum is $\mathrm{L} = 0$. Therefore, the total electronic angular momentum is $\mathrm{J} = 1/2$. We label this state $2^2\mathrm{S}_{1/2}$. Due to the hyperfine coupling, the interaction between the nuclear spin and the electronic angular momenta, this state splits into two manifolds with total atomic angular momenta $\mathrm{F} = 1/2$ and $\mathrm{F} = 3/2$. At zero magnetic field, they are energetically separated by the hyperfine splitting $\Delta E = h \times 228.2\,\mathrm{MHz}$ [76].
For the first electronically excited states, the orbital angular momentum is $\mathrm{L} = 1$. Therefore, the possible total electronic angular momenta are $\mathrm{J} = 1/2$ and $\mathrm{J} = 3/2$. The two resulting states, the 2P states, are labelled $2^2\mathrm{P}_{1/2}$ and $2^2\mathrm{P}_{3/2}$ and energetically split by $h \times 10.053\,\mathrm{GHz}$ [76].
The hyperfine interaction further splits the $2^2\mathrm{P}_{1/2}$ state into two manifolds with $\mathrm{F} = 1/2$ and $\mathrm{F} = 3/2$ which are separated by $\Delta E = h \times 26.1\,\mathrm{MHz}$ in the absence of an external magnetic field.
The $2^2\mathrm{P}_{3/2}$ state has $\mathrm{J} = 3/2$ and therefore splits into three hyperfine states with $\mathrm{F} = 5/2$, $\mathrm{F} = 3/2$ and $\mathrm{F} = 1/2$, where $\mathrm{F} = 1/2$ is the energetically highest and $\mathrm{F} = 5/2$ the energetically lowest state of this manifold. Their energy separation is only $h \times 4.4\,\mathrm{MHz}$ in zero magnetic field. For this reason, these states are not optically resolved, as the linewidth of the 2P states is $\Gamma = 5.87\,\mathrm{MHz}$ [77].
The corresponding term scheme of ^{6}Li in the magnetic zero field is shown in Figure 2.5. The 2P states can by optically accessed from the $2^2\mathrm{S}_{1/2}$ ground state by dipole transitions of frequency $\nu \approx 447\,\mathrm{THz}$, or $\lambda = c/\nu = 671\,\mathrm{nm}$. The corresponding transitions are called the D_1 and D_2 lines, which have a characteristic red color, see figure 4.2.

[3] In contrast, ^{7}Li has an additional neutron in its core, resulting in $\mathrm{I} = 3/2$ which makes it bosonic.

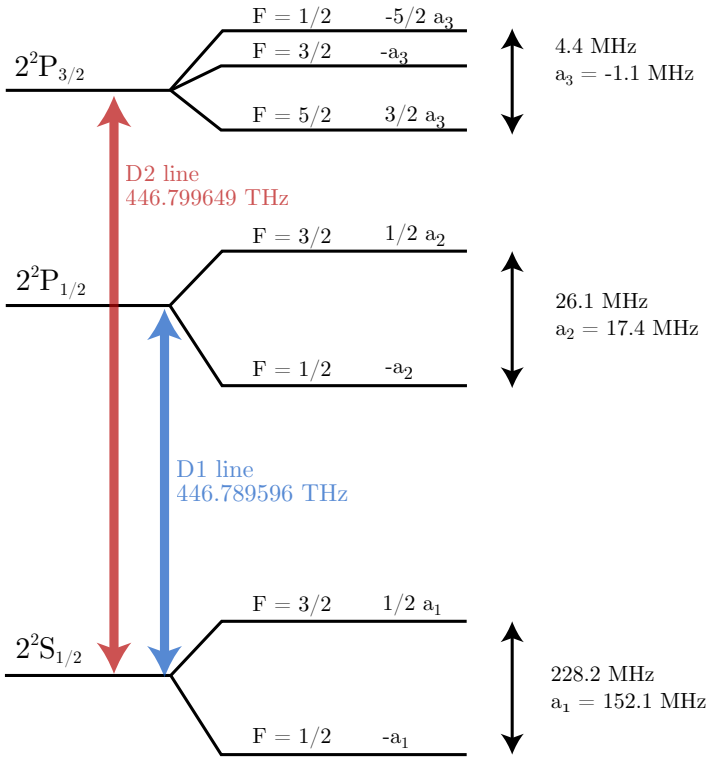

FIGURE 2.5: Term scheme of ^{6}Li showing the fine and hyperfine splittings of the lowest energy states in the absence of an external magnetic field. The origin of the different fine and hyperfine splittings is explained in the text in Section 2.4.1 Most of our experiments are performed with optical transitions from the hyperfine states of the $2^2S_{1/2}$ ground state to the hyperfine states of the $2^2P_{3/2}$ excited state. Values taken from [76].

2.4.2 ^{6}Li in the magnetic high field

The majority of our experiments are carried out at high magnetic fields, in the vicinity of the broad Feshbach resonance. When applying an external magnetic field, the $F = 1/2$ and $F = 3/2$ states of the $2^2S_{1/2}$ ground state split into a total of six states according to their magnetic quantum numbers $m_F = \pm 1/2$ for $F = 1/2$ and $m_F = \pm 3/2, \pm 1/2$ for $F = 3/2$.
For fields < 15 G the atoms are in the Zeeman regime. Here, J and I are coupled due to the hyperfine coupling and $F = J + I$ is a good quantum number. In this regime the energy splitting of the hyperfine states increases linearly with the magnetic field.
For stronger fields $\gg 100$ G, the magnetic moments of the electron and the nucleus decouple and couple individually to the external magnetic field. This regime is the Paschen-Back regime where F is no longer a good quantum number and the atoms have to be described by I and J (note that $J = S$, because $L = 0$ in the electronic ground state). The three states with $m_J = -1/2$ (and

$m_I = 1, 0, -1$), the so-called high-field-seeking states, linearly shift down in energy with approx $h \times 1.4$ MHz/G while the three states with $m_J = +1/2$ shift up with $\approx h \times 1.4$ MHz/G. We label these six states $|1\rangle$ - $|6\rangle$ where $|1\rangle$ is the energetically lowest and $|6\rangle$ the energetically highest state. The energy of these states as a function of the magnetic field is shown in Figure 2.6.

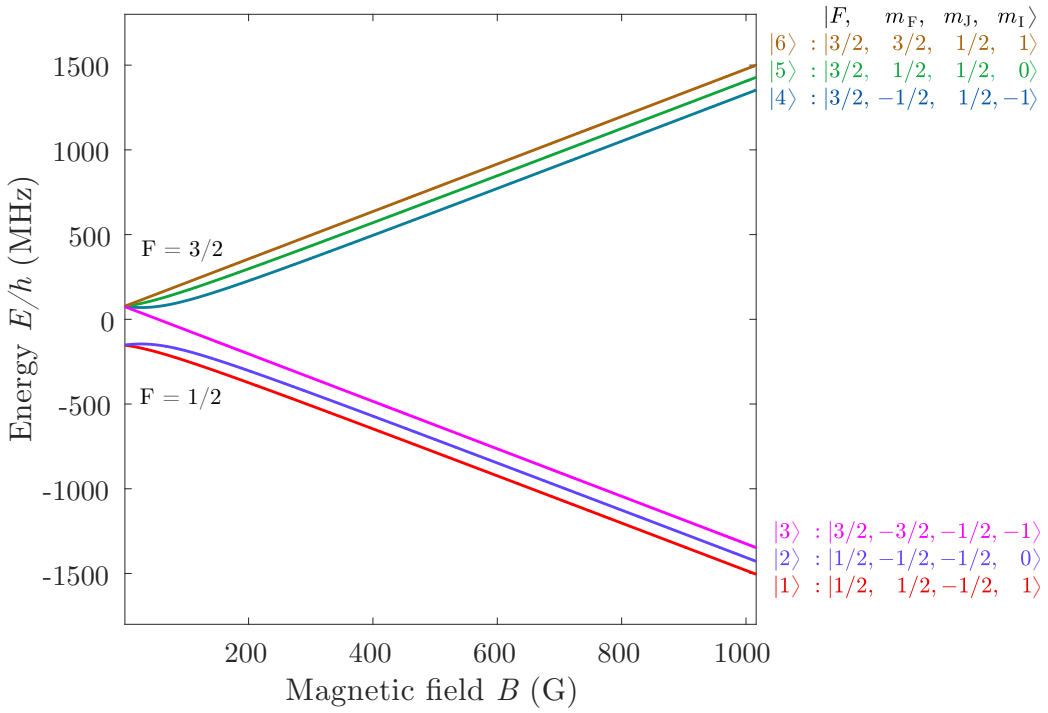

FIGURE 2.6: Zeeman splitting of the $2^2S_{1/2}$ ground state of ^{6}Li in the magnetic field range from 0 to ≈ 1000 Gauss. For a field $\lesssim 15$ G the atoms are in the Zeeman regime. For higher fields they enter the Paschen-Back regime.

In our experiments, we typically work with a spin-balanced mixture of atoms, where half of the atoms is in state $|1\rangle$ and the other half is in state $|2\rangle$. These states have a narrow magnetic Feshbach resonance at 543.3 G and an exceptionally broad resonance at 832.2 G [78]. The origin of this broad resonance is explained in the following section.

2.4.3 The broad Feshbach resonance of ^{6}Li

We carry out our experiments with a balanced mixture of atoms in two lowest Zeeman states $|1\rangle$ and $|2\rangle$. When these atoms scatter off each other, they feel different interaction potentials depending on the relative orientation of their electronic spin. The orientation can either be anti-parallel (singlet) or parallel (triplet).

In the Zeeman regime at low magnetic fields, the electronic and the nuclear spin are still coupled due to the hyperfine coupling. Therefore, the scattering state $|1\rangle|2\rangle$ is a superposition of singlet and triplet states.

Entering the Paschen-Back regime, the scattering potential is predominantly

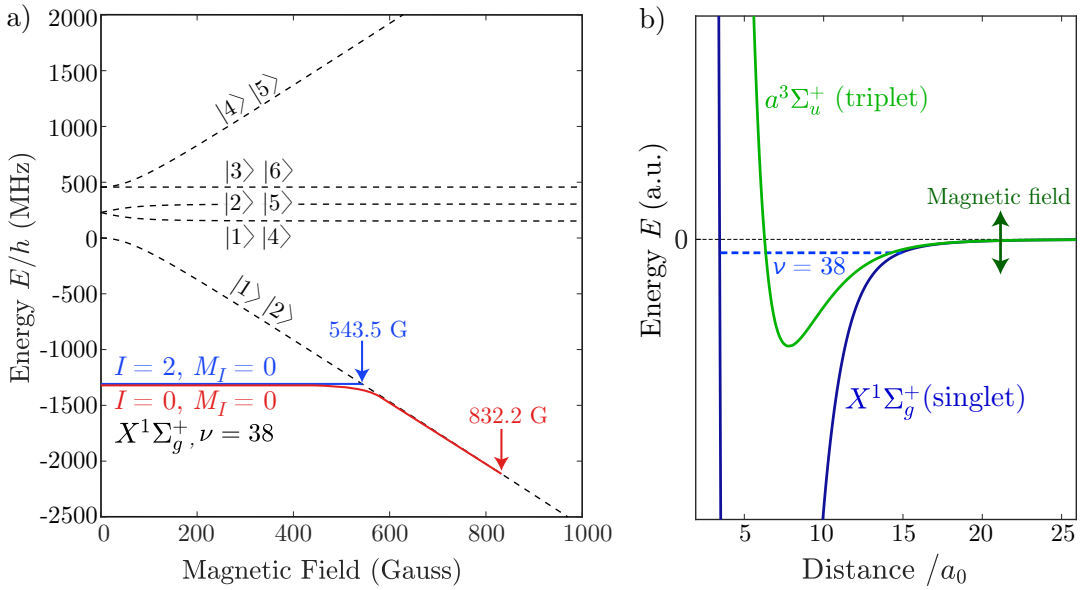

FIGURE 2.7: a) Zeeman energies of different atom-atom scattering channels with total spin projection $M_F = 0$. The energies are obtained by adding the respective Zeeman energies of the two separated atom channels (see Fig. 2.6). At 543.5 G and 832.2 G the energy of the $|1\rangle|2\rangle$ scattering state energetically crosses the energies of the most-weakly bound molecular states of the singlet potential $X^1\Sigma_g^+$ with vibrational quantum number $\nu = 38$ and molecular quantum numbers $I = 2$, $M_I = 0$ and $I = 0$, $M_I = 0$. These molecular bound states couple to the scattering state and cause the narrow and broad Feshbach resonance. The figure is recreated from Ref. [9], calculations of the molecular bound state energies have been provided by Jinglun Li. b) Singlet and triplet potentials for ^{6}Li. The energy of the atoms colliding in $|1\rangle|2\rangle$ can be magnetically tuned into resonance with the most-weakly bound state $\nu = 38$ of the singlet potential. The energy of this state (dashed blue line) is depicted exaggeratedly low with respect to the depth of the singlet and triplet potentials for illustrative reasons. Potential energy curves are taken from Ref. [79].

determined by the electronic state, which is $m_S = -1/2$ for both atoms. Consequently, the scattering state has almost pure triplet character at high magnetic fields. For this reason, the off-resonant background scattering length smoothly transitions from a linear combination of the singlet and triplet background scattering lengths a_{Si} and a_{Tr} at low magnetic fields to the pure triplet scattering length a_{Tr} at high fields. These scattering lengths are $a_{Si} = 45.154\,a_0$ and $a_{Tr} = -2113\,a_0$ [80]. The reason for the extraordinary large (negative) scattering length of the triplet potential is a virtual bound state just a few hundred kHz above fits energetic asymptote.

While the energy of the two colliding atoms linearly shifts down with ≈ -2.8 MHz/G at high magnetic fields due to the triplet nature of the scattering state (see Fig 2.7), the energy of the singlet molecular potential $X^1\Sigma_g^+$ is insensitive to magnetic fields. This potential has two (most-weakly) bound states with $\nu = 38$, $I = 2$, $M_I = 0$ and $\nu = 38$, $I = 0$, $M_I = 0$ approximately 1.321 GHz

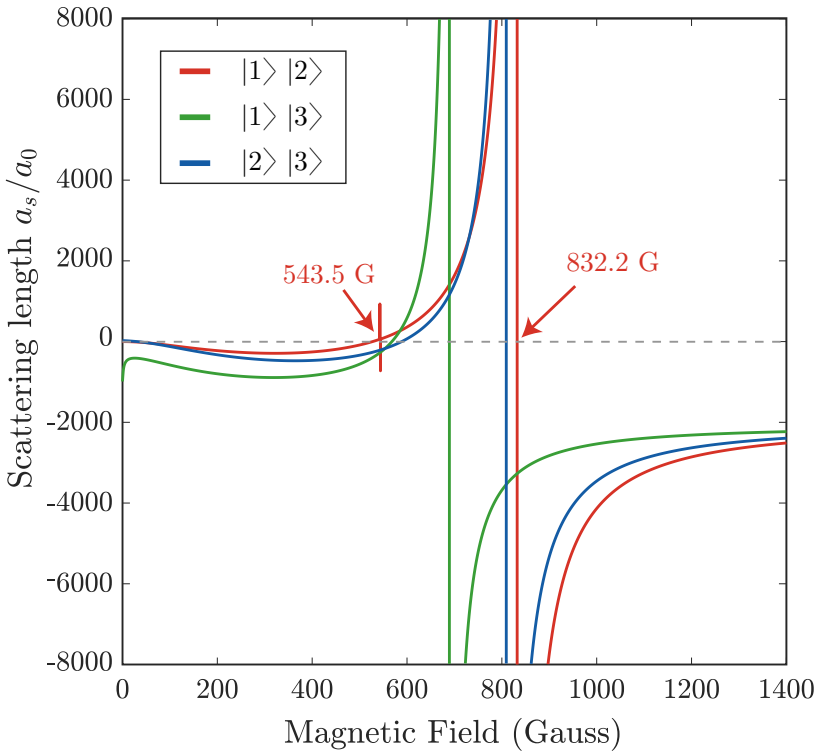

FIGURE 2.8: Magnetic field dependence of the s-wave scattering lengths for two colliding ^{6}Li atoms in the $|1\rangle|2\rangle$, $|1\rangle|3\rangle$ or $|2\rangle|3\rangle$ scattering states. All these mixtures experience exceptionally broad Feshbach resonances around $\approx$ 700-800 G. The figure is based on data from the supplemental material of [78].

and 1.308 GHz below its threshold [80]. At 543.5 G and 832.2 G these states couple to and energetically cross the scattering state $|1\rangle|2\rangle$ of the two colliding atoms, causing a narrow and a broad Feshbach resonance [80]. For $B < 832.2$ G the bound state of the singlet potential $X^1\Sigma_g^+$ with $\nu = 38$, $I = 0$, $M_I = 0$ lies energetically below the collision energy. This state strongly mixes with the scattering state which allows the colliding atoms to form Feshbach molecules (see Section 2.5.3 for more details). Using the parametrization from Equation (2.41), the broad Feshbach resonance can be characterized by $B_0 = 832.18$ G, $\Delta B = 262.3$ and $a_{bg} = -1582\,a_0$ [78]. The magnetic field dependent s-wave scattering lengths for atoms in the scattering states $|1\rangle|2\rangle$, $|1\rangle|3\rangle$ and $|2\rangle|3\rangle$ are shown in figure 2.8.
At 527.32 G, the s-wave scattering length a_s is zero, hence the two spin components $|1\rangle$ and $|2\rangle$ do not interact with each other as in an ideal non-interacting Fermi gas. For higher fields, a_s becomes large and positive and diverges to $+\infty$ at the resonance at 832.2 G. Above the resonance, the scattering length a_s is large and negative and slowly approaches the background scattering length of the triplet potential $a_{Tr} = -2113\,a_0$. The broad Feshbach resonance therefore allows for precisely tuning the interaction between the atoms in the two spin states, which allows us to realize and study fundamentally different gas phases.

2.5 The BCS-BEC crossover

The interactions between fermions of opposite spin are characterized by the so-called coupling constant or interaction parameter $(k_F a_s)^{-1}$. This parameter is dimensionless and essentially the ratio between the interparticle distance (as $k_F \sim n^{1/3}$) and their scattering length a_s. Thus, the smaller $|k_F a_s|^{-1}$ the stronger the interactions. Together with the temperature T of the gas in units of the Fermi temperature T_F, these two parameters fully parameterize a spin-balanced two-component Fermi gas [8, 81].
In our experiments, which we carry out with a balanced mixture of fermions in the two lowest hyperfine state $|1\rangle$ and $|2\rangle$, we have almost full control over both parameters. Using the broad Feshbach resonance at 832.2 G we can tune a_s and thus the coupling $(k_F a_s)^{-1}$. And by forced evaporative cooling (see Section 4.4.1 for more details), we can set the temperature T/T_F of the gas. This allows for experimentally realizing and studying all kinds of different superfluid and normal gas phases that are present in such a Fermi gas. These phases are illustrated in figure 2.9 and introduced in the following.

2.5.1 BCS regime

The Fermi gas is in the Bardeen-Cooper-Schrieffer (BCS) regime, when the interaction parameter $(k_F a_s)^{-1} \ll -1$, i.e. when the interactions between the atoms are weak and attractive.
In this regime, the atoms are in the normal thermal state when the chemical potential $\mu \ll E_F$ (see also figure 2.10). The atoms then obey Fermi statistics and the gas state is well described by the Fermi liquid theory [84, 85]. When the temperature is lowered, the chemical potential μ approaches the Fermi energy E_F and a Fermi sea starts to form where each quantum state up to E_F is occupied by one single fermion [8, 21, 22, 43]. Below the critical temperature T_C, the small attractive interactions allow for the formation of Cooper pairs at the surface of the Fermi sea, as predicted by the BCS theory and very recently also directly observed in mesoscopic ultracold Fermi gases [86]. Cooper pairs consist of two fermions of different spin (in our case the $|1\rangle$ and $|2\rangle$ states) and opposite momentum. For a homogeneous Fermi gas, the transition temperature T_C for Cooper pairs to form exponentially drops with $(k_F a_s)^{-1}$ in the BCS limit. From a simple mean-field approach one finds [19, 21]

$$\begin{aligned} T_{C,MF}^{\mathrm{hom}} &= \frac{8e^{\gamma}}{\pi e^2} \exp\left(-\frac{\pi}{2k_F|a_s|}\right) \times T_F^{\mathrm{hom}} \\ &\approx 0.614 \exp\left(-\frac{\pi}{2k_F|a_s|}\right) \times T_F^{\mathrm{hom}} \end{aligned} \tag{2.43}$$

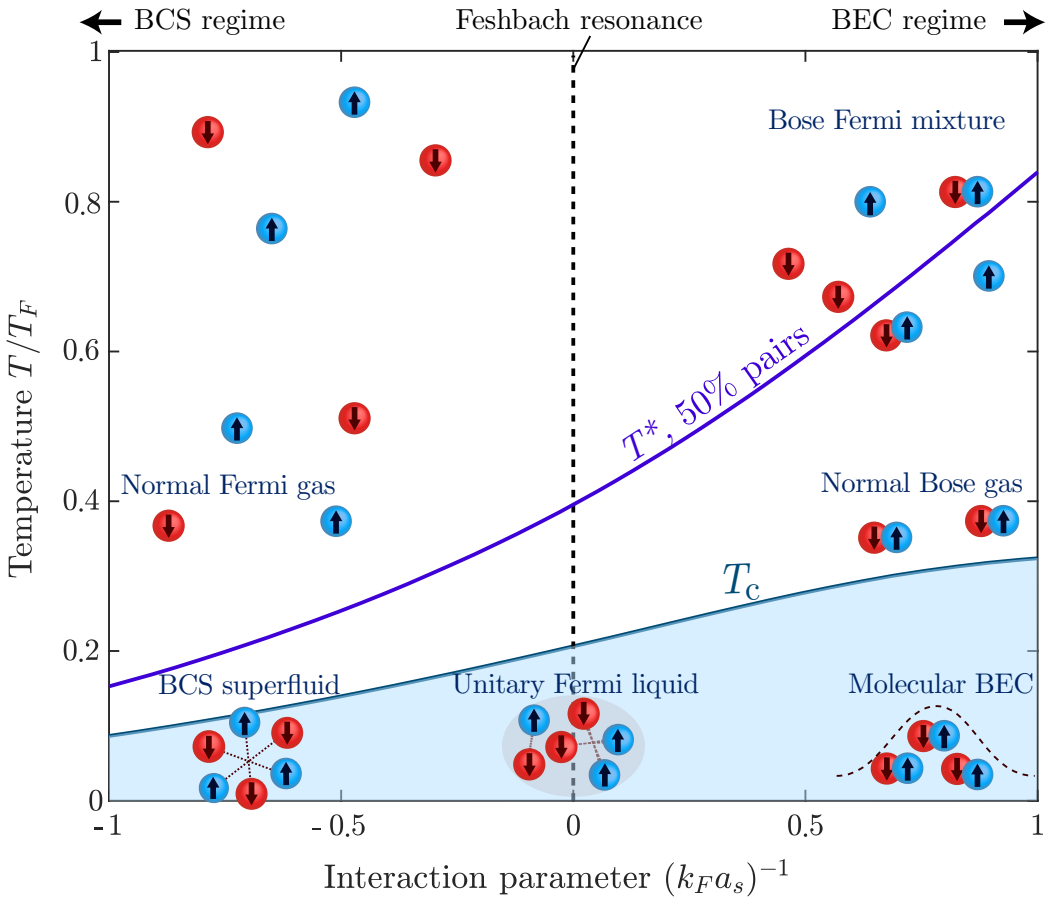

FIGURE 2.9: Phase diagram of a spin-balanced Fermi gas in the BCS-BEC crossover. The red and blue circles represent fermions of the two spin components and illustrate the different phases present in the crossover. The thin blue line marks the critical temperature for superfluidity T_C for a harmonically trapped Fermi gas, taken from [82]. Below the critical temperature, the gas is in a superfluid state. The superfluid state smoothly transitions from a BCS type superfluid in the BCS regime at $(k_F a_s)^{-1} \ll -1$ to a Bose-Einstein condensate of molecules in the BEC regime at $(k_F a_s)^{-1} \gg 1$. In between where $(k_F a_s)^{-1}$, we find the resonantly interacting unitary Fermi liquid. Above T_C the gas is in a normal (thermal) state. On the BEC side, the gas is in thermal equilibrium with unpaired fermions and diatomic molecules. The purple curve, taken from [83], marks T^*, the temperature at which 50% of the atoms are paired. Remarkably, this curve continues on the BCS side. This is a consequence of pair formation driven by the strong interparticle interactions in the vicinity of the Feshbach resonance. For more information, see text. T^* gradually approaches T_C for $(k_F a_s)^{-1} \to -\infty$.

while a more sophisticated calculation yields [22, 87]

$$T_C^{\text{hom}} = \frac{e^\gamma}{\pi}\left(\frac{2}{e}\right)^{7/3} \exp\left(-\frac{\pi}{2k_F|a_s|}\right) \times T_F^{\text{hom}}$$
$$\approx 0.277 \exp\left(-\frac{\pi}{2k_F|a_s|}\right) \times T_F^{\text{hom}}. \tag{2.44}$$

Here $\gamma \approx 0.5772$ is Euler's constant. For a harmonically trapped Fermi gas, T_C is shown in Figure 2.9. It is approximately $T_C = 0.02\,(0.05,\, 0.08)\,T_F$ for interaction parameters $(k_F a_s)^{-1} = -2\,(-1.5,\, -1)$ [16]. In our experiments, the lowest temperatures we can achieve on the BCS side are $\approx 0.03 - 0.04\,T_F$. For this reason, we can study the BCS superfluid phase up to $(k_F a_s)^{-1} \approx -1.75$. In the deep BCS limit, the formation of (Cooper) pairs goes hand in hand with the transition to the superfluid state. In contrast, pairs on the BEC side, which are present there as molecules, can also exist above T_C (see Section 2.5.3). These two different pairing phenomena smoothly merge into each other in the BCS-BEC crossover. In the vicinity of the Feshbach resonance, the concept of preformed pairs emerges, where pairing arises from many-body effects due to the strong interparticle interactions [15, 83]. These pairs already form above the superfluid transition temperature but do not yet condense into a superfluid state. Therefore, on the BCS side, pairing occurs even above T_C, but the pairs are more diffuse and exhibit strong correlations only at very low temperatures [16]. To describe this phenomenon, a temperature T^*, also called the pair-breaking temperature, is introduced. On the BEC side, it coincides with the temperature at which 50% of the atoms are paired to Feshbach molecules. For $(k_F a_s)^{-1} \to -\infty$ the pair-breaking temperature T^* gradually approaches the critical temperature T_C.

2.5.2 Unitarity

At the position of the Feshbach resonance, the scattering length a_s diverges to infinity and effectively drops out of the description of the gas properties [8]. In this regime, the thermodynamical properties of the resonantly interacting Fermi gas are universal and only depend on k_F (or the density n or Fermi energy E_F since $E_F \propto k_F^2 \propto n^{2/3}$) and T/T_F [21, 88].

At zero temperature , where also T/T_F drops out, there must therefore be a direct and universal relation between all thermodynamical properties and k_F (n, E_F) only. For example, the chemical potential μ of the homogeneous gas is related to the Fermi energy E_F^{hom} via [19]

$$\mu = \xi\, E_F^{\mathrm{hom}} \tag{2.45}$$

where ξ is the Bertsch parameter. Due to the universality, the precise determination of the Bertsch parameter has been an ongoing subject for both theoretical and experimental studies. While early estimations for ξ vary widely (0.32(13) [89], 0.44 [90], 0.74(7) [91]), more recent experiments and Monte Carlo simulations seem to come to an agreement on $\xi = 0.367$ [92, 93]. The Bertsch parameter does not only play a role in describing homogeneous Fermi gases at unitarity. For the harmonically trapped gas one finds [19]

$$\mu_0 = \sqrt{\xi}\, E_F \approx 0.61\, E_F \tag{2.46}$$

for the central chemical potential μ_0. From this, the zero-temperature density distribution

$$n_{U,T=0}(\mathbf{r}) = \frac{8N}{\pi^2 R_{U,x} R_{U,y} R_{U,z}} \left(1 - \frac{x^2}{R_{U,x}^2} - \frac{y^2}{R_{U,y}^2} - \frac{z^2}{R_{U,z}^2}\right)^{3/2} \tag{2.47}$$

of the unitary Fermi gas in a harmonic trapping potential can be simply deduced from the density distribution of an ideal Fermi gas (2.14) by rescaling the Thomas-Fermi radii $R_{U,i} = \xi^{1/4} R_{TF,i} \approx 0.78 R_{TF,i}$ [19]. As $R_{U,i} < R_{TF,i}$, one can see that the unitary Fermi gas has effectively attractive interactions.

At finite temperatures, the equation of state (EoS) has been determined experimentally [88] for a unitary homogeneous Fermi gas. The results of these measurements were functions of μ and T to rescale all thermodynamical observables of an ideal Fermi gas to the scenario of a resonantly interacting Fermi gas. Moreover, a sharp kink in the compressibility and the specific heat has been observed at $T_C \approx 0.167(13)$, indicating the onset of superfluidity [88].
For temperatures above $\approx T_F$, the unitary, resonantly interacting Fermi gas is almost thermal and therefore shows similar properties as a thermal ideal Fermi gas despite the large interparticle interactions [70, 88]. This can be seen e.g. in figure 2.10 where the chemical potentials for both a unitary and an ideal Fermi gas are shown as a function of temperature T/T_F.

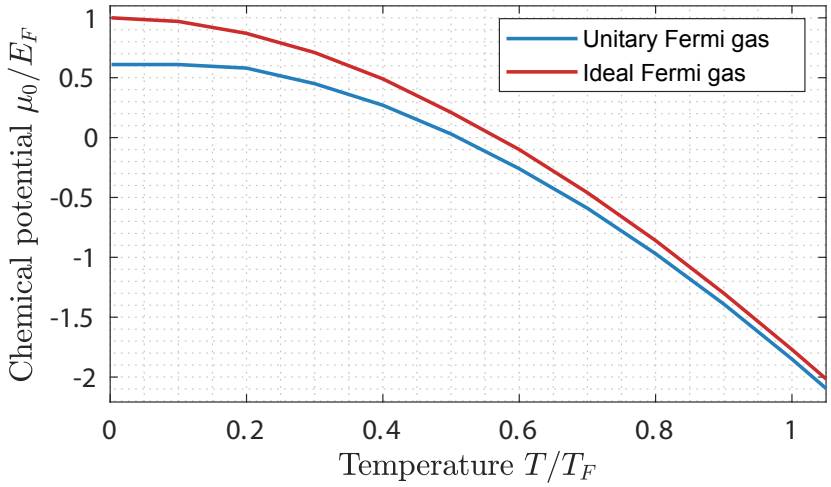

FIGURE 2.10: Central chemical potential μ_0/E_F for a harmonically trapped Fermi gas without interactions (blue) and resonant interactions (red). The result for the resonantly interacting, unitary Fermi gas was obtained from the equation of state measurements [88]. The ideal Fermi gas is characterized by an interaction parameter of $(k_F a_s)^{-1} \to -\infty$, while the unitary Fermi gas has $(k_F a_s)^{-1} = 0$. The temperature-dependent chemical potential on the BCS side, where $(k_F a_s)^{-1} < 0$, therefore lies between these two extremes.

2.5.3 BEC regime

In the BEC regime, the interparticle interactions are effectively repulsive and the most weakly bound state of the $X^1\Sigma_g^+$ singlet potential, with a vibrational quantum number $\nu = 38$, lies energetically below the scattering state (see Figure 2.7). This state strongly couples to the scattering state [80], enabling the formation of diatomic Feshbach molecules via exothermic three-body collisions. In these collisions, two fermions of different spin form a molecule while the third atom assures momentum and energy conservation. At low temperatures, the collision between two unpaired fermions of different spin is characterized by the scattering length a_s. For the collision between two dimers or a dimer and an unpaired fermion, the scattering lengths are given by $a_{dd} = 0.6\,a_s$ [94, 95] and $a_{ad} = 1.18\,a_s$ [8] respectively. In the vicinity of the Feshbach resonance, the binding energy of the dimers is given by [9]

$$E_b = \frac{\hbar^2}{2m_r a_s^2} = \frac{\hbar^2}{m a_s^2} \tag{2.48}$$

where $m_r = m/2$ is the reduced mass and m is the mass of each of the two atoms that form the dimer. Further away from the resonance for smaller a_s, the expression for the binding energy has to be modified [96]

$$E_b = \frac{\hbar^2}{m(a_s - \bar{a})^2}\left(1 + 0.9179\frac{\bar{a}}{a_s - \bar{a}} - 0.9468\frac{\bar{a}^2}{(a_s - \bar{a})^2}\right) \tag{2.49}$$

to take into account the finite range $r_0 = (mC_6/\hbar^2)^{1/4}$ of the molecular potential. The quantity $\bar{a} = \frac{2\pi}{\Gamma(\frac{1}{4})^2}\, r_0 \approx 0.478\, r_0 = 29.9\, a_0$ can be regarded as a mean scattering length and $\Gamma(\dots)$ is the gamma function.
In contrast to the BCS regime, where the sudden formation of Cooper pairs goes hand in hand with the transition to the superfluid phase at T_C, pairing on the BEC side already occurs well above T_C with the formation of Feshbach molecules. These molecules are in a thermal equilibrium with the unpaired atoms [97], and their chemical potentials are related via [19, 98]

$$\mu_B = 2\mu + E_b \tag{2.50}$$

where μ_B denotes the chemical potential of the dimers and μ the chemical potential of the unpaired atoms. This relation quantitatively represents the pairing of two atoms to form a diatomic molecule with the release of binding energy E_b. As the chemical potential changes with temperature T and the binding energy changes with scattering length a_s, the fraction of diatomic molecules (the pair fraction) consequently also depends on T and a_s. It indeed turns out, that the pair fraction is a function of the dimensionless quantities T/T_F and $(k_F a_s)^{-1}$ only [15, 16]. Qualitatively speaking, the molecules break up when their thermal energy $T \times k_B$ becomes larger than the binding energy E_b. So, for fixed interaction parameter $(k_F a_s)^{-1}$ the pair fraction drops when the temperature of the atom cloud is increased. On the other hand, at fixed temperature the pair fraction increases when $(k_F a_s)^{-1} \propto \sqrt{E_b}$ is increased. In earlier measurements,

we mapped out the pair fraction on the BEC side of a harmonically trapped Fermi gas as a function of $(k_F a_s)^{-1}$ and T/T_F (see Section 4.7 and References [15, 99] for more details).
At low temperatures $T \lesssim 0.5 T_F$ in the BEC regime where $(k_F a_s)^{-1} > 1$, essentially all atoms of a two-component spin-balanced Fermi gas are paired to molecules [15, 16]. These molecules can be regarded as bosons, since their binding energy sets the largest energy scale of the gas, compared to the interaction energy and the thermal energy. Below the critical temperature, the molecules undergo Bose-Einstein condensation and form a molecular Bose-Einstein condensate (mBEC) [19]. For $(k_F a_s)^{-1}$ the critical temperature for a harmonically trapped Fermi gas is $T_C \approx 0.518\, T_F$ and the ratio of condensed molecules to the total number is given by $N_0/N = 1 - (T/T_C)^3$ (see Section 2.1.2). Approaching the Feshbach resonance, the critical temperature decreases. The reason for this is are increasing repulsive interactions that prevent the gas from reaching the critical density required for condensation [71]. More details on pairing and the effects of the interparticle interactions on the BEC side are given in Chapter 9.

2.6 Particle correlations and Tan's contact

As outlined in the previous section, the crossover from the BCS to the BEC regime in a strongly interacting Fermi gas is a highly interesting physical setting. In the crossover, the superfluid gas state fundamentally changes its physical character. It transitions from the BCS regime of weak attractive interactions, where fermions of opposite spin pair up in momentum space to form Cooper pairs on top a Fermi sea to the weakly repulsive BEC regime, where pairing takes place in real space when diatomic molecules with bosonic character are formed. In between lies the unitary regime, where the two-body scattering length a_s diverges to $\pm$ infinity. The transition from the BCS to the BEC state happens smoothly and simply by changing the external magnetic field across the Feshbach resonance. This naturally raises the question of what happens in the intermediate region, the crossover, and how the physical properties of the Fermi gas can be quantified there.

2.6.1 Tan relations

In 2008, Shina Tan formulated a set of very fundamental relations for strongly interacting Fermi gases with two spin components and introduced a new and central quantity that appears in all these relations - the so-called Tan contact [10–12]. In a microscopic picture, the contact is a measure for short-range two-body correlations and quantifies the likelihood of finding two interacting fermions of opposite spin at very small distance [10, 32, 33]. However, the parameter also appears in various relations that describe the macroscopic state of the system.
To highlight the importance of the contact parameter for strongly interacting Fermi gases and to explain how its value can be determined, the relations are introduced in the following. Note that one often refers to two quantities when talking about the contact. The first one is the contact density C with dimension m^{-4}. This is usually used to describe homogeneous systems, where the density

(and thus the contact) is constant. The other quantity is the total contact of a system $\mathcal{I}$ with dimension m^{-1}. For homogeneous systems the total contact $\mathcal{I}$ is simply $\mathcal{I} = CV$ where V is the volume that the system occupies. For inhomogeneous (e.g. harmonically trapped) Fermi gases, $\mathcal{I}$ is obtained by integration $\mathcal{I} = \int \mathrm{d}^3 r\, C(\mathbf{r})$.

(1) The tail of the momentum distribution for fermions of both spin components σ ($\sigma = \uparrow, \downarrow$) is given by [32, 33]

$$\lim_{k\to\infty} n_\sigma(\mathbf{k}) = \frac{C}{k^4}. \tag{2.51}$$

So for large momenta k associated with short-range interactions, $n_\sigma(\mathbf{k})$ drops with $1/k^4$ and the prefactor is given by the contact density C. The momentum distribution $n_\sigma(k)$ for a spin-balanced Fermi gas with N_σ atoms per spin state is normalized such that $\int_0^\infty \mathrm{d}^3 k\, \frac{n_\sigma(k/k_F)}{(2\pi)^3} = N_\sigma$ [100]. In the zero-temperature BEC limit, relation (2.51) agrees well with the momentum distribution obtained from the Fourier transform of the molecular wave function

$$\Psi(\mathbf{r}) = \frac{1}{\sqrt{2\pi a_s}} \frac{1}{r} e^{-r/a_s} \tag{2.52}$$

which is[4] [101]

$$n(\mathbf{k}) = \frac{4}{3\pi}(k_F^{\mathrm{hom}} a_s)^3 \frac{1}{(k^2 a_s^2 + 1)^2} \xrightarrow{k\to\infty} \frac{4(k_F^{\mathrm{hom}})^3}{3\pi a_s} \frac{1}{k^4} = \frac{4\pi n}{a_s} \frac{1}{k^4}. \tag{2.53}$$

From this, one sees that the contact in the BEC limit must be $C = \frac{4\pi n}{a_s}$. As the density of molecules is $n_d = n/2$, each molecule contributes with $\frac{8\pi}{a_s}$.

(2) The total energy of a strongly interacting Fermi gas is the sum of the kinetic energy E_K, the interaction energy E_I and the potential energy E_V and is given by [33]

$$E = \sum_{\sigma,k} \int \frac{\mathrm{d}^3 k}{(2\pi)^3} \underbrace{\frac{\hbar^2 k^2}{2m}}_{\text{kinetic energy } E_K} \underbrace{\left(n_\sigma(\mathbf{k}) - \frac{C}{k^4} \right)}_{\text{interaction energy } E_I} + \underbrace{\frac{\hbar^2 C V}{4\pi m a_s}}_{\text{pot. energy } E_V}. \tag{2.54}$$

Note that the term $-C/k^4$ is not part of the kinetic energy E_K, but belongs to the interaction energy E_I. It has to be subtracted from $n_\sigma(\mathbf{k})$ before the integration, as otherwise the integral would be ultraviolet divergent [33].

(3) The correlation between the (real space) densities for the two spin states at points $\mathbf{r}$ separated by a distance $\mathbf{d}$ is given by [10, 33]

$$\Big\langle n_\uparrow(\mathbf{r} + \mathbf{d}/2)\; n_\downarrow(\mathbf{r} - \mathbf{d}/2) \Big\rangle = \frac{C(\mathbf{r})}{16\pi^2} \left(\frac{1}{d^2} - \frac{2}{a_s d} \right) + O(d^0). \tag{2.55}$$

[4] The Fourier transform of $\Psi(\mathbf{r})$ yields the momentum space wave function $\Psi(\mathbf{k}) = (2\pi)^{-3/2} \int \Psi(\mathbf{r}) \exp(-i\mathbf{k}\mathbf{r})\, \mathrm{d}^3 r = a_s^{3/2}(1 + k^2 a_s^2)^{-2}/\pi$, which satisfies $\int |\Psi(\mathbf{k})|^2 \mathrm{d}^3 k = 1$. As $n(\mathbf{k}) \propto |\Psi(\mathbf{k})|^2$ one obtains the result from Equation (2.53) after normalization.

The correlation function is closely related to the square of the two-body scattering wave function[5] $\Psi_s(r) \propto \frac{1}{r}(1-\frac{r}{a_s}) = \frac{1}{r} - \frac{1}{a_s}$ [102] given by

$$|\Psi_s(r)|^2 = \frac{1}{r^2} - \frac{2}{a_s r} + \frac{1}{a_s^2} \approx \frac{1}{r^2} - \frac{2}{a_s r}. \tag{2.56}$$

for $a_s \gg r$ where the prefactor in Equation (2.55) is proportional to the contact C.
If one integrates both side of Equation (2.55) over a small sphere with radius r_s, one obtains the number of pairs within the volume of the sphere $V = \frac{4}{3}\pi r_s^3$. The calculation yields [10, 33]

$$\iint_{\text{sphere}} \left\langle n_\uparrow(\mathbf{r}+\mathbf{d}/2)\, n_\downarrow(\mathbf{r}-\mathbf{d}/2)\right\rangle = N(\mathbf{r}) = \frac{r_s^4}{4} C(\mathbf{r}) \propto C(\mathbf{r})\, V^{4/3}. \tag{2.57}$$

which is the microscopic interpretation of the contact explained earlier. For this relation to hold, r_s has to be smaller than the absolute value of the scattering length $|a_s|$ but larger than the range of the scattering potential $r_0 = (mC_6/\hbar^2)^{1/4}$ which is $\approx 62.5\, a_0$ for ^{6}Li. Intuitively, one would expect that the number of pairs scales with $N_\mathrm{p}(\mathbf{r}) \propto V^2$. The determined proportionality $N_\mathrm{p}(\mathbf{r}) \propto V^{4/3}$ results from the strong correlations associated with the large scattering length and implies that the actual pair density in a small volume is larger than one would expect. See also Reference [33] for more details.
In addition, the correlation function is naturally linked to the pair fraction of a Fermi gas. In Reference [16], calculations of the pair correlation function based on a t-matrix approach were used to determine the fraction of paired fermions in a spin-balanced Fermi gas in the BCS-BEC crossover. This was achieved by fitting the spatial profile of the molecular wave function from Equation (2.38) to the obtained correlation functions. The goodness of fit serves as a measure of the pair fraction. This fraction was also experimentally determined in recent work of ours [15]. For more details on this, see Section 4.7.

(4) The adiabatic sweep theorem states, that the change of the systems total energy E with scattering length a_s at fixed entropy S and atom number N is given by [10, 33]

$$\left(\frac{\mathrm{d}E}{\mathrm{d}(-1/a_s)}\right)_{S,N} = \frac{\hbar^2 C V}{4\pi m} = \frac{\hbar^2 \mathcal{I}}{4\pi m} \tag{2.58}$$

which follows from the energy relation (2.54). Since this relation describes how the total energy E changes with $1/a_s$ (and not a_s), there is no conflict with convergence at the position of the Feshbach resonance, where a_s diverges.
In the low temperature BCS limit ($a_s \to 0^-$), the largest scattering length dependent contribution to the systems energy E is the mean-field energy. This yields a contact $C = 16\pi^2 a_s^2 (n/2)^2$ [11]. The result is essentially the product of

[5] This wave function is also recovered from the molecular wave function in Equation (2.52) in the limit of $a_s \gg r$, corresponding to the limit of the binding energy $E_b = \hbar^2/(m a_s^2)$ of a weakly-bound Feshbach molecule approaching zero.

the scattering cross sections $4\pi a_s^2$ (see eq. (2.39)) and the densities $(n/2)$ of the two spin components.

(5) The generalized virial theorem is another Tan relation, which provides an expression for the total energy [12, 33]

$$E = \frac{\beta+2}{2} E_V - \frac{\hbar^2 C V}{8\pi m a_s} \tag{2.59}$$

of a Fermi gas in an external trapping potential of the shape

$$V(\mathbf{r}) = r^\beta f(\mathbf{r}/r) \tag{2.60}$$

satisfying $\beta > -2$, $\beta \neq 0$ and $\beta\, f(\mathbf{r}/r) > 0$ where $f(\mathbf{r}/r)$ is any smooth function. For the case of a harmonic potential $\beta = 2$ and one obtains $E = 2E_V - \hbar^2 C V/8\pi m a_s$.

(6) The pressure relation for a homogeneous Fermi gas gives an expression for the pressure P in terms of the total energy E and is given by [12]

$$P = \frac{2}{3} E/V + \frac{\hbar^2 C}{12\pi m a_s}. \tag{2.61}$$

(7) Inelastic two-body losses in a strongly interacting Fermi gas lead to a decrease of the atom number N over time t at a rate $\mathrm{d}N/\mathrm{d}t$. Due to the presence of a loss channel, the total energy of the system acquires a small imaginary part $E \to E - E_i/2$. The time evolution of the Fermi gas can be effectively described by [31]

$$\exp\left[-i(E - iE_i/2)t/\hbar\right] \tag{2.62}$$

such that $-\mathrm{d}N/\mathrm{d}t = -2\mathrm{Im}[\mathrm{d}E] = E_i/\hbar$. Correspondingly, the scattering length also acquires a small imaginary part [31], due to the collisional loss[6]. The collision is then quantified by the complex scattering length

$$a = a_s + \mathrm{Im}[a]. \tag{2.63}$$

By taking the imaginary part of the adiabatic sweep theorem (2.58) and using the mathematical identity $\mathrm{Im}[1/a] = -\mathrm{Im}[a]/|a|^2$, one obtains a very fundamental relation between the two-body loss rate of a Fermi gas and the contact [31–33]

$$-\frac{\mathrm{d}N}{\mathrm{d}t} = -2\mathrm{Im}[\mathrm{d}E] = \frac{\hbar\,\mathrm{Im}[\mathrm{d}a]}{2\pi m} CV = -\frac{\hbar\,\mathrm{Im}[a]}{2\pi m|a|^2} CV = -\frac{\hbar\,\mathrm{Im}[a]}{2\pi m|a|^2}\mathcal{I} \tag{2.64}$$

where a is now a complex-valued scattering length. For more details, see Ref. [31]. This relation is qualitatively quite intuitive, because two-body loss naturally goes hand in hand with two atoms being at close range.

[6] According to Equation (2.38), the s-wave scattering phase shift δ_0 is proportional to the scattering length a_s for small a_s. Therefore, the scattering wave function of the colliding particles acquires a phase factor $\sim e^{i\delta(k)}$. If a_s has a small imaginary part, this leads to an exponential decay of the wave function, which is associated with collisional loss.

(8) Two more relations were found shortly after, relating the contact also to the tails of radio frequency (RF) spectra [103, 104] which drop with $C/\omega^{3/2}$ at high frequency ω and to the lineshape of Bragg spectra [105].

This whole set of relations highlights the importance of the contact parameter for understanding strongly interacting Fermi gases. For this reason, its value has been investigated experimentally and theoretically in various approaches over the years. Experimental approaches include measurements of the contact from the momentum distribution [100, 106], radio frequency (RF) spectroscopy [100, 107, 108], Bragg spectroscopy [109] and inelastic decay measurements in an ultracold gas mixture of fermions and a single bosonic impurity [110]. Theoretically, efforts for its determination were made using Monte Carlo simulations [111, 112], calculations based on the Luttinger-Ward formalism [113], large-N expansions [114], high temperature virial expansions [70, 105] and t-matrix calculations [16], to just name a few examples.
In all these studies, the contact was determined only in specific regions of the BCS-BEC crossover phase diagram, focusing either on the $T/T_F = 0$ or $(k_F a_s)^{-1} = 0$ regimes or the high temperature limits where $T \gtrsim T_F$. Within this thesis, I quite precisely determined the value of the contact in the entire phase diagram of the BCS-BEC crossover, using a recently proposed scheme based on photo-induced two-body loss [31]. It essentially makes use of relation (2.64), which links the contact to the loss rate of the Fermi gas. More details on this work are given in Chapters 6 and 7.

Chapter 3

Experimental setup

To study ultracold, strongly interacting Fermi gases, we cool, trap and manipulate dilute clouds of ^{6}Li atoms. This particular atomic species offers a broad magnetic Feshbach resonance, allowing for precise control of interparticle interactions. Our experimental design for this follows the setups in Innsbruck and Heidelberg [115, 116], which have proven to be simple and robust. In the following sections, I will introduce the current setup in Ulm and describe the main components of our experiment. These are the ultra-high vacuum system, the coil systems for the magnetic fields, the experimental control unit, and the laser systems. Detailed information on the individual components can also be found in several master's theses [117–121], in the PhD thesis of Daniel Hoffmann [99] and in the forthcoming PhD thesis of Thomas Paintner, which is currently under preparation.

3.1 Vacuum system

All experiments described in this thesis are conducted in an ultra-high vacuum (UHV) environment at a background pressure of $< 10^{-10}$ mbar. UHV conditions are essential for trapping and cooling atoms to reach the quantum degenerate regime. Without isolation from the ambient environment, a trapped ultracold atom cloud would become unstable due to collisions with room temperature ambient gas. At UHV, the lifetime of an ultracold gas can be extended to several ten seconds, sufficient for performing experiments in the quantum degeneracy regime. Figure 3.1 depicts our UHV system, which consists of two main components: the oven chamber and the main experimental chamber.

In the oven chamber, enriched Lithium-6 (consisting of 95 mole percent ^{6}Li and 5 mole percent ^{7}Li) is heated up in an oven (see section 3.2). The melting point of ^{6}Li is at around 485 K. By heating the lithium to a temperature of 720 K, we generate a small gas phase above the liquid lithium with a vapor pressure of $\approx 6 \times 10^{-4}$ mbar [122, 123]. The lithium vapor exits the oven through a small aperture, creating a constant flux of individual, optically addressable ^{6}Li atoms that travel towards the main experimental chamber. The oven is attached to a large titanium sublimation pump, to which an ion getter pump (Agilent VacIon Plus 40) with a pump volume of 40 l/s is connected (see Fig. 3.1). In the early stages of the bake-out, both pumps were used. We now only use the ion getter pump, as it can also maintain a sufficient pressure and we can preserve the titanium filaments for future bake-outs. Despite the high temperature of the

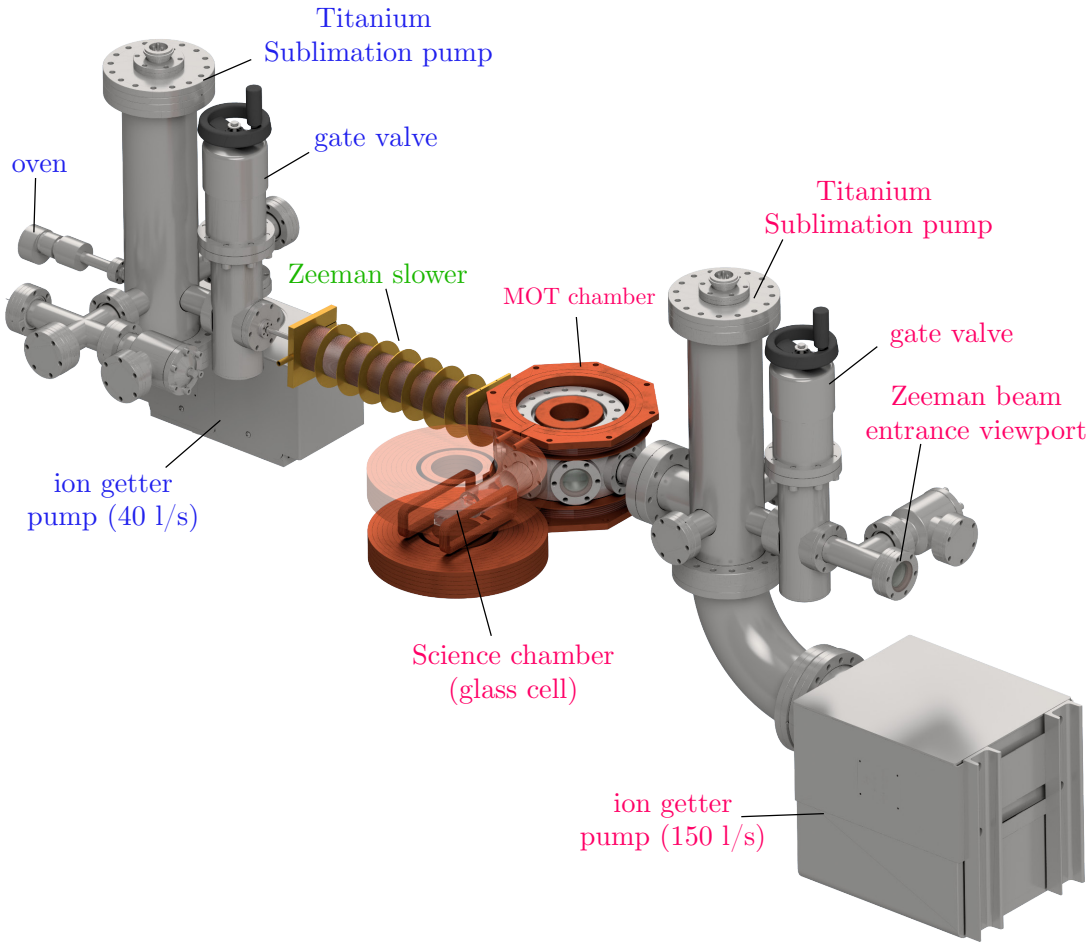

FIGURE 3.1: Illustration of our ultra-high vacuum system for creating ultracold, strongly interacting Fermi gases of ^{6}Li. The setup consists of the oven chamber (blue labeling) and the main experimental chamber (red labeling). In the oven, lithium is heated to 720 K to generate lithium vapor. An ion getter pump with a pump volume of 40 l/s reduces the oven chamber pressure to 6×10^{-10} mbar. The oven chamber is connected to the main experimental chamber by a 40 cm long tube located inside the Zeeman slower (green labeling), which also serves as a differential pumping stage. The experimental chamber includes the MOT chamber, the science chamber and an ion getter pump with a pump volume of 150 l/s. Each chamber is also equipped with a titanium sublimation pump. Two gate valves allow for isolating the experimental chamber from other parts of the vacuum system. More details are given in the text.

oven, we reach a background pressure of $\approx 6 \times 10^{-10}$ mbar in the oven chamber. With a gate valve, the oven chamber can be isolated from the rest of the vacuum setup. This enables us to refill the oven without having to bake out the main chamber experimental afterwards.

The main experimental chamber consists of the spherical octagonal MOT chamber (MCF600-SphOct-F2C8) from Kimball physics, the science chamber, which is

a glass cell from Hellma Analytics, another titanium sublimation pump and another ion getter pump (Agilent VacIon Plus 150) with a pump volume of 150 l/s [99]. The main chamber connects to the oven chamber through a ≈ 40 cm long cylindrical tube located inside the Zeeman slower. The tube acts as a differential pumping stage and provides a pressure gradient of ≈ 3 orders of magnitude between oven chamber and main chamber [99]. The ion getter pump in the main chamber attains a background pressure of $< 10^{-11}$ mbar. Another gate valve is connected to the main chamber (right hand side of Figure 3.1). Closing this valve enables us to change the entrance viewport for the Zeeman slower laser beam without breaking the vacuum in the main chamber. This must be done every few years, as the viewport gets coated with lithium over time which absorbs and gradually blocks the Zeeman slower laser beam. All viewports in our setup (VPZ38QWAR-LN) are from Torr scientific and have anti-reflective coatings for 671 nm, 1064 nm and 532 nm.
The atoms from the oven initially arrive in the MOT chamber, where we trap and cool them by means of a magneto-optical trap (MOT, see section 4.2). From there, we optically transport them to the glass cell (see section 4.4.1), where all experiments reported in this thesis are carried out. The glass cell not only provides better optical access for high numerical aperture (high NA) imaging of the atoms. It also facilitates the application of high magnetic fields, which are crucial for tuning the interparticle interactions by means of the magnetic Feshbach resonance at 832.2 G.

3.2 Lithium oven

The starting point for all our experiments is the lithium oven. It contains 4-5 grams of enriched ^{6}Li which is heated to 720 K to provide a sufficient atom flux into the experimental chamber. In the past, we had severe problems with the oven design at the time. It was based on the design of the Heidelberg group [116] and consisted of a cylindrical reservoir (inner diameter 37 mm, inner length 32 mm) and a cylindrical collimation tube (inner diameter 10 mm, inner length 60 mm). A sufficient atom flux was created by heating the reservoir to ≈ 720 K while keeping the collimation tube cold to prevent leakages at the connection flange of the collimation tube and the oven chamber. The problem with this design was that the collimation tube became clogged with lithium over time, which escaped from the reservoir and solidified. As a result, the oven had to be changed every 6 months on average. For this reason, a new oven was designed and implemented at the beginning of this thesis, which still provides sufficient lithium flux even after 5 years of permanent operation.
The new oven design is illustrated in Figure 3.2. It basically consists of four parts: the reservoir, the nozzle, the buffer zone and the collimation zone. In the reservoir, approximately 5 grams of enriched Lithium-6 are heated to 720 K, creating a vapor. The nozzle, which is heated to a higher temperature than

the reservoir[1], ensures the lithium remains in vapor form, preventing any liquid lithium from settling and causing blockages. It also collimates the atomic beam. For heating the oven, we use a heating wires from Thermocoax made of an Inconel alloy, which is a nickel-chromium-based superalloy suited for high temperatures. To prevent heat loss, the reservoir and the nozzle are wrapped with ceramic wool (from R.A. Schmidt-Feuerfest GmbH) and several layers of aluminum foil. The entire oven is made of solid steel (AISI 316L), which has a poor thermal conductivity. We further reduce heat conduction by choosing the wall between the reservoir and the nozzle to be thin (1 mm). This ensures that we can keep the nozzle at higher temperatures than the reservoir.

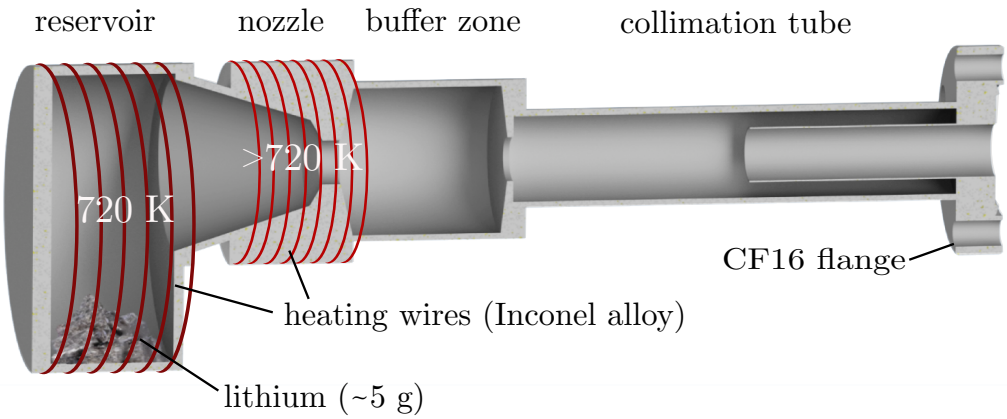

FIGURE 3.2: Design of the current lithium oven. The oven consists of four different zones. In the reservoir approximately 5 grams of enriched Lithium-6 are heated to 720 K. The nozzle provides collimation of the lithium flux and is heated to a higher temperature than the reservoir to prevent liquid lithium from settling there. Liquid lithium that passes the nozzle can solidify in the large volume of the buffer zone, preventing it from blocking the exit of the oven. The collimation zone serves both as a second buffer zone and for further collimating the atomic beam.

Any liquid lithium that might pass through the nozzle enters the buffer zone. The large volume of this zone allows the lithium to cool and solidify without blocking the oven's exit. Finally, the collimation zone serves both as a secondary buffer reservoir and further collimates the atomic beam. The oven is connected to our vacuum setup with a CF16 flange (outer diameter 1.33" $\approx$ 3.38 cm). A technical drawing with all dimensions can be found in Appendix A.1.

3.3 Experimental control system

The heart of our setup is the experimental control system, illustrated in Figure 3.3. It is based on an ADwin-Pro II system from Jäger Computergesteuerte Messtechnik and a custom-built LabView program.

For an experimental run, an array of time-sorted analog and digital signals is

[1]Note that the current oven design has only one temperature sensor to measure and regulate the temperature of the reservoir. We anticipate that the temperature at the nozzle is higher because we chose the winding density of the heating wires to be higher there.

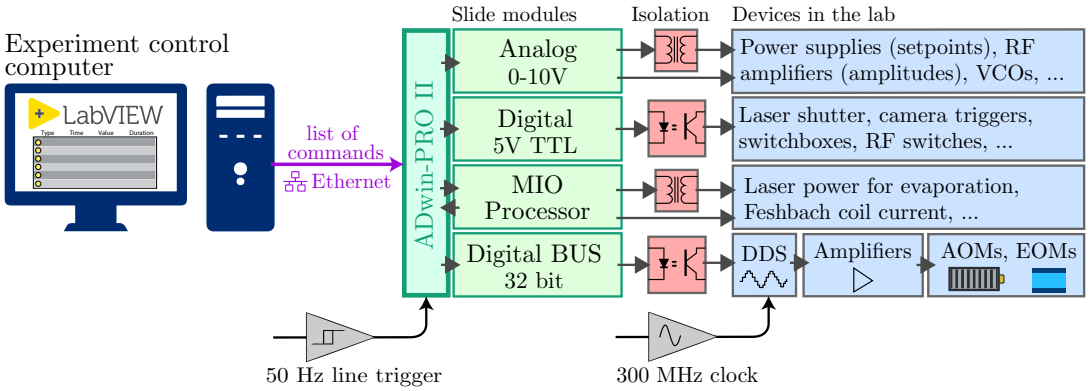

FIGURE 3.3: Experimental control system based on an ADwin-Pro II and a custom-built and home-made LabView program. For an experimental run, an array of time-sorted analog and digital commands is generated on the experimental control computer and sent to a real-time microprocessor (ADwin), which executes the commands by transmitting the appropriate digital and analog signals to its outputs. From there, the signals are distributed to the respective devices in the laboratory. To prevent ground loops and crosstalk between devices, the signals are partially isolated using optocouplers and isolation amplifiers. The ADwin further provides real-time signal regulation with separately programmable MIO (multi input-output) cards and is synchronized to the electric power grid using a 50 Hz line trigger, such that each experimental run starts in phase with the main power grid.

generated on the experimental control computer using a home-built LabView program. The signals are for controlling the devices in the laboratory such as lasers, coil power supplies, cameras, laser shutters, and frequency synthesizers for acousto-optical modulators (AOMs) and electro-optical modulators (EOMs). The graphical user interface of the LabView program allows for easily managing the devices and parameters for each experimental run. It also provides a graphical visualization of the programmed parameters and supports multi-dimensional parameter scans, which is the basis for our measurements.
Once an array of commands is prepared, it is transmitted to the ADwin-Pro II via Ethernet. The ADwin then executes the commands on a 300 MHz processor (TigerSHARC ADSP-TS101S, T11) by sending the corresponding signals to its outputs at the exact times. The time resolution for this is 10 µs and mainly limited by the main processor clock. The output signals (digital, analog) are generated in module cards that are plugged into the ADwin. From these cards, the signals are then distributed to the devices in the laboratory with coaxial and flat ribbon cables.
For the experimental control, we currently use four analog output cards (Pro II-AOut-8/16-B) with a total of 32 channels, two digital output cards (DIO-32) with a total of 64 channels, a co-processor card (Pro II-DIO-32-TiCo) with a 32-bit digital output and two multi-input-output cards (Pro II-MIO-4) with 4 analog outputs, 8 analog inputs and 8 digital inputs/outputs.
The co-processor DIO-32-TiCo with 32-bit output drives our bus system which

we use to digitally program direct digital frequency synthesizers (DDS). These synthesizers generate the frequencies for devices like acousto-optical and electro-optical modulators and are all synchronized by a common stabilized 300 MHz clock signal from a signal generator (Hewlett Packard ESG-D2000A).
The co-processors on the MIO cards are programmed as stand-alone real-time Proportional-Integral-Derivative (PID) regulators and support four individual control loops per card with a bandwidth to 40 kHz. This enables precise and dynamic control of critical signal levels, such as the current for the Feshbach coils (see section 3.5 or the power of the dipole trap laser which we use for the final step of trapping and cooling the atoms to quantum degeneracy (see section 4.4.1).
To prevent ground loops and crosstalk between devices, all digital signals and most of the analog signals are isolated using optocouplers and isolation amplifiers. For additional stability and synchronization, the ADwin processor is synchronized with the mains electric power grid using a 50 Hz line trigger. This synchronization ensures that each experimental run begins in phase with the power grid, reducing variability and enhancing repeatability of the measurements.

3.4 Laser systems

For cooling, trapping, manipulating and imaging the ^{6}Li atoms, we use a variety of lasers of all different types [99], including diode lasers, solid-state lasers and fiber lasers. These laser systems are described in the following.

The master, imaging and cooler/repumper lasers

Laser cooling and imaging of atoms relies on (near) resonantly driving optical transitions. This requires single-mode lasers with a narrow linewidth[2]. Additionally, these lasers must be stabilized to the respective optical transitions.
In our setup, all laser frequencies for cooling and imaging the atoms differ by less than 1.5 GHz from the frequency of the D_2 line of ^{6}Li (see Figure 2.5), even for imaging at the highest magnetic fields we can currently achieve ($\approx 1400\,\mathrm{G}$). To generate these frequencies, we stabilize one laser, the so-called master laser, to the D_2 line of ^{6}Li using saturated absorption spectroscopy [117]. More precisely, it is stabilized to the transition from the crossover of the $|2^2\mathrm{S}_{1/2}, \mathrm{F} = 1/2\rangle$ and $|2^2\mathrm{S}_{1/2}, \mathrm{F} = 3/2\rangle$ states to the $2^2\mathrm{P}_{3/2}$ manifold [117], see also Appendix A.2. The lasers for cooling and imaging the atoms are then stabilized to the master laser by a frequency offset stabilization scheme[3] [124].

[2] In order to optimally address the atoms, which is crucial for cooling and imaging, the linewidth of the lasers has so be smaller than the natural linewidth of the involved states. We cool and image the atoms using optical transitions from the $2^2\mathrm{S}_{1/2}$ ground state to the $2^2\mathrm{P}_{3/2}$ manifold, which has a natural linewidth of $2\pi \times 5.87$ MHz [77].

[3] A frequency offset stabilization (or frequency offset lock) is based on detecting the frequency beat of two lasers with a fast photo diode and converting the signal into an appropriate voltage, which than acts on one laser, to stabilize its frequency relative to the other laser.

The master laser is a commercial external-cavity diode lasers (ECDL) from Toptica Photonics with an output power of ≈ 35 mW and a linewidth of ≈ 150 kHz.

For imaging the atoms, we use another ECDL laser from Toptica Photonics with an output power of ≈ 15 mW and a linewidth of ≈ 150 kHz. For high field imaging in the vicinity of the Feshbach resonance, it is (red) detuned from the master laser by ≈ 1 GHz. For more details on the imaging scheme, see section 4.6.

For laser cooling of ^{6}Li, we require a combined optical power of $\approx$ 140 mW on the experimental table at the position of the atoms. This power is divided as follows: 60 mW for the Zeeman slower beam, 20 mW for both horizontal MOT beams, and 40 mW for the vertical MOT beam. Each of these beams contains 50% of *cooler light* (from $|2^2\mathrm{S}_{1/2}, \mathrm{F} = 3/2\rangle$ to $|2^2P_{3/2}\rangle$) and 50% of *repumper light* (from $|2^2\mathrm{S}_{1/2}, \mathrm{F} = 1/2\rangle$ to $|2^2P_{3/2}\rangle$) [117, 119], which is required for having a closed optical cooling cycle (see Figure 2.5). The frequencies for cooling and repumping are generated from a single laser using the devices and optics displayed in the optical table setup in Figure 3.4. Considering losses through optical fibers, optical isolators and AOMs, this laser has to provide at least 300 mW of optical power. Achieving such a high optical power at a wavelength of 671 nm is currently not possible with a single laser diode. In the past, we used the TA Pro system from Toptica Photonics for this purpose. This system consists of an ECDL with an optical power of approximately 25 mW, which is subsequently amplified to 400-500 mW by a semiconductor optical amplifier. However, these semiconductor amplifier chips suffer from bad transversal beam profiles and short lifetimes of only a few months, especially for the wavelength of 671 nm. For this reason, we have set up a new solid-state laser system with high power and narrow linewidth over the course of the last years [65, 66, 125]. The system is based on a laser system design of the Salomon Group in Paris [61–63] and consists of a home-built 1342 nm solid state laser which is subsequently frequency doubled to 671 nm in a home-built enhancement resonant.
Within this thesis, I further improved this laser system, especially optimizing it for short- and long-term stability and implemented it into the experiment. It reliably provides the light for laser cooling and therefore sets the basis for all our experiments. The laser system is in detail described in Chapter 5.

Lasers for optical dipole potentials

For optically trapping and forced evaporative cooling in the optical dipole trap, we use an ytterbium fiber laser from IPG photonics (YLR-200-LP-AC) with a wavelength of 1064 nm. This laser has linear polarization, a maximum output power of 200 W and an almost Gaussian beam quality, indicated by an M^2 factor of < 1.1. For more details on the optical dipole trap, see Section 3.6.1.

For creating optical lattice potentials and tight optical tweezers , we use a single mode polarization-maintaining 1064 nm fiber amplifier (Nufern NUA-1064-PB-0050-D0) with a maximum output power of 50 W [99]. The fiber amplifier is seeded with a home-built ECDL which has an output power of ≈ 50 mW. For

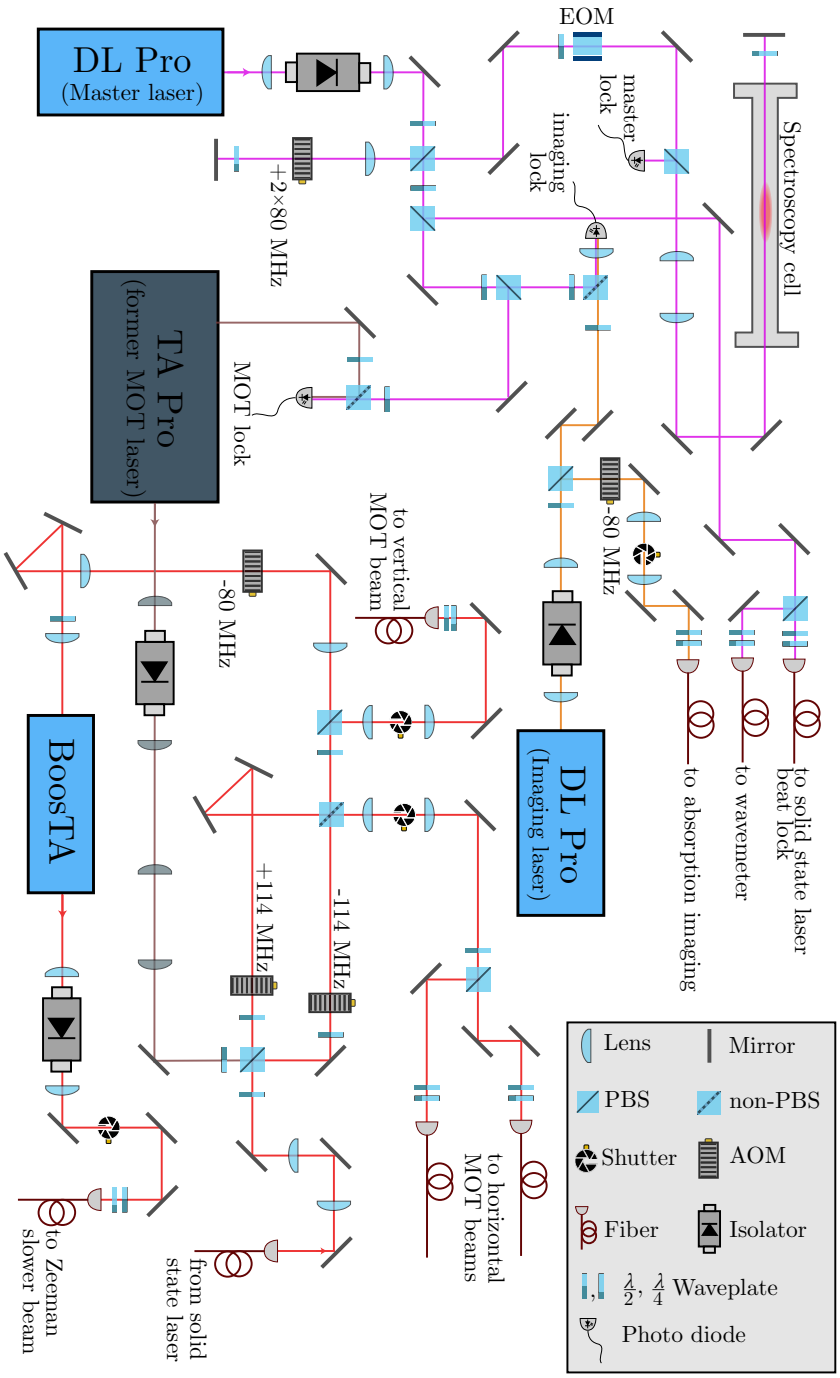

FIGURE 3.4: Optical table arrangement for the Master laser, the former cooling laser (greyed out) and the imaging laser, adapted and updated from [117]. The setup shows the optics and devices we use for preparing the light for laser cooling and imaging the atoms. The prepared light is guided to the experimental table using optical fibers. Although the former TA Pro cooling system is no longer in use, we still use the optics and devices by guiding the light from the new laser system (see Chapter 5) into the former optical path via the fiber labeled "from solid state laser".

seeding the fiber amplifier, we use around 15 mW of this power. For more details on the lattice projection, see [99].
Fermionic atoms with tunable interactions in optical lattices are ideal for simulating the physics of electrons in a solid state. This enables the investigation of fundamental aspects in condensed-matter physics [126]. For this purpose, we developed a non-destructive holographic imaging scheme for atoms in optical lattices [17]. This is in detail described in Chapter 8.

In addition, we can realize repulsive potentials for the atoms using a diode pumped solid state laser (Laser Quantum Opus 532) with a wavelength of 532 nm and a beam diameter of 1.85 mm. The maximum specified output power of the system is 4 W. Over time, however, this value has been reduced to 2.8 watts due to degradation. In previous experiments, this laser was used to confine the atoms in two dimensions by generating an appropriate optical potential with a phase plate [99, 127] and to excite sound waves of first and second sound [82]. In future experiments, we plan to use for creating a repulsive box potential for the atoms, which is discussed in Section 3.6.2. This allows for realizing and studying homogeneous Fermi gases.

Lasers for spectroscopy

For molecule spectroscopy and spectroscopy on the D_1 line, we have two more home-built ECDL lasers implemented in our setup.

The laser for spectroscopy on the D_1 line provides an output power of ≈ 35 mW at a wavelength of 671 nm with a linewidth better than 300 kHz.

The laser for molecular spectroscopy and photo-excitation of atom pairs to tightly bound molecular states has a wavelength of 673.3 nm (corresponding to a frequency of about 445.250 THz, see Figure 4.13) and provides an output power of 30 mW and a linewidth better than 500 kHz. It is subsequently amplified to ≈ 90 mW by means of a semiconductor optical amplifier (BoosTA from Toptica Photonics).

3.5 Coil systems

Manipulating the electronic states of the ^{6}Li atoms by means of external magnetic fields is crucial for laser cooling, trapping and tuning the interparticle interactions. For this reason, we have various coils implemented in our experimental setup as shown in Figure 3.5 and 3.6. The coils have been set up and characterized in previous master's theses [118–120] and are described in the following. For additional information on their purpose in the experiment, see Chapter 4.

The Zeeman slower coils

The ^{6}Li atoms leave the oven with mean velocities of ≈ 1600 m/s. To initially slow them down on their way to the MOT chamber, we expose them to a counter-propagating laser beam resonant to the D_2 line, which applies a scattering force

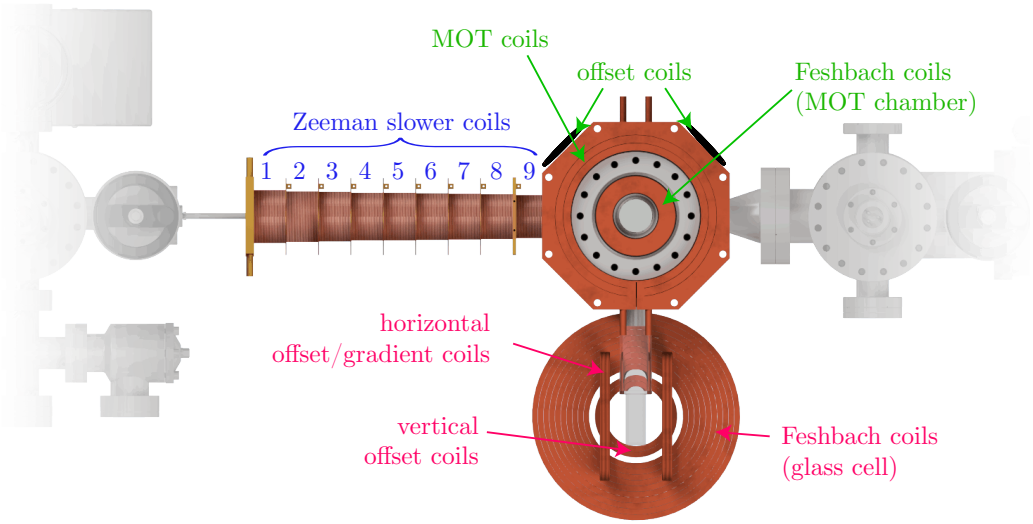

FIGURE 3.5: Top view presentation of the vacuum system showing the implemented coils. These include the nine Zeeman slower coils (blue), the MOT coils and the offset and Feshbach coils around the MOT chamber (green). Also shown are the lower Feshbach coils, lower vertical offset coils and horizontal offset/gradient coils around the glass cell (red). The upper Feshbach and vertical offset coils are hidden for illustrative reasons. These are shown in Figure 3.6.

on the atoms. As the atoms decelerate due to photon scattering, they would experience a Doppler shift that moves them out of resonance with the laser. To compensate for this shift, we use a configuration of nine coils to produce a spatially varying magnetic field. This field gradually shifts the atomic energy levels, keeping the atoms in resonance with the decelerating laser light as they slow down. This configuration is called a Zeeman slower.
The first eight coils (1-8) are connected in series and driven by the same power supply, while the last coil (9), closest to the MOT chamber, has a separate power supply. This final coil has the highest influence on the atoms in the MOT due to its proximity. By individually controlling it, we can use it for additional purposes, such as providing extra gradients or shifting the MOT center. The specifications of the coils are listed in table 3.1.

TABLE 3.1: Specifications and operation currents of the Zeeman slower coils [99].

Coils	Resistance R (Ω)	Current I (A)	Field per current B/I (G/A)
1-8	11.65(5)	6	92 - 50
9	0.74(2)	5.6	41.4

The MOT coils

A three-dimensional magneto-optical trap consists of six red detuned laser beams, arranged as counter-propagating pairs along each of the three spatial directions. This arrangement of laser beams is combined with a magnetic

quadrupole field. The laser beams apply a velocity-dependent force on the atoms, which is crucial for laser cooling. In addition, the magnetic field causes a Zeeman splitting of the atomic levels which, together with the laser beams, generates a position-dependent force, that ensures the spatial confinement of the atoms. For more details on the working principle of a MOT, see Section 4.2. In our setup, the magnetic field is realized by the two coils in anti-Helmholtz configuration, separated by a distance of 7.2 cm [118]. The other specifications are shown in table 3.2.

TABLE 3.2: Specifications and typical operation current of the MOT coils in anti-Helmholtz configuration. The gradient refers to the gradient in the center of the MOT. Resistance and gradient values taken from [120].

Resistance R (Ω)	Current I (A)	Gradient $\Delta B/I\Delta x_i$ (G/(A cm))
2.20(2), both	14.1	2.47(2) vertical, 1.27(2) horizontal

The MOT offset coils

To optimize the spatial overlap of the atoms in the MOT and the optical dipole trap (ODT), we utilize two offset coils, mounted close to the view ports of the MOT chamber (see Figure 3.5). With these coils, the center of the trapping potential of the MOT can be shifted horizontally for optimizing the transfer of the atoms into the ODT. Their properties are listed in table 3.3.

TABLE 3.3: Specifications and typical operation currents of the offset coils at the MOT chamber. The terms 'left' and 'right' refer to their location as shown Figure 3.5. Resistance and gradient values taken from [99].

Coil	Resistance R (Ω)	Current I (A)	Gradient $\Delta B/I\Delta x_i$ (G/(A cm))
Left coil	0.55(2)	2	≈ 1.1
Right coil	0.55(2)	6	≈ 1.1

The Feshbach coils for the MOT chamber

Most of our experiments exploiting the Feshbach resonance, are carried out in the glass cell. However, we also have Feshbach coils installed around the MOT chamber. Due to the high currents required to achieve the necessary magnetic fields of several hundred Gauss, these coils are made of hollow wires with an inner square cross-section of $2.4 \times 2.4\,\mathrm{mm}^2$ [120]. By circulating cooling water through the wires, we maintain steady state temperatures below $70°\mathrm{C}$ during operation with currents up to 200 A. Table 3.4 lists the coil properties.

TABLE 3.4: Specifications and typical operation current of the Feshbach coils around the steel chamber, constructed in Helmholtz configuration.

Resistance R/Ω	Current I (A)	Field per current B/I (G/A)
0.04(2), both	100-200	5.15

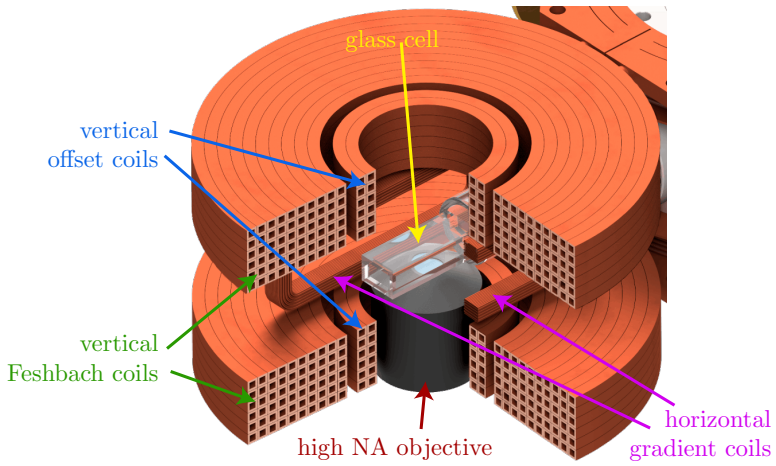

FIGURE 3.6: Three quarter view of the coil system around the glass cell/science chamber (yellow). The coil system includes the vertical offset coils (blue), the Feshbach coils (green) and the horizontal gradient coils (violet) and is used for magnetically trapping, levitating and manipulating the scattering properties of the atoms by means of the Feshbach resonance. Also shown is the high NA objective below the glass cell (red), which has an NA of 0.6 and a working distance of 8 mm.

The Feshbach coils for the glass cell

All experiments with degenerate, strongly interacting Fermi gases presented in this thesis are carried out in the glass cell. Both, evaporative cooling and realizing the different superfluid states in the BCS-BEC crossover exploit the broad Feshbach resonance at 832.2 Gauss. To achieve these fields, we use a set of coils, illustrated in Figure 3.5 and 3.6. The Feshbach coils are made of hollow wires with an inner core cross-section of $4 \times 4\,\mathrm{mm}^2$. Due to the large inner cross-section, the coils maintain a steady-state temperature of approximately 30°C at a current of 200 A. The other coil properties are listed in table 3.5.

TABLE 3.5: Specifications of the Feshbach coils around the glass cell, constructed in Helmholtz configuration.

Resistance R (Ω)	Current I (A)	Field per current B/I (G/A)
0.03(2), both	70-150	5.79

The vertical offset/gradient coils for the glass cell

The vertical offset/gradient coils around the glass cell, which are in Helmholtz configuration serve two purposes. First, they provide an additional offset field of $\approx 225\,\mathrm{G}$ for the current listed in table 3.6. Secondly, by driving both coils with different currents, they create a magnetic field gradient along the vertical direction which we use for levitating the atoms against gravity. The gradient necessary for this is $\mathrm{d}B/\mathrm{d}z = mg/\mu_B \approx 1.05\,\mathrm{G/cm}$ where $g = 9.81\,\mathrm{m/s}^2$ is the gravitational acceleration. Due to the high currents, these coils are also water cooled.

In combination with the Feshbach coils, these coils produce an almost harmonic confinement in the horizontal plane with a trap frequency of $\omega = 2\pi \times 21.5\,\mathrm{Hz}$ [82].

TABLE 3.6: Specifications of the vertical gradient/offset coils around the glass cell. The terms 'upper' and 'lower' refer to their location as shown Figure 3.6.

Coil	Resistance R (Ω)	Current I (A)	Field per current B/I (G/A)
Upper	0.004(1)	251.7	1.13
Lower	0.004(1)	153.5	

The horizontal offset/gradient coils for the glass cell

The horizontal offset/gradient coils were originally designed to generate a gradient along the horizontal direction. The primary function was to study fermions in two-dimensional optical lattices, where the gradient induces tunneling between lattice sites. In the experiments presented in this thesis, the atoms are confined in a harmonic potential and the coils are driven in Helmholtz configuration to provide another offset field of $\approx 24\,\mathrm{G}$. The coil specifications are listed in table 3.7.

TABLE 3.7: Specifications of the horizontal offset/gradient coils around the glass cell, currently operated in Helmholtz configuration.

Resistance R (Ω)	Current I (A)	Field per current B/I (G/A)
1.00(2), both	3.95	6.04

3.6 Optical trapping potentials

Charged particles can be efficiently trapped using electric fields due to the strong Coulomb interaction. This interaction is not present in neutral atoms, which makes trapping more challenging. For this purpose, optical dipole traps have proven to be a powerful tool. When atoms are placed in a light field (e.g. a laser), the oscillating electric field induces an atomic dipole moment that causes the atoms to interact attractively or repulsively with the driving field [128]. This mechanism is based on the Autler–Townes effect (or AC Stark effect), that shifts the energy levels of the atoms proportional intensity of the driving light field. In our experiment, this field is typically generated by lasers. When the frequency of the laser ω_l is largely detuned from the atomic transition frequency ω_0 between the ground state and the excited state, the resulting potential is given by [128]

$$U(\mathbf{r}) \approx \frac{3\pi c^2 \Gamma}{2\omega_0^3} \frac{I(\mathbf{r})}{\Delta}. \tag{3.1}$$

Here, $\Delta = \omega_l - \omega_0$ is the detuning and $I(\mathbf{r})$ the intensity distribution of the laser light. For $\omega_l < \omega_0$ ($\omega_l > \omega_0$) which is called red (blue) detuning, the atoms

are therefore attracted to (repelled from) the light field. As this mechanism is independent of the particular sub-levels of the ground state, optical dipole traps allow for confining the atoms while still providing the possibility to apply external magnetic fields for manipulating their scattering properties.

3.6.1 Optical dipole trap

For a Gaussian laser beam with power P propagating along the (axial) z-direction which is focused to a waist of w_0 at $x = y = z = 0$, the intensity distribution is given by

$$I(x, y, z) = I_0 \frac{w_0^2}{w(z)^2} e^{-2r^2/w(z)^2} \tag{3.2}$$

where $r = \sqrt{x^2 + y^2}$ and $I_0 = 2P/\pi w_0^2$. The quantity $w(z) = w_0\sqrt{1 + z/z_r}$ is the beam waist, $z_R = w_0^2\pi/\lambda_l$ the Rayleigh length and λ_l the wavelength of the laser. At $z = r = 0$ the resulting potential can be approximated by a harmonic trapping potential with axial and radial trap frequencies $\omega_z = \omega_{ax} = \sqrt{2U(0)/mz_R^2}$ and $\omega_r = \sqrt{4U(0)/(mw_0^2)}$ [129].
In our setup, we use a single beam optical dipole trap for trapping, transporting and forced evaporative cooling of the atoms. The dipole trap utilizes a focused 200 W fiber laser with a wavelength of $\lambda = 1064$ nm (see Section 3.4). Although the laser is far detuned from the D_1 and D_2 lines of ^{6}Li at a wavelength of ≈ 671 nm, its high power still provides a ~ 1 mK deep optical trapping potential for the atoms when focusing it down to a waist of $\approx 38\,\mu$m [99], corresponding to a Rayleigh length of 4.3 mm. During evaporative cooling, we subsequently lower the laser power down to $10 - 1000$ mW (see Section 4.4.1) to cool the atoms down to temperatures of $0.05 - 3\,T_F$. Typical optical trap frequencies are then on the order of $\omega_{ax,opt} = 2\pi \times 0.5 - 5$ Hz and $\omega_r = 2\pi \times 100 - 1000$ Hz. The axial confinement of the atomic cloud is therefore almost exclusively caused by the magnetic field of the Feshbach and offset coils, which together produce a potential with trap frequency $\omega_{ax,mag} = 2\pi \times 21.5$ Hz (see previous section).

3.6.2 Repulsive ring potential

All our experiments on pairing and superfluidity in the BCS-BEC crossover were carried out in a harmonic trapping potential [13, 15, 82, 130]. Although harmonically trapped Fermi gases are a well-defined and intensely studied physical system of high interest, homogeneous Fermi gases offer unique advantages and are gaining increasing interest in the field of ultracold atoms [131, 132]. One of the main advantages of homogeneous Fermi gases is the ability to study bulk properties of the system without the disturbing effects of the trapping potential. This can be particularly useful for exploring phenomena such as phase transitions and collective excitations in a more uniform and controlled way. Additionally, homogeneous Fermi gases allow for easier comparison with theoretical models, as the system can be described by simpler theoretical frameworks without the complications introduced by the trapping potential. Furthermore, homogeneous Fermi gases offer opportunities for exploring exotic phases that may not be accessible in trapped systems, such as the Fulde-Ferrell-Larkin-Ovchinnikov

(FFLO) phase [133].
For this purpose, I set up a repulsive ring potential along the lines of [131] and [132], which basically represents a two-dimensional optical box potential for the atoms. The optical setup consists of three axicons and two lenses and is presented in Figure 3.7. Axicons are conical prisms and can, within geometric optics, be regarded to only split and deflect an incident laser beam. In contrast, lenses also change the size of the beam by either focusing or diverging it.

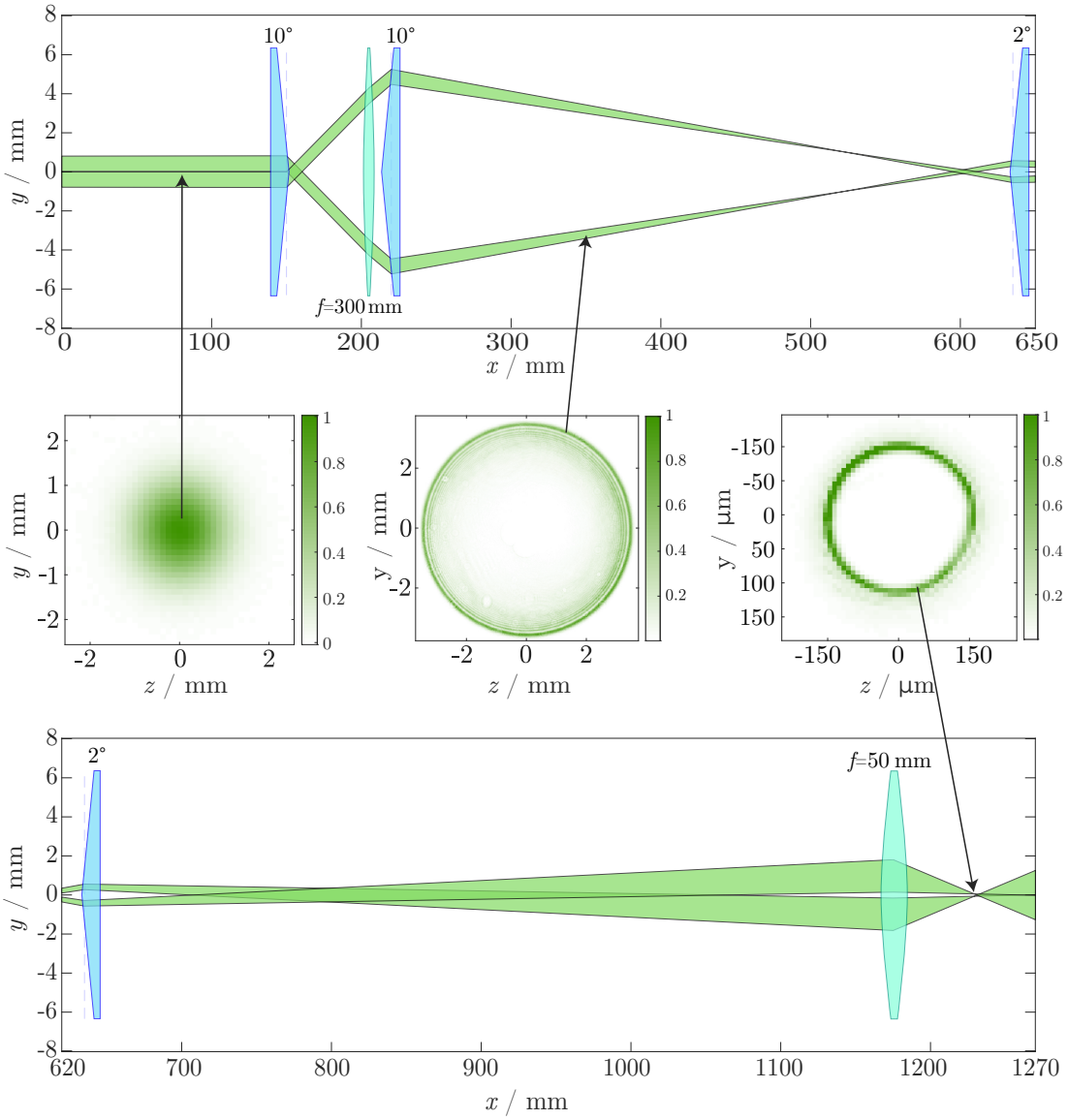

FIGURE 3.7: Optical setup for generating a ring potential from a Gaussian beam. The setup consists of three axicons and two lenses, arranged as shown in the top and bottom panels. The optics and the beam profiles are cylindrical symmetric in the y-z plane. While the axicons change the diameter of the ring, the two lenses also affect its width. The resulting ring has a diameter of $\approx 200\,\mu$m and a width of 13 µm (FWHM). The panel in the middle shows measurements of the beam profile at the marked locations. The beam path was calculated with ray tracing based on geometric optics. More details are given in the text.

The optical beam path

Our setup is strongly based on the design of the Quantum Matter Group in Hamburg [132, 134]. The advantage of this design, compared to design used in the Zwierlein Group at MIT [131], is that the ring generated by the first axicon is inverted by the consecutive two axicons, resulting in a sharp inner edge. For this purpose, we used the same set of axicons. The main difference in our concept is that we wanted to project the ring structure onto the atoms from a larger distance. Therefore, we used lenses with different focal lengths and a different beam path geometry that allows the projection to the position of the atoms from a distance $> 50\,\mathrm{mm}$. The purpose of the optical elements is explained in the following.

The setup starts with a collimated Gaussian beam from a Coherent Verdi V18 laser, which we spatially filter using a 2-meter-long single-mode optical fiber. The first $\alpha = 10°$ axicon transforms the Gaussian beam into a ring beam in the far field. The ring's diameter diverges at an angle of $\arcsin(n \sin \alpha) - \alpha \approx 4.48°$, where $n = 1.46$ is the refractive index of fused silica (the material from which the axicons are made) for $\lambda = 532\,\mathrm{nm}$. The width of the ring remains almost constant and is determined by the initial size of the Gaussian beam. If one follows the ray traces in Figure 3.7, based on geometric optics, one can see that the first axicon maps the inner, high intensity part of the Gaussian beam to the outside of the ring. Consequently, the outside of the Gaussian beam, where the intensity decreases with $\exp(-r^2)$, gets mapped to the inside of the ring. The resulting ring therefore has a sharp outer edge while the intensity towards the center decreases with $\exp(-r^2)$. This is also illustrated in the beam profile measurement shown in the middle panel of Figure 3.7. It represents the exact opposite of what we aim to achieve. In a box potential, the potential inside the box must be constant and then sharply increase at the edges. The purpose of the following optics is therefore to both invert the ring and decrease its diameter and width. We achieve this as follows:
After the first axicon, a lens with a focal length of $f = 300\,\mathrm{mm}$ reduces the divergence of the ring's diameter while slightly focusing its width. The width therefore reaches a minimum at the lens's focal point and increases again from there on. The second $10°$ axicon symmetrically deflects the ring, reducing its diameter until the ring is inverted[4]. The third axicon, with an opening angle of $\alpha = 2°$, nearly collimates the ring's diameter. The width, however, continues to increase due to the $f = 300\,\mathrm{mm}$ lens.
The final lens, with a focal length of $f = 50\,\mathrm{mm}$, focuses both the ring's diameter and its width. At a distance of $65\,\mathrm{mm}$ after this lens, the ring has a diameter of $200\,\mu\mathrm{m}$ and a width of $13\,\mu\mathrm{m}$ (FWHM). The inner part of the ring is now almost free of residual intensity due to the inversion. This is shown in the right plot of the middle panel of Figure 3.7 and in Figure 3.8 a).
Figures 3.8 b) and c) show a line cut through the measured intensity distribution of the ring profile on an linear and logarithmic scale. From these measurements, one can see that the intensity along the ring is more than a factor of 2000 larger than the intensity inside. Additionally, the intensity inside is a factor of 10 larger

[4]Without the $f = 300\,\mathrm{mm}$ lens, this axicon would simply collimate the ring's diameter. The ring would then propagate with constant diameter and width, as shown in Figure 3.10

thqn the background intensity far outside the ring. For further discussion, these ratios are called height-to-inner and inner-to-background, respectively. This result is by far superior to the reported ring potential in [132] where a height-to-inner ratio of ≈ 75 was reported.

Homogeneity

As a rule of thumb, ultracold atoms in thermal equilibrium energetically fill up their confining potential to about $1/5$ of its height [135, 136]. Moreover, their density distribution is to a first approximation proportional to their confining potential, see e.g. Chapter 2. For the ratio between the height of the potential

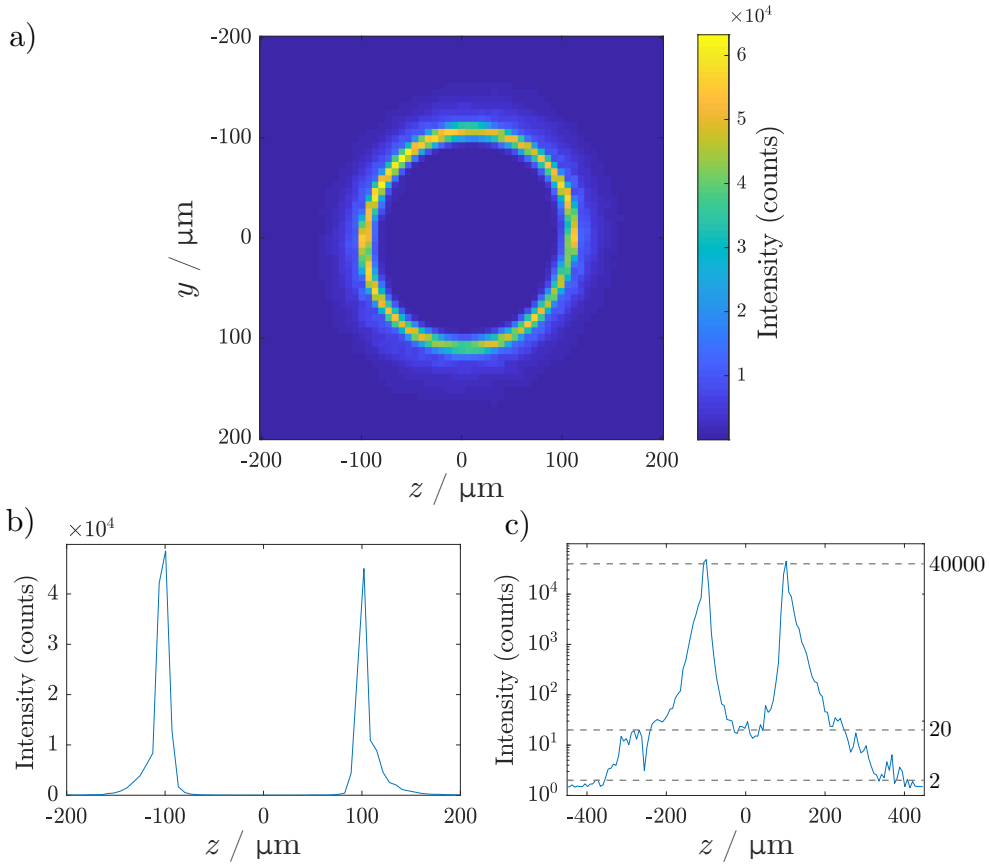

FIGURE 3.8: Repulsive ring potential created with the optics shown in Figure 3.7. All intensity values are given in camera counts per pixel (cpp). a) False color image of the ring potential taken with a CMOS camera (PCO Edge 4.2 LT). The color bar indicates the intensity which is $> 40\,000$ cpp along the ring and ≈ 20 in the center of the ring. The ring has a diameter of $\approx 200\,\mu$m. b) Line cut through the intensity profile along the center in horizontal direction. As the optical dipole potential is proportional to the intensity (see Equation (3.1)), the intensity distribution provides a sharp box potential for the atoms. c) Same line cut as in b), plotted on a logarithmic scale. Far outside the ring for $|z| > 400\,\mu$m, the intensity is approximately 2 cpp and mainly given by the background noise. In the center of the ring, the average intensity is 20 cpp, and exceeds $40\,000$ cpp along the ring.

and the potential fluctuations inside the ring, we measure a value $\gtrsim 2000$. The expected density variations for the atoms confined inside the ring potential are therefore on the order of $5/2000 = 0.25\%$. In Reference [131], the reported density variations were on the order of 15%, while Ref. [132] reported a standard deviation of 8.6%. This value in agreement with the reported height-to-inner ratio of 75, which would result in a fluctuation in the density of $5/75 \approx 6.6\%$ under the considerations mentioned above.

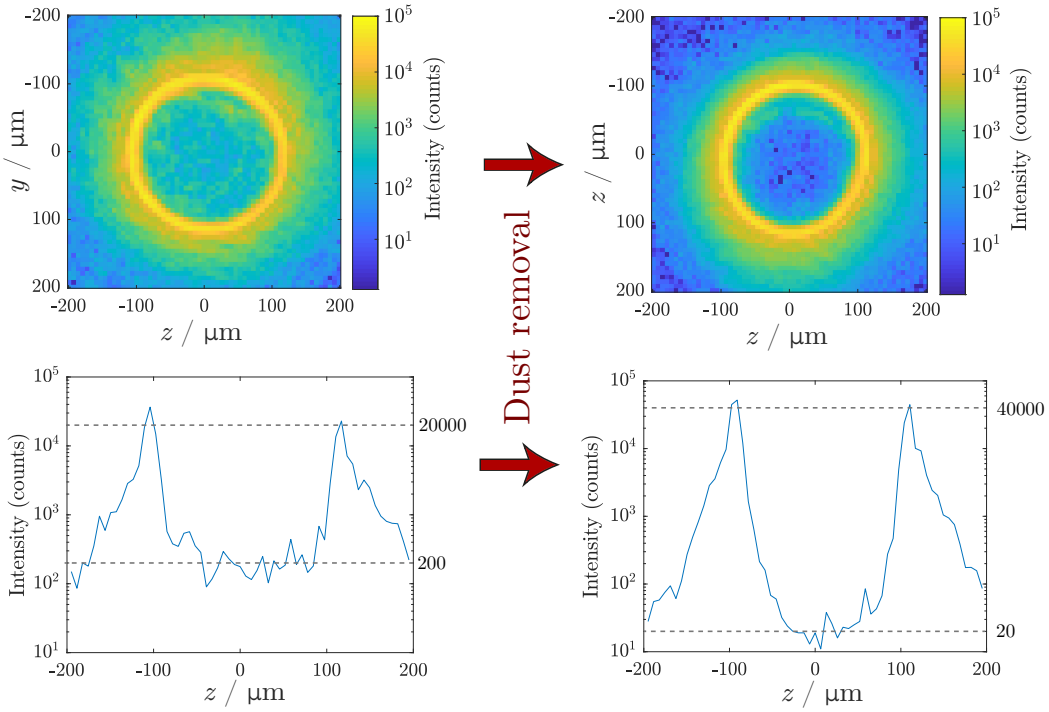

FIGURE 3.9: Effects of dust on the optics of the ring potential beam path. The intensity values are given in camera counts per pixel (cpp). The top left and top right false color images show the measured intensity distribution of the ring potential on a logarithmic scale (see color bar). The bottom left and bottom right plots are line profiles of the intensity, taken along the center of the ring at $y = 0$. The top and bottom left images correspond to measurements with dust on the optics, the top and bottom right ones show the scenario after dust removal. Before cleaning, the height-to-inner ratio was 100:1 which increased to 2000:1 after dust was removed. The background intensity far outside the ring is ≈ 10 cpp, see also Figure 3.9 c).

Projecting the ring potential

A main advantage of our setup is the fact, that the potential is created at a rather large distance of 65 mm after the last lens. This allows for projecting the potential onto the atoms from a larger distance, eliminating the need for high numerical aperture objectives that require a good optical access to the atoms.

Required optical power

In our experiments, the atom cloud temperatures are on the order of 200 nK. For this reason, the potential height has to be on the order of $k_B \times 1$ µK. With the

measured intensity distribution and Equation (3.1), the required power for this is 300 mW. The inner part of the ring would then have a residual potential depth of $k_B \times 0.5\,\mathrm{nK}$.

Effects of dust on the optics

Dust on optical components can significantly degrade performance by scattering and absorbing light. This can distort the beam profiles, leading to reduced beam quality and increased noise. When setting up the optical path for the ring potential, I observed similar detrimental effects.
Due to the significant impact on the ring profile, this issue is briefly discussed in the following. Even with a small amount of dust on the optics I could only achieve a height-to-inner ratio of ≈ 100. For such an intensity distribution, density variations on the order of 5% are expected. This significantly improved by carefully cleaning all the optics shown in Figure 3.7. After the dust removal, the height-to-inner ratio increased to $\gtrsim 2000$ while the inner-to-background intensity ratio dropped to 10, as stated earlier. This is also depicted in Figure 3.9.

Further explanation of the beam path

For a better understanding of the optical path, the influence of the axicons and lenses on the initial Gaussian beam can be viewed independently. For this, the same optical system depicted in Figure 3.7 is shown in Figure 3.10 with only the three axicons and in Figure 3.11 with only the two lenses. A ring potential which is subsequently inverted can also be achieved with only three axicons, as shown in Figure 3.10. However, to adjust the width of the ring, lenses are required. Within geometric optics, the position of the focal points is independent[5] of the

[5]This statement only applies approximately, as the axicons with refractive index $n \approx 1.46$ additionally increase the optical path length.

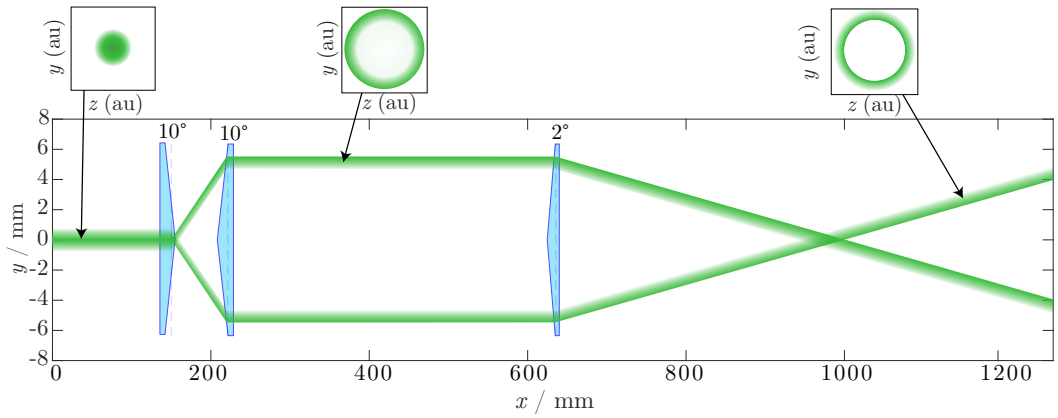

FIGURE 3.10: Creation of a diverging ring potential with a sharp inner edge using three axicons. The first axicon transforms the initial Gaussian beam into a ring with a sharp outer edge which diverges in diameter. The second axicon collimates the ring. The third axicon now symmetrically deflects the ring. The ring consequently converges and is inverted after the certain distance, creating a ring with a sharp inner edge. Note that the axicons do not influence the width of the ring.

axicon positions. For this reason, the width of the ring generated with the setup in Figure 3.7 has a minimum in the focal points of the setup depicted in Figure 3.11.

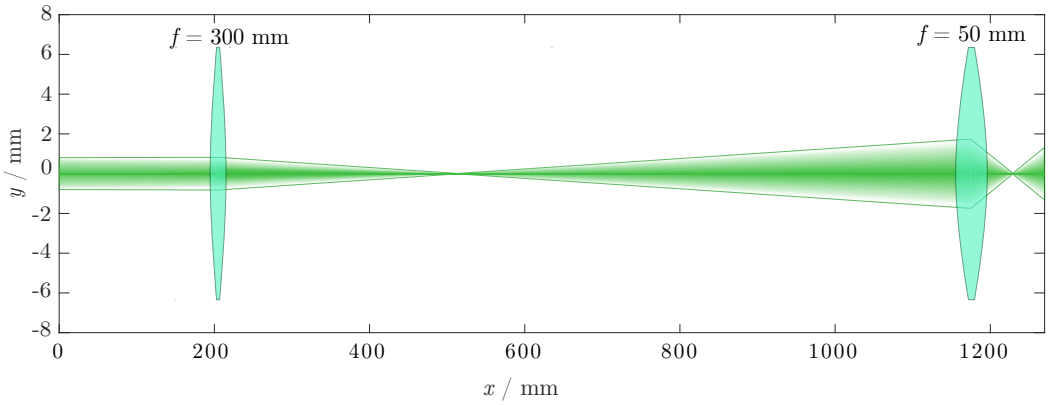

FIGURE 3.11: Optical beam path without axicons. The Gaussian beam is focused by the same pair of lenses at the same positions as in Figure 3.7. In contrast to the setup in Figure 3.7, the three axicons are missing. As the axicons only deflect the beam, the focal points of the optical system remain the same.

3.7 Antennas

In our experiments, we typically study balanced mixtures of ^{6}Li in the two energetically lowest hyperfine states referred to as $|1\rangle$ and $|2\rangle$ (see Figure 2.6). To drive transitions between the two states, as well as between these states and other states of the $2^2S_{1/2}$ manifold, we use two radio frequency (RF) antennas and one microwave (MW) antenna. These are described in the following. In addition, Figure A.2 shows level scheme with the addressable RF and MW transitions.

To drive transitions between $|1\rangle$ and $|2\rangle$, we use an RF antenna placed at a distance of ≈ 10 cm from the glass cell [120]. It consists of a copper loop with an inductance of $0.238\,\mu$H and a resistance of $25\,m\Omega$ which is terminated by an adjustable copper plate capacitor with a capacity of about 20 pF [120]. The antenna has a resonance frequency at ≈ 76.2 MHz and a bandwidth of 740 kHz. It can be adjusted by changing the distance of the two copper plates that form the capacitor. The frequency of 76.2 MHz matches the energetic difference of the states $|1\rangle$ and $|2\rangle$ at a field of ≈ 790 G. The emitted RF signal is linearly polarized perpendicular to the quantization axis of the atoms. Its projection on the atoms therefore matches the selection rules for the desired transition $|1\rangle$ $(m_I = 1) \leftrightarrow$ $|2\rangle$ $(m_I = 0)$. In our experiments, this antenna is typically used to create the balanced mixture of atoms in $|1\rangle$ and $|2\rangle$ (see Chapter 4) and also to calibrate the magnetic field by means of RF spectroscopy.

In addition, we can drive RF transitions between $|2\rangle$ and $|3\rangle$. For this, a similar antenna with a resonance frequency of ≈ 82.2 MHz is implemented [99] close to the glass cell. The resonance frequency matches the respective energetic splitting

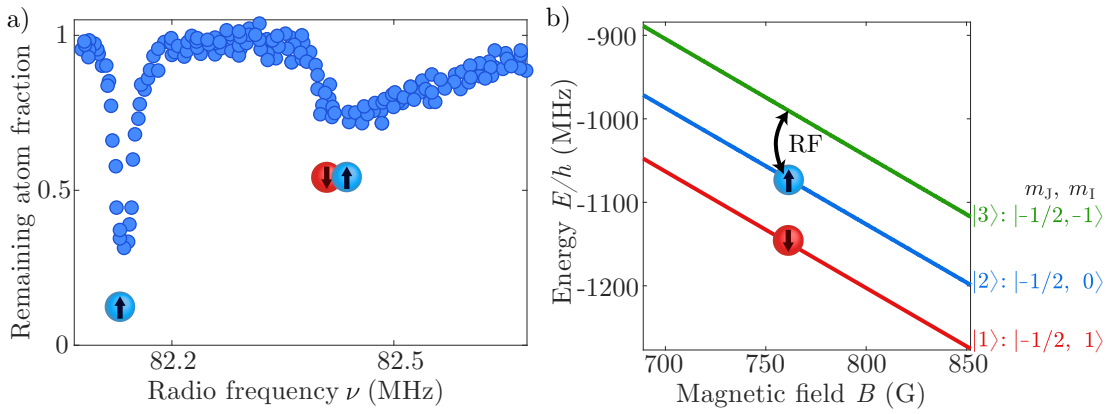

FIGURE 3.12: Radio frequency molecule spectroscopy at a magnetic field of 755 G, adapted from [99]. a) The investigated Fermi gas is initially prepared in a balanced mixture of atoms in states $|1\rangle$ and $|2\rangle$, with some forming Feshbach molecules. A radio frequency pulse transfers atoms from $|2\rangle$ to $|3\rangle$. The remaining atoms in $|2\rangle$ (bound or unbound) are then counted using absorption imaging. The RF spectrum shows two dips: the left dip corresponds to the loss of unbound atoms, while the right dip shows the loss of atoms bound to Feshbach dimers. These require a higher RF frequency for transferring them to $|3\rangle$ to overcome the binding energy, see also [78, 99, 137] for more details. b) Level scheme with the involved electronic states.

of $|2\rangle$ and $|3\rangle$ in the high magnetic field, as depicted in Figures 3.12 b) and 2.6. In our experiments, this antenna can be used to measure the binding energy of the Feshbach molecules by means of RF spectroscopy. Such a spectrum is shown in Figure 3.12 a) and explained in the figure caption. For more details, see also References [78, 99, 137].

Transitions between the high-field seeking states $|1\rangle$, $|2\rangle$ and $|3\rangle$ and the low–field seekers $|4\rangle$, $|5\rangle$ and $|6\rangle$ require microwave frequencies on the order of $2 - 3$ GHz, as depicted in Figure 2.6. For this, a microwave antenna is implemented in our setup, as described in [99]. With this antenna, transitions with $\Delta m_I = 0$ can be driven, e.g. $|2\rangle$ to $|5\rangle$. This enables us to remove atoms from the trap, as they are now repelled from the potential provided by the magnetic field of the Feshbach and offset coils.

3.8 Wavemeter based frequency stabilization

Cooling and imaging the atoms requires frequencies close to the D_2 transition of ^{6}Li, as explained in Section 3.4. We generate the necessary frequencies using a master laser stabilized to a spectroscopy cell. Additional lasers are then stabilized relative to the master laser through frequency offset stabilization [124]. This stabilization scheme, however, is only applicable when the frequency difference between the two lasers can be detected by a fast photo diode. This imposes a limit on the possible frequency difference, which is approximately 20 GHz for the fastest photo diodes currently available. To stabilize lasers at other

frequencies/wavelengths, we use a stabilization scheme based on the commercial wavelength meter WS7-60 from High Finesse. The working principle of this scheme is described below and depicted in Figure 3.13.

The wavelength meter WS7-60 can determine the frequency of a laser with

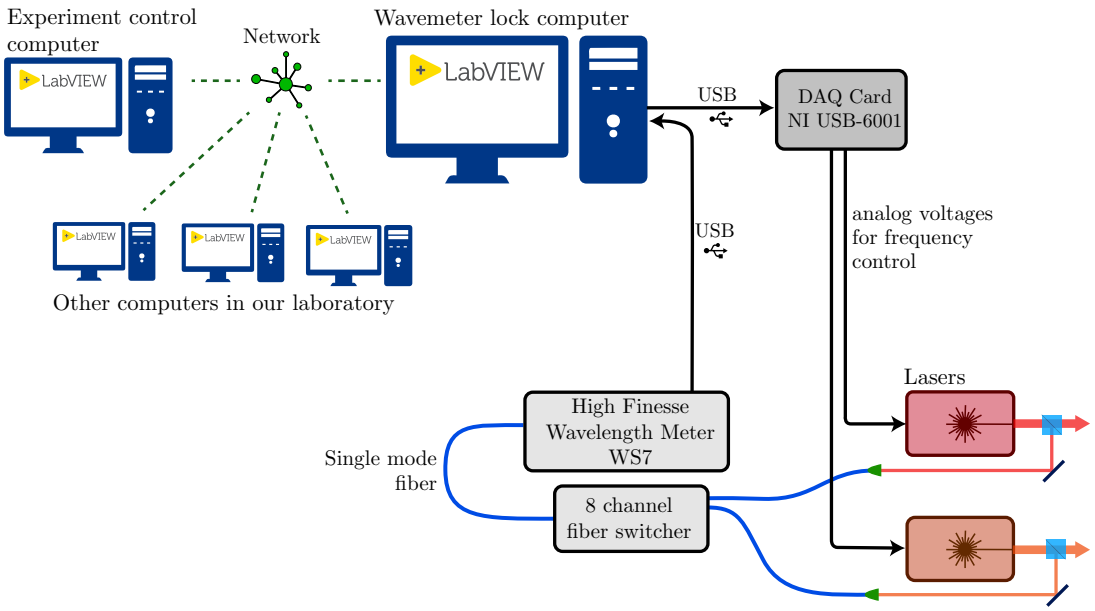

FIGURE 3.13: Setup of the wavemeter stabilization scheme. A fraction of the laser power ($\approx$ 1 mW) is guided in optical fibers to a fiber switcher that connects to a wavelength meter (WS7-60) with a single mode fiber. The wavelength meter interferometrically measures the wavelength with a specified relative accuracy of 2 MHz and sends this information to the wavemeter lock computer. On this computer, a LabView program stabilizes the wavelength to a setpoint by sending out a control voltage to the piezos of the respective lasers. This is done by a digital to analog converter (NI USB-6001) connected via USB. The actual and target values for the wavelengths can be read or set from any computer in our network.

a specified accuracy of better than 2 MHz[6]. The measurement is based on a Fizeau interferometer, which generates a laser frequency-dependent interference pattern detected by a CMOS sensor. The acquired pattern is compared to stored interferograms, allowing the determination of the laser frequency with the stated resolution. The CMOS sensor in our WS7-60 is silicon-based and can therefore detect wavelengths in the range of 400-1100 nm. To enhance the number of lasers that can be simultaneously measured, the wavelength meter is

[6]From our measurements, we estimate a significantly better resolution. This conclusion is based on comparing a cavity-stabilized laser with a linewidth of less than 10 kHz and a spectroscopically stabilized laser with a linewidth of about 200 kHz using the wavelength meter. For the 10 kHz laser, the wavelength meter typically shows a single value for the wavelength. For the broader laser, the wavelength meter displays wavelength values with a standard deviation corresponding to approximately 200 kHz of linewidth. We obtain these readings by directly accessing the wavelength data from the wlmData.dll file (Dynamic Link Library) via LabView, which provides a higher resolution (100 kHz) than the High Finesse software (10 MHz).

connected to an 8-channel fiber switcher by a single mode fiber. This switcher receives light from up to eight lasers, which is then sequentially transmitted to the wavelength meter using a multiplexer.
To stabilize a laser, we use a home-built LabView program that reads the wavelength measurements from the wavelength meter via USB and compares them to predefined setpoints. The LabView program then employs a PID loop to calculate an appropriate error signal. This signal is converted to an analog signal on a DAC card (USB-6001 from NI) connected to the same computer via USB. These analog signals act on the piezos in the respective lasers to stabilize the wavelength to the setpoint.
The bandwidth and precision of this stabilization technique is limited by the readout speed and resolution of the wavelength meter. For a single laser, the determination of the wavelength takes at least 1 ms, assuming proper exposure of the CMOS sensor[7]. This limits the bandwidth of the stabilization to 1 kHz.

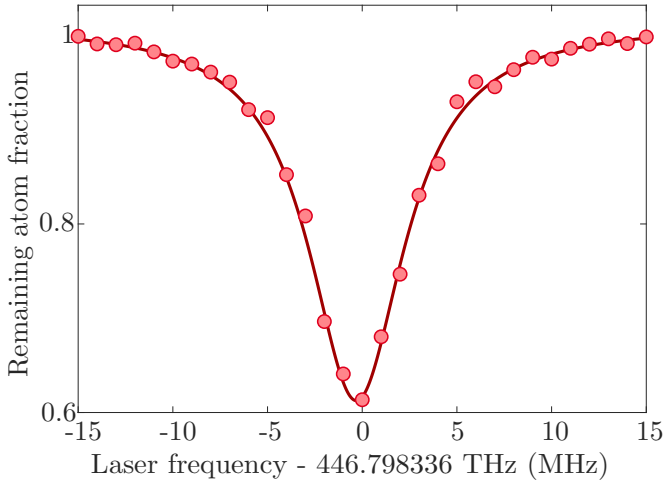

FIGURE 3.14: Spectroscopy signal for a spectroscopy performed with a laser stabilized by the wavemeter lock. The spectroscopy probes the transition from state $|1\rangle \equiv |2^2S_{1/2}, m_J = -1/2, m_I = 1\rangle$ to $|2^2P_{3/2}, m_J = -3/2, m_I = 1\rangle$ at a magnetic field of 820 G. The initial state is later imaged via absorption imaging to count the remaining number of atoms. From a Lorentzian fit (solid line), we extract a linewidth of 6.2 MHz (FWHM).

For eight lasers, the bandwidth for the stabilization therefore reduces to 125 Hz. As a result, the wavemeter lock cannot compensate for fluctuations on shorter timescales. Consequently, this stabilization technique is especially suited for lasers that are already quite stable intrinsically. For our home-built diode lasers, which have an intrinsic linewidth of $100-200$ kHz, we typically achieve stabilities better than 1 MHz on time scales > 10 seconds. This is also evidenced in Figure 3.14 which shows a spectroscopy signal of the $|2^2P_{3/2}, m_J = -3/2\rangle$ state at high magnetic field. This state has a natural linewidth of $2\pi \times 5.87$ MHz. The spectrum does not show any significant broadening of the line, even though the laser is stabilized solely with the wavelength meter lock. As also discussed in Chapter

[7]This requires about 1 mW of optical power.

5 and Ref. [138], the convolution of two Lorentzian lineshapes with linewidths $\Delta\nu_1$ and $\Delta\nu_2$ results in a signal with a total linewidth of $\Delta\nu_{\mathrm{res}} = \Delta\nu_1 + \Delta\nu_2$. From the known linewidth of the D_2 line and our measurement, from which we extract a linewidth of 6.2 MHz, we can estimate a laser linewidth of around 350 kHz. For a more detailed discussion on the capabilities and limits of the wavelength meter stabilization, see the forthcoming PhD thesis of Dominik Dorer, which is currently under preparation.

Chapter 4

Experimental steps and methods

In Chapter 3, our experimental setup for creating ultracold, strongly interacting Fermi gases of ^{6}Li was presented, mainly focusing on the technical components such as the vacuum apparatus, coils, and laser systems. The following chapter puts the focus on the underlying physics, explaining the necessary experimental steps and methods for cooling, manipulating, and imaging ^{6}Li atoms. For this, we follow a typical timeline of an experimental run, beginning with hot individual ^{6}Li atoms from the oven and ending up approximately 15 seconds later with a quantum degenerate, strongly interacting Fermi gas in the glass cell. This timeline together with the involved cooling steps and temperatures is illustrated in Figure 4.1.

4.1 Laser cooling

Laser cooling relies on the deliberate scattering of photons to reduce the momentum and thus the temperature of the atoms. Atoms in a continuous light field of a laser with intensity I and frequency ω_l can be effectively modelled as a two-level system with transition frequency $\omega_0 = 2\pi c/\lambda$. When the atoms scatter photons of momentum $\hbar k = hc/\lambda$, they experience a scattering force given by [129]

$$F_{sc} = \hbar k \frac{\Gamma}{2} \frac{S_0}{1 + S_0 + 4\left(\frac{\delta_0}{\Gamma}\right)^2} \tag{4.1}$$

where $S_0 = I/I_S$ denotes the saturation parameter and

$$I_S = \frac{\pi}{3} \frac{\hbar\Gamma}{\lambda^3} \tag{4.2}$$

the saturation intensity. For the D_2 line of ^{6}Li where $\lambda = 671\,\text{nm}$ and $\Gamma = 2\pi \times 5.87\,\text{MHz}$ [77], the saturation intensity is $I_S = 2.54\,\text{mW/cm}^2$. The quantity $\delta_0 = \omega_l - \omega_0$ is the detuning. The detuning can be additionally affected by the Doppler shift $\delta_D = kv$ when atoms move at a velocity v parallel to the laser beam, and by external magnetic fields due to the Zeeman effect $\delta_B = \mu_B g B/\hbar$. These mechanisms are exploited in the Zeeman slower and the magneto-optical trap (MOT) to decelerate/cool and confine the atoms.
In our experiments, we perform laser cooling on the D_2 line of ^{6}Li, from the $2^2S_{1/2}$ to the $2^2P_{3/2}$ manifold. While the $2^2P_{3/2}$ hyperfine states are not resolvable, the $2^2S_{1/2}$ ground state splits up into $|2^2S_{1/2}, F = 1/2\rangle$ and $|2^2S_{1/2}, F = 3/2\rangle$ with a

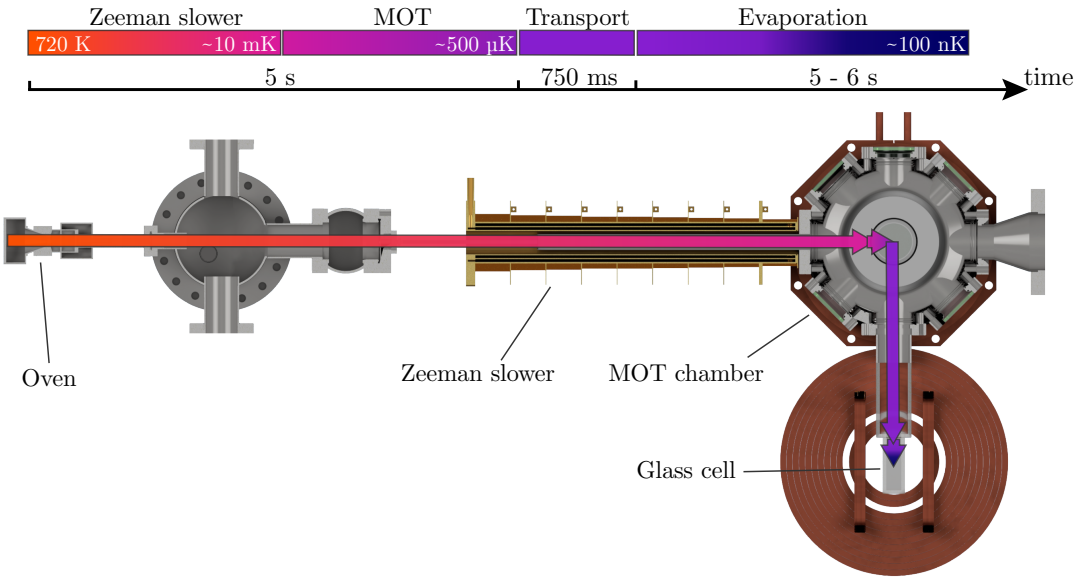

FIGURE 4.1: Illustration of the different cooling steps and their durations in a typical experimental run. The arrows show the trajectory of the atoms in the vacuum chamber, while the colors illustrate their temperatures. The atoms leave the oven with a temperature of $T = 720\,\mathrm{K}$, corresponding to a mean velocity of $\sqrt{8k_BT/\pi m} \approx 1600\,\mathrm{m/s}$. The atoms are decelerated (i.e. cooled) in the Zeeman slower to temperatures of 10 mK and trapped in the MOT which further cools them to $\approx 500\,\mu\mathrm{K}$ [99]. We load the MOT for 5 seconds collecting 5×10^8 atoms. Using an ODT, the atoms are then transported to the glass cell within 750 ms where evaporative cooling lowers their temperature by another three orders of magnitude to a few 10 nK. This last cooling step takes 5-6 seconds.

hyperfine splitting of $228.2\,\mathrm{MHz}$. For this reason, we need two laser frequencies to achieve a closed cooling cycle: the *cooler* and the *repumper* frequency. The cooler is (near-) resonant to the $|2^2\mathrm{S}_{1/2}, \mathrm{F} = 3/2\rangle$ to $|2^2\mathrm{P}_{3/2}\rangle$ transition, while the repumper drives the transition from $|2^2\mathrm{S}_{1/2}, \mathrm{F} = 1/2\rangle$ to $|2^2\mathrm{P}_{3/2}\rangle$. As the spontaneous decay from $|2^2\mathrm{P}_{3/2}\rangle$ into both hyperfine ground states is equally probable [123], we use the same optical power for the cooler and repumper light.

4.2 Zeeman slower

The atoms initially leave the oven with a temperature of around $720\,\mathrm{K}$ corresponding to a mean thermal velocity of $\sqrt{\frac{8k_BT}{\pi m}} \approx 1600\,\mathrm{m/s}$. We slow them down with the Zeeman slower laser beam which is counter-propagating with respect to the atomic beam and has an optical power of ≈ 60 mW. The beam has a waist of $2.5\,\mathrm{cm}$ at its entrance viewport (see Figure 3.1) and is weakly focused to a waist of $3\,\mathrm{mm}$ at the position of the oven. The frequency of the Zeeman slower laser beam ω_l is largely detuned from the atomic transition due to the

Doppler shift kv. The resonance condition [129]

$$\delta = \omega_l - \omega_0 + kv - \mu_B g B/\hbar \stackrel{!}{=} 0 \tag{4.3}$$

is now achieved through the external magnetic field produced by the Zeeman slower coils. The resulting scattering force, provides an almost constant deceleration of $8.4\,\mathrm{m/s^2}$ [99]. For a constant deceleration, the velocity of the atoms starting from the first coil at position $z = 0$ is given by

$$v(z) = v_0\sqrt{1 - \frac{z}{l_{ZS}}}. \tag{4.4}$$

where $l_{ZS} = 47$ cm is the length of the Zeeman slower. As the atoms decelerate, the Doppler shift changes the frequency of the light experienced by the atoms. This change in velocity is compensated by the external magnetic field which follows the same functional form

$$B(z) = B_0\sqrt{1 - \frac{z}{l_{ZS}}}. \tag{4.5}$$

Our Zeeman slower consists of nine coils, as described in Section 3.5. The coils produce a magnetic field which is to a good approximation given by Eq. (4.5) where $B_0 \approx 850$ G is the (largest) magnetic field of the Zeeman slower in the center of the first coil at $z = 0$. The quantization axis due to the coil arrangement is parallel to propagation direction of the atomic beam. For this reason, we use circularly polarized laser light.
The atoms leave the Zeeman slower with residual velocities of a $1 - 10\,\mathrm{m/s}$ [118], and a remaining temperature of $\approx 10\,\mathrm{mK}$. They then enter the MOT chamber, where we subsequently trap and cool them.

4.3 Magneto-optical trap

A three-dimensional magneto-optical trap consists of six red detuned laser beams, arranged as counter-propagating pairs along each of the three spatial directions. This arrangement of laser beams is combined with a magnetic quadrupole field, as shown in Figure 4.2 a). It produces a force on the atoms, which is both position- and velocity dependent. This force can be expanded around the center of the MOT at $x_i = 0$ and for $v_i = 0$ and is then given by [129]

$$F_{MOT,i} = m\ddot{x}_i = -\alpha v_i - \beta x_i \tag{4.6}$$

with $\alpha = 8\hbar k^2 \frac{\delta_0}{\Gamma} \frac{S_{0,i}}{(1+S_{0,i}+4(\delta_0/\Gamma)^2)^2}$ and $\beta = \frac{\alpha}{k}\frac{g\mu_B}{\hbar}\frac{\mathrm{d}B_i}{\mathrm{d}x_i}$. Equation (4.6) essentially represents the equation of motion for a damped harmonic oscillator with spring constant β and damping coefficient α. Thus, the MOT both confines and slows the atoms down, i.e. cools them. The smallest possible temperature achievable

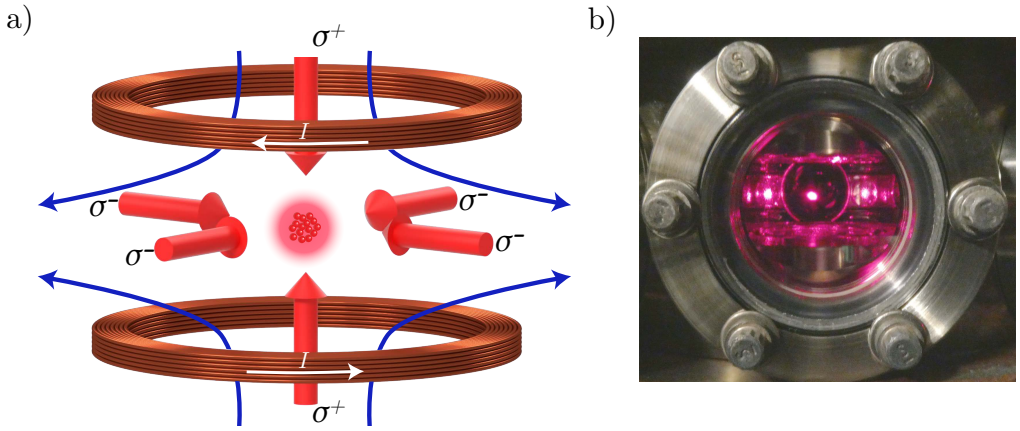

FIGURE 4.2: Working principle and photograph of a magneto-optical trap. a) Our magneto-optical trap consists of six pairwise counter-propagating laser beams with circular polarization in combination with a magnetic quadrupole field. This is realized by two coils in anti-Helmholtz configuration. The polarization of the beams is labeled with respect to the quantization axis defined by the magnetic field lines (blue). The resulting force on the atoms in the trap center, provides both trapping and cooling (see text). b) Photograph of 5×10^8 lithium-6 atoms trapped in the MOT. The atoms are visible, because they scatter the light from the laser beams. The size of the atom cloud is ≈ 3 millimeters (FWHM).

in a MOT is however not zero, but finite and given by [139]

$$T_D = \frac{\hbar\Gamma}{2k_B}\frac{1+S_0+4(\delta_0/\Gamma)^2}{-4\delta_0/\Gamma}, \quad \text{for } \delta_0 < 0 \tag{4.7}$$

which has a minimum of

$$T_{D,min} = \frac{\hbar\Gamma}{2k_B} \tag{4.8}$$

for $S_0 \ll 1$ and $\delta_0 = -\Gamma/2$ [129]. This temperature is called the Doppler temperature [129]. The Doppler cooling limit arises from the balance between the cooling effect of photon absorption from a counter-propagating laser beam and the heating effect due to spontaneous emission at rate Γ^{-1}. For laser cooling on the D_2 line ($2S_{1/2} \rightarrow 2P_{3/2}$) of ^{6}Li, $T_{D,min}$ has a value of 141 µK [1]. In the loading phase of the MOT, we use $\delta_0 \approx 2\pi \times 47\,\text{MHz} \approx 8\,\Gamma$, $S_{0,i} \approx 4$, $\frac{dB}{dx} = \frac{dB}{dy} = -\frac{1}{2}\frac{dB}{dz} \approx 18\,\text{G/cm}$ and $g = g_J \simeq 1$, which this leads to $T_D \approx 1\,\text{mK}$. This temperature is later lowered, when we compress the MOT (see next section).
Our MOT collects atoms which were initially slowed down in the Zeeman slower. We typically achieve loading rates of $\approx 10^8$ atoms/s. By loading the MOT for 5 seconds, we accumulate around 5×10^8 atoms, which are subsequently cooled to 1 mK [82]. They then form a dilute cloud with a typical size of 3-4 mm which

[1] Note that cooling on the $2S_{1/2} \rightarrow 3P_{3/2}$ was also demonstrated [140]. This transition uses UV light at a wavelength of $\approx 323\,\text{nm}$. The $3P_{3/2}$ state has a natural linewidth of $2\pi \times 754\,\text{kHz}$, which results in a Doppler cooling limit of $T_{D,min} = 18\,\mu\text{K}$.

is visible to the bare eye, as shown in Figure 4.2 b). The density is on the order of $n \sim 10^{16}\,\mathrm{m}^{-3}$, which corresponds to a Fermi momentum of $k_F \sim 1\,\mu\mathrm{m}^{-1}$ and a Fermi temperature of $\hbar^2 k_F^2/(2mk_B) \approx 50\,\mathrm{nK}$. As the absolute atom temperature in the MOT is $1\,\mathrm{mK}$, we have $T/T_F > 20\,000$ which is still orders of magnitude away from the quantum degenerate regime where $T/T_F \lesssim 0.5$. For this reason, further cooling steps are necessary.

4.3.1 Compressed MOT

As a first step, we compress the MOT by reducing the detuning of the laser beams from $2\pi \times 47$ MHz to $2\pi \times 5.5\,\mathrm{MHz}$ linearly within $30\,\mathrm{ms}$. This increases the restoring force on the atoms and also lowers their temperature according to Equations (4.6) and (4.7).
Simultaneously, we linearly reduce the optical power of the cooler and the repumper beam. While the cooler power is reduced to $\approx 10\%$ of its initial value ($S_0 \ll 1$), the repumper power is ramped completely to 0 ($S_0 = 0$). This ramp has two effects: First, the temperature of the atoms is further reduced as S_0 reduces (according to Equation (4.7)). Second, by maintaining the cooler beam at a slightly higher power then the repumper, the atoms are optically pumped into the $|2^2\mathrm{S}_{1/2}, \mathrm{F} = 1/2\rangle$ state. This state contains the hyperfine components $|1\rangle$ and $|2\rangle$, that we later want in our experiment. For a level scheme, see Figure A.2. The compression and optical pumping step takes $30\,\mathrm{ms}$ and lowers the atom cloud temperature to $250\,\mu\mathrm{K}$ [99] while simultaneously compressing it to a size of $\approx 200\,\mu\mathrm{m}$ (FWHM). During this process, we lose about half of the atoms. The final parameters correspond to $k_F \approx 11\,\mu\mathrm{m}^{-1}$, $T_F \approx 5\,\mu\mathrm{K}$ and consequently $T/T_F \approx 50$.

4.4 Transfer to optical dipole trap

At the end of the compressed MOT stage, we transfer the lithium-6 atoms into an optical dipole trap (ODT). The ODT is created by focusing a laser beam with $100\,\mathrm{W}$ of optical power at a wavelength of $1064\,\mathrm{nm}$ down to a waist of $38\,\mu\mathrm{m}$ which overlaps with in the center of the MOT. The optical beam path is shown in Figure 4.3. The wavelength of the ODT is far red-detuned from the atomic transitions at $671\,\mathrm{nm}$ which minimizes heating due to photon scattering (see Section 3.6). The transfer initiates by ramping up the optical power to $100\,\mathrm{W}$ (at the position of the atoms) in the last 10 ms of the MOT compression.
The efficiency is optimized by carefully tuning the frequency sweep responsible for the compression of the MOT. We further employ two offset coils (see Section 3.5) to shift the center of the MOT in order to optimize its spatial overlap with the ODT. We transfer a total 5% of the atoms from the compressed MOT to the ODT, which equals about 2.5×10^7 atoms. Due to the asymmetric ramp of the cooler and repumper power during the compression, these atoms are now in a mixture of the Zeeman states $|1\rangle$ and $|2\rangle$.

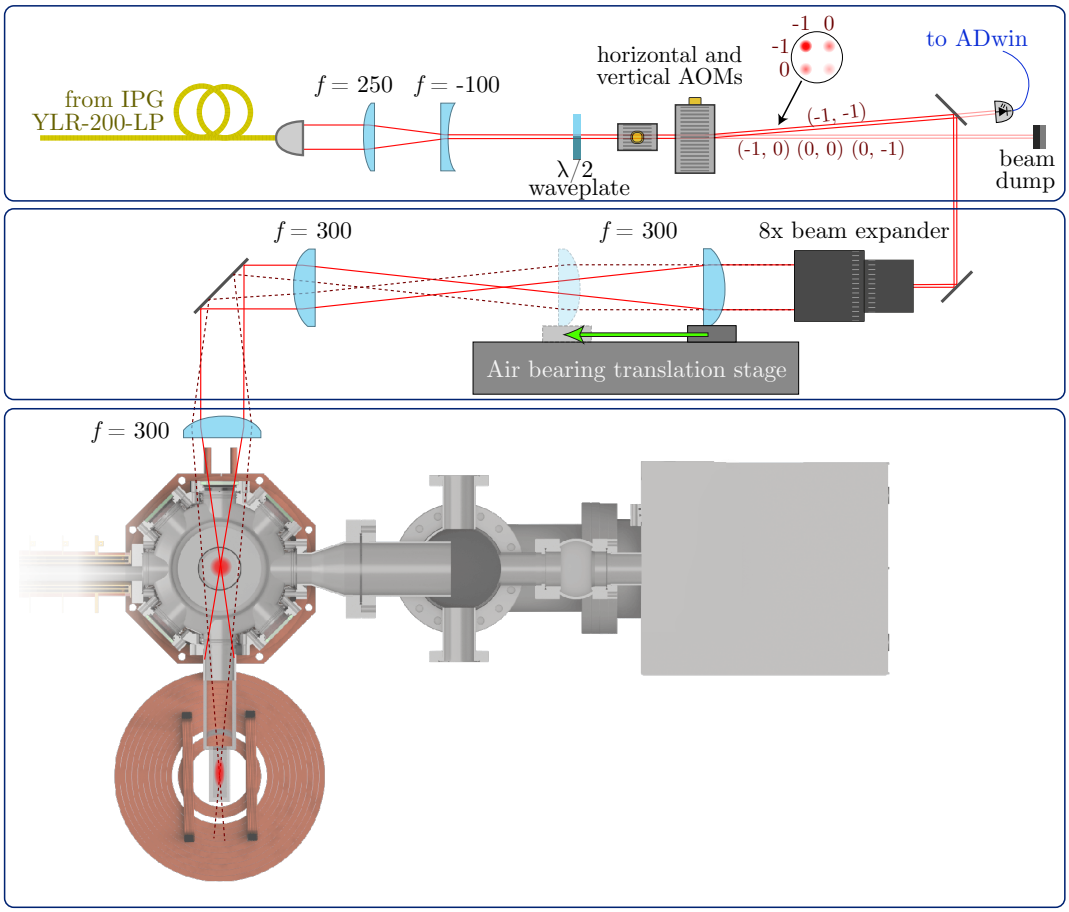

FIGURE 4.3: Setup for the optical dipole trap and the transport, conceptually adapted from [99]. A focused 200 W fiber laser (IPG YLR-200-LP) acts as an optical dipole trap. For intensity control and stabilization, a setup of two acousto-optical modulators (AOMs) in combination with a photo diode and a feedback control loop is used. The transport is realized with a lens of 300 mm focal length mounted on an air bearing translation stage from Nelson Air Corp (ATLAS-101- 400-HD). When the lens is in its initial position (here: right), the focus of the laser beam is in the center of the octagonal MOT chamber. By moving the stage to its final position (left) in a total time of 750 ms, the atoms are adiabatically transported to the glass cell in the focus of the laser beam. The other optics are for properly shaping the laser beam.

4.4.1 Optical transport

After transferring the atoms into the ODT, we optically transport them into the glass cell. This has several key advantages. In the glass cell, the atoms are shielded from the (relatively fast) lithium atoms arriving from the oven. Additionally, the glass cell provides a better optical access, which allows for high numerical aperture imaging and optical manipulation the atoms without being restricted to specific viewports. Moreover, the glass cell facilitates the application of high magnetic fields as the coils can be placed closer to the atoms. In addition, the absence of eddy currents in the glass eliminates distortive effects.

The transport is achieved by mechanically moving a lens in the beam path of the ODT as illustrated in Figure 4.3. For this purpose, we use micrometer precise air bearing translation stage from Nelson Air Corp (ATLAS-101- 400-HD) [120]. Moving the lens shifts the focus of the laser beam, thereby transporting the atoms from the MOT chamber into the glass cell within $750\,\mathrm{ms}$ over a distance of $27\,\mathrm{cm}$. To minimize atom loss during the transport process, the trajectory has been carefully optimized. As a result, we typically retain more than 90% of the atoms throughout the transport.

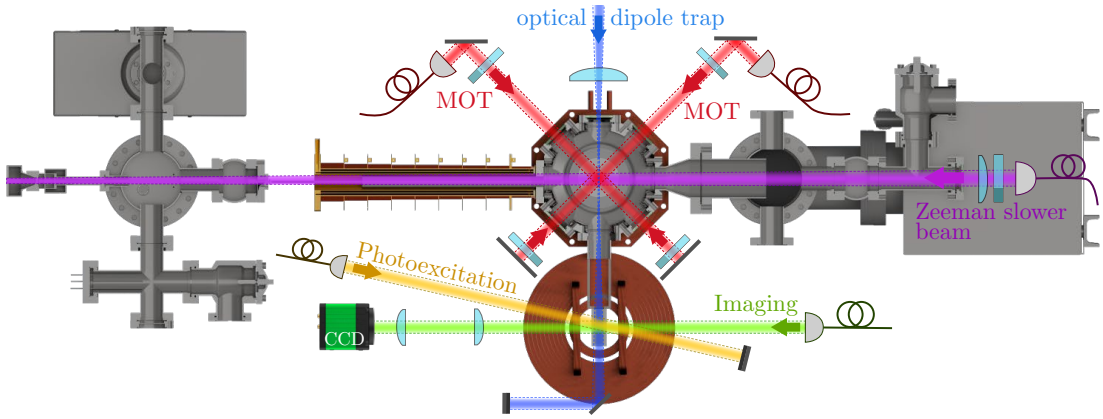

FIGURE 4.4: Top view of the vacuum chamber with all the relevant laser beams for the atom cloud preparation, manipulation and detection. These include the Zeeman slower beam (purple), the horizontal MOT beams (red), the optical dipole trap beam (blue), the photoexcitation beam (yellow) and the imaging beam (green). As the illustration represents a top view, the vertical MOT beam is not visible. The quantization axis in the glass cell is perpendicular to the picture plane.

4.5 Evaporative cooling in the vicinity of the Feshbach resonance

The final cooling step takes place in the glass cell, where we evaporatively cool the atoms by progressively lowering the ODT power over a total time of $5-6$ seconds. This allows the most energetic atoms to escape the trap. The remaining atoms thermalize via elastic collisions, lowering mean temperature[2] [129].
To optimize the thermalization, we do two things. First, we increase the magnetic field in the glass cell to $790\,\mathrm{G}$ using the Feshbach and offset coils. By this, we tune scattering length of the atoms to a large value of $a_s = 8300\,a_0$ [78], which enhances the elastic collision cross section. Second, we create a balanced mixture of the two hyperfine states $|1\rangle$ and $|2\rangle$. This is done by employing a $100\,\mathrm{ms}$ radio

[2]While the probability to find an atom at energy E follows a Boltzmann distribution $p_N(E) \sim \exp(-E/k_BT)$, the distribution of the energies follows $p_E(E) \sim E \times \exp(-E/k_BT)$. Due to the additional factor E, the distribution $p_E(E)$ has a tail which is more pronounced at higher energies compared to $p_N(E)$. Thus, removing atoms above a certain energy, removes a larger fraction of the total energy compared to the fraction of atoms that is removed. This effectively lowers the mean energy per atom once the atoms thermalize.

frequency pulse at a frequency of $76.2\,\mathrm{MHz}$ and a power of $\approx 2\,\mathrm{W}$ with the RF antenna described in Section 3.7. This pulse drives Rabi oscillations between the two hyperfine states creating an incoherent 50-50 mixture. As atoms in individual states do not interact, this mixture maximizes the collision rate for the gas.

The trap depth is lowered as follows. We first decrease the output power of the fiber laser linearly within 3 seconds from $200\,\mathrm{W}$ to $41\,\mathrm{W}$ using the analog control input of the laser. Considering the losses of the beam path, this corresponds to a power of $\approx 20\,\mathrm{W}$ at the position of the atoms. At this stage, the atom cloud has a relative temperature of $T/T_F \approx 10$. The final power ramp is realized with a feedback loop on one of the MIO cards of the ADwin system (see Section 3.3). The loop employs a photo diode to measure the intensity and two AOMs to adjust it, as shown in Figure 4.3. With this, we exponentially lower the power of the ODT with within 3 seconds from the previous $20\,\mathrm{W}$ down to $10 - 1000\,\mathrm{mW}$ depending on the desired atom temperature .
With our current setup, we can achieve final temperatures of $T \sim 10\,\mathrm{nK}$ corresponding to $T/T_F \sim 0.05$ with typical atom numbers of $N = 100\,000$. At this stage, the system is prepared for experiments in the quantum degenerate regime of the BCS-BEC crossover.

4.5.1 Stability

Although the atom cloud preparation takes approximately $12 - 15$ seconds and involves various intermediate steps and devices operating in a precisely timed manner, the preparation cycle has a great reproducibility.
As an example, Figure 4.5 shows the typical atom number over a period of 4

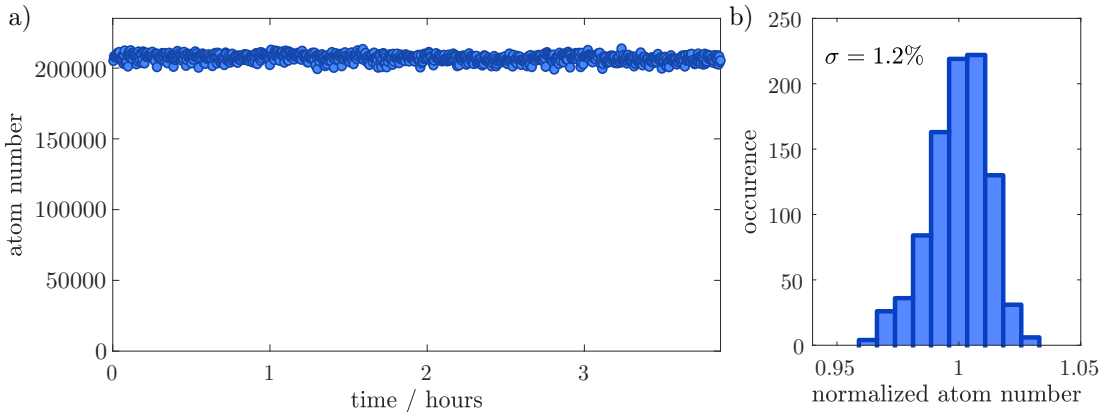

FIGURE 4.5: a) Atom number measurement in the glass cell over a period of 4 hours. For each measurement, a new cloud is prepared within 12 seconds using the steps explained in the text. b) A histogram over the atom number shows a standard deviation of only $\sigma = 1.2\%$, indicating the high stability of our setup.

hours, corresponding to around 900 experimental runs. In these runs, a cloud with 2.1×10^5 atoms at a temperature of $\approx 0.1\,T_F$ was prepared and imaged using absorption imaging. Throughout this period, we observed a standard deviation

in the atom number of only 1.2%, indicating the high stability and repeatability of our experimental cycle which sets the basis for precise measurements.

4.6 Absorption imaging

Absorption imaging is a crucial method in our experiment to determine the spatial distribution the trapped ^{6}Li atoms. From this we can infer important physical properties of the atom cloud. The fundamental principle behind absorption imaging is the interaction of the laser light with the atomic cloud. When resonant light passes the cloud, the atoms absorb and scatter photons, causing a reduction in the intensity of the transmitted light. Effectively, the atoms then cast a shadow, as illustrated in Figure 4.6.

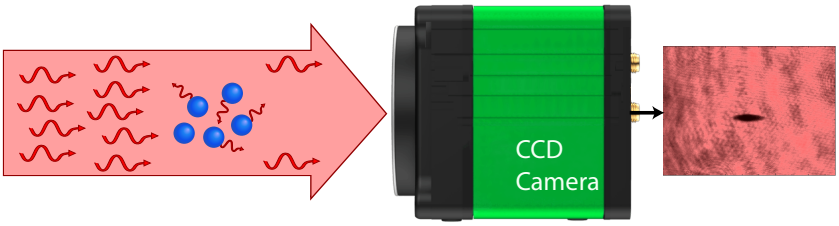

FIGURE 4.6: Principle of absorption imaging. A cloud of atoms (blue balls) is illuminated with a resonant laser beam. The atoms absorb and scatter the photons of the laser beam, reducing the intensity of the transmitted light and effectively casting a shadow. This can be measured with a CCD camera to gain information about the density distribution of the atoms.

As one thereby typically addresses single atomic transitions, laser light with a narrow linewidth is required. For a laser propagating in z-direction, the decrease of intensity is given by the Beer-Lambert law [141]

$$\frac{\mathrm{d}I(x,y,z)}{\mathrm{d}z} = -n(x,y,z)\frac{\sigma_\mathrm{a}}{\alpha^*}\frac{1}{1+\frac{I(x,y,z)}{\alpha^* I_S}+4(\frac{\delta_0}{\Gamma})^2}I(x,y,z) \tag{4.9}$$

where $I(x,y,z)$ is the intensity of the incident light and $n(x,y,z)$ is the atomic density. The quantity σ_a is the ideal absorption cross section given by

$$\sigma_\mathrm{a} = \frac{3\lambda^2}{2\pi}. \tag{4.10}$$

The additional factor $\alpha^* > 1$ in Equation (4.9) accounts for non-perfect polarization or magnetic field orientation, as well as for a reduction of the effective absorption cross section due imaging on non-closed optical transitions [141].
In the limit of a weak and resonant laser ($I(x,y,z) \ll I_S$ and $\delta_0 = 0$), a closed imaging transition and an ideal polarization ($\alpha^* = 1$), Equation (4.9) simplifies to

$$\frac{\mathrm{d}I(x,y,z)}{\mathrm{d}z} = -\sigma_\mathrm{a}\, n(x,y,z) I(x,y,z). \tag{4.11}$$

This can be integrated, to find the intensity distribution $I_\mathrm{f}(x,y)$ after passing the atom cloud, which yields

$$I_\mathrm{f}(x,y) = I_\mathrm{i}(x,y)\, e^{-\sigma_a \int n(x,y,z)\mathrm{d}z} = I_i(x,y)\, e^{-\sigma_a n_{2D}(x,y)} = I_\mathrm{i}(x,y)\, e^{-OD(x,y)} \quad (4.12)$$

where $I_\mathrm{i}(x,y)$ is the initial intensity distribution and $OD(x,y)$ the so-called optical density. For a Gaussian density distribution, the corresponding decrease of intensity is shown in Figure 4.7. The calculation represents a typical scenario in our experiments and is based on Equation (4.12) with $\lambda = 671\,\mathrm{nm}$ corresponding to $\sigma_\mathrm{a} = 2.15 \times 10^{-13}\,\mathrm{m}^2$.

According to Equation (4.12), we can deduce the column densities $n_{2D}(x,y)$ of

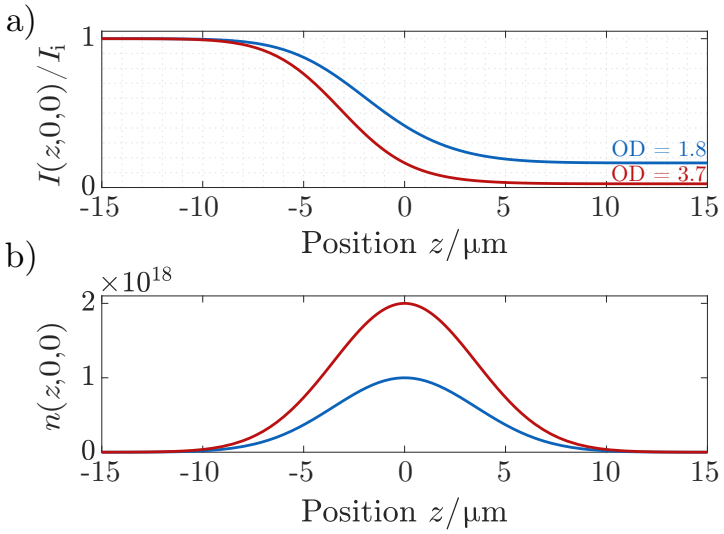

FIGURE 4.7: Intensity $I(z,0,0)$ of a resonant laser beam when passing the center ($x = y = 0$) of ^{6}Li atom clouds. The laser propagates in z-direction. a) Intensities as a function of distance z for two atom cloud density profiles shown in b). The clouds have different peak densities of 1×10^{18} (blue) and 2×10^{18} (red). The overall decrease of intensity corresponds to an optical density of $OD = 1.8$ for the dilute cloud (blue) and $OD = 3.7$ for the denser cloud (red).

the atom cloud by measuring the intensity distributions $I_\mathrm{i}(x,y)$ and $I_\mathrm{f}(x,y)$, e.g. with a CCD camera. In addition, usually also a third image $I_\mathrm{d}(x,y)$ is taken with the laser turned off to correct for camera dark counts and background light. From these three measurements, the column density is then calculated as

$$n_{2D}(x,y) = \frac{1}{\sigma_a} \ln\left(\frac{I_\mathrm{i}(x,y) - I_\mathrm{d}(x,y)}{I_\mathrm{f}(x,y) - I_\mathrm{d}(x,y)}\right). \quad (4.13)$$

For a better visualization, this calculation is illustrated in Figure 4.8. From the column density, we can then determine important properties of the atom cloud, such as the atom number or its temperature (see Chapters 2 and 9).

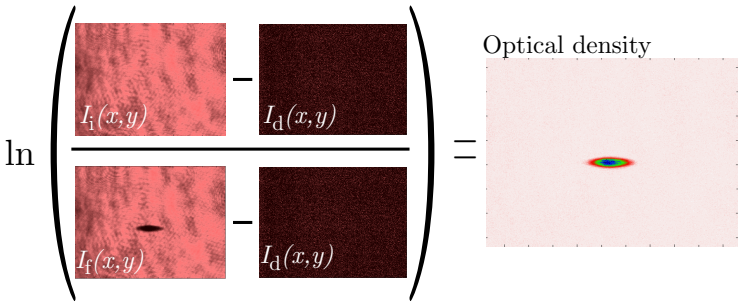

FIGURE 4.8: Graphical illustration of Equation (4.13) for calculating the optical density from three different images (see text). By subtraction, division and taking the logarithm, the optical density is obtained. In contrast to the raw images, the result is almost free of noise.

4.6.1 Absorption imaging of ^{6}Li

Equation (4.13) only holds for the ideal case, when the imaging laser is weak and resonant and when the imaging transition is closed and addressed with the correct polarization.
In our experiments, we perform spin-selective absorption imaging in the high magnetic field on the transitions $|1\rangle = |2^2\mathrm{S}_{1/2}, m_J = -1/2, m_I = 1\rangle \leftrightarrow |2^2\mathrm{P}_{3/2}, m_J = -3/2, m_I = 1\rangle$ and $|2\rangle = |2^2\mathrm{S}_{1/2}, m_J = -1/2, m_I = 0\rangle \leftrightarrow |2^2\mathrm{P}_{3/2}, m_J = -3/2, m_I = 0\rangle$ which requires circularly polarized σ^- light. As the excited state has $m_J = -3/2$, and m_I cannot change, the atoms can only decay back into the same states, thus providing a closed transition [115]. We image the atoms with a collimated laser beam which propagates perpendicular to the quantization axis (see Figure 4.4). To satisfy the selection rules, we use linearly polarized light perpendicular to both the quantization axis and the propagation direction of the laser. At the position of the atoms, this light drives the desired σ^- transition therefore with 50% efficiency, corresponding to $\alpha^* = 2$. We further use intensities as low as $0.02\, I_S$ and employ a resonant laser beam ($\delta_0 = 0$). Equation (4.9) therefore becomes

$$\frac{\mathrm{d}I(x,y,z)}{\mathrm{d}z} = -n(x,y,z)\frac{\sigma_\mathrm{a}}{2} I(x,y,z). \tag{4.14}$$

which eventually yields

$$n_{2D}(x,y) = \frac{2}{\sigma_a} \ln\left(\frac{I_\mathrm{i}(x,y) - I_\mathrm{d}(x,y)}{I_\mathrm{f}(x,y) - I_\mathrm{d}(x,y)}\right) \tag{4.15}$$

for the column density.

4.6.2 ^{6}Li as a lightweight scatterer

There is one major problem that complicates the matter. As ^{6}Li is fairly light atom, and the lightest of the Alkali atoms, the recoil from photon scattering during the absorption plays a significant role. As the atoms scatter photons, they experience an acceleration in the direction of the imaging laser beam. This leads to a Doppler shift that shifts them out of resonance over time. This gradually

lowers the absorption cross section and the atom cloud appears to be more dilute. The recoil velocity per scattered photon of wavelength λ given by $v_{rec} = h/(m\lambda) \approx 0.1\,\mathrm{m/s}$. As a rough estimation, scattering 10 photons already leads to a Doppler shift of $kv \approx \Gamma/4$. In the limit of $S_0 \ll 1$, this lowers the cross section by a factor of $(1 + 4(0.25)^2) = 1.25$ from its initial value. For a long exposure time τ_{im} with the imaging light, the apparent atom number therefore drops.
The duration of the imaging pulse, however, does not appear in the whole absorption imaging treatment so far. To estimate this effect, we consider a single ^{6}Li atom at rest, exposed to imaging light of constant intensity. To match our experimental setting, we set $\alpha^* = 2$, which effectively lowers the intensity the atom experiences by this factor. The force on the atom is then given by

$$F_{sc} = \hbar k \frac{\Gamma}{2} \frac{S_0/\alpha^*}{1 + S_0/\alpha^* + 4(\frac{\delta_0 + kv}{\Gamma})^2} = m\ddot{x}. \tag{4.16}$$

where $\frac{S_0/\alpha^*}{1+S_0/\alpha^*+4(\frac{\delta_0+kv}{\Gamma})^2} = \frac{\sigma_{\mathrm{eff}}(S_0,kv)}{\sigma_0} < 1$ can be regarded as an attenuation factor accounting for the Doppler shift and power broadening. Equation (4.16) represents an equation of motion for the atom. We can solve this equation for an imaging light exposure time τ_{im} and take the time average

$$\left\langle \frac{S_0/\alpha^*}{1 + S_0/\alpha^* + 4(\frac{\delta_0 + kv}{\Gamma})^2} \right\rangle_{\tau_{\mathrm{im}}} \tag{4.17}$$

to get the effective attenuation of the atom signal. This quantity thus represents the scaling factor between the apparent atom number and the real atom number. Note that this procedure is only applicable to a large number of atoms, when all atoms in the cloud experience the same intensity. For this, the atom cloud has to be dilute.
To verify this approach, we measure the two-dimensional optical density $OD(x, y)$ of dilute atom clouds[3] for four different imaging exposure times $\tau_{\mathrm{im}} = 10\,\mu s$, $20\,\mu s, 30\,\mu s, 50\,\mu s$ and various intensities I/I_S. To calculate the column density distribution $n_{2D}(x, y)$, we use the formula from Equation (4.15). By integrating $n_{2D}(x, y)$ over x and y, we get the atom number $N = \int n_{2D}(x, y)\,\mathrm{d}x\mathrm{d}y$.
The results are shown in Figure 4.9 and nicely agree with the calculation. For both, larger imaging light exposure times τ_{im} and intensities I/I_S, the observed apparent atom number decreases. To determine I/I_S, we measure the intensity with a photo diode and include a scaling factor to obtain the intensity at the position of the atoms. This is the only free parameter and effectively only scales the abscissa in Figure 4.9. It has therefore no effect on the real atom number, which is recovered in the limit of $I/I_S \to 0$ for all exposure times τ_{im}. Nevertheless, we compare the intensity from the model calculations with the intensity obtained by measuring the laser power (before the uncoated glass cell) with an optical power meter (PM160 from Thorlabs) and the intensity profile of the imaging laser beam with the CCD camera. Both values are in reasonable agreement, whereby the value from the model calculations is about $5 - 10\%$ below the measured value. The reason for the deviation may be due to the outdated

[3] The peak optical density in the center of the cloud was $OD_{\mathrm{peak}} \approx 0.5$.

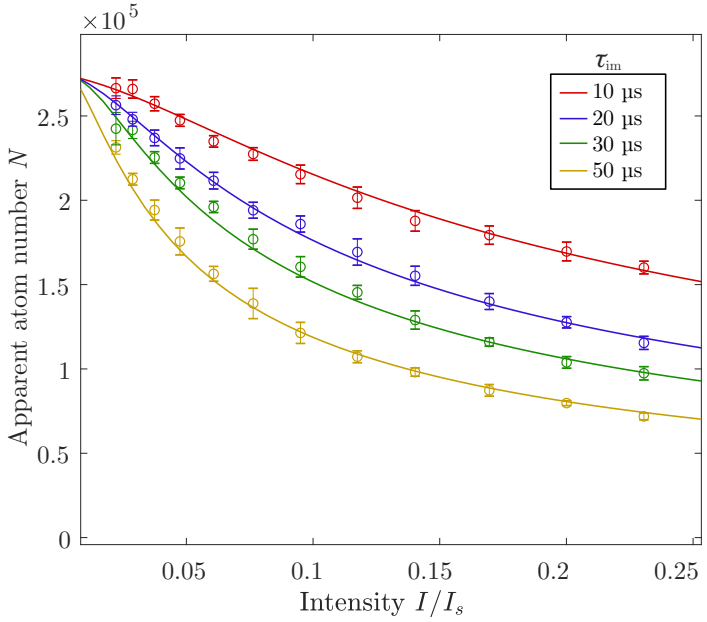

FIGURE 4.9: Measured signal for the atom number as a function of the imaging light intensity for imaging pulse durations of $\tau_{\mathrm{im}} = 10\,\mu\mathrm{s}$, 20 µs, 30 µs and 50 µs. The apparent atom number drops with higher intensity and imaging pulse duration due to an increasing Doppler shift that the atoms acquire while scattering photons. This effectively lowers the cross section for absorption and thus the measured atom numbers. In the limit of zero intensity, the real atom number is recovered.

calibration of the optical power meter, but can also be explained as follows.
The atom clouds in the presented measurements were dilute with a largest optical density of $OD_{\mathrm{peak}} = OD(0,0) = 0.5$ in the center of the cloud. This corresponds to a $1 - \exp(-0.5) = 40\%$ decrease of the intensity from I_i before the center of the cloud to I_f after passing the center of the cloud. The reason why the results in Figure 4.9 still agree nicely with the theory is the following. First, the peak optical density of $OD_{\mathrm{peak}} = 0.5$ only holds in the central region of the cloud for a small fraction of atoms. Atoms far outside experience an even more homogeneous intensity. This becomes clear in Figure 4.10, where we calculate the decrease of the lasers intensity from its initial value I_i when passing the atom cloud (in positive z-direction).
The central region hereby refers to $y = x = 0$, while "far outside" corresponds to $|y| \gtrsim 50\,\mu\mathrm{m}$. The atoms on average experience an intensity $< I_i$ due to the absorption of the light as it passes the atomic cloud. As one can see from Figure 4.9, the decrease of the apparent atom number with intensity is almost linear for all intensity regimes where the intensity changes by $< 40\%$. For this reason, one can approximately replace intensity all atoms experience by an averaged intensity (see Figure 4.11). The deviation from the measured intensity I_i before the cloud is thus simply absorbed by in the scaling factor mentioned above, that we use to translate the photo diode signal to an intensity at the position of the atoms. In the limit of $I \to 0$, we therefore still recover the real atom numbers.

The Doppler shift the atoms acquire from the imaging beam also becomes

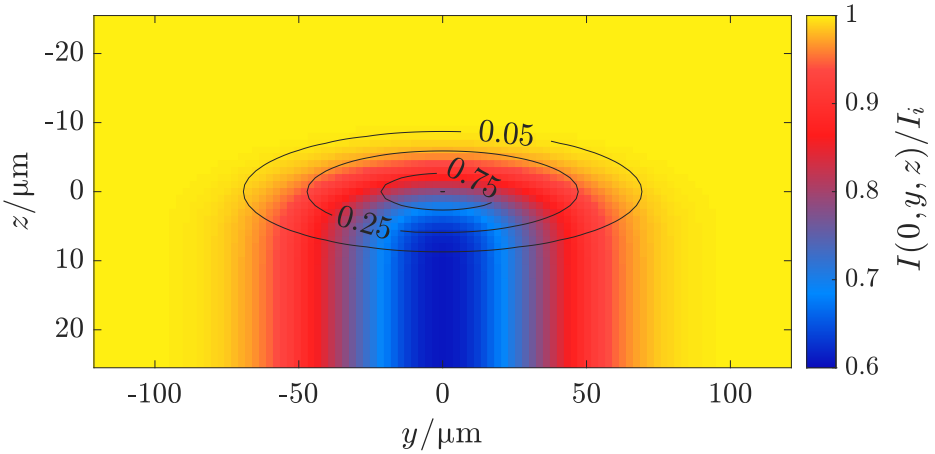

FIGURE 4.10: Intensity distribution of a resonant laser beam when passing a dilute atom cloud centered around $x = y = z = 0$. The color represents the intensity distribution $I(0, y, z)/I_i$ of the laser beam, which propagates in positive z-direction with $I_i = 0.05\, I_S$ at $z \ll 0$. The black contour lines illustrate the density distribution $n(0, y, z)/n(0, 0, 0)$ of the cigar shaped atom cloud. As the light passes the cloud, it is absorbed by the atoms. In the central region around $y = 0$, the intensity decreases by about $1 - \exp(-0.5) = 40\%$, equivalent to an optical density of $OD_{\text{peak}} = 0.5$ at $x = y = 0$. This corresponds to the scenario shown in Figure 4.11.

clearly visible by spectroscopy. For this, we performed spectroscopy of dilute atom clouds at two imaging exposure times τ_{im} of $10\,\mu s$ and $40\,\mu$ and two intensities $I = 0.07\, I_S$ and $I = 0.25\, I_S$. The clouds were prepared with $\approx 255\,000$ atoms per spin state. As shown in Figure 4.12, the observed signals strongly

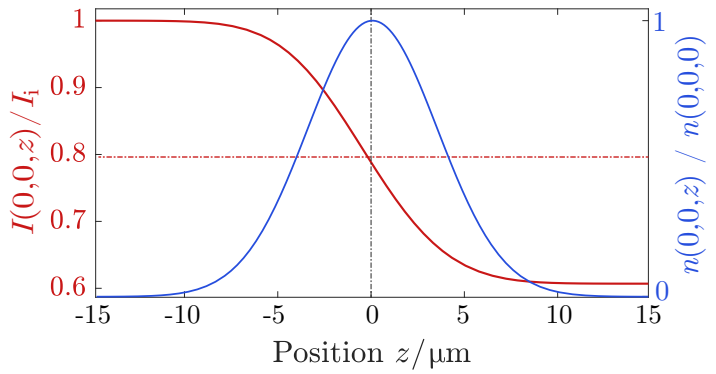

FIGURE 4.11: Intensity $I(0, 0, z)$ of a resonant laser beam when passing the center ($x = y = 0$) of a dilute ^{6}Li atom cloud (solid red line). The density distribution $n(0, 0, z)$ (solid blue line) corresponds to an optical density of $OD(0, 0) = n_{2D}(0, 0)\, \sigma_a/\alpha^* = 0.5$. For such small optical densities, the decrease of intensity within the cloud is almost symmetrical. The atoms on average therefore experience an intensity given by $\frac{I_i+I_f}{2}$ (red dashed line), where $I_i = I(z = 0)$ and $I_f = I(z \gg 0)$.

deviate from the expected Lorentzian lineshape with a theoretical linewidth of $\Gamma = 2\pi \times 5.87\,\mathrm{MHz}$. When the light was initially blue detuned for the atoms at rest ($\delta_0 = \omega_l - \omega_0 < 0$), the imaging beam accelerates the atoms in its propagation direction. This causes a red shift, which enhances the absorption. For this reason, the resonance curve is shifted towards a blue detuned imaging laser frequency. Additionally, power broadening of the lineshape becomes visible. In the limit of $\tau_{\mathrm{im}} \to 0$ the power broadened linewidth is $\Gamma\sqrt{1+S_0}$. When both $S_0 \to 0$ and $\tau_{\mathrm{im}} \to 0$, the typical Lorentzian lineshape of linewidth Γ is recovered, which reaches a maximum at the real atom number of $\approx 255\,000$.

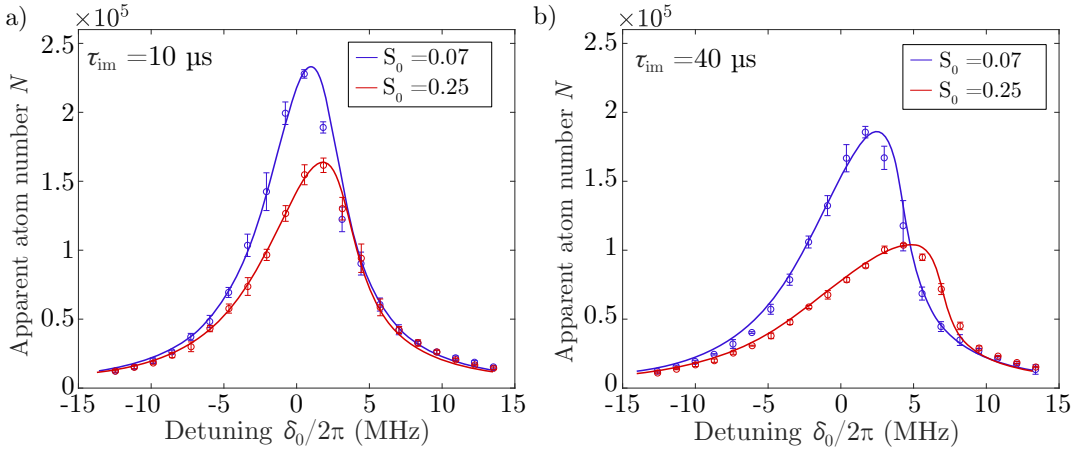

FIGURE 4.12: Atom number signal N as a function of the initial detuning $\delta_0 = \omega_l - \omega_0$ of the imaging laser frequency relative to the dipole transition (from $|1\rangle$ to $|2^2\mathrm{P}_{3/2}, m_J = -3/2\rangle$). a) Measured and calculated spectra for $S_0 = 0.07$ and $S_0 = 0.25$ and an imaging pulse duration of $10\,\mu\mathrm{s}$. b) Data for the same intensities and an imaging pulse duration of $40\,\mu\mathrm{s}$. Both curves strongly deviate from the Lorentzian lineshape with a FWHM of $\Gamma/2\pi = 5.87\,\mathrm{MHz}$ [77], which is recovered in the limit of zero intensity and pulse duration.

4.7 Photoexcitation

With our experimental setup, we investigate pairing in the BCS-BEC crossover. In previous experiments of ours, this involved mapping out the fraction of molecules on the BEC side for various temperatures and interaction strengths [15], or characterizing molecule dissociation dynamics in ultracold collisions [130]. For all these investigations, we need to selectively obtain the number of dimers and free atoms.

To do so, we first determine the total number of atoms (bound or unbound) in the gas via absorption imaging. This works, because the binding energy E_b of these pairs is always less than $h \times 1\,\mathrm{MHz}$ for magnetic fields $B > 650\,\mathrm{G}$ [9]. Therefore, the imaging laser is resonant with both free atoms and pairs.

In the second step, we quickly remove the weakly bound molecules via optical excitation before performing absorption imaging. The molecules, initially in the $X^1\Sigma_g^+, \nu = 38$ state, are transferred to the $A^1\Sigma_u^+, \nu' = 68$ state which has the

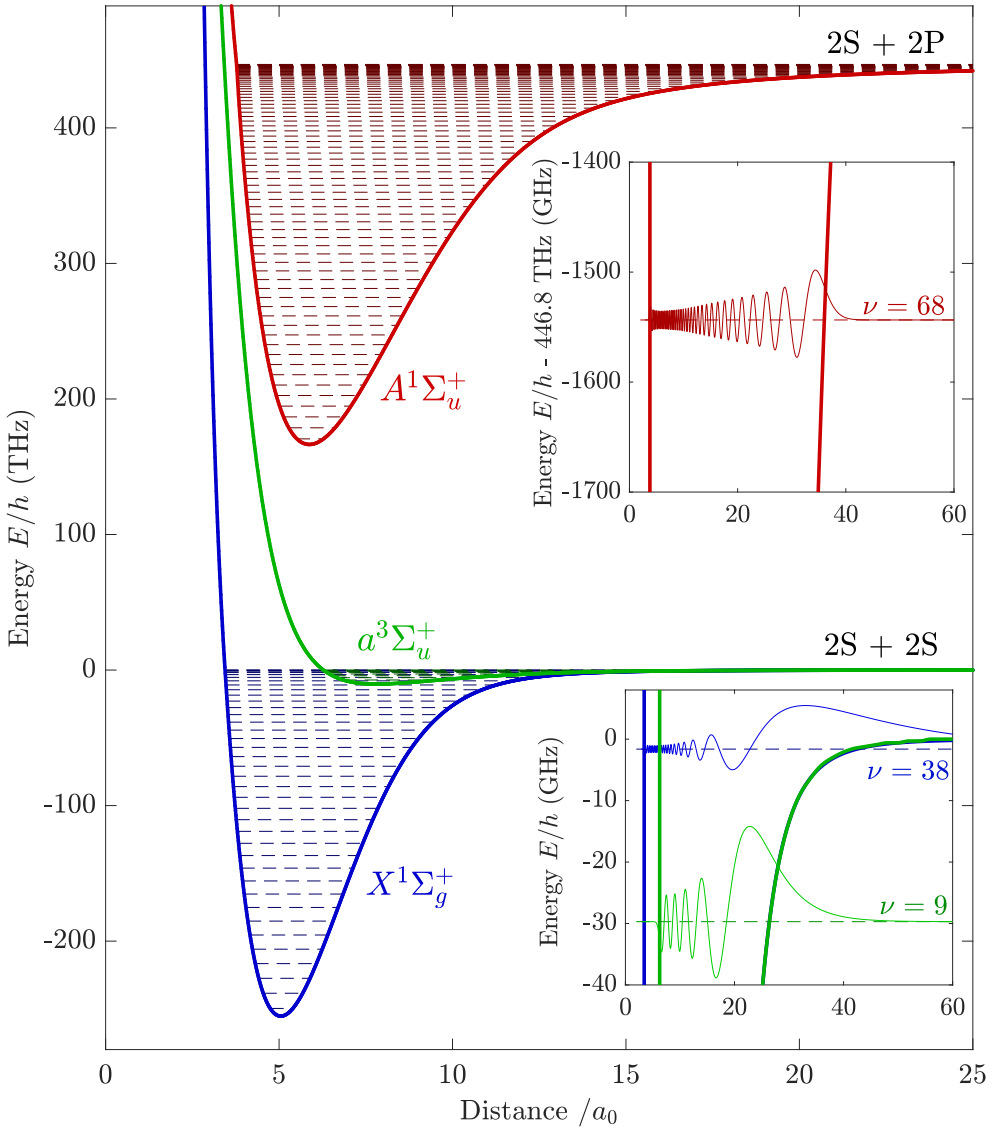

FIGURE 4.13: Potential energy curves (thick solid lines) for the $X^1\Sigma_g^+$ singlet and $a^3\Sigma_u^+$ triplet state of the electronic ground state and the $A^1\Sigma_u^+$ singlet excited state. Also shown are the binding energies (dashed lines) and wave functions (thin solid lines) of the two most-weakly bound vibrational states of the ground state potential ($\nu = 38$ for $X^1\Sigma_g^+$ and $\nu = 9$ for $a^3\Sigma_u^+$) and the wave function of the deeply-bound state of $A^1\Sigma_u^+$ with vibrational quantum number $\nu = 68$. The potential energy curves (PECs) for the singlet ground and excited states have been provided by E. Tiemann, while the triplet PEC is interpolated from data given in [79]. Binding energies and wave functions are calculated by solving the Schrödinger equation for the respective potentials.

largest Franck–Condon overlap of 7.7% with the initial state [142]. For more Frank-Condon factors see e.g. [99]. This molecular excited state $A^1\Sigma_u^+, \nu' = 68$ is shifted by approximately 1550 GHz from the 2S + 2P asymptote, as shown in

Figure 4.13. For this reason, the photoexcitation requires a laser frequency of approximately 445.250 THz, corresponding to a wavelength of about $\approx 673.3\,\mathrm{nm}$. For this, we use a home-built ECDL as presented in Section 3.4. The laser is locked to the optical transition using the wavemeter lock (see Section 3.13), which ensures a linewidth < 1 MHz. From the molecular excited state, the molecules then either dissociate into highly excited unbound atoms, which quickly leave the trap, or decay into deeply bound molecular states invisible to our particle detection.
Spin selective absorption imaging after this excitation pulse gives the number of free atoms per spin state. Removing the pairs and counting the remaining atoms has to be done fast within $\approx 1\,\mathrm{ms}$, as otherwise the pairs start to reform again via three-body recombination [15, 130]. We therefore observe an atom loss when exposing the atoms to the photoexcitation laser light. Figure 4.14 shows typical loss curves in the BEC regime for the remaining atom fraction as a function of the photoexcitation laser exposure time τ_p. The three curves

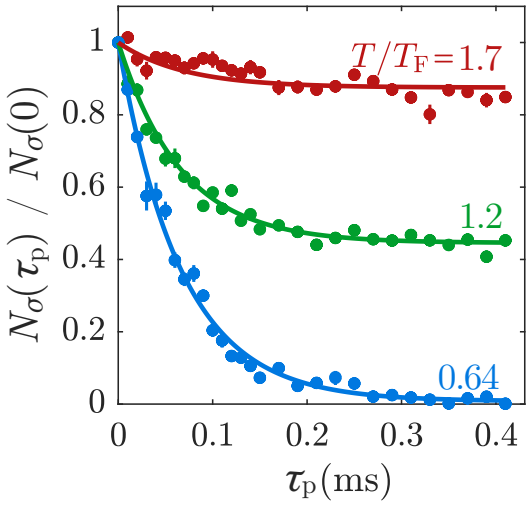

FIGURE 4.14: Remaining fraction $N_\sigma(\tau_\mathrm{p})/N_\sigma(0)$ of atoms per spin state σ as a function of the photoexcitation pulse duration τ_p. The measurements were carried out at a magnetic field of 726 G and temperatures of $T/T_F = 1.7$, $T/T_F = 1.2$, and $T/T_F = 0.64$. The solid lines are exponential fits according to Equation (4.18). For a large τ_p, all molecules are *lost* due to photoexcitation. The remaining atom fraction then reaches a plateau, corresponding to the fraction of unbound atoms. The data is taken from [15].

correspond to measurements where $(k_F a_s)^{-1} > 1$ and dimers can be treated as purely bosonic molecules. The remaining atom number per spin state $N_\sigma(\tau_\mathrm{p})$ then follows an exponential decay [143]

$$N_\sigma(\tau_\mathrm{p}) = N_P e^{-\tau_\mathrm{p}\, a} + N_{\sigma,A}. \tag{4.18}$$

from the total number of atoms per spin state $N_\sigma(0) = N_P + N_{\sigma,A}$, bound or unbound, towards the number of unbound atoms $N_{\sigma,A}$. Here a is an auxiliary parameter, that depends, among other things, on the laser power.

In our previous experiments, we used such measurements to determine the fraction of molecules [15, 130]. However, there is more to learn from the decay curves. While the plateau[4] on the BEC side reflects the fraction unpaired atoms, the initial decay rate and the shape of the decay curve towards and even beyond the Feshbach resonance reveal the strength and the nature of the underlying pair correlations [31–33, 143]. These correlations are quantified by the Tan contact (see Section 2.6) and are comprehensively investigated both experimentally and theoretically within this thesis. The details and results are presented in the Chapters 6 and 7.

[4] A true plateau is reached only in the BEC regime [14, 15, 143]. Towards the Feshbach resonance, many-body interactions become dominant and the binding energy vanishes. The atomic cloud can then no longer be regarded to be composed of (bosonic) molecules and unpaired fermionic atoms. Additionally, the cross-section for photoassociating previously unbound atoms into pairs increases [15]. Therefore, the atom loss due to photoexcitation no longer follows an exponential decay towards a plateau.

Chapter 5

High power solid-state laser system for laser cooling at 671 nm

For laser cooling of the ^{6}Li atoms, we utilize the D_2 transition at a wavelength of approximately $671\,\text{nm}$. This requires a combined optical power of several $100\,\text{mW}$ for the Zeeman slower and the magneto-optical trap. In the past, this was provided by the TA Pro system from Toptica Photonics [99, 117, 119, 144] consisting of a diode laser which is subsequently amplified by a semiconductor optical amplifier. As semiconductor amplifiers for $671\,\text{nm}$ typically suffer from bad transversal beam profiles and short lifetimes, we have set up a new solid-state laser system over the last years [65, 66]. The system is based on the design of the Salomon Group in Paris [61–63] and consists of a home-built $1342\,\text{nm}$ solid-state laser [65] which is subsequently frequency doubled to $671\,\text{nm}$ in a home-built enhancement resonant [66].
In this thesis, I significantly improved the laser system's long-term stability as well as its linewidth. Additionally, I integrated the improved laser system into the experimental setup. It reliably provides the necessary optical power for laser cooling, which sets the basis for all our experiments. To our knowledge, this is the only laser system of its kind that is still being used successfully and on a daily basis to create degenerate, strongly interacting Fermi gases of ^{6}Li. In this Chapter, the laser system and the additional steps that lead to its stable operation are described.

5.1 Fundamental laser at 1342 nm

The fundamental laser is a home-built diode-pumped solid-state laser (DPSS). It provides an output power of $3.5\,\text{W}$ and a gapless tunable output frequency of $223.300 - 223.410\,\text{THz}$, corresponding to a wavelength range of $1341.9 - 1342.6\,\text{nm}$. A comprehensive overview over the general working principle of the DPSS laser for $1342\,\text{nm}$ be found in [61–63, 145, 146]. For a detailed description of our system, see References [65, 66].

5.1.1 Laser setup

The fundamental laser system is built around a neodymium-doped yttrium orthovanadate (Nd:YVO_4) crystal, chosen for its lasing transition at 1342 nm, as illustrated in Figure 5.1. For this, the crystal is optically pumped by an

888 ± 3 nm fiber-coupled diode laser (M1F4S22-888.3-50C) from DILAS (now part of Coherent) which delivers an output power of 45 − 50 W.

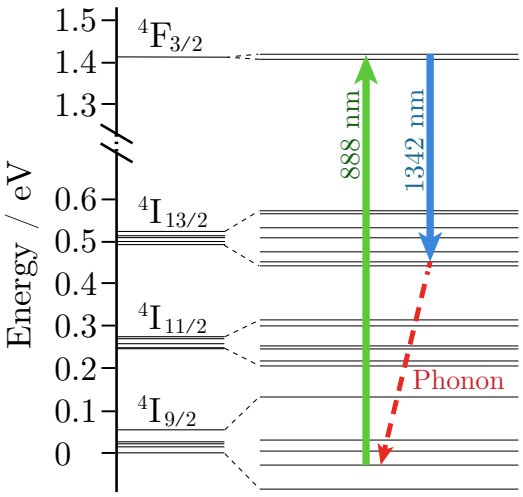

FIGURE 5.1: Term scheme of an Nd^{3+} ion in yttrium orthovanadate. We optically pump from $|^4I_{9/2}, Z_2\rangle \rightarrow |^4F_{3/2}, R_2\rangle$ with a wavelength of 888 nm. Emission at 1342 nm then happens via the transition from $^4F_{3/2}, R_2\rangle \rightarrow |^4I_{13/2}, X_2\rangle$ from which the ion relaxes through subsequent phononic transitions. The letters R, X and Z denote different Stark sublevels of the Nd^{3+} ion (not shown in Figure). Figure adapted from [145, 146].

For single frequency operation and optical amplification, the Nd:YVO_4 crystal is placed in a ring resonator in bow-tie configuration. This setup enhances the stimulated emission, while simultaneously preventing spatial hole burning. An illustration of the laser cavity with all relevant components and dimensions is shown in Figure 5.2. The cavity design includes three highly reflective mirrors at 1342 nm to maximize the intra-cavity power and one outcoupling mirror with a transmission of 8%. When the Nd:YVO_4 crystal is optically pumped, it emits the 1342 nm light bidirectionally. To ensure unidirectional lasing, the cavity includes a terbium gallium garnet (TGG) crystal placed in an arrangement of strong magnets which acts as a Faraday rotator. Together with a $\lambda/2$ wave plate and the laser crystal, acting as a polarization-dependent analyzer, these elements form an optical diode. The cavity further includes two Fabry-Pérot etalons E_1 and E_2 for coarse frequency tuning. For frequency stabilization, one cavity mirror is mounted on a ring piezo actuator (HPSt 150/14-10/12 VS22) from Piezomechanik Dr. Lutz Pickelmann GmbH. Both the laser crystal and the etalon E_2 are temperature stabilized.

5.1.2 Frequency selection and tunability

Nd:YVO_4 features a slightly asymmetric emission gain profile with a width of ≈ 280 GHz [61] and a maximum at a frequency of $\nu_{max} = 223.355$ THz, as shown in Figure 5.3. This frequency corresponds to a wavelength of 1342.2 nm. In

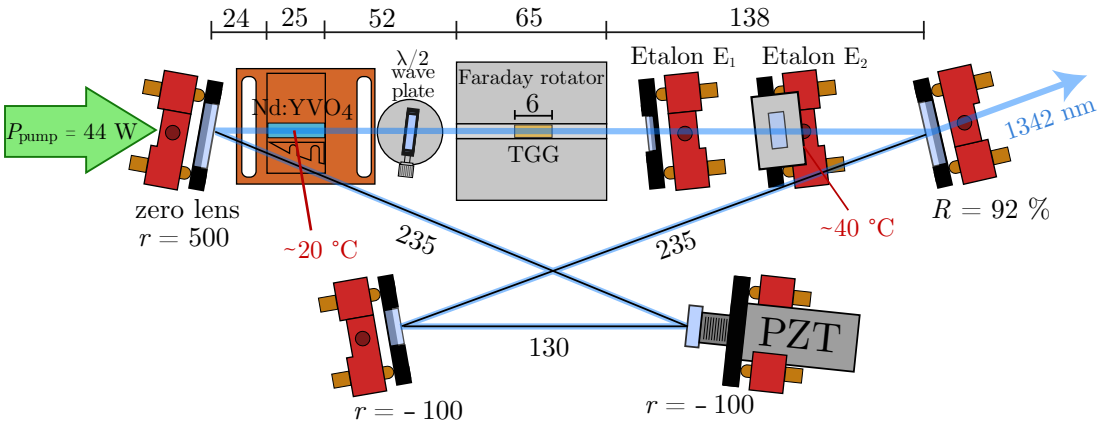

FIGURE 5.2: Detailed sketch of the 1342 nm laser cavity in bow-tie configuration. All dimensions and mirror curvature radii are given in millimeters. The cavity design includes the Nd:YVO_4 laser crystal, two Fabry-Perot etalons E_1 and E_2, a $\lambda/2$ wave plate and Faraday rotator consisting of a TGG crystal and strong magnets. The wave plate, the Faraday rotator and the crystal form an optical diode for a unidirectional laser operation. To stabilize the laser frequency, one cavity mirror is mounted on a piezoelectric transducer (PZT). Figure adapted and updated from [66].

the absence of additional frequency-selective elements, the laser system would naturally operate at $\nu_{\max}$ because it provides the highest gain. However, this frequency 45 GHz below the desired frequency of 223.400 THz, which is half the frequency of the D_2 line of ^{6}Li. For this reason, two Fabry-Pérot etalons E_1 and E_2 are placed in the cavity whose specifications are listed in Table 5.1.
The frequency-dependent transmission $\mathcal{T}(\nu)$ of a Fabry-Pérot resonator with reflectivity R in the plane-wave approximation is given by

$$\mathcal{T}(\nu) = \frac{1}{1 + \left[\frac{2\mathcal{F}}{\pi} \sin(\pi \frac{\nu - \nu_{\text{offs}}}{\nu_{\text{fsr}}})\right]^2} \tag{5.1}$$

where $\mathcal{F} = \frac{\pi\sqrt{R}}{1-R}$ denotes the finesse and $\nu_{\text{fsr}} = \frac{c}{2nL}$ the free spectral range determined by the length L and the refractive index n of the etalon. The transmission of the etalon is periodic in ν_{fsr} and becomes 1, when $\nu = \nu_{\text{off}} + b\,\nu_{\text{fsr}}$, where ν_{offs} is some offset (frequency) and $b \in \mathbb{Z}$. The offset depends on the optical path length of the etalon, with respect to the propagating laser beam. It can be tuned by either tilting the etalon with respect to the beam propagation[1] or by changing its temperature, which affects both its refractive index and length. The frequency

[1]When passing a Fabry-Pérot etalon, the laser beam experiences multiple reflections from both end facets of the etalon. An initial Gaussian beam therefore becomes displaced and distorted. This introduces so-called walk-off losses [147]. For this reason, one normally avoids etalon tilting.

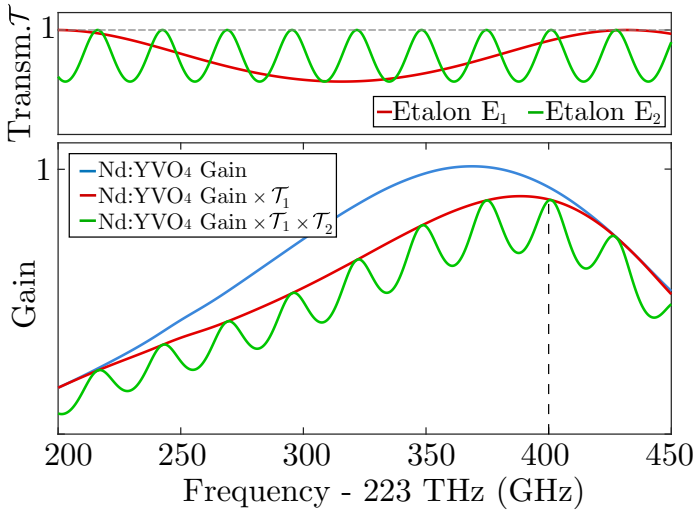

FIGURE 5.3: Gain profile of the fundamental laser with and without etalons E_1 and E_2. The overall gain of the laser cavity is given by the product of the crystal gain profile (solid blue line) and the transmission functions $\mathcal{T}_1$ (solid red line) and $\mathcal{T}_2$ (solid green line) of the two etalons. By adjusting both etalons, the laser can be tuned to operate at $223.400\,\mathrm{THz}$. The figure shows exactly this configuration. The data for the crystal gain profile is extracted from Ref. [61].

change by temperature is given by

$$\frac{\mathrm{d}\nu_{\mathrm{offs}}}{\mathrm{d}T} = -\nu\left(\frac{1}{L}\frac{\partial L}{\partial T} + \frac{1}{n}\frac{\partial n}{\partial T}\right) \tag{5.2}$$

which is a value that only depends on the material properties and the wavelength, not on the geometric properties of the etalon. Changing ν_{offs} therefore effectively shifts the transmission function of the etalon. For fused silica glass, this shift at room temperature is given by $-1.49\,\mathrm{GHz/K}$. For the calculation the values listed in Table 5.1 were used. The overall gain of the laser cavity is given by multiplying the gain profile of the crystal with the transmission functions $\mathcal{T}_1(\nu)$ and $\mathcal{T}_2(\nu)$ of the two etalon, as shown in Figure 5.3.

Given that the gain profile of the crystal is constant and for a fixed transmission function $\mathcal{T}_1$ (corresponding to a fixed angle and temperature of etalon E_1), one would expect that the laser frequency ν shifts almost linearly with the temperature of etalon E_2, as also demonstrated in [61]. In our measurements, we however observe a different behaviour, which we could not explain at first. Specifically, as we increase the temperature of etalon E_2, the laser frequency ν decreases in a step-like manner with steps occurring approximately every 2.8 GHz, as shown in Figure 5.4. The frequency of 2.8 GHz coincides with the free spectral range of the laser crystal, given by $\nu_{\mathrm{fsr,cr}} = \frac{c}{2L_{\mathrm{cr}}n_{\mathrm{cr}}} = 2.76\,\mathrm{GHz}$ which turns out to be more than a mere coincidence. The step-like frequency dependence arises from a residual reflectivity of the laser crystal of about $R_{\mathrm{cr}} = 0.15\%$[2]. Although this value might seem rather low, it is still comparable to the reflectivity of the

[2]We infer this value from our calculations, see Figure 5.4 b).

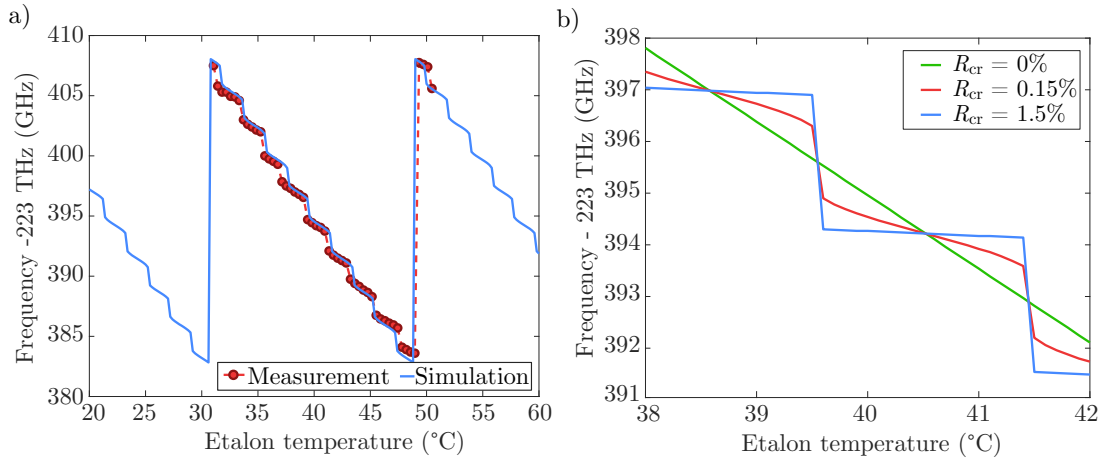

FIGURE 5.4: a) Frequency of the fundamental laser as a function of the temperature of etalon E_2. Measurements are shown as red dots, the dashed red line serves as a guide to the eye. When increasing the temperature of E_2, the laser frequency decreases with an overall slope of approximately $\partial\nu/\partial T = -1.4\,\mathrm{GHz/K}$, in agreement with the calculation based on Equation (5.2). The step-like decrease is explained by a residual reflectivity of the laser crystal surface which itself acts as an etalon. This can be confirmed by numerical simulations (solid blue line). The sudden large jumps frequency of $\approx 25\,\mathrm{GHz}$ at $31\,^{\circ}\mathrm{C}$ and $49\,^{\circ}\mathrm{C}$ are caused by the periodicity of the etalon's transmission function. b) Simulations of the step-like frequency change for different crystal surface reflectivities. For $R_{\mathrm{cr}} = 0\%$ no step is observed. For larger values of R_{cr}, the step becomes more pronounced.

etalons, which have $R_{\mathrm{E1}} = R_{\mathrm{E2}} = 3.3\%$. Consequently, the laser crystal itself acts as an etalon, suppressing the laser operation at certain frequencies spaced by $2.76\,\mathrm{GHz}$. This suppression causes the observed sudden jumps in laser frequency when scanning the temperature of etalon E_2.
We confirmed this behaviour with numerical simulations that account for the crystal's gain profile and the transmission functions of all optical elements in the laser cavity, as listed in Table 5.1. With these simulations, we can recreate the measured frequency scan almost perfectly, as indicated by the solid blue line in Figure 5.4 a). Figure 5.4 b) presents the same simulations for different crystal reflectivities. For $R_{\mathrm{cr}} = 0\%$, we observe the expected linear change in laser frequency with etalon temperature.
Underestimating the influence of the residual crystal reflectivity was for a long time the reason we could not achieve a stable laser operation. Previously, the laser crystal was cooled by our house cooling water, which provides a high pressure of up to 8 bar and a temperature of approximately $15\,^{\circ}\mathrm{C}$. However, instabilities in the cooling water temperature caused fluctuations in the crystal temperature on the order of $0.5\,\mathrm{K}$ in. This leads to shifts of the crystal's transmission function which changes by $-1\,\mathrm{GHz/K}$, as shown in Table 5.1. These shifts resulted in instabilities in the laser operation, when the frequencies that the crystal suppresses coincided with the desired laser frequency.
To address this issue, we installed a temperature-regulated water chiller (TCube

TABLE 5.1: Optical elements in the fundamental laser cavity.

	Etalon E_1	Etalon E_2	Laser crystal	TGG crystal
Length L	0.488 mm	3.9 mm	25 mm	6 mm
Refractive index n	1.446 [148]	1.446 [148]	2.17 [149]	1.94 [150]
Free spectral range ν_{fsr}	212 GHz	26.6 GHz	2.76 GHz	12.9 GHz
Reflectivity	3.3%	3.3%	0.15%	-
Therm. exp. coeff. $\frac{1}{L}\frac{\partial L}{\partial T}$	5.5×10^{-7}/K [151]	5.5×10^{-7}/K [151]	8.4×10^{-6}/K [152]	7.0×10^{-6}/K [153]
Thermo-optic coeff. $\frac{\partial n}{\partial T}$	8.4×10^{-6}/K [154]	8.4×10^{-6}/K [154]	7.92×10^{-6}/K [155]	17.5×10^{-6}/K [153]
Freq. tuning $\frac{\mathrm{d}\nu}{\mathrm{d}T}$	−1.49 GHz/K	−1.49 GHz/K	−1.00 GHz/K	−1.16 GHz/K

Edge 3S from Solid State Cooling Systems) and added a Peltier element for fine regulation of the crystal temperature. By setting a cooling water temperature of 8 °C, we achieve a crystal temperature of 20 °C in steady state operation, at an optical pumping power of 45 W. With these improvements, the temperature is stabilized with fluctuations of less than 10 mK. By carefully adjusting the temperature of etalon E_2 and the crystal temperature, a stable laser operation at 223.400 THz with an output power of 3.8 W could be achieved. This frequency is subsequently frequency doubled via second harmonic generation (SHG) to 446.800 THz as explained in the next section.

5.2 Second harmonic generation of 671 nm

For second harmonic generation, we use a nonlinear crystal made of periodically poled magnesium-oxide-doped lithium niobate (ppMgO:LN) from Covesion (MSHG1350-0.5-20) which has a length of $L = 20$ mm. In the crystal, the optical power P_{ω_1} of the fundamental laser at a frequency of 223.400 THz is converted to an optical power P_{ω_2} at a frequency 446.800 THz. For a Gaussian laser beam in the TEM_{00} transverse mode, which is focused into the center of the nonlinear crystal, the second harmonic power is given by [66, 156, 157]

$$P_{\omega_2} = \frac{2\omega_1 d_{\text{eff}}^2}{\pi\epsilon_0 n_1 n_2 c^4} L\, h(\xi, \sigma_T)\, P_{\omega_1}^2 \tag{5.3}$$

where $\omega_1 = 2\pi \times 223.400$ THz is the fundamental frequency, n_1 and n_2 are the refractive indices of the crystal for the fundamental and second harmonic frequency, d_{eff} is the effective nonlinear coefficient, ϵ_0 is the vacuum permittivity and $h(\xi, \sigma_T)$ the Boyd-Kleinman factor [156, 157]. It depends on the focusing parameter $\xi = \frac{L}{2z_R}$ given by the ratio of the crystal length L and the Rayleigh length z_R of the Gaussian beam and the phase-matching parameter σ_T which is a function of the crystal temperature T. The Boyd-Kleinman factor has a global maximum of $h(\xi = 2.84, \sigma_T = 0.573) = 1.068$ [61]. A detailed derivation and further information to second harmonic generation with ppMgo:LN can be found in References [61, 66, 156, 157].
From Equation (5.3), one can see that the second harmonic power P_{ω_2}, scales

quadratically[3] with the fundamental power P_{ω_1}. All the prefactors in this equation can be summarized in the conversion efficiency η, such that

$$P_{\omega_2} = \eta P_{\omega_1}^2. \tag{5.4}$$

Typical values for a bulk SHG crystal are $\eta \simeq 0.1\,\% - 2\,\%/\mathrm{W}$. Even with our highest available input power of $3.5\,\mathrm{W}$ at $1342\,\mathrm{nm}$, this would only yield a converted power of about $250\,\mathrm{mW}$ at $671\,\mathrm{nm}$. For this reason, the ppMgO:LN crystal is placed in a running wave enhancement resonator in bow-tie configuration. Within the resonator, the fundamental power is enhanced to $P_{\mathrm{circ}} = 20 - 30\,\mathrm{W}$, significantly increasing the effective conversion efficiency to $60 - 75\%$ [66].

5.2.1 Enhancement resonator

Our home-built enhancement resonator consists four mirrors arranged in bow-tie configuration. It is in detail described in [66] and in illustrated in Figure 5.5 will all important dimensions. All cavity mirrors are anti-reflective coated for

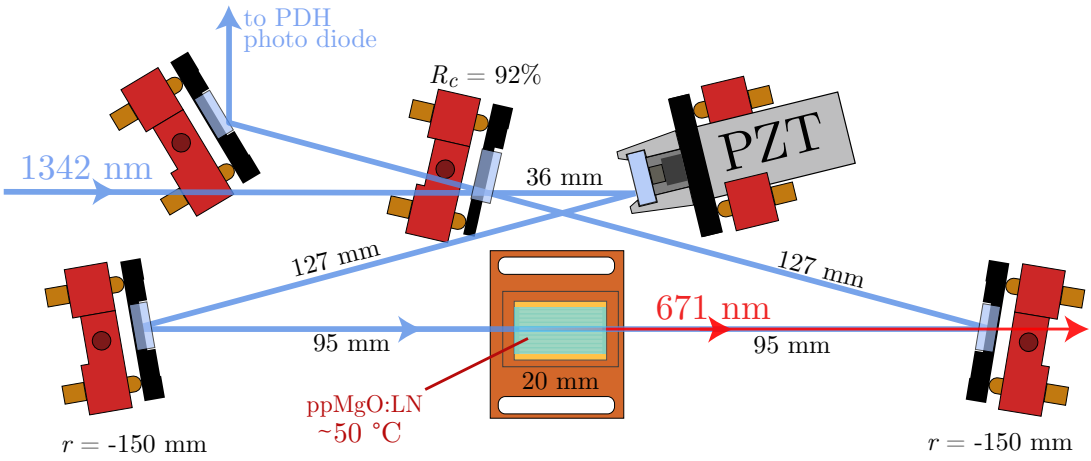

FIGURE 5.5: Illustration of the second harmonic enhancement resonator. It consists of four mirrors arranged in a bow-tie configuration. The $1342\,\mathrm{nm}$ light is coupled into the resonator through the incoupling mirror (top left) with reflectivity $R_C = 92\%$. Light which is reflected from this mirror is used to stabilize the resonator via a Pound-Drever-Hall (PDH) stabilization scheme [158]. The other three mirrors are highly reflective at $1342\,\mathrm{nm}$ and anti-reflective at $671\,\mathrm{nm}$. The SHG crystal is temperature stabilized and placed between the two curves mirrors with radii of curvature of $r = -150\,\mathrm{mm}$. The mirror in the top right is movable by means of a piezoelectric transducer to adjust the length of the cavity. The converted light exits the resonator through the curved mirror on the bottom right. Figure adapted from [66].

$671\,\mathrm{nm}$. Three of these mirrors are also highly-reflective coated for $1342\,\mathrm{nm}$, with a reflectivity of $R_M = 99.5\%$. The remaining mirror with a reflectivity of $R_c =$

[3]Due to energy conservation, this only holds in the limit of a small conversion efficiency, when the fundamental power P_{ω_1} is constant over the whole crystal length L. Considering losses due to conversion, one finds $P_{\omega_2} = P_{\omega_1} \tanh^2(\sqrt{\tilde{\eta} P_{\omega_1}^2} L)$.

92% serves as the incoupling mirror for the fundamental light. Its reflectivity is chosen to fulfill the optical impedance matching condition, approximately given by [61, 66]

$$R_c = R_M^3 e^{-\alpha_{\mathrm{abs}} L}(1 - \eta P_{\mathrm{circ}})(1 - l_{\mathrm{aux}}) \tag{5.5}$$

which translates into the statement that the transmission of the incoupling mirror should equal the sum of all round-trip losses of the fundamental power [62, 63, 66, 159]. These losses include leakages through the three other mirrors with reflectivity R_M, absorption in the ppMgO:LN crystal with absorption coefficient of $\alpha_{\mathrm{LN}} = 0.2\,\%/\mathrm{cm}$ [160], losses due to the second harmonic generation and additional losses l_{aux} due to e.g. dust on the optics.
As the resonator is a running-wave resonator, its length has to be stabilized to a multiple of the fundamental wavelength of $1342\,\mathrm{nm}$. Our stabilization is based on the PDH technique [158] and detailed in Section 5.3 and Ref. [66]. To adjust the length, one of the cavity mirrors is mounted in a home-built piezo actuated mirror holder with a travel range of $2.4\,\mu\mathrm{m}$ and a bandwidth of $10\,\mathrm{kHz}$ [66].
The resonator has a stable TEM_{00} eigenmode with a beam waist of $126\,\mu\mathrm{m}$ in the center of the crystal [66], which leads to an overall conversion efficiency of $0.19\,\%/\mathrm{W}$ according to Equation (5.3). Due to the strong enhancement of the fundamental light, we still achieve a decent output power and conversion efficiency.

5.2.2 Performance

We typically operate the resonator with a fundamental power of $P_{\omega_1} = 820\,\mathrm{mW}$ which is converted into $420\,\mathrm{mW}$ of second harmonic power at $671\,\mathrm{nm}$ corresponding to a conversion efficiency of about 50%. This optical power is typically enough for efficient laser cooling in our experimental setup, see Section 3.4.
When increasing the fundamental power further to $1.6\,\mathrm{W}$, we reach an output power of more than one watt at $671\,\mathrm{nm}$. This is shown in Figure 5.6 a) and corresponds to a conversion efficiency of 65%. We typically do not go beyond this value, as the system is optimized for lower optical powers and to stay well below the optical damage threshold of lithium niobate which is $0.001 - 2\,\mathrm{MW/cm^2}$ [61, 161]. From a numerical calculation, shown in Figure 5.6, we can infer a saturation at an efficiency of over 70%, which would ideally provide a power of about 2.5 watts at $671\,\mathrm{nm}$ for a fundamental power of $P_{\omega_1} = 3.5\,\mathrm{W}$.
The second harmonic light has an almost Gaussian transversal beam profile, as shown in Figure 5.6 b). This facilitates a measured fiber coupling efficiency of more than 80% into a single mode polarization maintaining fiber (PMJ-3AF,3AF-633-4/125-3-10-1 from OZ Optics).

5.3 Stabilization and linewidth

To achieve the frequency required for laser cooling, both the fundamental and the second harmonic cavity have to be actively stabilized. The entire laser system and stabilization scheme with all optical, electro-optical and electronical components is illustrated in Figures 5.7 and 5.8 and works as follows.

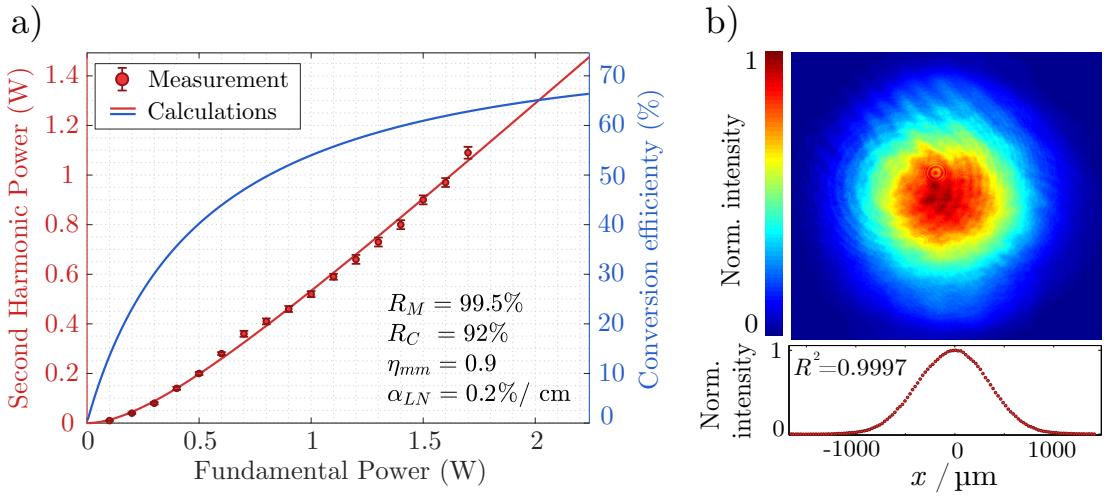

FIGURE 5.6: a) Measurement (red dots with error bars) and calculation (solid red and blue lines) of the second harmonic power and effective conversion efficiency. The simulation uses a crystal conversion efficiency of $0.19\%/\text{W}$ and the parameters shown in the figure. The parameter η_{mm} includes incoupling losses into the cavity due to a non-ideal mode matching of the fundamental laser to the SHG resonator eigenmode. b) Measured transversal beam profile of the converted $671\,\text{nm}$ light, taken with a CCD camera. A Gaussian fit with an R-squared value of 99.97% indicates an almost prefect Gaussian beam profile.

We first stabilize the SHG resonator to the free running fundamental laser[4]. This is done by a PDH stabilization scheme which utilizes an EOM for creating sidebands on the fundamental laser frequency and a fast photo diode to detect the reflection of the sidebands from the resonator[5]. From the reflected light, we generate a corresponding error signal, which is fed into an analog PID regulator (PID 110) from Toptica Photonics. The electronical components for this are shown in Figure 5.8 in blue colors. The PID regulator provides an appropriate feedback voltage which acts on piezoelectric transducer in the enhancement cavity to stabilize its length and maintain resonance with the fundamental light.

The enhancement resonator also supports higher transversal modes. These are strongly suppressed compared to the TEM_{00} mode, but also feature a zero-crossing in the generated error signal. To ensure, that we always stabilize to the TEM_{00} mode, we use a second photo diode (not shown) to capture a fraction of the converted light. This signal is also given to the PID regulator and compared to a threshold value which ensures stabilization to the correct mode.

In the next step, the fundamental laser cavity is stabilized. This is done by means of a frequency offset lock [124]. For this, we impose about $1\,\text{mW}$ of optical power from both our master laser (see Section 3.4) and the second harmonic light and detect the frequency beat on a fast photodiode. With the electronical components shown in Figure 5.8 in green colors, we generate an error signal

[4]To be more precise: This is done permanently, as our feedback control loop for the PDH stabilization is permanently active.

[5]The basic idea is, that the cavity is exactly on resonance with the incoming light, when the red and blue sideband are reflected at the same strength.

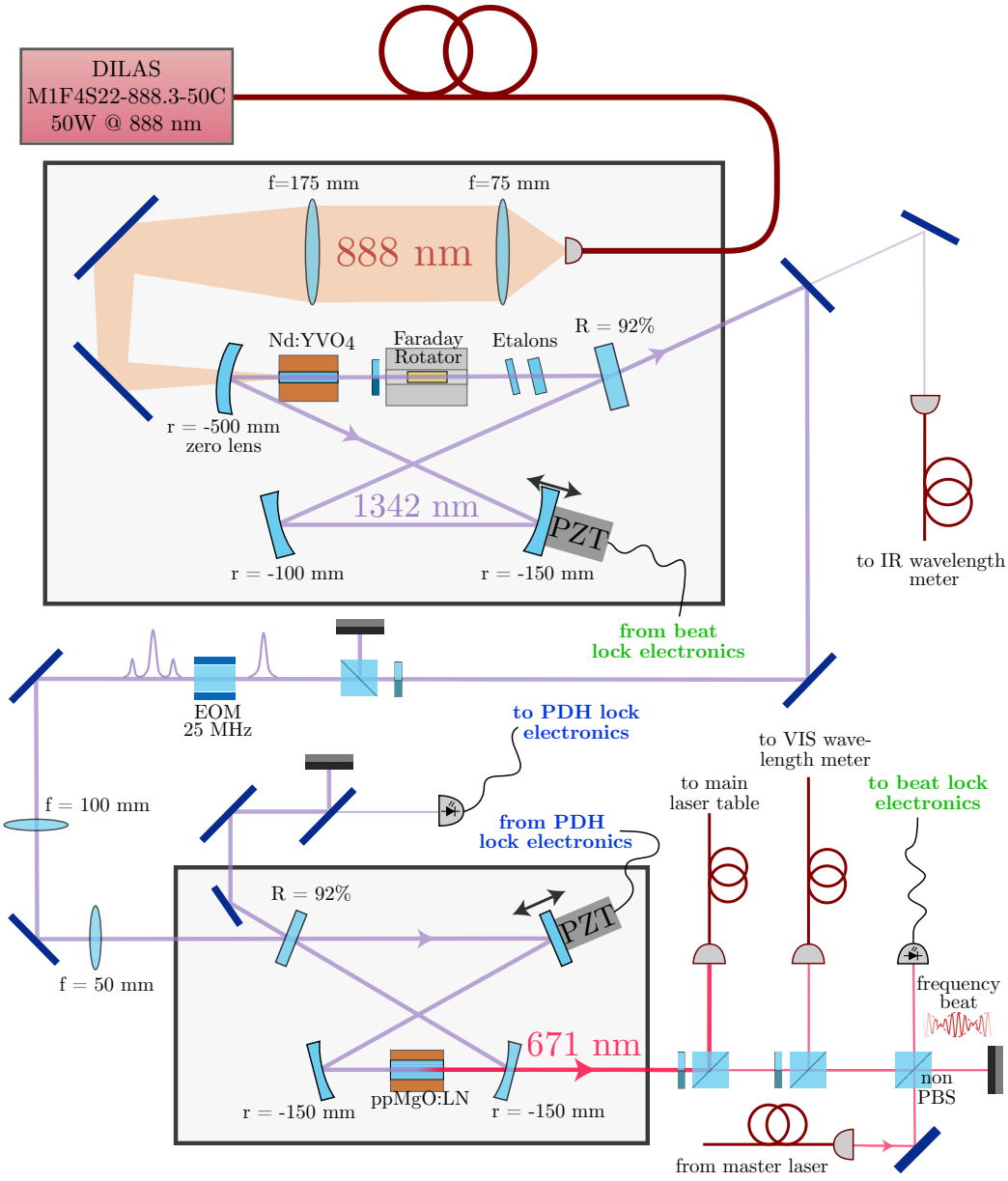

FIGURE 5.7: Complete overview of the home-built solid-state laser system for laser cooling of ^{6}Li. The figure shows all optical and electro-optical components. The electronical devices for stabilizing both laser cavities are indicated by the blue and green colored labels and shown in Figure 5.8 in detail. For more information, see text.

whose zero-crossings can be shifted with an voltage controlled oscillator. This allows for adjusting the relative frequency of the lasers, which is needed laser for compressing the MOT (see Section 4.2). The error signal is fed to another analog PID regulator (PID 110) from Toptica Photonics, to produce a feedback voltage that acts on the piezoelectric transducer in the fundamental cavity. By tuning the length of the fundamental resonator, the frequency of the fundamental light

- and by this the frequency of the doubled light - changes accordingly[6]. The

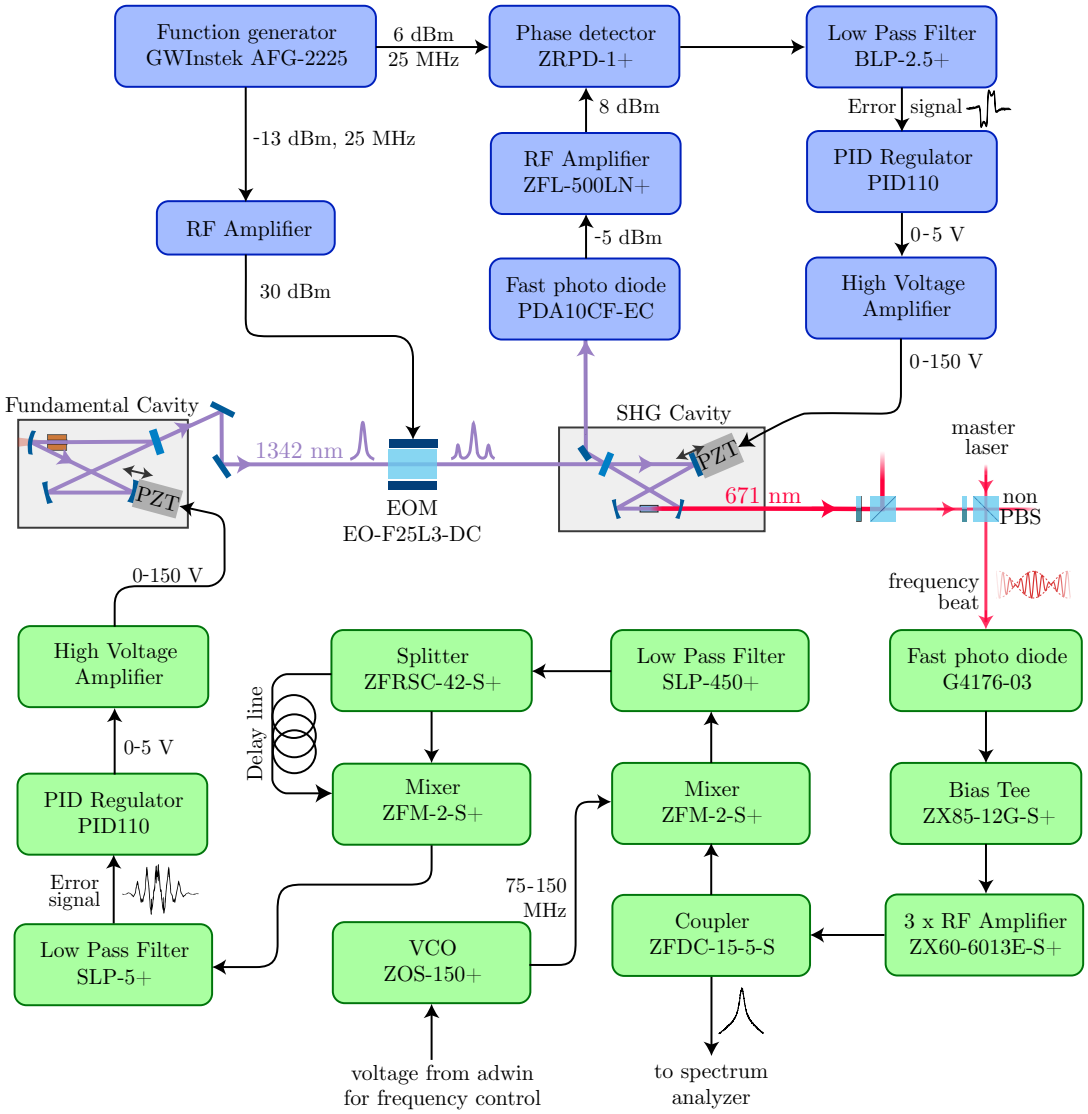

FIGURE 5.8: Overview of the solid-state laser system, only showing the electronical devices for stabilizing both cavities. Blue colors show the components for generating the PDH error signal and for utilizing it to stabilize the SHG resonator. Green colors show the components of the frequency offset lock, whose locking points can be shifted with an analog voltage from the AdWIN. This enables us to easily tune the laser frequency. A readout of the beat signal allows for determining the linewidth of the solid-state laser.

locking scheme provides precise frequency control while simultaneously minimizing the linewidth of the laser. We can estimate the linewidth by observing

[6]This scheme requires that the SHG cavity lock can follow the frequency changes of the fundamental laser, which works without any problems in our case. One reason for this is also the naturally small finesse of the SHG cavity of $\mathcal{F} = 37$ [66], resulting in a cavity linewidth of about 10 MHz. This provides a large acceptance window for the fundamental frequency.

the frequency beat of the master laser and the second harmonic frequency on a spectrum analyzer (see Figure 5.8).

5.3.1 Narrowing the lineshape

For off-resonant laser cooling as done in our red detuned magneto-optical trap, the linewidth of the laser plays a rather inferior role. However, for imaging the ^{6}Li atoms or other applications in the future, having a narrow linewidth can be quite advantageous. In the past, the linewidth of the home-built solid-state laser system was on the order of $1.5\,$MHz. By a mechanical frequency analysis and

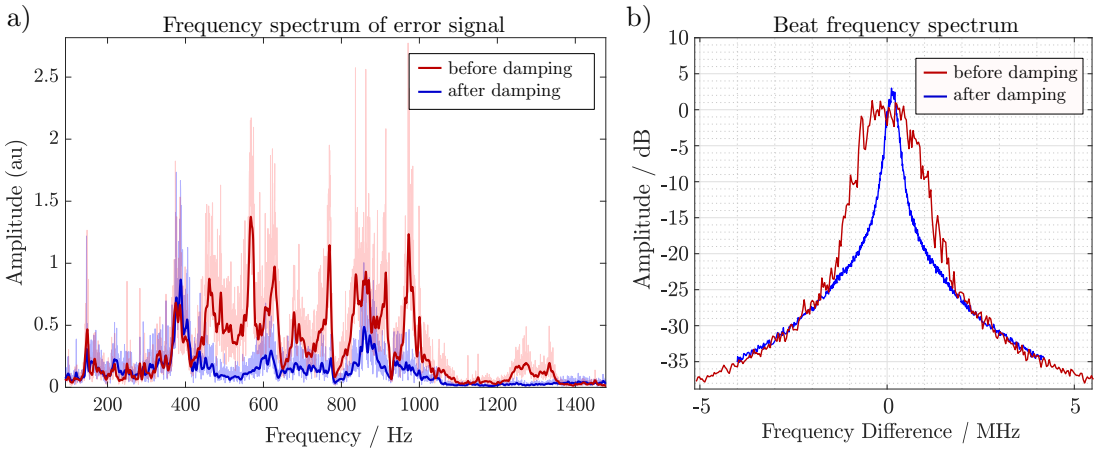

FIGURE 5.9: Effects of damping the vibrations of the cavity mirrors. a) Fourier transform of the frequency offset lock error signal before (red) and after (blue) damping the four cavity mirrors of the fundamental cavity. The pale colored signals in the background show the actual Fourier transform while the darker signals in the foreground show the same signal, but slightly smoothed with a low pass filter. As clearly visible, all frequencies above $400\,$Hz are drastically reduced by the damping measures. One can still see a prominent feature at $390\,$Hz, which we assign to either the water pump of the crystal chiller or to the eigenfrequency of the cavity base plate. By stopping the water for a very short time, the peak disappears. b) Beat spectrum of the frequency beat with the master laser. After the damping (blue) the lineshape resembles an almost pure Lorentzian lineshape. Before, the high amplitude region was broadened by mechanical noise following a Gaussian distribution.

subsequent improvements on the mechanical components in the fundamental laser cavity, I could reduce this value to less than $220\,$kHz[7].

[7]The value is determined by the beat frequency spectrum of the master laser and the solid-state laser. A typical spectrum of the laser line is shown in Figure 5.9 b). The FWHM linewidth of this signal is given by the convolution of the lineshapes of the individual lasers. For two (independent) lasers that have Lorentzian lineshapes with linewidths $\Delta\nu_1$ and $\Delta\nu_2$, the linewidth of the beat signal is given by $\Delta\nu_{\mathrm{res}} = \Delta\nu_1 + \Delta\nu_2$. For Gaussian lineshapes, the squares add up, such that $\Delta\nu_{\mathrm{res}} = \sqrt{(\Delta\nu_1)^2 + (\Delta\nu_2)^2}$. In both cases, the linewidth of the beat signal sets an upper limit for the individual linewidths.

The frequency of the laser is given by the length of the fundamental cavity. Mechanical vibrations of the optical elements therefore lead to a broadening of the laser linewidth. These components typically oscillate with their mechanical eigenfrequencies/their resonance frequencies.
For identifying these frequencies, I used a acoustical sound generator to create sound waves while simultaneously observing the beat signal and the error signal of the frequency offset lock. A Fourier transform of this error signal is shown in Figure 5.9 a) and already hints at the resonance frequencies of the optical components (red signal traces). When generating sound waves with precisely the frequencies corresponding to peaks of the shown signal, a sudden increase of the laser linewidth and the amplitude of the error signal could be observed. This procedure helped to find the resonance frequencies.
To assign them to individual components, I subsequently started to add metal weights on the mirror holders of the cavity. These weights caused both a damping and a shift of the resonance frequencies. After a comprehensive analysis, we found that the vibrationally induced linewidth broadening was primarily caused by the four mirror holders. These are mirror holders from the company Radiant Dyes (MDI-HS-2-3021, MDI-HS-2-3025). By either adding a large weight to the mirror holder plates to increase their mass or damping the mirror holder plates with additional mirror holders (see Figure 5.10), the laser linewidth could be reduced by almost a factor of seven. Since we did not want to completely rebuild and realign the entire laser system from the start[8] simply for the purpose of testing other mirror holders, the approach described above was an elegant solution and proved to be quite effective.

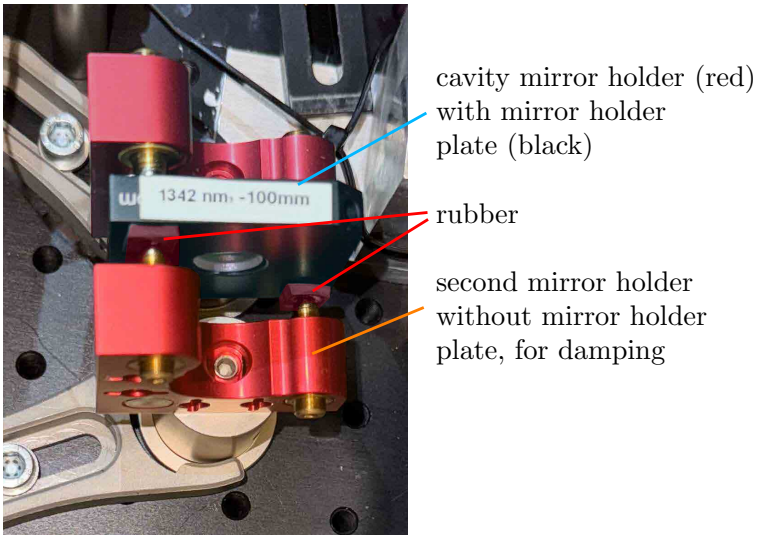

FIGURE 5.10: Modified cavity mirror holder with damped mirror holder plate. Damping is achieved by utilizing a second mirror holder with a removed mirror holder plate to exert pressure against the cavity mirror holder plate from the front. To allow for fine adjustments later, hard rubber plates are inserted between the components.

[8]Rebuilding and aligning the laser cavity is quite time-consuming as explained in the master's thesis of Stephan Maier [65].

Figure 5.9 shows this improvement. In the Fourier transform of the error signal depicted in a), one can see that almost all resonance frequencies were drastically damped in amplitude. In b) one can see the beat spectrum before (red) and after (blue) the damping. The signal before the damping represents a typical spectrum of a laser with an intrinsic Lorentzian lineshape in the low amplitude tails of the spectrum, which is broadened by a perturbation with Gaussian noise (e.g. mechanical vibrations).

After the damping procedure, we can infer from the spectrum that the laser

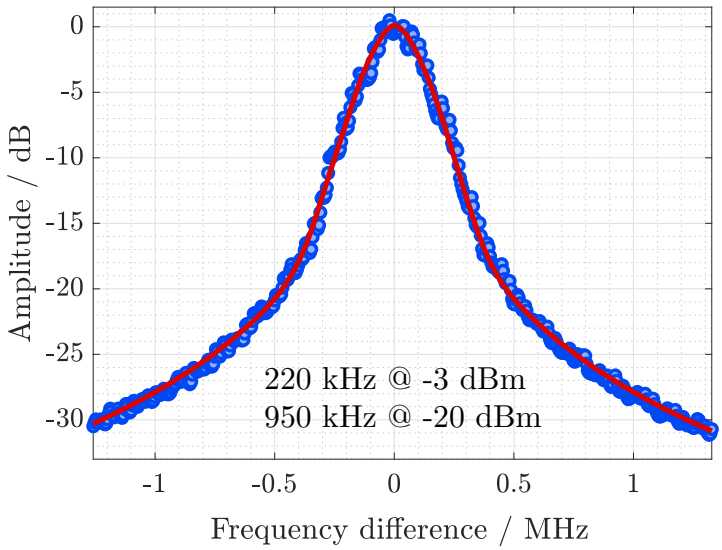

FIGURE 5.11: More detailed analysis of the beat signal spectrum after damping the vibrations. It shows a FWHM (measured at -3 dB) of 220 kHz. Extracting the linewidth from the signal's width at -20 dB yields a value of 95 kHz. For more information, see text.

is almost as narrow as it could be. For a pure Lorentzian lineshape, namely, the width at -3 dB corresponds to the FWHM linewidth. The width extracted at -20 dB ideally should correspond to ten times the FWHM linewidth. By extracting these widths from the beat signal, we find the results shown in Figure 5.11. While the width at -3 dB is 220 kHz, we find a width of 950 kHz at -20 dB. This tells us to things: First, the lineshape is still slightly broadened by some noise. Second, the intrinsic Lorentzian linewidth of the laser, is even smaller than 100 kHz FWHM. Moreover note, that this value is still an upper limit, as is represents the sum of the master laser linewidth and the solid-state laser linewidth.

5.4 Stability and every-day operation

As stated at the beginning, this laser system now sets the basis for all our experiments by providing a stable optical power for laser cooling. This requires an easy maintenance and a good overall stability.

Thermal stability

Although the system consists of two rather large cavities with geometric lengths of $90\,\text{cm}$ for the fundamental and $50\,\text{cm}$ for the SHG resonator, it is thermally quite stable and typically stays locked for more than one full day. From the piezo actuator voltages for maintaining the lock, we estimate length drifts of less than $0.5\,\mu\text{m}$ throughout the day for both cavities.

Mode-hop free tuning range

Without adjusting the etalons, the frequency of the laser can be tuned mode-hop free by about $640\,\text{MHz}$. This limitation is given by the length of the fundamental laser, which has an free spectral range of $\frac{c}{L} = 319\,\text{MHz}$[9]. Therefore, the frequency doubled light is mode-hop free tunable by twice this value. For laser cooling, this range is more than enough. To further increase it for other possible applications, one could add another piezo actuator to tilt the etalon E_2 while scanning the frequency with the piezo actuated mirror.

Output power

As our laboratory does not provide cleanroom conditions, there will be always some dust in the air. This is attracted by the circulating laser power in both cavities and subsequently burned into the optical elements, leading to a decreasing efficiency for both the fundamental and the enhancement cavity. As a consequence, the second harmonic power gradually decreases by $\approx 1\%$ per week. However, as we only use around $1/4$ of the available fundamental power for conversion, we have a large margin and could basically compensate for this decrease in power for more than a year.

Optical cleaning

We still clean the four SHG cavity mirrors and the SHG crystal facets on a two-monthly basis with a mixture of methanol and acetone. This takes approximately 10 minutes and prevents a long-term degradation of the coatings.
The fundamental laser requires a greater maintenance approximately once a year due to mechanical drifts and dust accumulation on the optical elements. As some of these elements (e.g. etalon E_2 and the TGG crystal) are not directly accessible for optical cleaning, they have to be removed, cleaned and reinserted into the cavity. This makes a small realignment of the laser cavity necessary. The whole process takes roughly one hour and is detailed in Appendix A.3. After every cleaning and realigning process, we typically achieve the same output power and observe no degradation in performance.

[9] Note that one has to use c/L rather than $c/(2L)$, because the resonator is a running wave resonator.

Chapter 6

Precise photoexcitation measurement of Tan's contact

The contents of this chapter have been published in Ref. [13]:

Manuel Jäger and Johannes Hecker Denschlag
"Precise Photoexcitation Measurement of Tan's Contact in the Entire BCS-BEC Crossover",
Physical Review Letters **132**, 263401 (2024).

6.1 Abstract

We study two-body correlations in a spin-balanced ultracold harmonically trapped Fermi gas of ^{6}Li atoms in the crossover from the Bardeen-Cooper-Schrieffer (BCS) to the Bose-Einstein-Condensate (BEC) regime. For this, we precisely measure Tan's contact using a novel method based on photoexcitation of atomic pairs, which was recently proposed by Wang *et al.* [31]. We map out the contact in the entire phase diagram of the BCS-BEC crossover for various temperatures and interaction strengths, probing regions in phase-space that have not been investigated yet. Our measurements reach an uncertainty of $\approx 2\%$ at the lowest temperatures and thus represent a precise quantitative benchmark. By comparison to our data, we localize the regions in phase space where theoretical predictions and interpolations give valid results. In regions where the contact is already well known we find excellent agreement with our measurements. Thus, our results demonstrate that photoinduced loss is a precise probe to measure quantum correlations in a strongly interacting Fermi gas.

6.2 Introduction

A Fermi gas of ultracold atoms with tunable interactions is an excellent platform for studying pair correlations and superfluidity. The interactions can be controlled, e.g., via a magnetically tunable Feshbach resonance where the scattering state of two atoms is coupled to a weakly-bound molecular state of a closed channel at close range. This allows for investigating the crossover from the BCS to the BEC regime, where the system fundamentally changes its physical character. In the weakly interacting BCS regime, weakly-bound Cooper pairs

form on the surface of the atomic Fermi sea with its strong interparticle correlations, while in the BEC regime fermionic atoms combine to form tightly-bound bosonic molecules with small correlations between them. Tan's contact, first introduced by Shina Tan in 2008 [10–12], is a measure for short-range two-body correlations and quantifies the likelihood of finding two interacting fermions at very small distance. From a thermodynamical point of view the total contact $\mathcal{I}$ is an extensive quantity, linearly scaling with the system size. It appears in a number of important thermodynamic relations for a strongly interacting Fermi gas.

The contact and several of its thermodynamic relations have been investigated experimentally in various approaches, including radio-frequency (RF) spectroscopy [100, 107, 108], mapping of the momentum distribution [100, 106], Bragg spectroscopy [109] and collisional decay [110, 162]. In recent years, contact measurements reached uncertainties as low as two percent [106, 108, 109]. So far, however, contact investigations were only carried out in particular areas of phase space, i.e. close to unitarity and at the lowest temperatures. A precise and comprehensive study across the entire phase diagram of the BCS-BEC crossover, providing a full picture of the contact, has been missing. Tan's contact is expected to change smoothly from the BCS to the BEC limit, but precise calculations of the contact are still challenging especially in the regime of strong, near resonant interactions between the particles. Therefore, precise measurements in this area will result in an important step forward towards a complete understanding of the crossover physics.

Here, we provide a high precision measurement of Tan's contact across the full phase diagram of the BCS-BEC crossover for temperatures up to two times the Fermi temperature T_F. Due to a careful calibration the data reach a combined statistical and systematic uncertainty of $\approx 2\%$ for the lowest temperatures ($T \approx 0$), and up to 10% for $T/T_F \approx 1.5$. Therefore, they represent a quantitative benchmark to test theoretical model predictions. For the contact measurements, we demonstrate yet another method which is based on laser-induced loss in the atomic gas, as outlined in [31]. Atom pairs at close range are photoexcited to a short-lived excited molecular bound state, producing an atom loss rate which is proportional to Tan's contact. In our specific system, photoexcitation occurs via a coherent admixture of a closed-channel molecular bound state to the pair-wavefunction. This closed-channel bound state is also responsible for the Feshbach resonance. Measurements of the closed-channel fraction have been previously measured in the group of R. Hulet [142] and in the group of J.W. Pan [163] and they are closely related to the method reported here. The measured closed-channel fraction in [163] indicated a deviation by a factor of three from the well-understood theoretical predictions on the BCS side. This deviation does not occur in our measurements.

6.3 Results

6.3.1 Photoinduced two-body loss

As pointed out in [32, 33] there is a very general and fundamental link between the total contact $\mathcal{I}$ and the two-body loss rate of a two-component Fermi gas

$$-\frac{\mathrm{d}N}{\mathrm{d}t} = \frac{-\hbar \mathrm{Im}[a]}{2\pi m|a|^2}\mathcal{I}, \tag{6.1}$$

where N is the total atom number, m is the atomic mass and a is the scattering length. If a has a finite imaginary part, loss due to a two-body process is present. Thus, the total contact of the spin-balanced Fermi gas can be simply deduced from the induced two-body loss rate. This is quite intuitive as two-body loss goes naturally along with two atoms being at close range. Equation (6.1) holds for collisional losses in s-wave collisions. For losses in p-wave collisions, a similar relation was recently found [18, 162].

We now consider the special situation where an atomic s-wave collision takes place in the vicinity of a single, magnetically tunable, intrinsically lossless Feshbach resonance. Furthermore, two-body loss is induced via resonant photoexcitation of an atom pair at close range to an electronically-excited, short-lived molecular state with a lifetime $1/\gamma$. For photoexcitation, the bare, closed-channel bound state of the Feshbach resonance is coupled to the excited molecular state with Rabi frequency Ω. For this system, reference [31] has calculated the complex scattering length a and Eq. (6.1) becomes

$$-\frac{\mathrm{d}N}{\mathrm{d}t} = \frac{\hbar\mathcal{I}}{2\pi m a_{bg}} \frac{\Omega^2/(2\gamma W)}{\left[1-a_{bg}/a_s\right]^{-2} + \left[\Omega^2/(2\gamma\, W)\right]^2}. \tag{6.2}$$

Here, a_s denotes the real-valued scattering length without the photoexcitation coupling, a_{bg} is the corresponding background scattering length and W the width of the Feshbach resonance. For all practical purposes, the term $\left[\Omega^2/(2\gamma\, W)\right]^2$ in the denominator can be neglected in our experiments.

6.3.2 Experiment

For our measurements we use an ultracold Fermi gas of ^{6}Li atoms in the two lowest hyperfine states $|F=1/2, m_F=1/2\rangle$ and $|F=1/2, m_F=-1/2\rangle$ with $N/2$ atoms per spin state. The atoms are trapped in a 3D harmonic trap which consists of a combination of an optical dipole trap and a magnetic trap. The atom cloud is cigar shaped, corresponding to the trapping frequencies $\omega_{ax} = 2\pi \times 21$ Hz in axial and $\omega_r = 2\pi \times 150 - 2000$ Hz in radial direction, respectively. Using forced evaporative cooling at a magnetic field of around 790 G we set a precise atomic temperature in the range of $0.04 - 2\ T_F$ for clouds with atom numbers between 5×10^5 and 2×10^6. For a harmonically trapped gas, the Fermi temperature is given by $T_F = E_F/k_B = \hbar\left(\omega_{ax}\omega_r^2 3N\right)^{1/3}/k_B$, where E_F is the Fermi energy and k_B is the Boltzmann constant. By tuning the magnetic field B, we control the particle interaction with the help of the broad s-wave Feshbach

resonance at $832.18(8)$ G [78], which allows for entering both the BCS ($a_s < 0$) and BEC regimes ($a_s > 0$) of the crossover. For this resonance the width is $W = -2\mu_B \times 262.3(3)\,\mathrm{G} = -2\pi\hbar \times 734(1)$ MHz, and $a_{bg} = -1582(1)\,a_0$ [78] where a_0 is the Bohr radius.

To optically induce two-body loss, we excite atom pairs, bound or unbound, to a deeply-bound molecular level with vibrational quantum number $v' = 68$ in the electronically excited state $A^1\Sigma_u^+$ with a linewidth of $\gamma = 2\pi \times 12(1)$ MHz, as measured in our experiment[1]. For this, we make use of the fact that the initial atom pair wavefunction has an admixture from the (bare) molecular state $X^1\Sigma_g^+(v = 38)$, from which the state $A^1\Sigma_u^+(v' = 68)$ can be reached via an electric dipole transition [142]. The photoexcitation scheme is shown in Figure 5 of [14]. To drive the transition we employ a 673 nm laser beam with an intensity of a few μW/cm^2 (where $\Omega \lesssim 2\pi \times 1$ MHz). At each magnetic field, the laser is tuned to be resonant on the photoexcitation transition. The photoexcitation leads to a decay of the total atom number N within a few hundred milliseconds. This slow decay ensures that the system stays in thermal equilibrium during the exposure. This is in contrast to previous experiments of ours where we used fast loss to measure the pair fraction in the Fermi gas, see [15].

We use high-field absorption imaging to measure the number of the remaining atoms, bound or unbound, as described in [15, 82]. Pairs that had been previously photoexcited to the molecular bound state are not detected because they quickly decay to states that do not respond to our absorption imaging scheme.

In Fig. 6.1 we show on a logarithmic scale the remaining atoms as a function of time. The three data sets are recorded at 753 G, 832 G and 1078 G with initial interaction parameters $(k_F a_s)^{-1} = 1.5,\ 0$ and -1.65, corresponding to the BEC, unitarity and BCS regimes, respectively. Here $k_F = (2mE_F/\hbar^2)^{1/2}$ is the Fermi momentum[2]. For better comparison, the data were normalized to the initial atomic numbers $N(t = 0)$. The laser power was adjusted so that the initial relative loss rates are the same. Further details of the measurement parameters can be found in the Supplemental Material of [13]. While on the BEC side at $(k_F a_s)^{-1} = 1.5$ the loss is well described by an exponential, it is clearly non-exponential on resonance and in the BCS regime. This behavior was predicted theoretically [143] and also studied recently in [163]. The exponential decay is typical for a pure, weakly-interacting, molecular ensemble which is present in the BEC limit at zero temperature. At unitarity and on the BCS side the non-exponential decays reflect the internal changes of the degenerate Fermi gas for different densities. These decays and changes go hand-in-hand with a drop of the chemical potential of the gas, see also Supplemental Material of [13].

Using Eq. (6.2) and the respective density-dependence of the contact in the BCS, unitarity and BEC limit one can show [14, 143] that the decays at zero

[1]The measured value of $\gamma = 2\pi \times 12(1)$ MHz is in agreement with earlier measurements [164] and theoretical calculations [165] predicting a molecular linewidth of nearly twice the atomic linewidth of the $2P$ state [77].

[2]Here, we ignore the slight anharmonicity of our trap, for details see [14]. This leads to a small relative shift of k_F on the level of less than 1%.

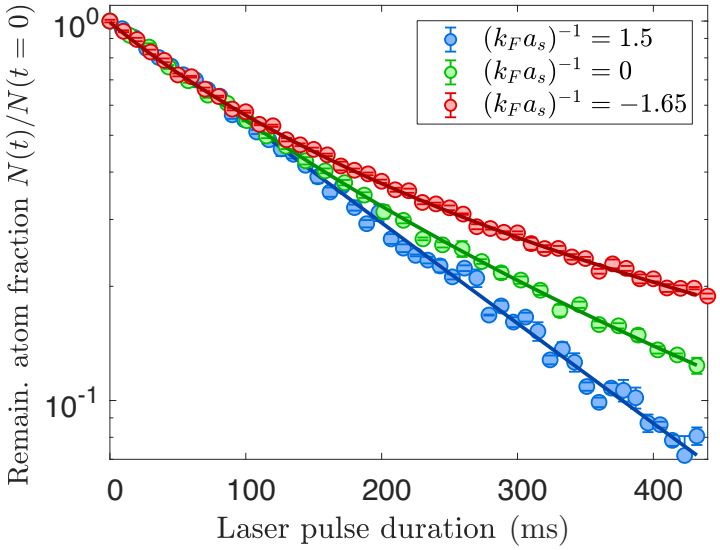

FIGURE 6.1: Remaining atom fraction as a function of the photoexcitation laser pulse duration. The measurements were carried out at magnetic fields of 753 G, 832 G and 1078 G with the initial $(k_F a_s)^{-1} = 1.5,\ 0,\ -1.65$ corresponding to the BEC, unitarity and BCS regimes of the crossover. The initial temperatures were $T/T_F = 0.07,\ 0.05$ and 0.04, respectively. The continuous red and green lines are fits according to Eq. (6.3), while the blue line is an exponential (i.e. $b = \infty$).

temperature can be described by

$$N(t) = N_0/(1 + \Gamma_0 t/b)^b \tag{6.3}$$

with the initial decay rate Γ_0 and $b = 2$ in the BCS limit, $b = 6$ at unitarity and $b \to \infty$ in the BEC limit. Our fits to the data in Fig. 6.1 yield $b = 1.6 \pm 0.2$ at $(k_F a_s)^{-1} = -1.65$ and $b = 3.9 \pm 0.9$ at $(k_F a_s)^{-1} = 0$. For the decay curve at $(k_F a_s)^{-1} = 1.5$ we find that a pure exponential (or any $b \gtrsim 20$) fits well. Despite the quantitative deviations, this shows that we already have a qualitative understanding of the decay. The deviations might be explained by a slight increase of the atom gas temperature for long photoexcitation laser pulse durations (for further discussion see [14]). We note, however, that it is the initial loss rate Γ_0, rather than b, which is relevant for the determination of the contact $\mathcal{I}$ in our experiments. The decay rate at $t = 0$, according to Eq. (6.3), is simply $\dot{N} = -N_0\Gamma_0$. At $t = 0$, the atom number is the highest and therefore uncertainties are the smallest. This has advantages compared to other methods that rely on measuring the tails of RF-spectra or momentum distributions, where atomic signals are generally low. In order to get precise results we accurately determine the atom numbers, the (effective) trapping frequencies, the magnetic fields and the corresponding scattering lengths, as explained in [14] where also effects due to slight trap anharmonicities are discussed. In the following we investigate the contact in the entire BCS-BEC crossover, first for $T \approx 0$ and afterwards also for T up to 2 T_F.

6.3.3 Contact in the zero temperature limit

For $T \approx 0$ there exist already some experimental data and calculations of the contact from other groups which we can use for comparison with our results. In our measurements we typically achieve temperatures of $T < 0.04\,T_F \lesssim T_C$ where T_C is the critical temperature for superfluidity. According to Eq. (6.2) we need to measure $\mathrm{d}N/\mathrm{d}t$ and Ω in order to determine the contact $\mathcal{I}$. We extract the initial decay rate $\mathrm{d}N/\mathrm{d}t$ from decay curves which are similar to those shown in Fig. 6.1. Ω is given by $\Omega^2 = k\,I$, where I is the photoexcitation laser intensity and k is a constant which is independent of the magnetic field B and therefore of a_s. We can conveniently determine k by measuring $\mathrm{d}N/\mathrm{d}t$ for a given I at an interaction regime where the contact $\mathcal{I}$ is known. (We note that when using this k, the constants γ, W and m effectively drop out of Eq. (6.2), see [14].) Concretely, we chose $(k_F a_s)^{-1} \gtrsim 1$ where the contact approaches the analytical result $\mathcal{I}/Nk_F = 4\pi/k_F a_s$ [143]. With this calibration we can then determine $\mathcal{I}$ from measurements of $\mathrm{d}N/\mathrm{d}t$ at any $(k_F a_s)^{-1}$ throughout the crossover.

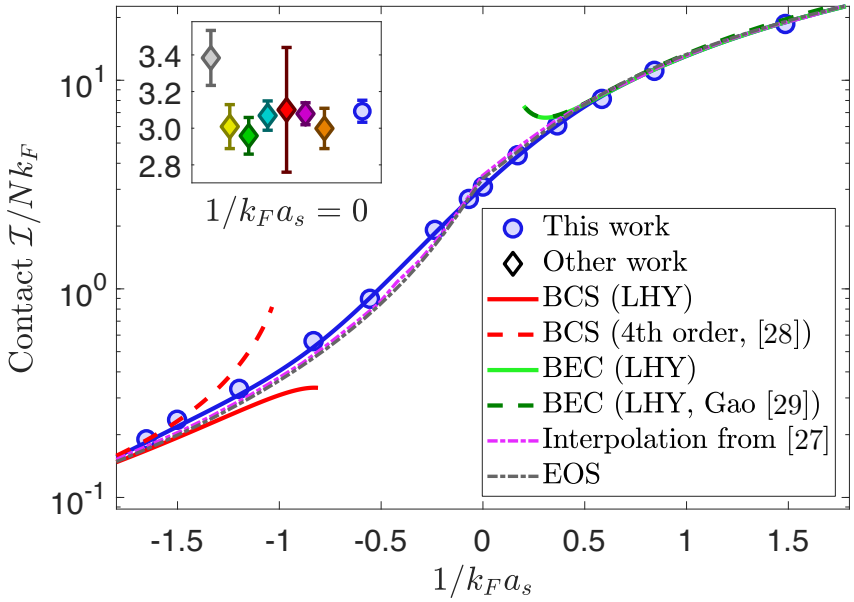

FIGURE 6.2: Normalized contact $\mathcal{I}/Nk_F$ of a harmonically trapped Fermi gas in the crossover from the BCS to the BEC regime at $T \approx 0$. Our data (blue circles) are shown together with a guide to the eye (blue line). Uncertainties are smaller or comparable to the size of the markers. Also shown are trap-integrated calculations of the contact based on different approaches (see text) as well as an interpolation [143] (purple). The inset shows our data point (blue circle) at unitarity and data from other groups (diamonds), namely the EOS measurement [166] (grey), Bragg spectroscopy measurements by [167] (yellow) and [109] (cyan), a Quantum Monte Carlo calculation [168] (green), an inelastic decay measurement [110] (red), and RF spectroscopy measurements [108] (purple) and a momentum distribution measurement [106] (orange).

Our results are shown in Fig. 6.2 along with theoretical calculations based on ground state energy expansions in the BCS and BEC regimes (see [14, 143]). The

statistical uncertainties of our data for $\mathcal{I}/Nk_F$ are below 2% and the systematic errors due to anharmonic effects are below 0.3%. The solid red and dashed red lines are based on expansions up to second order (fermionic Lee-Huang-Yang correction) and up to the fourth order [169], respectively. The results apparently converge for $(k_F a_s)^{-1} < -1.5$. The solid green and dashed dark green lines are based on the expansions to second order (bosonic Lee-Huang-Yang correction) in the BEC regime. While for the green solid line the binding energy of a dimer is calculated via $E_B = -\hbar^2/ma_s^2$, a more accurate binding energy formula is employed for the dashed dark green line [96]. This leads to a 0.6% (1.3%) larger total contact at $(k_F a_s)^{-1} = 1\,(2)$.

In the inset we show a comparison to other measurements and calculations at unitarity where we also find excellent agreement. In order to compare results for homogeneous systems at unitarity with values for the contact for harmonically trapped ensembles, we divided the homogeneous results by the factor $(C/nk_F^{\mathrm{hom}})/(\mathcal{I}/Nk_F) = (105\pi/256)\xi^{1/4} = 1.003$ [143], using $\xi = 0.367$ for the Bertsch Parameter [92, 93]. Here, C is the homogeneous contact density, n is the atom density and k_F^{hom} is the homogeneous Fermi momentum (see also [14]). We further compare our data to calculations based on the equation of state (EOS) measurements [166] (see [14]) and an interpolation from [143]. Here, we find small deviations in the region $-1 < (k_F a_s)^{-1} < -0.2$ where we obtain slightly higher values for the contact.

The contact is closely related to the closed-channel fraction in the scattering state of two particles. In [14] we discuss this relation and compare various experimental and theoretical studies of the closed-channel fraction. The results partially differ substantially from each other.

6.3.4 Finite temperature contact

We now perform measurements at various temperatures and couplings to map out the contact in the entire phase diagram of the BCS-BEC crossover. For this, we vary the temperature of our atom cloud between 0.04 and 2 T_F by changing the depth of our dipole potential for forced evaporative cooling. As a result we end up with around 5×10^4 (2×10^6) atoms at our coldest (hottest) temperatures. To tune the interaction we set the magnetic field to values between 703 G and 1080 G leading to couplings in the range $-1.5 < (k_F a_s)^{-1} < 2.5$.

Our measurement results are shown as colored circles in Fig. 6.3a). Since the contact changes by three orders of magnitude within the investigated range of temperatures and couplings we plot the results logarithmically. By interpolating the data, we obtain a continuous map of the contact. Close inspection shows that this map consists of slanted, parallel stripes of color. This indicates that the description of the map might be simplified within the given range. Indeed, as shown in the Supplemental Material of [13], to a first approximation one can effectively replace the 2D map by a 1D function. Although this observation is interesting, at this point we cannot offer a simple physical explanation for this. To compare our measurements to theoretical predictions we calculated the contact within the quantum virial expansion [170] as done in [70] at unitarity. These calculations are shown in Fig. 6.3b) and described in detail in [14]. As the

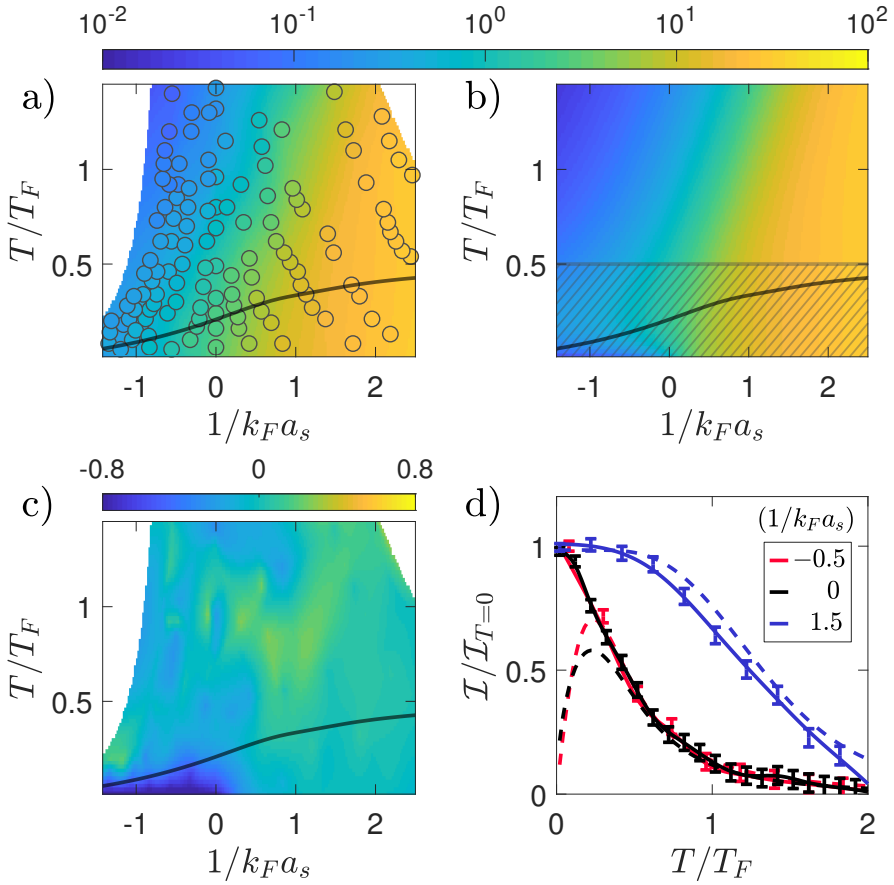

FIGURE 6.3: Map of the contact in the BCS-BEC crossover. a) Colored circles are measurements for the contact $\mathcal{I}/Nk_F$, where the values are indicated by the color bar. The typical statistical uncertainties are $\approx 2\%$ $(4\%, 6\%, 9\%)$ for $T/T_F = 0$ $(0.5, 1, 1.5)$ and the systematic deviations due to the trap anharmonicity are smaller than 0.3% $(1.3\%, 3.0\%, 3.2\%)$ for the same temperatures, see also[3]. The colored background area is an inter- and extrapolation of the measured data. The continuous black line marks the critical temperature for superfluidity T_C, taken from [82]. b) The contact $\mathcal{I}_{QV,2}/Nk_F$ calculated from the second-order quantum virial expansion. The shaded area below $T = 0.5\,T_F$ marks the region where the virial expansion is expected to lose its validity. c) Relative difference $(\mathcal{I}_{QV,2} - \mathcal{I})/\mathcal{I}$ of our measurements and the second order quantum virial calculation. d) Contact $\mathcal{I}$ normalized by the corresponding measured zero-temperature contact as a function of temperature for three different couplings $(k_F a_s)^{-1}$. The data points are interpolations from the measured data in a). The continuous lines are guides to the eye. The dashed lines are quantum virial calculations taken from b).

quantum virial expansion is a series expansion in the fugacity $z = \exp(\mu/k_B T)$, it is valid at high temperatures and low chemical potentials μ. A table of chemical potentials throughout the phase-space is provided in the Supplemental Material of [13]. The calculations show that for a harmonically trapped system the virial expansion should give valid results for the contact for temperatures as low as

$T = 0.5\,T_F$, since in this regime the fugacity is small. Below this temperature the contact values calculated with the second and third order expansion start to deviate from each other, as already discussed in [70].

Fig. 6.3c) is the relative difference between experimental data and the second order virial calculation. It shows that our measurements are in good agreement with the calculations in the given range of validity at temperatures above $0.5\,T_F$ throughout the entire crossover. On the BEC side our results agree well even down to the lowest measured temperatures of $0.04\,T_F$. This can be expected since the major contribution to the contact arises from the binding energy of the dimers, which is included in the second order virial expansion. At unitarity and on the BCS side for low temperatures, the Fermi gas is a system with genuine many-body correlations. Since the second-order virial expansion effectively only considers interactions between two bodies, it fails to describe these regimes quantitatively. Furthermore, on the BCS side the effective chemical potential approaches the Fermi energy at low temperatures. Therefore, the fugacity is not small anymore, violating the validity of the virial expansion. Therefore, in the low-T regime stretching from unitarity towards the BCS limit our measurements are particularly important and can serve as a benchmark for theoretical models.

The different regimes in the BCS-BEC crossover also show up very clearly in Fig. 6.3d), where we plot the contact as a function of temperature for $(k_F a_s)^{-1} = -0.5,\ 0$ and 1.5. On the BEC side at $(k_F a_s)^{-1} = 1.5$ the dimers dominate the contribution to the contact. For low enough temperatures, when all atoms are bound in dimers, the contact is a constant (as a function of temperature). When $T \times k_B$ becomes comparable to the binding energy, the dimers become thermally unstable, break up and the contact starts decreasing (see Fig. 6.3d) blue curves). On the BCS side and at unitarity where $(k_F a_s)^{-1} \leq 0$, no weakly-bound Feshbach molecular state exists. There, the decrease of the contact with increasing temperature is mainly due to overall decreasing atom density and to a breakdown of short-range pair correlations. Here, at low temperatures, our measurements for the contact strongly deviate from the results of the second-order quantum virial expansion (see Fig. 6.3d) red and black curves).

6.4 Summary and conclusion

In conclusion, we have precisely measured Tan's contact in the full phase diagram of the BCS-BEC crossover using photoexcitation of fermion pairs. Our results bridge the gap between the well-understood BCS and BEC regimes and are in line with recent measurements and calculations at unitarity. They extend previous measurements of Tan's contact to the finite temperature regime and are consistent with the quantum virial expansion for temperatures above $0.5\,T_F$.

For the future, we plan to extend our contact measurements to homogeneous Fermi gases. It has been predicted (and measured at unitarity [108]) [31, 171] that a sudden change in Tan's contact should appear at the critical temperature T_C

[3]The statistical uncertainties decrease with decreasing temperature T, since in our experiments evaporative cooling leads to more stable atom numbers at lower temperatures. The increase of the systematic uncertainty with T is explained in [14].

of superfluidity. Therefore, one could use such measurements to precisely map out T_C within the BCS-BEC crossover. In the harmonically trapped system this sudden change is washed out due to the inhomogeneous density distribution in the trap. In addition, we also aim for studying the contact for systems of lower dimensionality or that feature spin imbalance. Here, probing pair correlations by measuring the contact might uncover the presence of the Fulde-Ferrell-Larkin-Ovchinnikov (FFLO) phase [133].

6.5 Supplemental Material

6.5.1 Experimental parameters to the measurements

In Table 6.1 we list the experimental parameters for the three curves shown in Figure 6.1.

TABLE 6.1: Experimental parameters for the measurement data shown in Figure 6.1 The values for atom numbers, couplings and temperatures are the initial values at $t = 0$.

Magnetic field	Atom number	Coupling $(k_F a_s)^{-1}$	Temperature	Photoexc. laser power
753 G	5.9×10^5	1.5	0.07 T_F	6 µW
832 G	6.05×10^5	0	0.05 T_F	38 µW
1078 G	4.8×10^5	-1.65	0.04 T_F	610 µW

6.5.2 Quasi 1D Projection

We make an interesting observation when plotting our measurements from Fig. 6.3 in a three-dimensional coordinate system, as shown in Fig. 6.4 a).

By rotating the graph by the azimuthal and polar angles, we can align the data points so that, at a particular line of sight, they approximately fall onto a single universal 1D curve, as shown in Fig 6.4 b). We parameterize the line of sight by two angles (ϕ, θ). The azimuthal angle ϕ is the angle between the line of sight and the negative y-axis (temperature) and the angle of elevation θ is the angle between the line of sight and the x-y (coupling-temperature) plane. We find that for angles of $\phi = -24°$ and $\theta = -8°$ the convergence of data onto a single line is best. This behavior, however, only works in a limited realm of $T/T_F \lesssim 2$ and $-1 \lesssim 1/k_F a_s \lesssim 2$. Second order quantum virial calculations at high temperatures and calculations using the ground state energy expansions of the BCS and BEC limits [14] show this.

6.5.3 Chemical potentials

In Figure 6.3, we show the measured contact in the BCS-BEC crossover as a function of temperature T/T_F and coupling $(k_F a_s)^{-1}$. For the investigated range of temperatures and couplings, we list the approximate normalized chemical potentials μ_0/E_F in the trap center in table 6.2. We calculate μ_0 by using the EOS

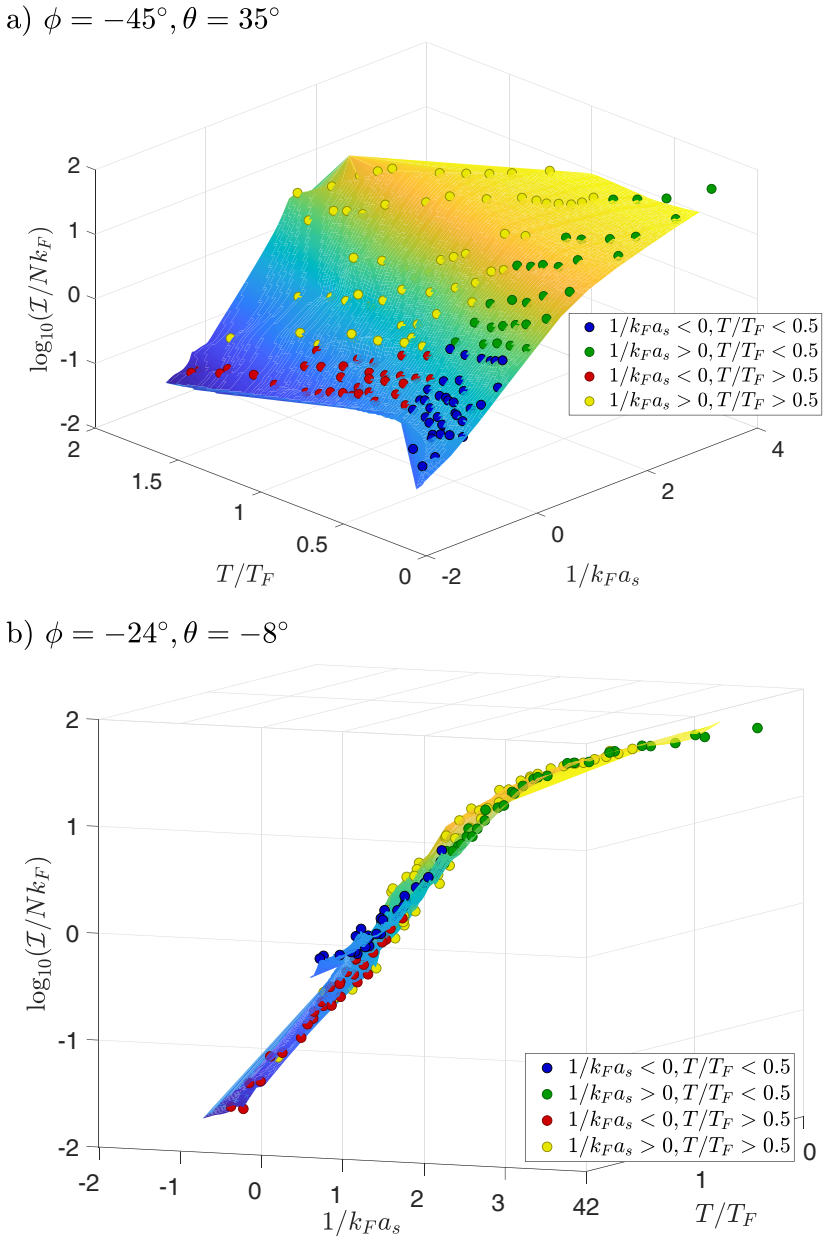

FIGURE 6.4: a) Measured contact values (dots) in a 3-dimensional representation. The colored plane is a linear interpolation of the data as shown in Figure 6.3 a). By changing the viewer's line of sight onto the dataset, the data approximately collapse onto a single curve, see b). The angles ϕ and θ specify the line of sight (see text). In order to better distinguish the measured data points belonging to the BEC and BCS regimes and to low and high temperatures, we used different colors for the plot symbols (see legend).

measurements at $T = 0$ [166] and the 2nd order virial expansion for $T \geq T_F$ [170]. The chemical potentials on the BEC side ($a_s > 0$) include the molecular binding energy given by $\frac{\hbar^2}{ma_s^2}/E_F = 2/(k_Fa_s)^2$. In the experiment, the photoinduced two-body loss slowly changes the chemical potential μ_0 over time due to the decreasing atom number and slightly increasing temperature. Therefore, during

the decay, the atom cloud generally follows a trajectory in the phase diagram towards increasing $|(k_F a_s)^{-1}| \sim N^{-1/6}$ and temperature T/T_F.

TABLE 6.2: Calculated, normalized chemical potentials μ_0/E_F of a harmonically trapped Fermi gas as a function of temperature T/T_F and coupling $(k_F a_s)^{-1}$. The values at $T = 0$ are obtained from the EOS measurements [166], while the values for $T \geq T_F$ are deduced from the 2nd order virial expansion [170].

T/T_F \ $(k_F a_s)^{-1}$	-1	0	1	2
0	0.9	0.6	-0.6	-3.6
1	-1.8	-1.8	-2.3	-4.9
2	-7.7	-7.8	-7.8	-8.8

6.5.4 Interpolated Contact Values

In Figure 6.3, we show our measurements of the contact together with an interpolation. The numerical values of this interpolation are given in Table 6.3 for the parameter range $-0.8 \leq (k_F a_s)^{-1} \leq 1.6$ and $0 \leq T/T_F \leq 1.5$.

TABLE 6.3: Numerical values of the interpolated contact $\mathcal{I}/Nk_F$ shown in Figure 6.3 a).

T/T_F \ $(k_F a_s)^{-1}$	-0.8	-0.6	-0.4	-0.2	0	0.2	0.4	0.6	0.8	1.0	1.2	1.4	1.6
0	0.55	0.83	1.27	1.99	3.08	4.57	6.4	8.6	10.8	13.1	15.5	17.9	20.4
0.1	0.56	0.76	1.17	1.91	2.99	4.44	6.22	8.22	10.9	12.9	15.3	18.1	20.3
0.2	0.48	0.69	1	1.69	2.52	3.85	5.61	7.6	10.1	12.4	14.7	18.3	20.2
0.3	0.4	0.62	0.88	1.42	2.07	3.33	4.92	6.61	9.1	11.7	14.2	17.8	20
0.4	0.34	0.51	0.73	1.17	1.74	2.9	4.34	5.87	8.1	11	13.9	17.3	19.8
0.5	0.27	0.4	0.54	0.92	1.41	2.38	3.81	5.07	7.3	10.1	13.2	16.8	18.9
0.6	0.21	0.35	0.41	0.66	1.03	1.75	3.01	4.15	6.15	8.8	12	16.4	18.4
0.7	0.17	0.28	0.35	0.5	0.78	1.27	2.16	3.19	5.01	7.6	10.6	15.4	17.6
0.8	0.15	0.21	0.28	0.39	0.69	0.88	1.52	2.4	4	6.5	9.2	13.5	16.4
0.9	0.12	0.14	0.2	0.28	0.55	0.68	1.09	1.92	3.27	5.6	8.1	11.9	15
1.0	0.1	0.13	0.19	0.225	0.42	0.55	0.85	1.62	3.05	4.95	7.2	10.6	13.5
1.1	0.08	0.099	0.16	0.195	0.29	0.45	0.73	1.21	2.72	4.35	6.4	9.3	11.8
1.2	0.07	0.08	0.12	0.167	0.238	0.405	0.67	1.12	2.5	3.81	5.5	8.2	10.6
1.3	0.05	0.07	0.097	0.141	0.208	0.385	0.6	1.03	1.84	3.01	4.6	7.1	9.2
1.4	0.047	0.06	0.087	0.125	0.19	0.328	0.5	0.84	1.42	2.31	3.65	5.9	7.4
1.5	0.038	0.051	0.076	0.108	0.16	0.27	0.41	0.67	1.09	1.74	2.75	4.4	5.9

Chapter 7

Tan's contact in the BCS-BEC crossover: Methods and theory

The contents of this chapter have been published in Ref. [14]:

Manuel Jäger and Johannes Hecker Denschlag
"Methods for studying Tan's contact in the BCS-BEC crossover",
Physical Review A **109**, 063330 (2024).

7.1 Abstract

In a parallel publication [13] we demonstrate that photo-induced two-body loss can be used to measure Tan's contact with high precision in a two-component Fermi gas. Here, in the present companion paper, we provide relevant background information on this work and describe in detail the methodology for both the experiments and the data analysis. We first review various theoretical approaches for calculating the contact and identify areas in phase space of the spin-balanced Fermi gas where Tan's contact has not yet been determined. Next, we provide detailed information on our experimental methods, in particular explaining the measurement and calibration procedures to achieve a high precision results for the contact. Afterwards, we study the variation of the decay laws of two-body loss in a Fermi gas in the crossover from the Bardeen-Cooper-Schrieffer (BCS) to the Bose-Einstein-condensate (BEC) regime, verifying previous predictions. Finally, we determine the closed-channel fraction of the Fermi gas and compare it to previous measurements and theoretical calculations.

7.2 Introduction

Tan's contact, first introduced by Shina Tan in 2008 [10–12], is a measure for short-range two-body correlations and quantifies the likelihood of finding two interacting fermions at very small distance. It is an important quantity for describing strongly interacting Fermi gases [10–12, 32, 33]. Tan's contact has been investigated both experimentally and theoretically in various approaches [18, 70, 100, 106–110, 143, 162, 171]. One experimental approach to measure Tan's contact is by studying two-body loss in the gas, where the loss is laser-induced. This was theoretically discussed in [31, 143] and demonstrated by us

in recent work [13]. Using this method we have measured the contact across the entire phase diagram of the BCS-BEC crossover, thus providing a comprehensive picture of the pair correlations. We found that the method is quite convenient and allows for high precision measurements.

Within the present companion paper, we provide additional background information on this work. In particular, we give a rough overview over previous work related to the contact in the BCS-BEC crossover, mapping out the so far charted and uncharted phase space regions of the BCS-BEC crossover with respect to the contact. Furthermore, we lay out the experimental methods which allow for contact measurements at high precision. In addition, we discuss previous work on the closed-channel fraction of a Fermi gas which is closely related to the contact. Finally, we provide details on our experimental investigation on the decay laws of the photo-induced loss of atoms. As predicted by [143] and experimentally shown by [163] we confirm that the power law of the decay varies across the BCS-BEC crossover.

7.3 Tan's contact in the BCS-BEC crossover

In the following we consider the phase space of the BCS-BEC crossover for a spin-balanced two-component Fermi gas with contact interactions which is trapped in a harmonic potential [8, 81, 172] . Such a Fermi gas has essentially only two degrees of freedom. 1) The coupling strength $(k_F a_s)^{-1}$, where k_F is the Fermi wave number and a_s is the s-wave scattering length. 2) The normalized temperature T/T_F where T_F is the Fermi temperature. Figure 7.1 shows the core of the BCS-BEC crossover phase space, in which the nature of the Fermi gas and its pair correlations fundamentally change. Below the critical temperature T_c (continuous line) superfluidity sets in. Here, one distinguishes three limiting regimes [8, 81]. For $(k_F a_s)^{-1} \approx 0$ we have resonant superfluidity. For $(k_F a_s)^{-1} \gg 1$ we have the regime of Bose-Einstein condensation (BEC) of molecules. And finally for $(k_F a_s)^{-1} \ll -1$ we have the regime of Bardeen-Cooper-Schrieffer superfluid of atom pairs. For $T \gg T_c$ the gas is in the normal state. For the BEC and BCS regimes at $T = 0$ there are analytical ground state energy expansions which can be used to describe properties of the gas for coupling strengths down to $|(k_F a_s)^{-1}| \approx 1$, see Fig. 7.1. For $T \gtrsim 0.5\, T_F$ the gas properties of the harmonically trapped Fermi gas can be described in the framework of the quantum virial expansion [170]. At unitarity (i.e. $(k_F a_s)^{-1} = 0$) the scattering length a_s drops out of the description and therefore simplifies the problem. A variety of numerical calculations (e.g. [111–113] have provided predictions for the gas properties and its contact for this regime. Furthermore, experimental investigations have measured the equation of state (EOS) at $T \sim 0$ [166] filling the theoretical gap for $|(k_F a_s)^{-1}| \lesssim 1$. In addition, measurements where carried out at unitarity), determining among other things the contact [88, 106–109].

Figure 7.1 shows that there are still large uncharted areas in phase space, especially for a strongly interacting gas close to unitarity at low temperature. Filling this area with precise data for the contact, was one of the main motivations for our work. In order to verify that our measurements of the contact (of a harmonically trapped Fermi gas) are consistent with previous measurements

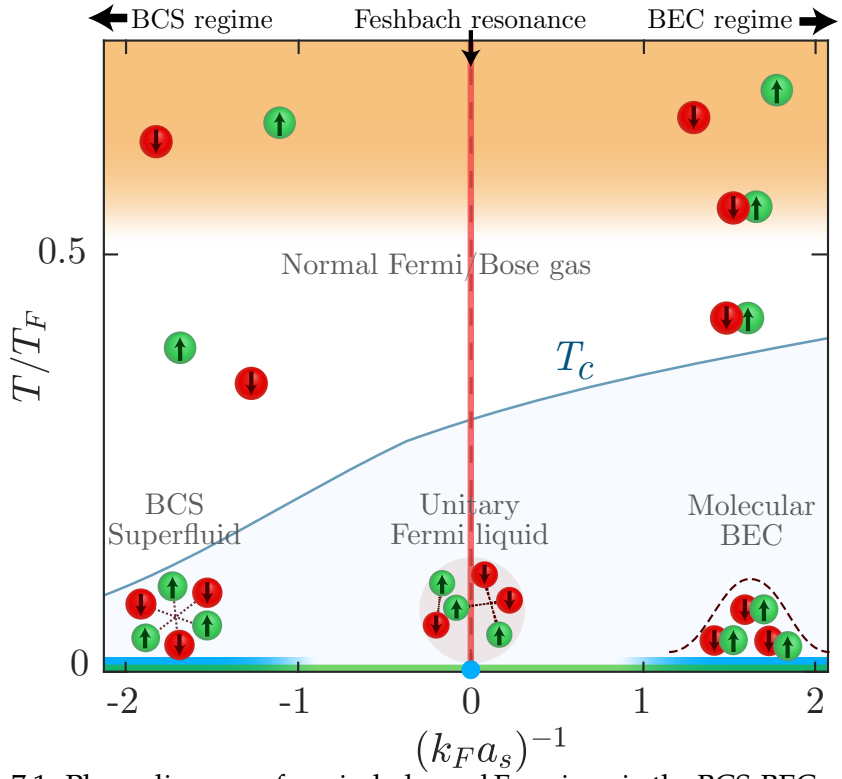

FIGURE 7.1: Phase diagram of a spin-balanced Fermi gas in the BCS-BEC crossover. The green and red circles represent fermions of the two spin components and illustrate the different phases present in the crossover (see text). The thin blue-grey line marks the critical temperature for superfluidity T_C for a harmonically trapped Fermi gas, taken from [82]. In selected regions, the contact has been studied intensely theoretically and experimentally. For example, at zero temperature in the regions where $(k_F a_s)^{-1} < 1$, $= 0$, and > 1 (thick blue lines and blue dot), the contact can be calculated from the BCS-, unitarity and BEC ground state energy expansions. In the orange marked area above $T/T_F \approx 0.5$, the quantum virial expansion is expected to start providing accurate results for a harmonically trapped Fermi gas [70]. For both the $T = 0$ (green broad line) and $(k_F a_s)^{-1} = 0$ (red broad line) regions, there are numerous theoretical and experimental studies for the contact (see text).

by other groups and established theoretical descriptions of the gas we carried out comparisons. For this, the contact had to be extracted from several of these works and partially recalculated for our situation of a harmonically trapped Fermi gas. In the following we explain in detail how this was achieved.

The general approach is that we start out with an expression for the total energy E of a homogeneous Fermi gas in a volume V. Here, E is the total energy of the system including kinetic energy and interaction energy. We then make use of the relation [11]

$$\frac{\mathrm{d}E}{\mathrm{d}(1/a_s)} = -\frac{\hbar^2}{4\pi m} CV. \tag{7.1}$$

that connects the homogeneous contact density C to the derivative of total systems energy E with respect to the s-wave scattering length a_s. This relation in general holds for a two-component Fermi gas at any temperature.

Next we use this C to calculate the total contact $\mathcal{I}$ of a harmonically trapped Fermi gas. In a harmonic trapping potential, the atom density is position dependent and thus the contact changes locally. In the spirit of the local density approximation (LDA), the total contact of the system $\mathcal{I}$ is then obtained by integrating $C(\vec{r})$ over the trap volume $\mathcal{I} = \int \mathrm{d}^3 r\ C(\vec{r})$. For this we follow the approach discussed in Appendix C of [143].

7.3.1 Ground state energy expansions

In this section, we closely follow the derivation of Tan's contact from the ground state energy expansions as laid out in [143]. Only for the binding energy of molecule, we use a slightly improved expression.

At zero temperature T the total energy E is known analytically at various regions of the BCS-BEC crossover. For a homogeneous Fermi gas in the BCS limit the energy per volume V at zero temperature is given by the expansion

$$E/V = \frac{3}{5}\frac{\hbar^2 (k_F^{\mathrm{hom}})^2}{2m} n \left(1 + \frac{10}{9\pi} k_F^{\mathrm{hom}} a_s + 0.1855 (k_F^{\mathrm{hom}} a_s)^2 + \dots\right), \tag{7.2}$$

where n is the atom density and $k_F^{\mathrm{hom}} = (3\pi^2 n)^{1/3}$ is the Fermi momentum of the homogeneous gas [143, 169, 173]. The first three terms are the energy of the non-interacting Fermi gas, the Hartree-Fock mean-field correction, and the (fermionic) Lee-Huang-Yang correction, respectively.

Using relation (7.1) we obtain the contact density [11]

$$C = \mathcal{I}/V = 4\pi^2 n^2 a_s^2 \left(1 + 1.049 k_F^{\mathrm{hom}} a_s + 0.2584 (k_F^{\mathrm{hom}} a_s)^2 + \dots\right). \tag{7.3}$$

At unitarity, the ground state energy density is

$$E/V = \frac{3}{5}\frac{\hbar^2 (k_F^{\mathrm{hom}})^2}{2m} n \left(\xi + \frac{\zeta}{k_F^{\mathrm{hom}} a_s} + \dots\right), \tag{7.4}$$

where $\xi \approx 0.367$ [92] is the Bertsch parameter and the constant $\zeta \approx 0.8$ [108]. Therefore, the contact density is

$$C = \frac{6\pi k_F \zeta}{5} n + \dots. \tag{7.5}$$

In the BEC limit of tightly bound dimers the energy density at zero temperature can be approximated by

$$E/V = -n_d \frac{\hbar^2}{m a_s^2} + \frac{2\pi\hbar^2 a_{dd}}{2m} n_d^2 \left(1 + 4.81\sqrt{n_d a_{dd}^3} + \dots\right), \tag{7.6}$$

where the first term arises from the molecular binding energy for $a_s \to \infty$ and the next two terms from the mean-field and the (bosonic) Lee-Huang-Yang correction, respectively [143]. Here, $n_d = n/2$ is the dimer density and $a_{dd} = 0.6\, a_s$ is the dimer-dimer scattering length [94]. The contact density becomes

$$C = \frac{4\pi n}{a_s} + 0.6\pi^2 n^2 a_s^2 \left(1 + 12.03\sqrt{n_d a_{dd}^3} + \dots\right). \tag{7.7}$$

The homogeneous contact densities calculated from Eqs (7.3), (7.5) and (7.7) are shown in Figure 7.2.

Note that for finite scattering lengths a_s the expression for the binding energy per molecule,

$$\frac{\hbar^2}{m a_s^2},$$

in Eq. (7.6) has to be modified by higher order corrections [80, 96]. At a coupling of $(k_F^{\mathrm{hom}} a_s)^{-1} = 1\,(2)$ these result in corrections of 1.4% (2.9%) towards a larger contact density, as shown in Fig. 7.2.

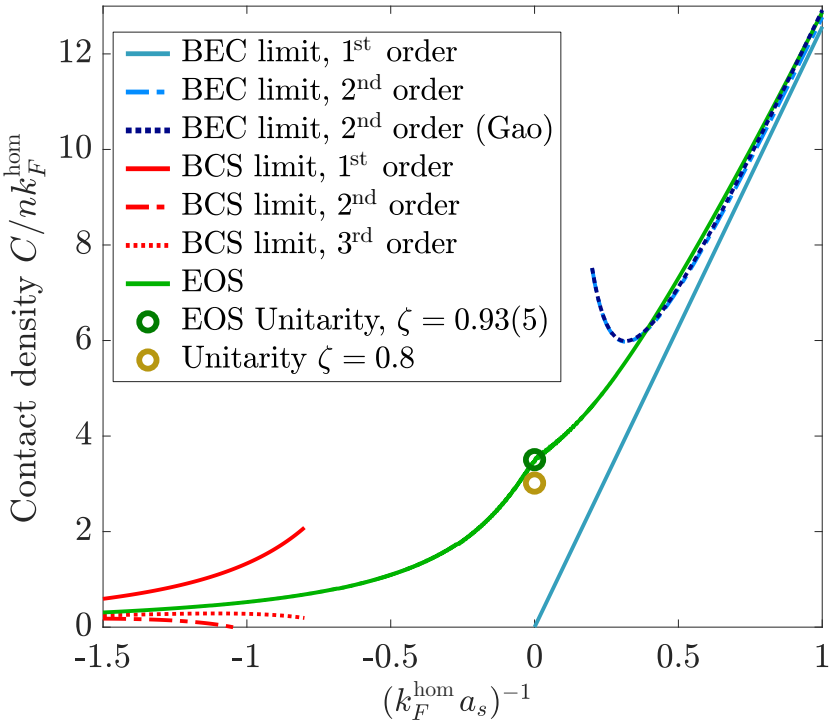

FIGURE 7.2: Normalized contact density of a homogeneous system calculated from the ground state energy expansions (equations (7.3), (7.5) and (7.7)) and the equation of state (EOS) measurements. Also shown is the contact in the BEC limit with the binding energy correction for small a_s [96]. The different orders refer to the number of orders in equations (7.3) and (7.7).

7.3.2 Equation of state measurements

Navon *et al.* carried out measurements of the equation of state (EOS) of a zero-temperature Fermi gas in the BCS-BEC crossover [166]. Here, we briefly explain the procedure to first obtain the contact density C and then the trap-integrated total contact $\mathcal{I}$ based on these measurements. The resulting curves are shown in Fig. 7.2 and Fig. 2 of [13]. In general, the total energy of a Fermi gas at zero temperature can be expressed as

$$E/V = \frac{3}{5}\frac{\hbar^2 (k_F^{\mathrm{hom}})^2}{2m} n\, \xi(\delta) - \Theta(a_s)\frac{n}{2}\frac{\hbar^2}{m a_s^2}, \tag{7.8}$$

where $\xi(\delta)$ can be viewed as a generalized Bertsch parameter relating the systems total energy to the Fermi energy at a given interaction parameter δ. Θ is the Heaviside step function and accounts for the existence of the Feshbach bound state with binding energy $\hbar^2/ma_s^2$ for $a_s > 0$. In the Supplementary Material of [166] the function $\xi(\delta)$ is defined as

$$\xi(\delta) = \frac{h(\delta) - \frac{\delta}{3}h'(\delta)}{(h(\delta) - \frac{\delta}{5}h'(\delta))^{5/3}}. \tag{7.9}$$

Here, δ is related to the coupling parameter $(k_F^{\mathrm{hom}} a_s)^{-1}$ through an implicit equation,

$$(k_F^{\mathrm{hom}} a_s)^{-1}(\delta) = \frac{\delta}{(h(\delta) - \frac{\delta}{5}h'(\delta))^{1/3}}, \tag{7.10}$$

which can be solved numerically.
For the function $h(\delta)$, Padé-approximations were given for both the BEC ($a_s > 0$) and BCS ($a_s < 0$) regime. The approximations, whose parameters were deduced from the EOS measurements, were made such that $h(\delta)$ is continuous at unitarity $(k_F^{\mathrm{hom}} a_s)^{-1} = 0$. The function $h'(\delta)$ denotes the derivative of $h(\delta)$. By combining equations (7.8), (7.9) and (7.10) we find the systems energy E as a function of $(k_F^{\mathrm{hom}} a_s)^{-1}$. From this, the contact density C across the BCS-BEC crossover can be determined as in the previous section. The resulting curve is shown in Fig. 7.2.
We then integrate over the trap volume as described in Appendix C of [143] to get the total contact $\mathcal{I}$ for the harmonically trapped Fermi gas. Note that although the Padé-approximations for $h(\delta)$ are continuous at unitarity, they are not continuously differentiable there. As a result, both the calculated contact density and the total contact exhibit a kink there (see Fig. 7.2 and Fig. 2 of [13]).

7.3.3 Quantum virial expansion

The quantum virial expansion has shown to be a powerful tool for investigating strongly-interacting Fermi gases at high temperatures T [170]. In the high temperature limit, the chemical potential μ of a Fermi gas approaches $-\infty$. Therefore the fugacity $z = \exp(\mu/k_B T)$ becomes a small parameter, even for strong interparticle interactions as present in the BCS-BEC crossover [174]. Here k_B is the Boltzmann constant. In this limit, any physical quantity of the Fermi gas can be

expanded as a series expansion in the fugacity z with corresponding expansion coefficients, i.e. the virial coefficients.
We employ the quantum virial expansion to calculate Tan's contact, following [70] where this approach was described and used to present the contact at unitarity and at $T = 0.5\,T_F$ for $-2 < (k_F a_s)^{-1} < 0.5$. Using the same approach, we show results for the contact in the entire BCS-BEC crossover for $-1.5 < (k_F a_s)^{-1} < 2.5$ and $0 < T/T_F < 1.5$ in Fig. 3 b) of [13] and for four different couplings $(k_F a_s)^{-1}$ in figure 7.3. In figure 7.4 we further provide a map of the central fugacity z_0 of a harmonically trapped Fermi gas the BCS-BEC crossover.

To quickly rederive the calculation of the contact within the quantum virial expansion, we start from Tan's adiabatic sweep theorem for the grand canonical ensemble

$$\left(\frac{\partial \Omega_G}{\partial(1/a_s)}\right)_{T,V,\mu} = -\frac{\hbar^2 C V}{4\pi m}. \tag{7.11}$$

In the virial expansion, the grand canonical potential

$$\Omega_G = -2k_B T V/\lambda_{dB}^3 \left(z + b_2 z^2 + b_3 z^3 + \dots\right) \tag{7.12}$$

is expanded as a series expansion in the fugacity $z = \exp(\mu/k_B T)$ where b_n are the virial coefficients, V is the volume and λ_{dB} is the thermal de Broglie wavelength [170]. The virial coefficients are functions of λ_{dB} and the scattering length a_s. Using equations (7.11) and (9.22) we find the homogeneous contact density

$$C_{QV} = \frac{16}{\pi^2 \lambda_{dB}^4}\left(c_2 z^2 + c_3 z^3 + \dots\right) \tag{7.13}$$

for a given temperature T, chemical potential μ and scattering length where $c_n = \partial b_n/\partial(\lambda_{dB}/a_s)$. Using the local density approximation, one can calculate the total contact for the harmonically trapped Fermi gas with trap frequency ω by replacing the chemical potential μ with a local chemical potential $\mu(r) = \mu_0 - \frac{1}{2}m\omega^2 r^2$ and then integrating

$$\begin{aligned}\mathcal{I}_{QV} &= \int \mathrm{d}^3 r\; C(r) = \frac{16}{\pi^2 \lambda_{dB}^4}\int \mathrm{d}^3 r\;\left(c_2 z^2(r) + c_3 z^3(r) + \dots\right)\\ &= \frac{16}{\pi^2 \lambda_{dB}}\left(\frac{k_B T}{\hbar\omega}\right)^3\left[\frac{c_2}{2^{3/2}} z_0^2 + \frac{c_3}{3^{3/2}} z_0^3 + \dots\right].\end{aligned} \tag{7.14}$$

Here, μ_0 is the chemical potential in the center of the trap and $z_0 = \exp(\mu_0/k_B T)$ is the corresponding fugacity. In a harmonically trapped Fermi gas, the chemical potential in the trap center is usually not known. Instead, the total atom number N is known, as it can be measured. Starting from the thermodynamic relation

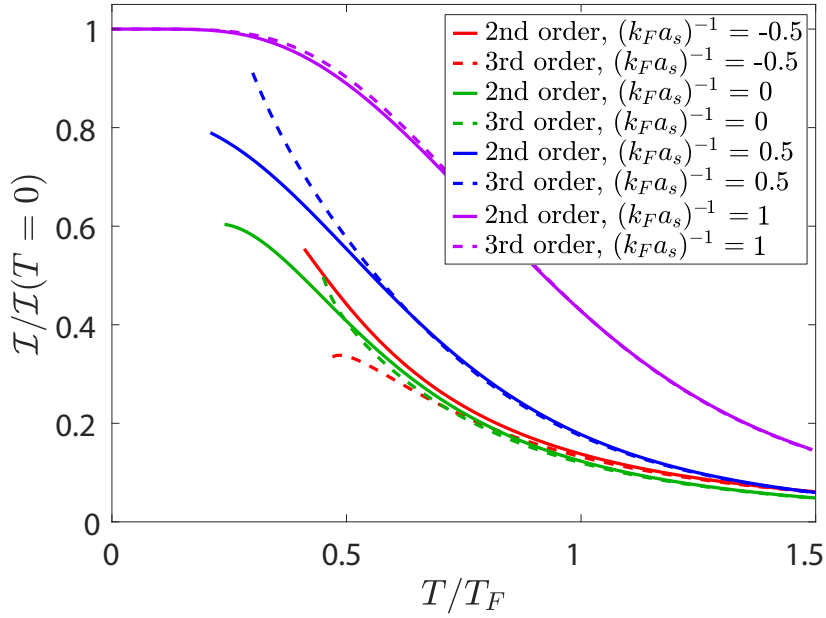

FIGURE 7.3: Contact $\mathcal{I}$ of a harmonically trapped Fermi gas, as calculated with the second and third order virial expansions for couplings $(k_F a_s)^{-1} = (-0.5, 0, 0.5, 1)$. We normalize each contact curve $\mathcal{I}(T/T_F)$ with the respective zero-temperature value, $\mathcal{I}(0)$, taken from our interpolation of the zero-temperature measurement, as shown in Fig. 2 of [13].

$n = -\frac{1}{V}\frac{\partial \Omega_G}{\partial \mu}$, and using again the local density approximation one finds

$$\begin{aligned} N &= \int \mathrm{d}^3 r\; n(r) = 2\left(\frac{k_B T}{\hbar\omega}\right)^3 \left[z_0 + \frac{b_2}{\sqrt{2}} z_0^2 + \frac{b_3}{\sqrt{3}} z_0^3 + \dots\right] \\ &= 2\left(\frac{k_B T}{\hbar\omega}\right)^3 \left[z_0 + \frac{b_2^{(0)} + \Delta b_2}{\sqrt{2}} z_0^2 + \frac{b_3^{(0)} + \Delta b_3}{\sqrt{3}} z_0^3 + \dots\right] \\ &= 2\left(\frac{k_B T}{\hbar\omega}\right)^3 \left[z_0 - \frac{z_0^2}{2^3} + \frac{z_0^3}{3^3} + \dots + \frac{\Delta b_2}{\sqrt{2}} z_0^2 + \frac{\Delta b_3}{\sqrt{3}} z_0^3 + \dots\right] \\ &= 2\left(\frac{k_B T}{\hbar\omega}\right)^3 \left[-\mathrm{Li}_3(-z_0) \; + \frac{\Delta b_2}{\sqrt{2}} z_0^2 + \frac{\Delta b_3}{\sqrt{3}} z_0^3 + \dots\right], \end{aligned} \tag{7.15}$$

where we separated the virial coefficients in parts Δb_n that take into account the n-body interactions (e.g. scattering properties, bound states,...) and parts that account for quantum statistics $b_n^{(0)} = \frac{(-1)^{n+1}}{n^{5/2}}$. The infinite sum $z_0 - z_0^2/2^3 + z_0^3/3^3 + \dots$ can be identified as the polylogarithm function $\mathrm{Li}_3(-z_0)$ of degree 3 and argument $-z_0$. The polylogarithm function is related to the integral of the Fermi-Dirac distribution function. The second order virial coefficient is analytically

known and reads [170, 175]

$$b_2 = b_2^{(0)} + \Delta b_2 \tag{7.16}$$

$$= \frac{-1}{2^{5/2}} + \sqrt{2}\Theta(a_s)\mathrm{e}^{\lambda_{dB}^2/2\pi a_s^2} - \frac{\sqrt{2}}{2}\mathrm{sgn}(a_s)\left(1 - \mathrm{erf}\left[\sqrt{\lambda_{dB}^2/2\pi a_s^2}\right]\right)\mathrm{e}^{\lambda_{dB}^2/2\pi a_s^2}, \tag{7.17}$$

where $\Theta(\dots)$ is the Heavyside step function, $\mathrm{sgn}(\dots)$ is the sign function and $\mathrm{erf}(\dots)$ is the error function. By applying the virial expansion up to the second order, equation (7.15) can be solved numerically to determine μ_0 for a given atom number N, temperature T, scattering length a_s and trap frequency ω. With the chemical potential, one can then calculate the contact of the trapped Fermi gas using equation (7.14). The result is shown in Fig. 4 b) of [13]. From the calculation of the central chemical potential μ_0, we also obtain the corresponding fugacity z_0 which is shown in Figure 7.4. Its value indicates in which regimes the second order virial expansion is expected to provide reliable results.
We also performed calculations of the contact with the third order virial expansion. For this, we extracted b_3 from [176]. Above $(k_F a_s)^{-1} \approx 1.5$, the second and third order calculation give the same results for the contact. As also observed in [70], we find that the second and third order results at unitarity start to deviate from each other for temperatures lower than $\approx 0.5\,T_F$. Additional calculations for couplings $(k_F a_s)^{-1} = (-0.5, 0.5, 1)$ are shown in Fig. 7.3. When we go deeper into the BCS regime, the second and third order results start to deviate at temperatures even higher than $0.5\,T_F$. This is because in the BCS regime the fugacity $z_0 = \exp(\mu_0/k_B T)$ is not small anymore as the chemical potential μ_0 is positive and approaches the Fermi energy for $(k_F a_s)^{-1} \to -\infty$. As a result, the virial expansion loses its validity and the higher order expansions do not converge.

7.4 Measurement of Tan's contact via photoexcitation

As pointed out in [32, 33] there is a very general and fundamental link between the total contact $\mathcal{I}$ and the two-body loss rate of a two-component Fermi gas

$$-\frac{\mathrm{d}N}{\mathrm{d}t} = \frac{-\hbar\mathrm{Im}[a]}{2\pi m|a|^2}\mathcal{I}, \tag{7.18}$$

where N is the total atom number, m is the atomic mass and a is the scattering length. If a has a finite imaginary part, loss due to a two-body process is present. Thus, the total contact of the spin-balanced Fermi gas can be simply deduced from the induced two-body loss rate, as long as the scattering length is known. Note that relation (7.18) holds for collisional loss during s-wave collisions. A very similar relation was recently found for a collisional p-wave loss rate [18, 162]. We now consider a special situation of two fermions colliding in an s-wave while they are subjected to a photoexcitation laser beam, see Fig. 7.5. Atomic collisions

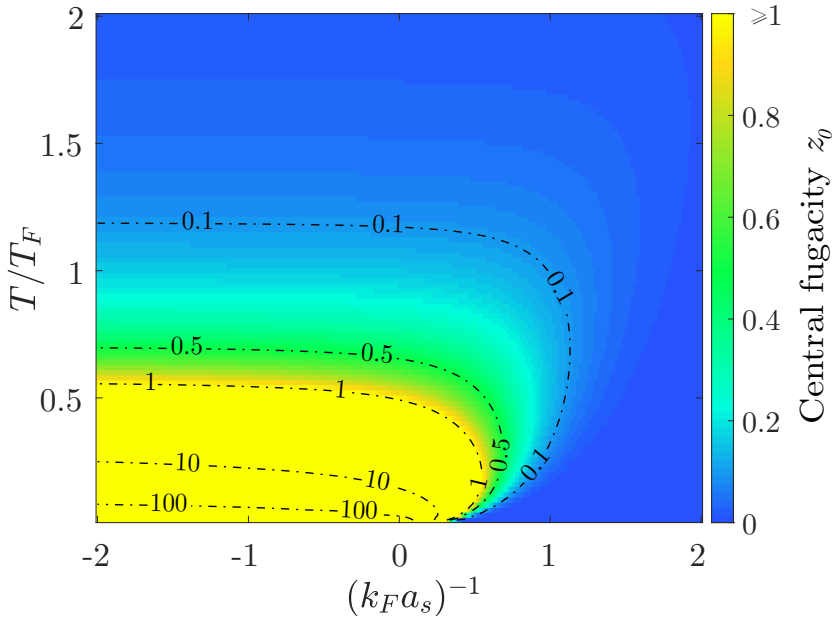

FIGURE 7.4: Calculation of the fugacity z_0 in the center of a harmonically trapped Fermi gas in the BCS-BEC crossover. The calculation is based on the second order quantum virial expansion. In regions where $z_0 \ll 1$ the expansion is expected to be valid.

take place in the vicinity of a single, magnetically tunable Feshbach resonance. The Feshbach resonance comes about as a bare, closed-channel molecular bound state is coupled (via hyperfine interaction) and admixed to the scattering state of the colliding atoms. The Feshbach resonance is intrinsically lossless. Now, two-body loss is induced via resonant photoexcitation of the atom pair at close range to an electronically-excited, short-lived molecular state with a lifetime $1/\gamma$. Photoexcitation takes place via the closed-channel bound state of the Feshbach resonance which is coupled to the excited molecular state with Rabi frequency Ω. For this system, reference [31] has calculated the complex scattering length a and Eq. (7.18) becomes

$$-\frac{\mathrm{d}N}{\mathrm{d}t} = \frac{\hbar\mathcal{I}}{2\pi m a_{bg}} \frac{\Omega^2/(2\gamma W)}{\left[1 - a_{bg}/a_s\right]^{-2} + \left[\Omega^2/(2\gamma W)\right]^2}. \tag{7.19}$$

Here, a_s denotes the real-valued scattering length without the photoexcitation coupling, a_{bg} is the corresponding background scattering length and W the width of the Feshbach resonance. In our experiments the resonance width is $W = -2\mu_B \times 262.3(3)\,\mathrm{G} = -2\pi\hbar \times 734(1)\,\mathrm{MHz}$, and $a_{bg} = -1582(1)\,a_0$ [78] where a_0 is the Bohr radius. The linewidth γ is $\gamma = 2\pi \times 12(1)\,\mathrm{MHz}$, as measured in our experiment [13]. The spectroscopic details of the excited and closed-channel molecular bound states, as well as the scattering state of our experiment can be found in Fig. 7.5 and the caption. For all practical purposes, the term $\left[\Omega^2/(2\gamma W)\right]^2$ in the denominator can be neglected in our experiments, because we have $\Omega \lesssim 2\pi \times 1\,\mathrm{MHz}$. Even for Ω up to $2\pi \times 250\,\mathrm{MHz}$, the term $\left[\Omega^2/(2\gamma W)\right]^2$ is smaller than 10^{-3}.

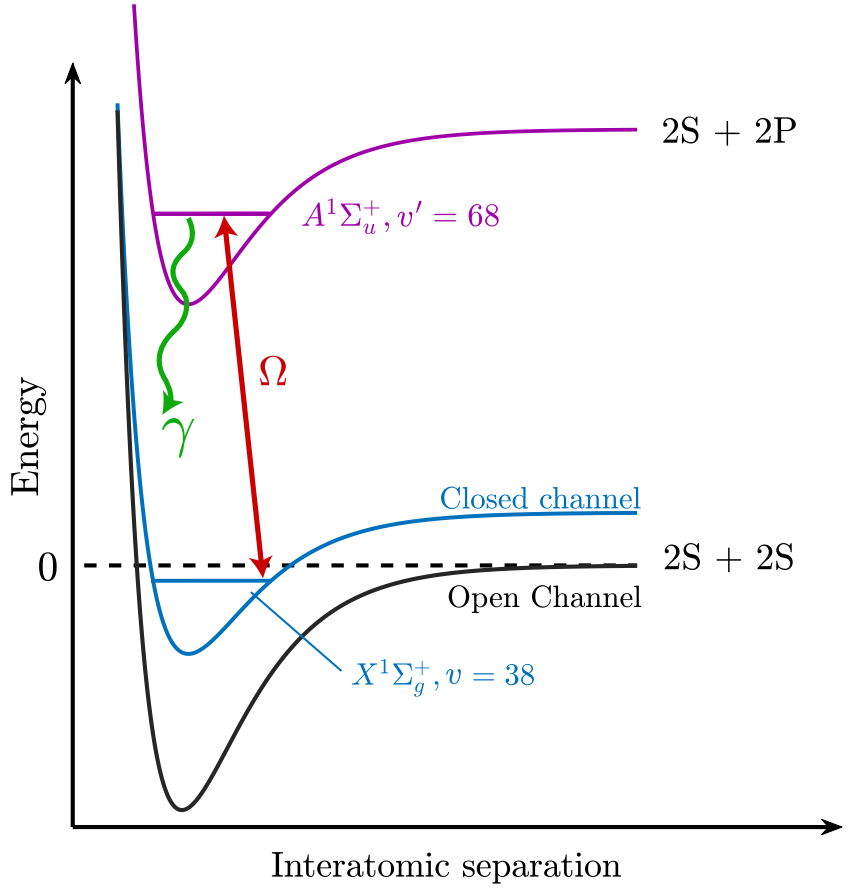

FIGURE 7.5: Photoexcitation scheme for the measurements of Tan's contact via two-body losses, using the example of two colliding ground state ^{6}Li atoms in the lowest hyperfine levels $|F = 1/2, m_F = 1/2\rangle$ and $|F = 1/2, m_F = -1/2\rangle$. The magnetic field is close to 832.2 G where a broad Feshbach resonance is located. In the Feshbach resonance the scattering state of the atoms is coupled via the hyperfine interaction to the bare weakly-bound molecular level $X^1\Sigma_g^+, v = 38$. This Feshbach resonance is essentially lossless. We induce two-body loss photoexcitation using a laser at 673 nm which couples the bare weakly-bound molecular level $X^1\Sigma_g^+, v = 38$ state to the excited deeply-bound molecular state $A^1\Sigma_u^+$ $v' = 68$. The two states have a large Franck-Condon overlap of 0.077 [142]. The excited state has a lifetime γ. Ω is the Rabi frequency associated with this optical transition.

According to Eq. (7.19) the contact $\mathcal{I}$ can be determined by measuring the atom loss rate $\mathrm{d}N/\mathrm{d}t \equiv \dot{N}$, the Rabi frequency Ω and the scattering length a_s in a given experimental run. In order to achieve a high precision for the value $\mathcal{I}$ at a particular $(k_F a_s)^{-1}$ and T/T_F, we need to precisely determine the Rabi frequency Ω, the atom number N, the trapping frequencies ω_{ax} and ω_r, as well as the scattering length a_s. (Note that $k_F = (2m/\hbar)^{1/2}(\omega_{ax}\omega_r^2 3N)^{1/6}$). How this is achieved is described in the following sections.

7.4.1 Calibration of the Rabi frequency Ω

As a first step, we simplify (7.19), by omitting the term $[\Omega^2/(2\gamma W)]^2$ in the denominator, as it can be neglected in our experiments,

$$-\dot{N} = \frac{\hbar\mathcal{I}}{2\pi m a_{bg}} \frac{\Omega^2/(2\gamma W)}{[1-a_{bg}/a_s]^{-2}}. \tag{7.20}$$

Next, we make use of the fact that Ω is linked to the photoexcitation intensity I via the relation $\Omega^2 = k\,I$ where k is a constant. We use a calibration process to determine k and with it Ω. For this, we choose a convenient parameter setting for which the contact $\mathcal{I}$ is known. This parameter setting corresponds to a specific photoexcitation intensity I_{cal}, scattering length $a_{s,\text{cal}}$ (via tuning of the magnetic field B), particle density and temperature. Concretely, we chose the low-temperature BEC regime which has the advantage that the contact there is quite insensitive to temperature (see Fig. 7.3) and its value is $\mathcal{I}/Nk_F = 4\pi/(k_F a_s)$ [143]. We then measure the loss rate $\dot{N}_{\text{cal}}$ at these parameters and this yields

$$k = -\dot{N}_{\text{cal}} \frac{2\pi m a_{bg}}{\hbar\mathcal{I}_{\text{cal}}} \frac{[1-a_{bg}/a_{s,\text{cal}}]^{-2}}{I_{\text{cal}}/(2\gamma W)}. \tag{7.21}$$

Using (7.21) and the relation $\Omega^2 = k\,I$, equation (7.20) becomes

$$\dot{N} = \dot{N}_{\text{cal}} \frac{\mathcal{I}}{\mathcal{I}_{\text{cal}}} \frac{I}{I_{\text{cal}}} \frac{[1-a_{bg}/a_{s,\text{cal}}]^{-2}}{[1-a_{bg}/a_s]^{-2}}, \tag{7.22}$$

where the parameters m, γ and W have dropped out as a consequence of the calibration.

7.4.2 Atom number calibration

For determining the atom number, we perform absorption imaging at high magnetic fields. For this purpose, we typically use a short laser pulse of τ =10 μs at an intensity of $I/I_S = 0.05$ to drive the quasi-closed transition to the $|2^2P_{3/2}; m_J = -3/2\rangle$ state with linewidth $\Gamma_a \approx 2\pi \times 5.87$MHz [77], where $I_S = 2.54\,\text{mW/cm}^2$ is the saturation intensity.

During the exposure with the imaging light, the atoms scatter photons. This accelerates them and leads to an increasing Doppler shift (see e.g. [177]) which effectively lowers the cross section for absorption over time. In order to take this effect into account, we calibrated our imaging routine using a simple classical mechanical model. In this model, we consider the acceleration of the atoms

$$a = \frac{\hbar k \Gamma_a}{2m} \frac{I/I_S}{1 + I/I_S + 4(kv/\Gamma_a)^2} \tag{7.23}$$

by scatting photons from the imaging beam with intensity I and wavelength $\lambda = 2\pi/k \approx 671$ nm [129]. Solving this differential equation yields the time-dependent atom velocity v and Doppler shift kv. From this, we can calculate a time-averaged cross section for absorption imaging which is lowered from the

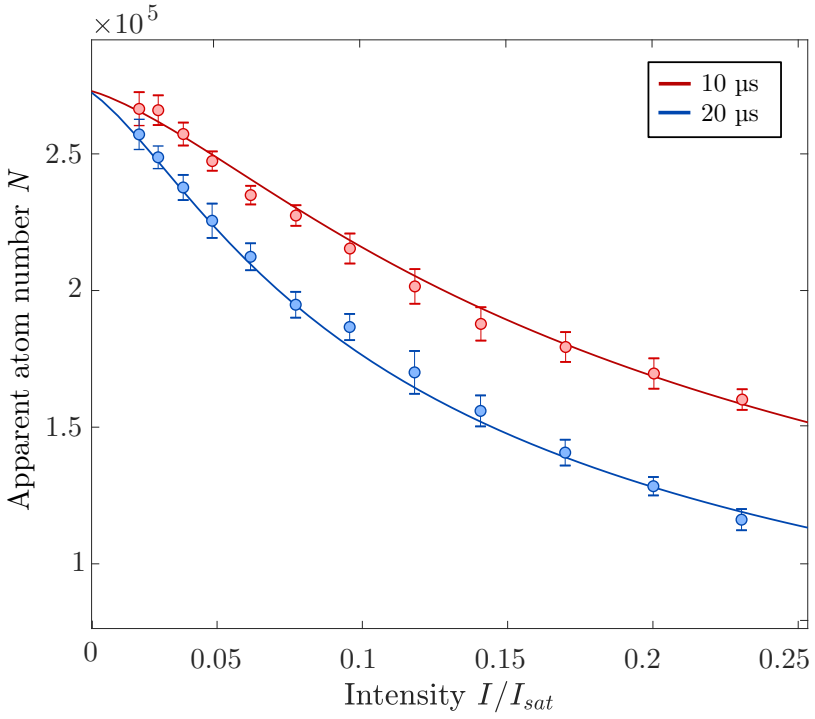

FIGURE 7.6: Measured signal for the atom number as a function the imaging light intensity of for an imaging pulse duration of 10 µs and 20 µs. The apparent atom number drops with higher intensity and imaging pulse duration due to an increasing Doppler shift that the atoms acquire while scattering photons. This effectively lowers the cross section for absorption and thus the measured atom numbers. In the limit of zero intensity, the real atom number is recovered.

largest possible cross section by a factor $\langle 1 + I/I_s + 4(kv/\Gamma_a)^2\rangle_\tau$ due to the acquired Doppler shift and power broadening. We fit this model to our measured atom numbers with the intensity I and (real) atom number N as free parameters (see Fig. 7.6). This allows for extracting the accurate atom number at any given intensity and pulse duration. With this, we can determine atom numbers with a typical uncertainty of 5%, corresponding to an uncertainty in $k_F \propto N^{1/6}$ of 1%. We further tested this calibration using calculations of the atom cloud density distribution in the trap based on the equation of state at unitarity [88] and with a mean-field model in the low temperature BEC regime which we describe in detail in the Supplementary of [82]. With this, we calculate the 2D column density and 1D line density for given total atom numbers, trapping frequencies and temperatures and compare the calculated densities to the measured ones.

7.4.3 Trap frequency measurement and anharmonicities

While the trapping potential of the atoms in our experiment in axial direction is harmonic for all practical purposes, this is not quite the case in radial direction where a single-beam optical dipole trap provides confinement. Therefore, the radial-trapping potential has a Gaussian shape, thus increasingly deviating from a perfect harmonic potential with the distance from the trap center. The larger

the atomic cloud size, the larger are the effects due to the anharmonicity [178]. Cloud sizes increase, e.g., due to stronger repulsive interparticle interactions and higher temperatures. Nevertheless, it turns out that the anharmonicity effects are comparatively small in our experiments, so that we can neglect them to first order in our data analysis in [13]. This has the advantage that it keeps our data analysis simple. However, it induces a small systematic error on our results which nominally represent the normalized total contact $\mathcal{I}/Nk_F$ for a perfectly harmonically trapped gas. We have estimated this systematic error as follows. We carried out calculations to describe the properties and behaviour of the atomic gas in an anharmonic trap. For temperature $T \approx 0$ these calculations are based on the EOS [166] and for $T/T_F > 0.5$ they are based on the quantum virial expansion [70, 170]. For our given anharmonic trap, temperature T, total atom number N, and scattering length a_s, we calculated the atomic density distribution, the effective trap frequency ω_{eff}, and the total contact using the local density approximation (LDA). The effective trap frequency ω_{eff} is the frequency of the center of mass motion of the atom cloud in the anharmonic trap. It generally differs slightly from the trap frequency ω_r at the trap center [178]. Next, we follow our analysis protocol of [13] where we ignore anharmonicity and set $\omega_r = \omega_{\text{eff}}$ to calculate E_F, T_F, k_F and the normalized total contact $\mathcal{I}/Nk_F$. Finally, we compare this value for the normalized contact to the one for the perfect harmonic trap. We find, that they deviate by less than 0.3% $(1.3\%, 3.0\%, 3.2\%, 3.6\%)$ at $T/T_F = 0\,(0.5, 1.0, 1.5, 2.0)$. These systematic deviations are smaller than the respective statistical uncertainties in our measurements which are typically $\approx 2\%$ $(4\%, 6\%, 9\%, 12\%)$ at $T/T_F = 0$ $(0.5, 1.0, 1.5, 2.0)$. The statistical uncertainties decrease with decreasing temperature T, since in our experiments evaporative cooling leads to more stable atom numbers at lower temperatures.

For determining the trapping frequencies ω_{ax} and ω_{eff}, we perform either parametric heating by modulating the potential of the optical dipole trap or we observe the center of mass motion of the atom cloud after an initial small displacement of a few micrometers. Both methods give consistent results with approximately 2% uncertainty for the parametric heating method and 3% uncertainty for the center of mass motion measurement.

7.4.4 Determination of the scattering length a_s

In order to determine the scattering length a_s precisely, we we precisely measure the measured magnetic field at the location of the atoms. We then assign a scattering length to the measured magnetic field by using reference [78]. For measuring the magnetic fields precisely, we perform radio-frequency (RF) spectroscopy between the two lowest atomic hyperfine states. For this, we first use a short laser pulse to depopulate the $|F = 1/2, m_F = 1/2\rangle$ state. We then apply a 50 ms RF pulse and scan stepwise the RF frequency of ≈ 76.2 MHz to find resonant population transfer to this state from the still populated $|F = 1/2, m_F = -1/2\rangle$ state. Using the Breit-Rabi formula we are able to determine the magnetic field with an uncertainty < 0.5 G. Together with the typical uncertainty in k_F of 1%, this results in an uncertainty of $(k_F a_s)^{-1} \approx 0.01$ in the investigated range of magnetic fields.

7.4.5 Thermometry

For determining the temperature of our atoms, we fit a second order virial expansion of the density distribution to the outer wings of the atom cloud (see [15, 82]). This works well even at low temperatures, as the local fugacity $z(\vec{r})$ in the outer wings is still a small parameter which makes the virial expansion applicable. With this method, we can determine the temperature with a typical precision of $\approx 0.02\, T/T_F$ at small temperatures ($T < 0.5T_F$) and up to $0.05\, T/T_F$ at high temperatures ($T \gtrsim 1\, T_F$).

7.5 Related studies

In this section, we present additional results and insights that we obtain from our measurements. More precisely, we compare the photo-induced atom decay measurements to predictions from [143] and measurements from [163] where a dependency of the decay law on the interaction regime was predicted and observed. We further extract the closed-channel fraction Z from our measurements and compare the results to various theoretical predictions [31, 179–182] and experimental results [142, 163].

7.5.1 Two-body decay laws in a Fermi gas

According to equation (7.19) the photo-induced two-body loss rate in the Fermi gas is proportional to the total contact $\mathcal{I}$ [31]. If the dependency of the contact on the atom number N is known, one can deduce the corresponding decay law for $N(t)$.

As calculated in [143] in the zero temperature BCS limit, the integration of the homogeneous contact density over the trap volume yields the proportionality $\mathcal{I} \propto k_F^3 N$ and therefore $\dot{N}/N \propto N^{1/2}$. At unitarity one finds $\mathcal{I} \propto k_F N$ and hence $\dot{N}/N \propto N^{1/6}$. In the BEC limit $\mathcal{I} \propto N$ such that $\dot{N}/N = \text{const}$. Here $k_F = \sqrt{2mE_F}/\hbar$ is the Fermi momentum of the trapped gas, $E_F = k_B T_F = \hbar\bar{\omega}(3N)^{1/3}$ is the Fermi energy, and $\bar{\omega}$ is the geometric mean of the trapping frequencies. Thus, these differential equations have the form $\dot{N}/N \propto N^{1/b}$, where $b = 2$ in the BCS limit, $b = 6$ at unitarity and $b \to \infty$ in the BEC limit. Their solutions, i.e. the decay laws, are given by the power law

$$N(t) = N_0/(1 + \Gamma_0 t/b)^b, \tag{7.24}$$

with the initial decay rate Γ_0. We can now compare these predictions with our measurements.

From our measurements shown in Fig. 7.7 we obtain the parameters b listed in table 7.1. We observe a deviation in the fit parameters b (see Eq. (7.24)) compared to the theoretical predictions. We attribute this deviation to an increase of the atom cloud temperature during the photoexcitation pulse, especially for longer times ($>$ 400 ms). Note, however, that we have not investigated this heating effect properly as after 400-500 ms thermometry based on the atom density distributions becomes increasingly difficult, because the density and

Coupling $(k_F a_s)^{-1}$	Temperature	Photoex. laser power	Theo. param. b	Fit param. b	Fit param. b $t < 250$ ms
1.5	0.07 T_F	6 μW	∞	> 20	> 20
0	0.05 T_F	38 μW	6	3.9 ± 0.9	5.7 ± 3.1
-1.65	0.04 T_F	610 μW	2	1.6 ± 0.2	2.1 ± 0.5

TABLE 7.1: Experimental parameters for the measurement data shown in Fig. 7.7. The values for couplings and temperatures are the initial values at $t = 0$.

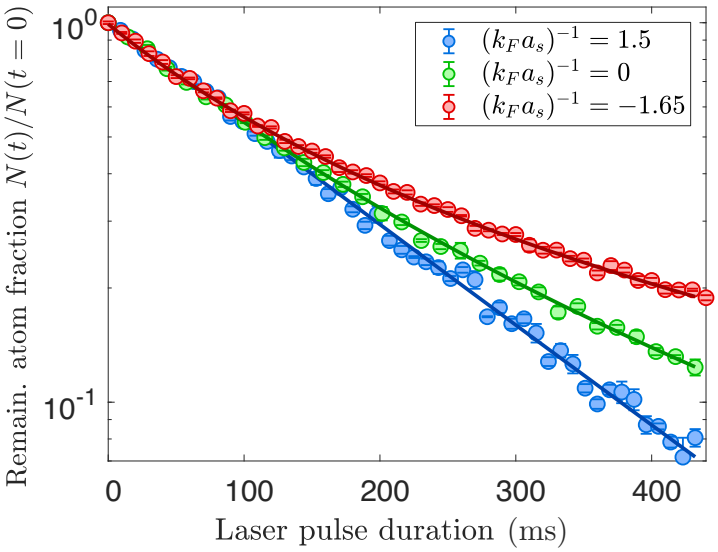

FIGURE 7.7: Remaining atom fraction as a function of the photoexcitation laser pulse duration, taken from [13]. The measurements were carried out at magnetic fields of 753 G, 832 G and 1078 G with the initial $(k_F a_s)^{-1} = 1.5, 0, -1.65$ corresponding to the BEC, unitarity and BCS regimes of the crossover. The initial temperatures were $T/T_F = 0.07, 0.05$ and 0.04, respectively. For a better comparison, the laser powers for the three data sets were manually adjusted so that their initial relative loss rates were the same (see table 7.1). The continuous red and green lines are fits according to Eq. (7.24), while the blue line is an exponential (i.e. $b = \infty$).

therefore the signal decreases. We find, however, that during the first 250 ms, the temperature stays rather constant within 5-10%. If we only include these data points, the fitted parameters tend towards the theoretical values. However, the uncertainty increases since we lower the number of data points for the fit. Our results for b are compatible with measurements of [163], who measured $b \approx 6$ at unitarity and $b = 1.78\ (1.43)$ in the BCS regime at 925 G (1000 G).

7.5.2 Closed-Channel fraction

As discussed previously, in the vicinity of the Feshbach resonance the scattering wavefunction Ψ of an atom pair has a closed-channel admixture of the bare highest bound molecular state $X^1\Sigma_g^+\,(v = 38)$. It can be written as

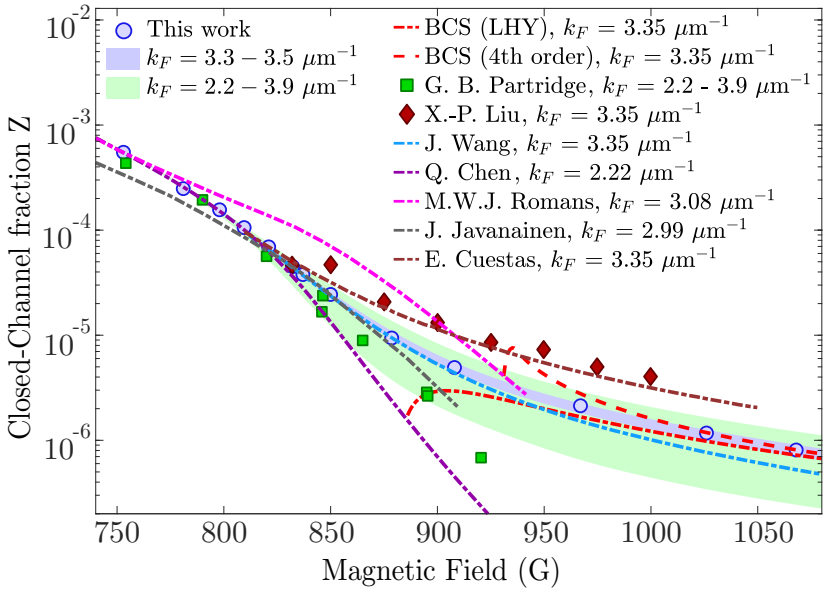

FIGURE 7.8: Closed-channel fraction Z as a function of magnetic field, taken from various studies. Blue lilac circles are extracted from our measured contact data using equation (7.25). The blue lilac (green) shaded area is a calculation of the closed-channel fraction based on these results for the range of k_F from 3.2 to 3.5 μm^{-1} (2.2 to 3.9 μm^{-1}). Data from other studies (calculations and measurements) have plot symbols as indicated by the legend. This includes photoexcitation measurements from G.B. Partridge *et al.* [142] and from X.-P. Liu *et al.* [163], as well as calculations by J. Wang *et al.* [31], Q. Chen *et al.* [179], M.W.J. Romans *et al.* [179], J. Javanainen *et al.* [182], and E. Cuestas *et al.* [181]. We further show calculations based on the BCS ground-state energy expansions as in Fig. 2 of [13].

$\Psi = \sqrt{Z}\,\Psi_{\text{closed}} + \sqrt{1-Z}\,\Psi_{\text{open}}$ where Z is the so-called closed-channel fraction. For a weak probe laser intensity ($\Omega^2 \ll \gamma W$) this quantity is directly linked to Tan's two-body contact via [143]

$$Z = \frac{\mathcal{I}}{Nk_F}\frac{\hbar k_F}{2\pi m a_{bg} W}\left[1 - \frac{a_{bg}}{a_s}\right]^2, \tag{7.25}$$

and has been experimentally and theoretically investigated by several groups [31, 142, 163, 179, 181, 182]. It is therefore natural to compare all these data, see Fig. 7.8. However, since the closed-channel fraction is not a normalized quantity it can only be compared directly for measurements and calculations with similar parameters W, k_F, m, a_{bg}, a_s. Apart from some variations in the Fermi momentum k_F the parameters are indeed the same for the different data sets. Therefore, a quantitative comparison is approximately possible.
To calculate the magnetic field dependence of the closed channel fraction for any given Fermi momentum k_F we use the interpolation of our measurements of the total contact as presented in figure 2 in [13]. The measured quantity $\mathcal{I}/Nk_F$

only depends on $(k_F a_s)^{-1}$ to a good approximation. Thus, for a given Fermi momentum k_F and magnetic field B to which we assign a corresponding scattering length a_s, we can determine $\mathcal{I}/Nk_F$ from our interpolation. Using this result and equation (7.25), we can then calculate the closed-channel fraction Z. We use this procedure to calculate the blue lilac and green shaded areas in figure 7.8.

With the blue lilac shaded area we illustrate a lower and upper bound for the closed channel fraction deduced from our zero-temperature contact measurements where the atom number ranges from $4.8\times10^5-6.5\times10^5$ (corresponding to $k_F = 3.3-3.5\,\mu\text{m}^{-1}$). We further plot the closed channel fraction calculated for $k_F = 2.2-3.9\,\mu\text{m}^{-1}$. This allows for comparing our measurements to the ones presented in [142] where the Fermi momentum k_F ranges from 2.2 to $3.9\,\mu\text{m}^{-1}$ and to the calculation presented in [179] for $k_F = 2.2\,\mu\text{m}^{-1}$. The plot shows that up to this point there is still a large discrepancy between different measurements and theories on the BCS side of the Feshbach resonance. This highlights the importance of high precision measurements in this regime.

7.6 Summary and conclusion

In this companion paper, we present relevant background information on measuring Tan's contact in the BCS-BEC crossover with a novel photo-excitation method. After a brief overview over various previous approaches to determine the contact we have identified areas in phase space of the strongly interacting Fermi gas where the contact is not known. We then lay out in detail the novel experimental method for measuring Tan's contact via photo-excitation, focusing on how to achieve contact measurements with high precision. Afterwards we use our measurements to study and confirm various predicted decay laws in a Fermi gas due to two-body loss [143]. Finally, we extract the closed-channel fraction from our measurements and compare them to several previous theoretical and experimental studies. In the future it will be particularly worthwhile to employ the described photo-excitation method to measure Tan's contact in homogeneous Fermi gases, as this will allow for resolving details of Fermi gas properties which are washed out in our current experiments with trapped Fermi gases [31].

Chapter 8

Holographic Imaging

Contents of this chapter have been published in Ref. [17]:

Sebastian Kölle, Manuel Jäger, Markus Müller, Wladimir Schoch, Wolfgang Limmer and Johannes Hecker Denschlag
"Holographic imaging of an array of submicron light scatterers at low photon numbers",
Applied Physics B **129**, 180 (2023).

Sections which have not been published are marked with (*)

8.1 Abstract

We experimentally test a recently proposed holographic method for imaging coherent light scatterers which are distributed over a 2-dimensional grid. In our setup the scatterers consist of a back-illuminated, opaque mask with submicron-sized holes. We study how the imaging fidelity depends on various parameters of the set-up. We observe that a few hundred scattered photons per hole already suffice to obtain a fidelity of 96% to correctly determine whether a hole is located at a given grid point. The holographic method demonstrated here has a high potential for applications with ultracold atoms in optical lattices.

8.2 Introduction

In recent years, ultracold atoms in optical lattices have become a promising platform for fundamental research of many-body and solid-state physics as well as for applications in quantum information. Quantum gas microscopes have been developed which use fluorescence imaging to detect atomic distributions in 2D optical lattices, resolving single atoms at individual lattice sites, see e.g. [41, 183–187]. In these quantum gas microscopes an individual atom typically scatters thousands of photons. This leads to heating, and therefore additional cooling techniques such as Raman sideband cooling [186] are typically required to prevent the atom from leaving its lattice site during imaging. A main motivation for the work presented here was to test a site-resolved imaging method with small numbers of scattered photons so that additional cooling is not needed. Indeed, fluorescence imaging with small photon numbers and single-atom sensitivity has been recently demonstrated [188], but only for atoms propagating in

free space. Furthermore, other imaging methods for atoms exist which are not based on fluorescence imaging. For example, these include spatially resolved ionization of atoms followed by ion detection [189, 190]. A review on various single-atom imaging techniques can be found in Ref. [191]. Holographic imaging of cold atomic clouds has been developed and demonstrated in recent years, see e.g. [192–194], but not yet with μm- and single-atom-resolution. We have

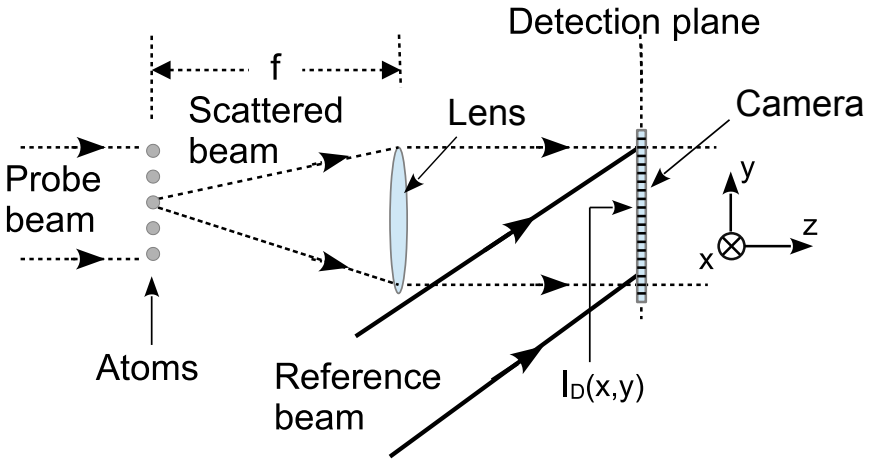

FIGURE 8.1: Coherent light scattered by the atoms is superimposed with a reference laser beam of the same frequency. For clarity, only the scattered light of one atom is shown. The atomic array is located in the objective's front focal plane. The digital camera sensor is the detection plane.

recently proposed a novel approach to site-resolved detection of atoms in a 2D optical lattice which is based on holographic techniques [50]. The main idea is schematically illustrated in Fig. 8.1. An ensemble of atoms is exposed to a near-resonant laser beam from which they coherently scatter light via fluorescence. The scattered light is collimated by a lens and then superimposed with a collimated reference laser beam of the same frequency. The resulting interference pattern is recorded by a digital camera sensor. A fast Fourier transform (FFT) of the recorded interference pattern $I_{\mathrm{D}}(x, y)$ yields a site-resolved image of the atomic distribution in the lattice. The role of the reference beam is to amplify the weak atomic signals and to shift the information on the atomic distributions in the hologram to the FFT positions where technical background noise is small. Our calculations predicted that this holographic imaging is better than 99% error-free already for about 200 scattered photons per atom. Therefore, as a rough estimate, for a lattice which is deeper than a few times 200 photon recoil energies, holographic imaging might work without additional cooling. For example, for ^{6}Li where the recoil energy is 3.5 $\mu\mathrm{K}\times k_B$ for the resonant wavelength of 671 nm, a trap depth of about 2 $\mathrm{mK}\times k_B$ should be sufficient to keep the atoms trapped in their respective lattice sites. Here, k_B is the Boltzmann constant.

In this work, we take a first experimental step to test our proposed holographic detection scheme. For this, we replace the atomic scatterers by an array of circular submicron-sized holes in an opaque flat mask, see Fig. 8.2. The mask

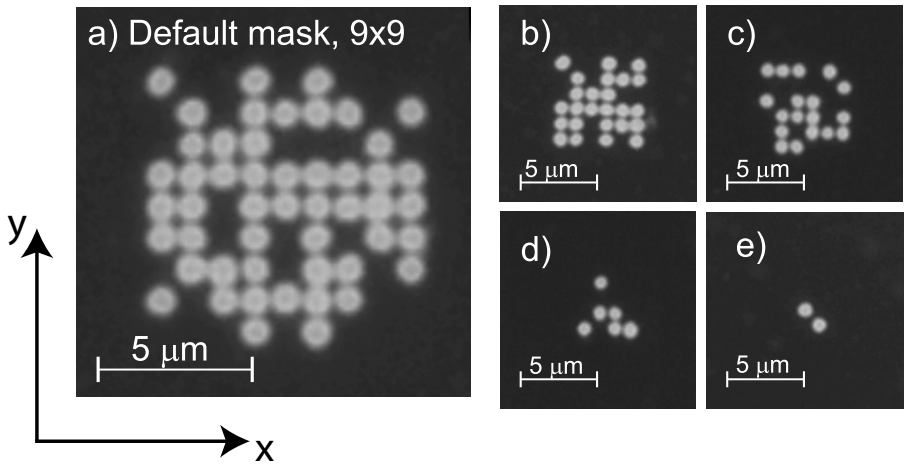

FIGURE 8.2: Pictures of various hole masks taken with an optical microscope. Each hole is circular and has a radius of $0.3 \pm 0.03\,\mu$m. For each mask, the holes are positioned on a 9×9 square lattice with a lattice constant of $1\,\mu$m. The hole pattern within each mask is arbitrary.

is homogeneously back-illuminated with laser light which is diffracted when passing through the holes. The holes are randomly arranged in a square lattice with 1μm lattice constant, similar to the distribution of real atoms in a partially occupied 2D optical lattice [1]. Clearly, this setup is much simpler than working with an array of cold atoms, yet it offers all necessary ingredients for the scheme.

Besides experimentally demonstrating holographic imaging, we measure the fidelity of reconstructing the hole positions of the known mask. We study how this recognition fidelity depends on various parameters such as the scattered photon number, the reference laser power and the incidence angle of the reference laser. We discuss various noise sources and resolution limits and we investigate how to optimize the setup given these limits. We find that about 200 diffracted photons per hole are sufficient to reconstruct the hole positions in the masks with a fidelity of 96%.

8.3 Results

8.3.1 Experimental setup

The hole masks were fabricated in the cleanroom of the Microelectronics Technology Center, University of Ulm, via e-beam lithography. Details of the fabrication can be found in Appendix 8.5.1.

A scheme of the holography setup is depicted in Fig. 8.3. It resembles the one for digital holographic microscopy which is based on a Mach-Zehnder interferometer [195, 196]. The beam of a laser with wavelength $\lambda = 671$ nm and

[1] We note that many optical lattice set-ups in the literature exhibit lattice constants of about 500 nm. Performing holography with a smaller lattice constant as compared to ours requires an optical lens with a correspondingly larger NA than ours.

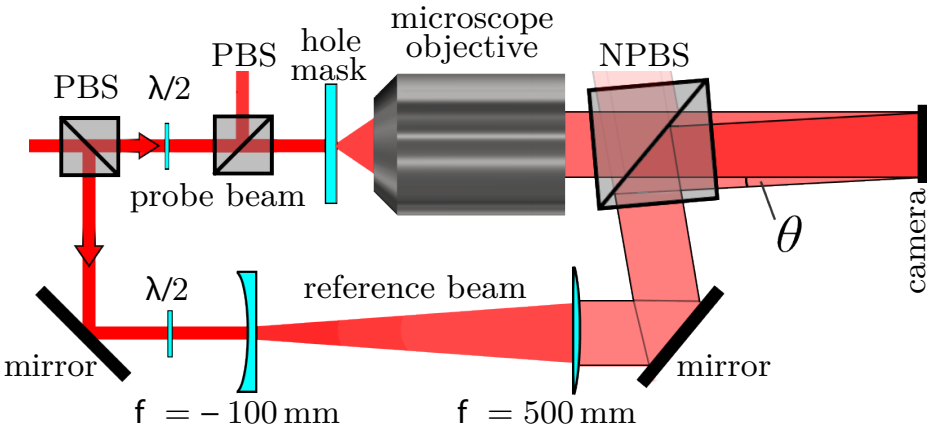

FIGURE 8.3: Scheme of the experimental setup. The 671 nm laser beam (red color) is split by a PBS into a probe beam (upper path) and a reference beam (lower path). A $\lambda/2$ plate and PBS control the intensity of the probe beam which illuminates the hole mask. The diffracted light is collected by an infinity-corrected microscope objective lens and hits the sensor of a digital camera as a collimated beam. A tilted NPBS is used to superimpose this probe beam light with the collimated reference beam. The resulting interference pattern is recorded by the camera sensor.

≈ 1 MHz linewidth is split by a polarizing beam splitter (PBS) into a probe beam and a reference beam. The probe beam is attenuated by the combination of a $\lambda/2$ plate and a second PBS. It is diffracted at the hole mask and the diffracted light is collected by an infinity-corrected microscope objective with numerical aperture (NA) between 0.5 and 0.75, (e.g. Zeiss Epiplan Neofluar 50x, 0.75 HD Dic, 44 23 55 with an effective focal length of about $f = 4$ mm). The distance between the back side of the objective lens and the sensor is 16 cm. Since the distance between mask and objective equals the focal length f, light scattered from a hole in the mask is collimated by the lens and subsequently propagates as a plane wave with a beam diameter of about 5 mm towards the camera. The diffracted probe beam and the reference beam are merged at a tilted non-polarizing beam splitter (NPBS) such that they overlap well at the camera in the detection plane. While the diffracted probe beam hits the camera approximately under vertical incidence, the reference beam has a small tilt angle $\theta \approx 1°$. The reference beam is roughly Gaussian with a waist of 5.3 mm and a power of 120 μW behind the NPBS. A cross section of the beam profile is shown in Fig. 8.4, labelled as I_R. The beam illuminates the CMOS sensor chip (13.3 mm $\times$ 13.3 mm) of the digital camera pco.edge 4.2LT which has 2048$\times$2048 pixels. Further details on the camera can be found in appendix 8.5.2. We verified that measurements with a broader and thus more uniform reference beam profile did not produce a higher recognition fidelity. The exposure time t_{exp} was typically 144 μs and the intensity of the reference beam was set such that the linear detection range of the camera sensor was optimally used while avoiding saturation. This intensity corresponds to a peak photon number per pixel of about 40,000. In the following, we show how the hole pattern of the mask is reconstructed via FFT from the

holographic image taken by the digital camera.

8.3.2 Reconstruction of the hole pattern of the mask

The light intensity distribution $I_{\mathrm{D}}(x, y)$ in the sensor plane of the digital camera is given by

$$\begin{aligned} I_{\mathrm{D}}(x,y) &= \frac{c\epsilon_0}{2}\left|E_{\mathrm{S}}(x,y)+E_{\mathrm{R}}(x,y)\right|^2 \\ &= \frac{c\epsilon_0}{2}(|E_{\mathrm{S}}|^2+|E_{\mathrm{R}}|^2)+c\epsilon_0\, Re\{E_{\mathrm{S}}E_{\mathrm{R}}^*\}, \end{aligned} \tag{8.1}$$

where E_{S} and E_{R} are the electric fields (in complex notation) of the diffracted and reference beams in the detection plane, respectively. c is the speed of light in vacuum and ϵ_0 is the permittivity of free space. In the limit of a very weak scattered light field we can neglect the term $|E_{\mathrm{S}}|^2$. Ideally, the term $|E_{\mathrm{R}}|^2$ is just a constant. The information about the hole pattern is contained in the third term, the interference term.

For simplicity, we first consider a single hole n in the mask at position $\mathbf{r}_n = (x_n, y_n)$ which emits a scattered, spherical light wave. The lens at the focal distance f collimates the wave into a plane wave with the wavevector component $\mathbf{k}_n$ in (x, y) direction,

$$\mathbf{k}_n = \frac{k}{\sqrt{x_n^2+y_n^2+f^2}}\begin{pmatrix} -x_n \\ -y_n \end{pmatrix} \approx -\frac{k}{f}\mathbf{r}_n, \tag{8.2}$$

where $k = 2\pi/\lambda$ is the wavenumber of the light. The origin of the coordinate system is located on the optical axis of the microscope lens. The approximation in Eq. (8.2) is valid for holes close to the optical axis, i.e. $x_n, y_n \ll f$. At the camera sensor, this plane wave interferes with the plane wave of the reference beam with wavevector $\mathbf{k}_R$, leading to a 2D sinusoidal fringe pattern $\propto \cos((\mathbf{k}_n - \mathbf{k}_R)\cdot\mathbf{r} + \varphi)$. Here, $\mathbf{r} = (x, y)$ is the position vector in the sensor plane of the camera and φ is a constant phase. The FFT of this pattern produces an output that only contains two single peaks at $\pm(\mathbf{k}_n - \mathbf{k}_R)$, corresponding to opposite momenta. After subtraction of the constant vector $\mathbf{k}_R$ we obtain $\mathbf{k}_n$ which, according to Eq. (8.2), corresponds to the hole position $\mathbf{r_n}$, apart from a factor $-k/f$. The constant vector $\mathbf{k}_R$ depends on the incidence angle of the reference beam with respect to the detection plane. In spherical coordinates we have

$$\mathbf{k}_R = k\begin{pmatrix} \sin\theta\cos\phi \\ \sin\theta\sin\phi \end{pmatrix}, \tag{8.3}$$

where θ and ϕ are the polar and azimuthal angles of the reference beam, respectively.

If there is more than one hole in the mask, each hole contributes a corresponding sinusoidal pattern. All these patterns add up linearly under the condition that the reference beam has much higher intensity than the scattered probe beam. Since the FFT is a linear operation it reproduces the hole pattern of the mask.

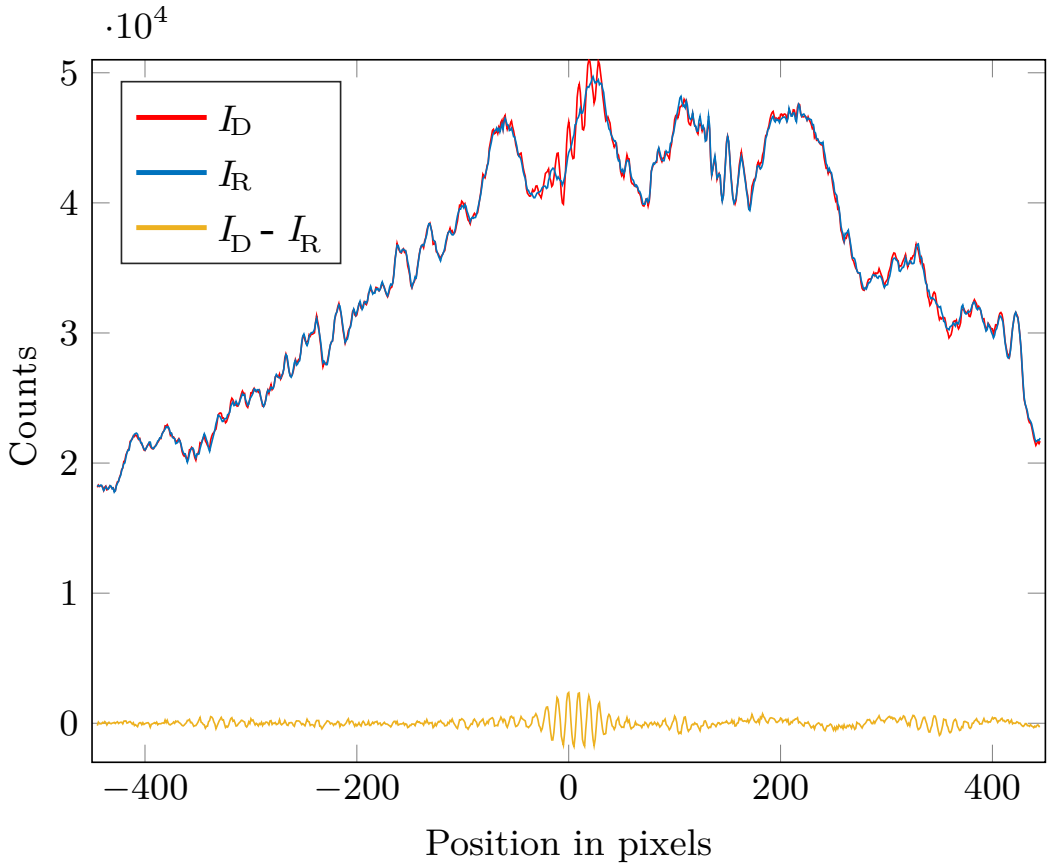

FIGURE 8.4: Line profiles of the digital images of the hologram $I_D(x, y)$ and the reference beam $I_R(x, y) = c\epsilon_0|E_R|^2/2$, as well as their difference $I_D - I_R$. Here, x and y are positions in units of pixels. The profiles are taken along the x-direction around the y-center (i.e. $y = 0$) of the image. In order to reduce noise we have averaged over 11 pixel rows, for details see[2]

In practice, the $|E_\mathrm{R}|^2$ term in Eq. (8.1) is not just a constant, but it exhibits corrugations e.g. due to diffraction from dust on top of optical surfaces. This hampers the reproduction of the hole pattern. We find that most of these perturbations can be removed by subtracting an image I_R taken with only the reference beam by blocking the probe beam ($E_\mathrm{S} = 0$) and averaging over 30 recordings to reduce noise. Figure 8.4 shows line profiles of the hologram before (red) and after the I_R-subtraction (yellow). The blue line is the profile of the reference signal. The line profiles run along the x-direction through the y-center of the hologram.

[2]In order *not* to average out the interference fringes between probe beam and reference beam, the averaging is done in a diagonal fashion. This is because the interference fringes for the given hologram are at an angle of 45° (see also Fig. 8.5a), as set by the chosen angle θ of the reference beam. Concretely, the diagonal averaging is calculated as $\sum_{i=-5}^{5} I_{D,R}(x+i, +i)/11$ over 11 pixel rows.

Fig. 8.5a) depicts a hologram after I_R-subtraction, along with a magnified section. For this, the default mask shown in Fig. 2a) and an objective with a NA of 0.75 was used. The angles of the reference beam were $\theta = 0.84°$, $\phi = 45°$ [3] and about 40,000 photons were transmitted through each hole of the mask. We only show the section of the hologram that contains the relevant features. It exhibits five dominant spots, arranged in a cross-like fashion, with weaker signals in between.

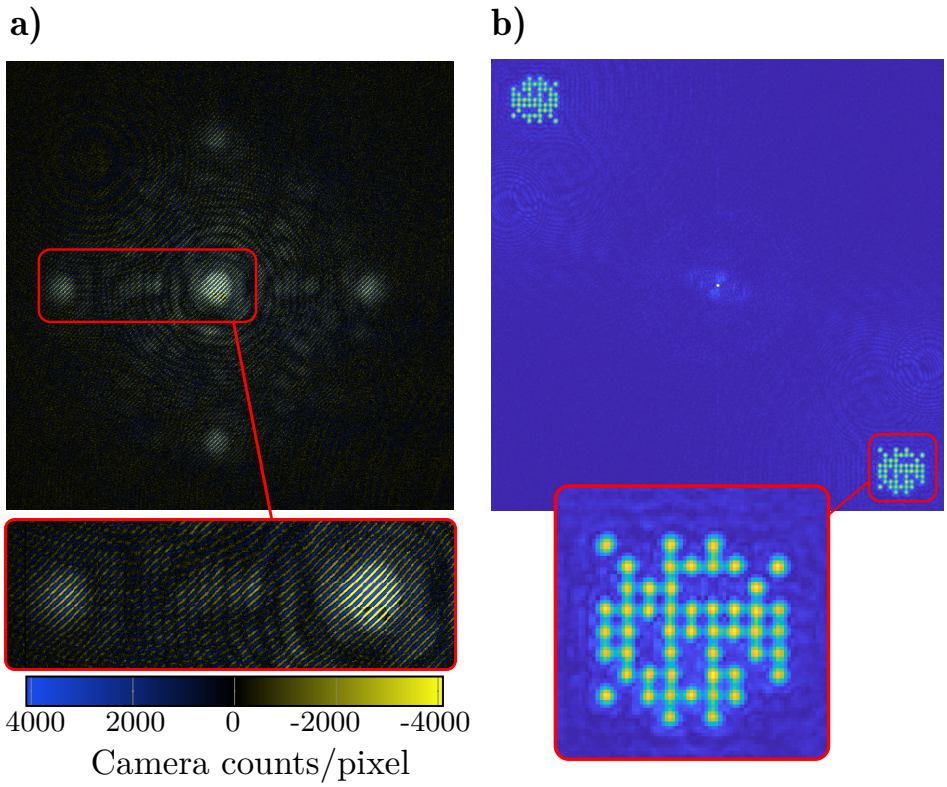

FIGURE 8.5: a) Section of the recorded hologram $I_D - I_R$. For this recording, each hole of the mask scattered roughly 40,000 photons. The panel below is a magnification. The color bar gives the number of counts per pixel. This count number can be negative as we are dealing with a difference of two images. b) Section of the FFT of the hologram with a magnified view of the reconstructed hole pattern of the mask.

The origin of the five dominant interference peaks can be understood as follows. To a first approximation, the holes in the mask form a 2D square lattice. The far-field diffraction pattern of a 2D square lattice is again a square lattice. The spot in the center of the hologram is the zeroth-order diffraction peak of this square lattice, while the surrounding spots are first-order peaks. The array of holes in the mask, however, is not a perfect square lattice since a number of lattice sites are not occupied. As a consequence, the intensity in between the major diffraction peaks is non-zero and this is most relevant for the reconstruction of the hole positions. The hologram is modulated with high spatial frequency by

[3] We choose $\theta = 45°$ in the experiment because this has technical advantages. For one, diagonal pixel lines have a distance which is reduced by a factor of $\sqrt{2}$ as compared to the horizontal and vertical pixel lines. This increases the spatial resolution for measuring fringes.

a sinusoidal wave at an angle $\phi = 45°$. This oscillatory pattern is due to the interference of the reference beam with the scattered probe beam. In the FFT it leads to a diagonal shift of the reconstructed hole pattern of the mask from the center, see Fig. 8.5b). Mathematically this shift is equivalent to the shift of the vectors $\mathbf{k}_n$ by $\mathbf{k}_R$, as previously discussed in the paragraph following Eq. (8.2). As a result, the reconstructed hole pattern after the FFT is located in the upper left and lower right corners. The two patterns are inverted with respect to each other, as they correspond to opposite momenta $\pm(\mathbf{k}_n - \mathbf{k}_R)$.
The shift of the reconstructed pattern is advantageous because it reduces noise. Without the shift, both patterns would be located in the center where they would overlap with each other, with the noisy signal from the reference beam, and with the $|E_S|^2$ term in Eq. (8.1). We find that a shift in diagonal direction is helpful because there the noise background is particularly small[4].
The FFT in Fig. 8.5b) clearly reproduces the hole pattern of mask a) in Fig. 8.2, which shows that the holographic imaging scheme works.

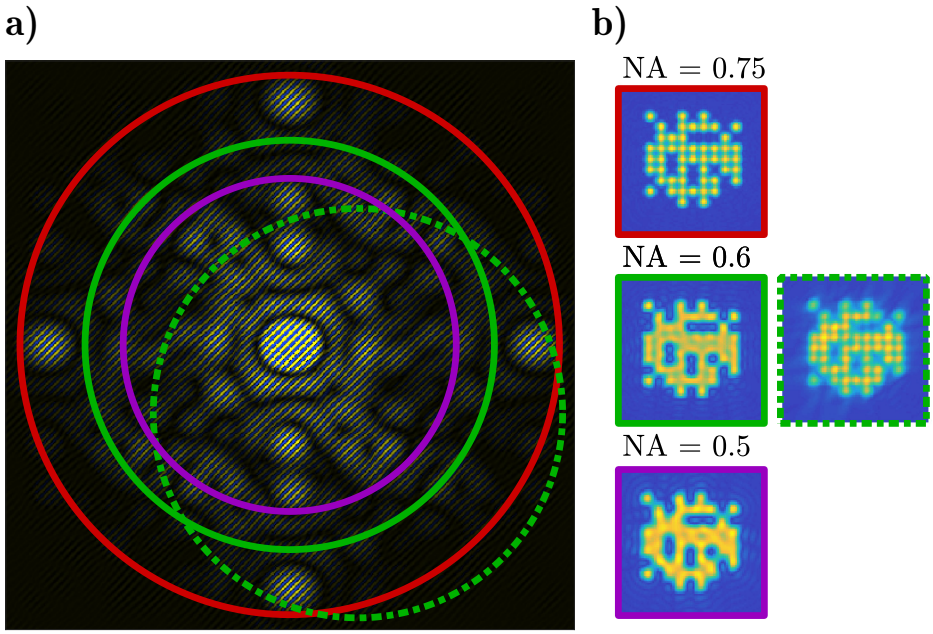

FIGURE 8.6: a) The circles drawn on the calculated diffraction pattern represent various numerical apertures: NA = 0.5 (purple), NA = 0.6 (green), and NA = 0.75 (red). For a given NA, only the pattern inside the circle ends up on the camera sensor. Continuous lines correspond to a hole mask that is centered on the optical axis of the lens, while for the green dashed line it is off-center. b) The relevant sections of the corresponding Fourier transforms are shown.

[4]The angle of $\theta = 45°$ shifts the holographic signal away from spurious horizontal and vertical lines running through the center of the hologram. These lines stem from clipping of the reference beam at the edges of the camera chip. Figure 8.5b) shows such line which is weak and runs vertically through the center of the hologram.

8.3.3 Numerical aperture

According to Abbe's theory of imaging, the first order diffraction peaks of a lattice need to be recorded in order to clearly resolve the individual lattice sites. Therefore, the numerical aperture (NA) of the microscope objective needs to be large enough. Figure 8.6 shows a calculated hologram for our default hole mask from Fig. 2a). If the hole mask is centered on the optical axis, the NA of the objective can be represented by a circle in $\vec{k}$ momentum space. In Fig. 8.6a) such circles are drawn for NA = 0.5, 0.6, and 0.75. The relevant sections of the FFTs of the inner parts of the circles are displayed in Fig. 8.6b). The sharpness of the hole pattern increases with increasing NA.

When the mask is centered on the aperture of the objective with NA = 0.6 (green solid line), none of the first-order peaks are caught. By shifting the mask diagonally, however, one can include two first-order peaks while still retaining the central area which includes most of the hologram's information (green dashed line). (We note that for a small displacement of the mask, the solid angle at which light is collected by the objective decreases only minimally and the resulting ellipse can be still approximated by a circle.) This inclusion of the first-order peaks can help to better resolve individual lattice sites. However, because the positions of the sites of the regular lattice are known, the hole pattern can still be clearly determined even for the centered case and low NA.

8.3.4 Photon shot noise

We now investigate how the reconstruction quality of the hole pattern decreases as the probe light power is lowered. From Eq. (8.1) it is clear that the holographic signal scales with the electrical field amplitude of the diffracted laser beam E_S and therefore with the square root of the number of scattered photons per hole. The noise, on the other hand, is fundamentally dominated by the shot noise of the light of the reference beam, corresponding to the $|E_R|^2$ term in Eq. (8.1).

As a consequence, for a fixed value of the reference beam power, signal to noise diminishes for a lower probe beam power, or in other words, for a smaller number of scattered probe beam photons N_{ph} per mask hole. We find that once N_{ph} is reduced to below about 500, the signal to noise ratio is so weak that a simple determination by eye of the hole pattern is no longer possible. Fig. 8.7a) shows the FFT image for an extreme case where the average photon number per hole was only about 100. With the following algorithm we can still decide with high fidelity whether a lattice site is occupied or empty. For this, we make use of the known positions of the lattice sites in the Fourier plane. A black pixelmask consisting of a 2D array of circular slots (see Fig. 8.7b)) is overlaid with the FFT image such that the midpoints of the slots coincide with the positions of the lattice sites. Within each slot the FFT signal is added up, yielding a value S_n where the index n labels the respective slot, see Fig. 8.7c). If the value S_n of a lattice site is larger than an appropriate threshold value, $S_n > S_{\mathrm{thr}}$, the site is declared to be occupied, otherwise empty. The threshold value S_{thr} needs to be

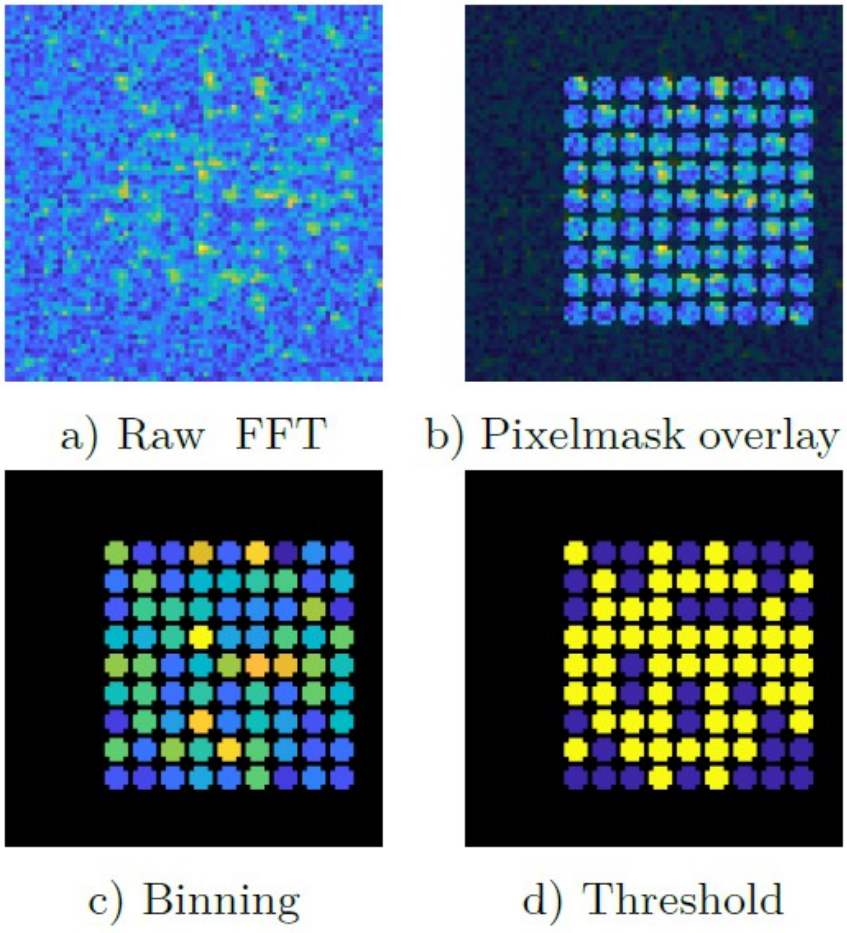

FIGURE 8.7: Reconstruction of the mask for $N_{ph} = 100$ photons per hole. a) Region of interest in the FFT. b) Processing via overlaying of a digital template. c) Binning of the pixels assigned to each lattice site. d) Subsequent application of a threshold to distinguish between occupied and empty sites. For simplicity we chose here an experimental sample for which the hole pattern was correctly reproduced. For 100 photons we typically only assign 90% of the holes correctly, see Fig. 8.8.

determined independently, e.g. by using a known hole pattern or by another statistical method[5].

With this discrimination method, the assignment of the occupation of the lattice site becomes a probabilistic process. We define the recognition fidelity F as the probability that the assignment for the lattice site is correct.

Figure 8.8 shows this fidelity F as a function of N_{ph} for the hole masks in Figs. 8.2 a) - e). Experimental data are shown as circles. From the diagram we infer that 300 diffracted photons per hole are sufficient to obtain a nearly perfect reconstruction of the hole arrays.

[5]For a variety of lattice sites many measurements of the occupation signals are taken and a histogram of the occupation signals is generated. Ideally, the histogram will exhibit two peaks, corresponding to an empty and occupied site. The minimum between the two peaks can then be used to set the threshold value S_{thr}, see also [50].

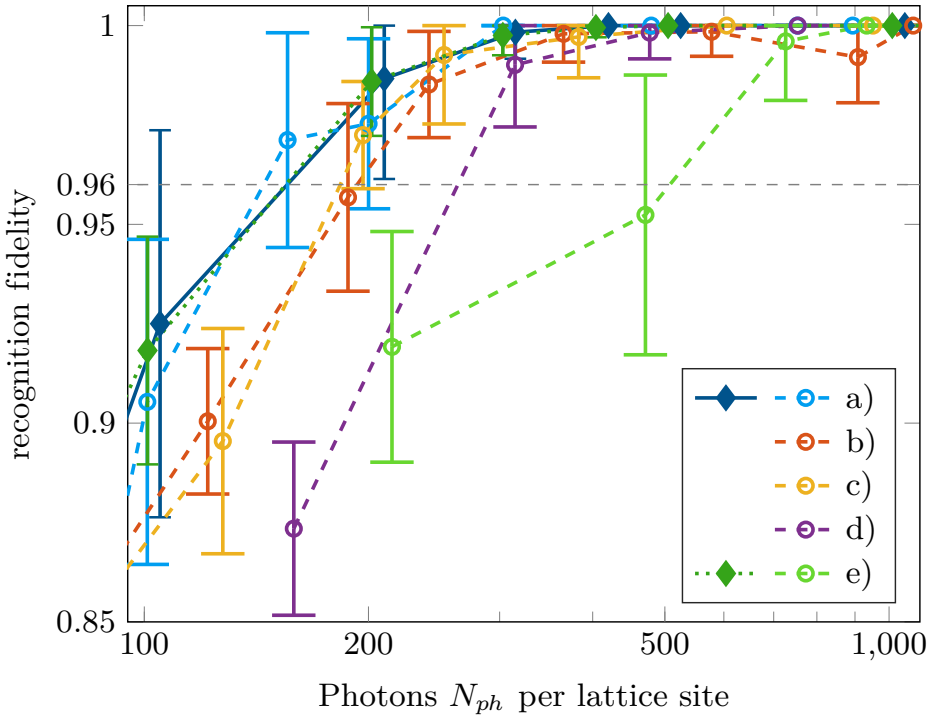

FIGURE 8.8: Recognition fidelity F for different masks (see Fig. 8.2) and photon numbers per hole. Circles are experimental data. The settings for the measurements were NA = 0.75, $\theta = 0.64°$, and $t_{exp} = 144\,\mu$s. For each experimental data point we took ∼14 images and determined the fidelity for each image. From this list of values the mean value and standard deviation were obtained. Diamonds are simulations which have been rescaled for better comparison with the experimental data. Namely, for a given calculated data point the actual photon number N_{ph} is 10 times smaller than indicated in the plot. For the simulations we use over 50 images per data point. Each image has a different (random) photon shot noise. The 96% fidelity benchmark, which we chose arbitrarily, is represented by the black dashed line.

By lowering the probe beam intensity, the signal-to-noise ratio degrades and finally, below $N_{ph} \approx 300$, the fidelity F starts to decline. The characteristics of the decline is similar for all masks under study.

In addition to measuring experimental fidelities, we also calculated them, using simulations as layed out in the Appendix 8.5.3. While the calculations confirm the trend that the fidelity suddenly drops below a critical photon number, the absolute agreement with the experiment is not good. For a given fidelity the calculated required photon number N_{ph} is about a factor of 10 smaller than for the experiment. In order to conveniently compare the trends of experiment and theory in Fig. 8.8 we have rescaled the theoretical N_{ph} values, multiplying them by 10. These data are shown as diamonds. At this point it is not clear what the reason for the discrepancy between theory and experiment is. Possibly wavefront distortions of the light passing through optical lenses might play a role. This will be subject of future work.

In the following we investigate in how far the onset of the decline depends on

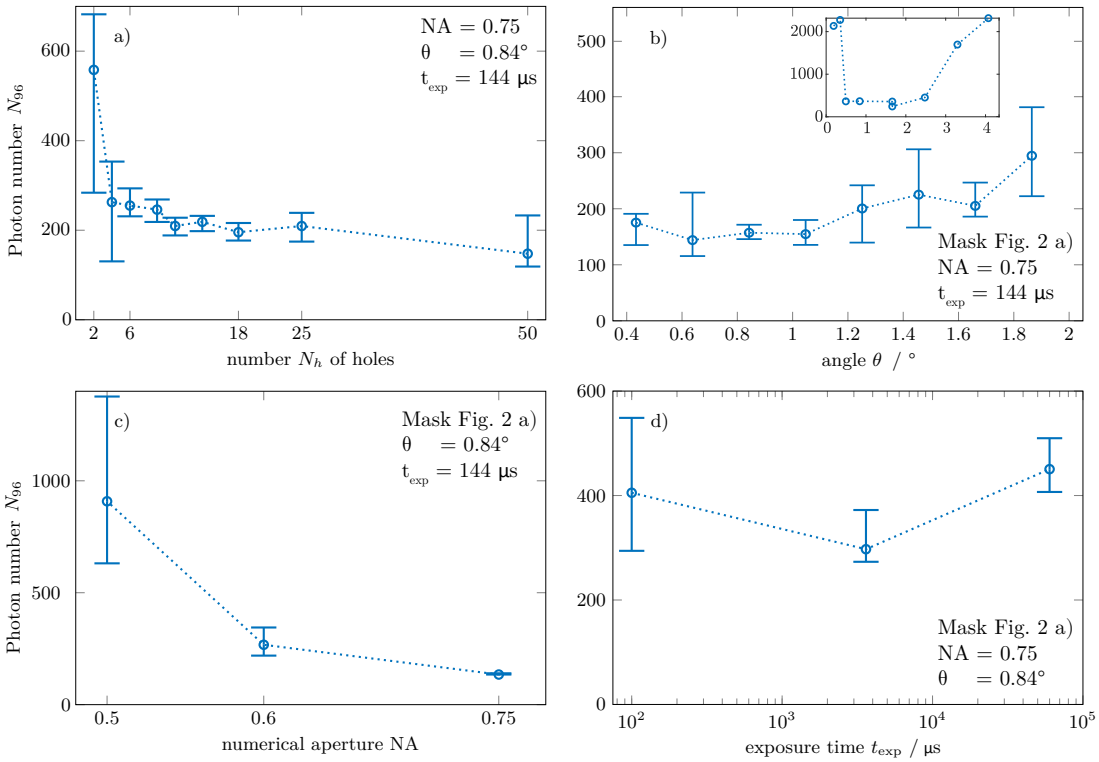

FIGURE 8.9: Required photon number N_{96} per hole for 96% recognition fidelity, plotted as a function of a) the number of holes in the mask, b) the angle θ between reference beam and z-axis (see Fig. 8.1), c) the numerical aperture NA of the microscope lens, and d) the camera exposure time (for constant total photon number). N_{96} and the corresponding error bars are derived from an interpolation, see Fig. 8.8.

certain parameters of the set-up. This will provide us with the minimal number of photons that need to be scattered per hole to still achieve a high fidelity in the reconstruction of the hole pattern.

8.3.5 Minimal photon number

In order to quantify the onset of the decline in fidelity, we introduce the quantity N_{96} which is the required number of photons per hole to achieve a fidelity of 96%. It can be extracted from Fig. 8.8 by reading off the photon number N_{ph} for which the data interpolations (colored lines) cross the 96% fidelity line (gray dashed line).

In Figs. 8.9 a)- d), N_{96} is plotted as a function of four parameters.

Figure 8.9 a) shows N_{96} as a function of the number of holes N_h in a mask. A first glance at the measured data seems to indicate a decrease of N_{96} with N_h. However, we note that given the error bars this decrease is statistically not significant.

Figure 8.9 b) shows that N_{96} only moderately depends on the angle θ between the reference beam and the z-axis within the range $0.4° < \theta < 2°$. As already discussed in section 8.3.2, an angle θ that is too small leads to a reconstructed hole pattern which is overshadowed by noise in the vicinity of the center of the

FFT. For a θ that is too large, the fringes in the hologram are too closely spaced and therefore cannot be resolved by the camera sensor. Using the Nyquist-Shannon sampling theorem we estimate that this limit sets in at a critical angle of $\theta = 4^\circ$ for our experimental set-up. Therefore, if we reach angles that are either too small or too large, the experimentally determined numbers for N_{96} strongly increase. This can be seen in the inset where we show a coarse scan from $\theta = 0.2^\circ$ to 4°. For optimized settings in our experiment we chose the angle $\theta = 0.7^\circ$.

With Fig. 8.9 c) we return to our discussion in Sec. 8.3.3 on how the reconstruction quality of the hole pattern depends on the numerical aperture NA of the objective lens. For these data, the mask was centered on the optical axis of the microscope lens. We plot N_{96} for NA = 0.75, 0.6, and 0.5. The first order peaks in the hologram are only included for NA = 0.75 (see also Fig. 8.6). The experimental data show that N_{96} strongly increases as the NA is lowered. This is in contradiction to our simulations in Fig. 8.6b) where we found that that despite the blurring the the overall signal of a site did not strongly change.

Finally, in Fig. 8.9 d) we study the dependence of N_{96} on the exposure time of the digital camera. Here, the light intensity is adjusted such that the total numbers of photons from the probe and reference beams hitting the camera are kept constant. We do not observe a significant dependence on exposure time for the shown time window. This is expected as long as, e.g., mirror vibrations and long-term interferometric drifts, as well as accumulated thermal camera noise do not strongly affect the hologram.

8.4 Summary and conclusion

We have successfully tested a recently proposed holographic method for imaging μm-scale patterns which are arranged on a 2D grid. Such patterns consist of a random array of submicron holes in an opaque mask. We experimentally and theoretically searched for the minimum number of photons that need to be scattered off the pattern in order to reconstruct the pattern holographically with high fidelity. After optimization, we found experimentally that about 200 diffracted photons per hole are sufficient to reconstruct the hole positions in the masks with a fidelity of 96%. Our simulations predict that this number can still be improved by about a factor of 10. In the future we anticipate that this method can be applied to image ultracold atoms in optical lattices with single-site and single-atom resolution, without the need of additional cooling.

8.5 Supplementary information

8.5.1 Fabrication of the hole mask

Circular areas were exposed by means of a Leica EBPG 5 HR electron beam writer applied on fused silica photo mask blanks. The mask blanks (size: $100\times100\,\mathrm{mm}^2$, thickness: 2.3 mm) were coated with chrome (thickness: 90 nm, optical density: 3.0) and a positive e-beam resist. After e-beam exposition and

developing the round holes were produced by wet chemical etching. The finished structures were controlled by means of optical microscopy. Atomic force microscopy revealed a typical hole radius of 300±30 nm. After fabrication the masks were protected with the polymer Crystalbond$^{\mathrm{TM}}$ and cut into square pieces ($\approx 25 \times 25\,\mathrm{mm}^2$).

8.5.2 Properties of the digital camera

The CMOS sensor of the pco.edge 4.2LT camera has a pixel size of 6.5 μm × 6.5 μm. It has a digital resolution of 16 bit, 37,500:1 dynamic range, and 73% quantum efficiency at 671 nm. The full well depth is about 30,000 electrons. Therefore, the signal saturates at about 40,000 photons/pixel. There is a signal conversion of 0.46 e^-/count. Dark current is negligible for our experiments. A short exposure without light has a constant offset of 100.3 ± 0.6 counts and the corresponding rms-noise is 2.2 counts. The nominal readout noise is 1.3 e^- (rms) which agrees roughly with the 2.2 count noise. The noise of our holographic signals is generally dominated by the photon shot noise. According to the Poisson distribution, if the average number of incoming photons is N, then the shot noise on that number is $\sqrt{N}$ (standard deviation). Since the conversion of photons into electrons is probabilistic with probability $p = 0.73$, the Poisson distribution for the photons is thinned out to produce a Poisson distribution for the electrons with an expectation value (and variance) of Np, i.e. a shot noise of $\sqrt{Np}$.

8.5.3 Details of the simulation

In the simulation shown in figure 8.8 the hole mask is represented by a matrix of square pixels, each with 160 nm × 160 nm size. A pixel which is located within a hole has a transmission of 1. A pixel which is located on the edge of a hole has a transmission lower than one, as only a part of pixel area is covered by the hole aperture. We assume the holes to be illuminated by a Gaussian probe laser field. We calculate the FFT of the electrical field amplitude of the transmitted light and clip off parts which lie outside the numerical aperture of the lens. This results in the electrical field amplitude of the probe laser at the plane of the CCD sensor. This field is superposed with the electrical field amplitude of the Gaussian beam of the reference laser. We take into account signal loss due to the finite quantum efficiency of the camera, the finite transmission of the NPBS, and reflections on optical surfaces. Next, we calculate the expectation value of the photon count for each pixel on the CCD chip and add photon shot noise. Photon shot noise strongly dominates over other noise sources such as the read-out and thermal noise of the CMOS camera and speckle noise. Speckle noise takes into account interference fringes originating from dust particles on the optics and from apertures and we use a speckle noise model as described in [50].

8.5.4 (*) Effects of the hole size and the obliquity factor

In the simulations presented above, the diffraction patterns were calculated in the far-field approximation, which facilitates the employment of the Fast

Fourier Transform. This was computationally done using MATLAB's FFT2 function, which calculates the two-dimensional fast Fourier transform of the input matrix, i.e. the hole mask. However, the FFT2 function does not account for physical constraints, such as the diffraction limits. Specifically, nowhere in the calculation of the Fourier transform, the ratio between wavelength and hole size is employed. This means, that in the FFT calculated by MATLAB, also orders appear which are physically not possible, i.e. orders n where $n\lambda$ is larger than the lattice constant a. In our case where $\lambda = 671\,\text{nm}$ and $a = 1\,\mu\text{m}$, the ratio a/λ is 1.49, such that already the 2$^{\text{nd}}$ diffraction orders do not appear. In the simulation, this is partially corrected by subsequently cutting the calculated diffraction pattern such that only the part landing in the NA is considered. This is illustrated in Figure 8.10.

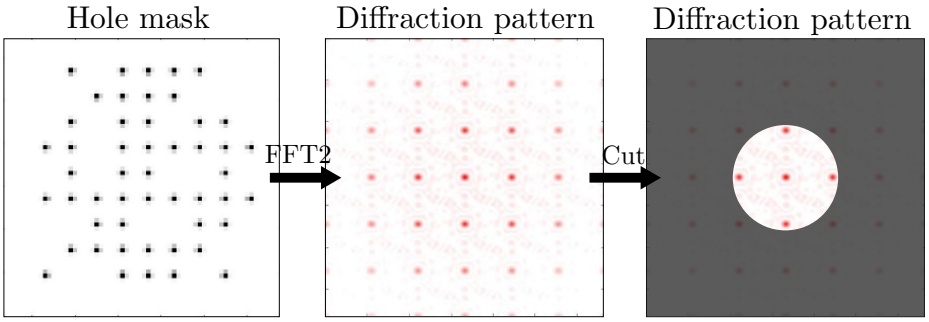

FIGURE 8.10: Calculation of the diffraction pattern of a hole mask using the FFT2 function of MATLAB. Diffraction orders which are non-physical are computationally cut out by the limited field of view of the numerical aperture, see also Figure 8.6.

The simplification however still neglects the obliquity factor $\frac{1+\cos(\theta)}{2}$, which appears in the Kirchhoff diffraction formula (see below) as derived in [197]. This factor enhances diffraction towards the zeroth order ($\Theta = 0$) and weakens diffraction at higher angles ($\Theta > 0$).

To address these issues, we conducted additional calculations using Kirchhoff's diffraction formula. For an incident plane wave parallel to the surface of the hole mask, the amplitude of the electric field behind the hole mask at coordinates (x, y, z) is given by [197]

$$E_{\text{D}}(x, y, z) = \frac{a_S}{\lambda i} \int_{\text{mask}} \text{d}S f_S \frac{e^{i2\pi d/\lambda}}{d} \frac{1 + \cos(\theta)}{2} \tag{8.4}$$

where $d = \sqrt{(x_n - x)^2 + (y_n - y)^2 + z^2}$ and $(x_n, y_n, 0)$ are the coordinates at the position of the mask. The angle Θ is the angle between the surface normal of the mask/the plane wave and the direction where the diffraction pattern is observed. The quantity a_S is the amplitude of the plane wave, λ its wavelength and f_S is the aperture function of the hole mask. It is 1 at the position of a hole and 0, otherwise. The scenario is illustrated in Figure 8.11.

The general shape of the diffraction pattern in the far field is of course not affected by the more precise calculation according to the Kirchhoff diffraction

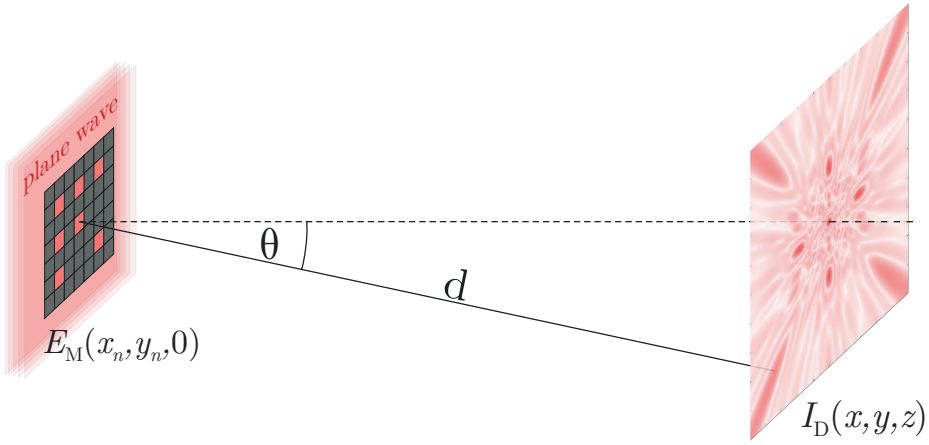

FIGURE 8.11: Diffraction pattern of a hole mask illuminated by a plane wave. $E_{\mathrm{M}}(x_n, y_n, 0)$ is the electric field of the plane wave at the position of the hole mask. The corresponding intensity $I_{\mathrm{D}}(x, y, z)$ at a screen separated by a distance z from the mask can be calculated using Kirchhoff's diffraction formula given by Equation (8.4).

integral. However, the approach yields a more accurate representation of the intensity distribution within the diffraction pattern.

Hole size

We first calculated the fraction of photons landing within the numerical aperture (NA) as a function of hole size. Notably, for an increasing hole size, the lower diffraction orders become more pronounced and a larger fraction of the incoming photons is captured by the numerical aperture of the objective and thus contributes to the reconstruction of the image. The reason is, that the diffraction pattern is given by the convolution of a single hole of finite size and a point-like hole grid. For an increasing hole size, diffraction towards the zero order is enhanced (just as in the diffraction at a single slit). In the limit of the hole size going to zero (which represents the case of single point-like atoms as scatterers), the number of photons should theoretically distribute equally amongst all diffraction orders. In this case, still around 50% of the total number of photons behind the mask are captured by the numerical aperture. The reason is, that due to the diffraction limit of the hole mask, the second orders do not exist at all, as $2\lambda > a$. At the same time, the numerical aperture of $\mathrm{NA} = 0.75$ fully captures the $(1, 0)$ and $(0, 1)$ order peaks (first order horizontally and vertically) and also partially the $(1, 1)$ (first orders diagonally) order peaks. As the second orders do not exist, these five orders include almost all diffracted photons. For a hold radius of $450\,\mu\mathrm{m}$, the diffraction towards the zero order peak is even more pronounced. As a consequence, over 99% of the diffracted photons are captured by the objective with $\mathrm{NA} = 0.75$. This is specified quantitatively in Table 8.1 and shown qualitatively in Figure 8.12.

With our simulations, we find that for the hole pattern shown in Figure 8.2 a) and a hole size of $400\,\mathrm{nm}$, 14 photons per hole should be sufficient to reach a

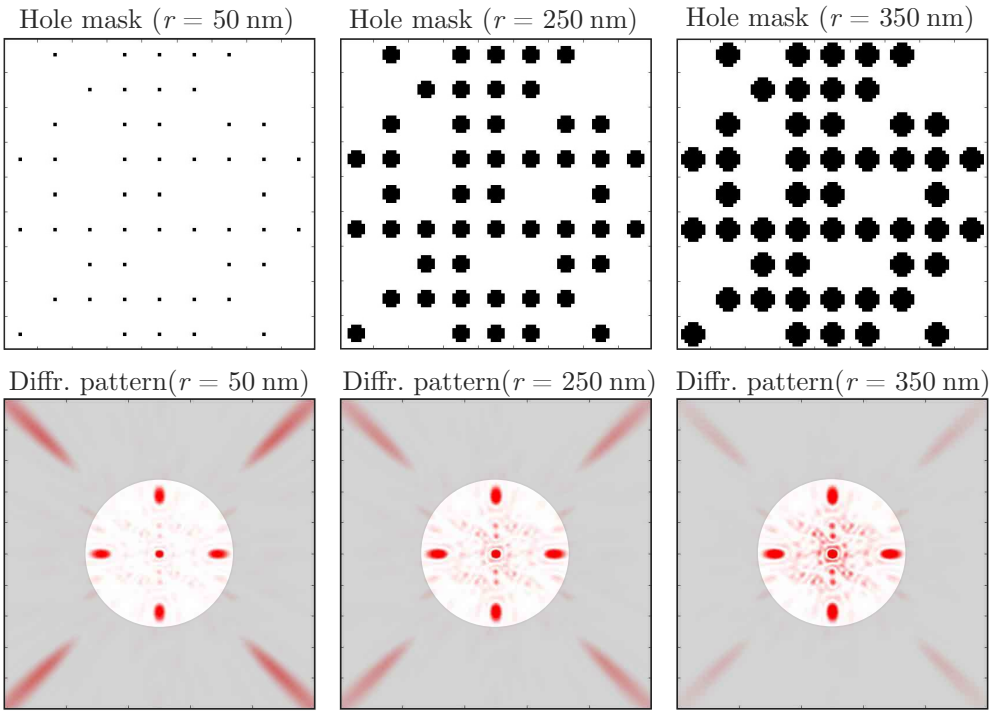

FIGURE 8.12: Intensity distributions (lower panels) of the diffraction pattern for hole masks with different hole sizes (upper panels). The regions of the diffraction pattern which do not fall into the field of view of the numerical aperture, centered around the zeroth order peak, are greyed out. For increasing hole size, more photons are captured by the numerical aperture, as the intensity of the diffraction pattern is more concentrated towards the zeroth order. Note that the intensity pattern is warped towards the outside, as the calculation maps the pattern onto a planar screen, as illustrated in Figure 8.11.

TABLE 8.1: Number of photons N_{96} to reach a recognition fidelity of 96% for the mask shown in Figure 8.2 a) calculated for different hole sizes. Also listed is the fraction of photons, that is captured by the numerical aperture of the objective.

Hole radius	N_{96} per hole	N_{96} total	N_{96} in NA	% in NA
50 nm	40	1960	969	49.4
75 nm	39	1911	952	49.8
100 nm	37	1813	954	52.6
150 nm	28	1372	846	61.7
200 nm	23	1127	800	71.0
250 nm	20	980	792	80.8
300 nm	16	784	702	89.5
350 nm	15	735	706	96.1
400 nm	14	686	683	99.6

recognition fidelity of 96%. As the utilized hole mask has 49 holes, this equals a total number of 686 photons, from which 683 photons land within the NA. For a hole radius of 50 nm $\ll \lambda$, all diffraction orders become more equally pronounced

(see Figure 8.12). This includes also the orders which can not be captured by the numerical aperture and therefore do not contribute to the reconstruction of the hole pattern. For this reason, the number of photons per hole necessary to reach a fidelity of 96% increases to 40. This equals a total of 1960 photons, from which 50% (≈ 969) land within the NA. Both values are of similar magnitude as the experimentally reported value in Reference [188] where about 20 photons per atom were necessary for single atom detection using fluorescence imaging.

Obliquity factor

The Kirchhoff diffraction formula additionally includes the obliquity factor. This factor enhances diffraction towards the zeroth order peak and ensures that no light is diffracted back into the direction of the incident plane wave. For a lattice

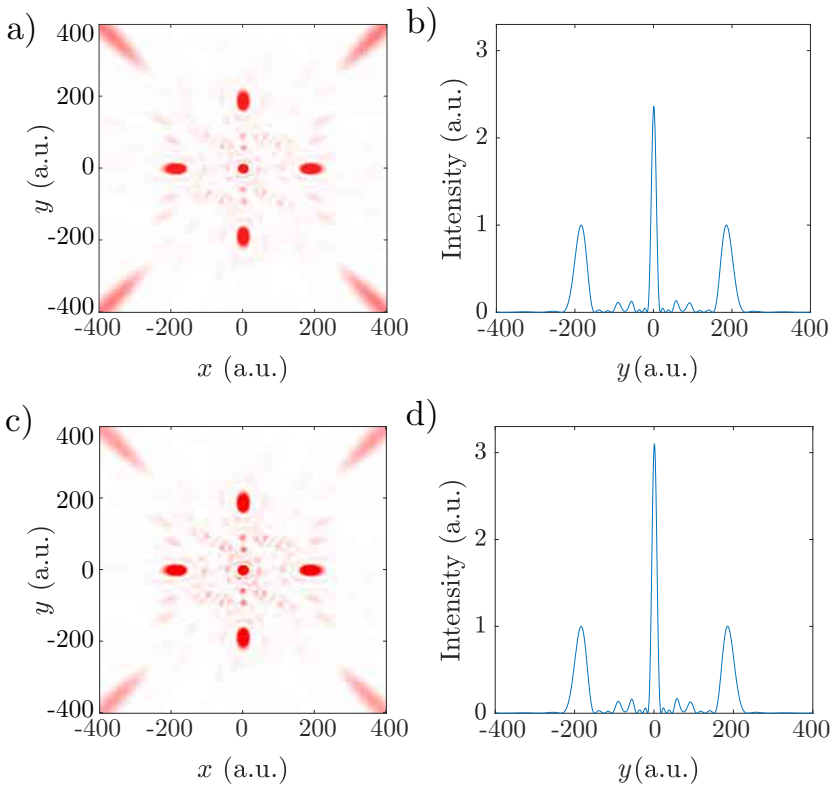

FIGURE 8.13: a) and b) show the calculation of the intensity distribution neglecting the obliquity factor. While a) shows the full two-dimensional intensity distribution, b) shows the distribution along the y-direction at $x = 0$, where the zero and the two first order peaks are clearly visible. c) and d) show the same calculation including the obliquity factor. One can see a slight enhancement of the signal in the region between the zero order and first order peaks. Figures b) and d) have been normalized to the intensity of the first order peaks. As expected, the relative intensity of the zero order peak in d) is slightly increased.

constant of 1 µm and a wavelength of 671 nm, the four first order diffraction peaks (horizontal and vertical) appear under an angle of $\Theta_{01} = \Theta_{10} = \sin(671/1000) = 42.1°$, while the diagonal first order peaks appear at $\Theta_{11} = \sin(\sqrt{2}671/1000) =$

$71.6°$. These orders are therefore weighted by the factors $(1 + \cos(\Theta_1)/2 = 0.89$ and $(1+\cos(\Theta_{11})/2 = 0.79$. This small attenuation barely changes the diffraction pattern, as shown in Figure 8.13. Although the effects are barely visible, it is still notable, that the factor additionally enhances the fraction of photons which are collected by the numerical aperture of the objective and therefore contribute to the reconstruction of the hole mask.

Chapter 9

A Fermi gas in the BCS-BEC crossover

In our experiments, we create and study ultracold strongly-interacting two-component Fermi gases of lithium-6 atoms. These systems can also be modeled theoretically. This enables us to make predictions and gain additional insights that are difficult to obtain from measurements alone.
Within this thesis, I set up two models for simulating various properties of an interacting two-component Fermi gas on the BEC side of the Feshbach resonance. These properties include the density distribution, pair fraction, condensate fraction, and the critical temperature for condensation. The models employ a mean-field approach and have been developed for earlier measurements [15, 82] for both verifying experimental findings and simultaneously testing the models. Mean-field approaches are well-established methods for treating small interparticle interactions and particularly effective in describing macroscopic properties of systems [6, 8, 198–202]. A third established approach for theoretically modeling strongly-interacting Fermi gases, which has also been used throughout this thesis, is the quantum virial expansion. This expansion is especially suited for describing Fermi gases in the high temperature limit.
In addition, the equations of state (EoS) of a strongly-interacting Fermi gas have been determined experimentally at $T = 0$ and $(k_F a_s)^{-1} = 0$ [88, 166, 203].
This chapter provides a conceptual explanation of two mean-field models and presents several key calculations. Additionally, the quantum virial expansion and the equation of state (EoS) measurement results are introduced and some practical examples of how to obtain useful results from both are given.

9.1 Thermal Bose-Fermi mixture

On the BEC side of the Feshbach resonance above the critical temperature, a spin-balanced interacting Fermi gas in thermal equilibrium consists of free unbound atoms and non-condensed dimers [97]. In recent experiments, we investigated this region in phase-space by measuring the fraction of paired and unpaired fermions using photo-excitation, see [15] and 4.7. As detailed in Chapter 2, for the non-interacting case the density distribution of both components within the local density approximation is given by

$$n_F(\mathbf{r}) = -\frac{1}{\lambda_{dB}^3}\mathrm{Li}_{3/2}\left(-e^{(\mu_F - V(\mathbf{r}))/k_B T}\right). \tag{9.1}$$

for the unbound, fermionic atoms (F) and

$$n_B(\mathbf{r}) = +\frac{1}{\lambda_{dB}^3}\mathrm{Li}_{3/2}\left(+e^{(\mu_B - V(\mathbf{r}))/k_BT}\right). \tag{9.2}$$

for the bosonic dimers (B). In thermal equilibrium, the chemical potentials are related via [19, 98]

$$\mu_B = 2\mu_F + E_b \tag{9.3}$$

where $E_b = \hbar^2/ma_s^2$ is the binding energy of the Feshbach molecules. The Equations (9.1) and (9.2), however, only hold for the case of non-interacting particles.

9.1.1 Model

One method for including interactions into the description is the so-called mean-field approach. The mean-field approach simplifies the many-body problem by approximating the interactions between particles in an averaged manner with a pseudo-potential

$$V_{int}(\mathbf{r}) = \frac{2\pi\hbar^2}{m_r}a_s\, n(\mathbf{r}) = g\, n(\mathbf{r}) \tag{9.4}$$

where g is the coupling constant. This method is particularly effective in describing the macroscopic properties of the system for small interparticle interactions [6, 71, 198–202], i.e. when $|a_s| \ll n^{1/3}$ as also done in the Gross-Pitaevskii equation, see Section 2.1.2.
For two colliding fermions (FF), the reduced mass is $m_{FF} = \frac{1}{2}m$. For two bosonic dimers (BB) or a dimer and an unpaired fermionic atom (FB), the reduced masses are given by $m_{BB} = m$ and $m_{FB} = \frac{2}{3}m$, and the scattering lengths are $a_{BB} = 0.6\, a_s$ [94, 95] and $a_{FB} = 1.18\, a_s$ [8]. This yields the coupling constants

$$g_{FF} = \frac{4\pi\hbar^2}{m}a_s, \qquad g_{FB} = \frac{2\pi\hbar^2}{3m}1.18a_s \qquad \text{and} \qquad g_{BB} = \frac{2\pi\hbar^2}{m}0.6a_s \tag{9.5}$$

for atom-atom, atom-dimer and dimer-dimer interactions.
Within the mean-field approach, one therefore gets a set of coupled equations for the density distributions of the unbound fermionic atoms and bosonic Feshbach dimers in a harmonic trapping potential $V_F(\mathbf{r}) = \sum_i m\omega_i^2 x_i^2/2$, which reads

$$n_F(\mathbf{r}) = -\frac{1}{\lambda_{dB}^3}\mathrm{Li}_{3/2}\left(-e^{(\mu_F - V_F(\mathbf{r}) - g_{FF}n_F(\mathbf{r}) - g_{FB}n_B(\mathbf{r}))/k_BT}\right) \tag{9.6}$$

$$\begin{aligned} n_B(\mathbf{r}) &= +\frac{1}{\lambda_{dB}^3}\mathrm{Li}_{3/2}\left(+e^{(\mu_B - V_B(\mathbf{r}) - 2g_{BB}n_B(\mathbf{r}) - g_{FB}n_F(\mathbf{r}))/k_BT}\right) \\ &= +\frac{1}{\lambda_{dB}^3}\mathrm{Li}_{3/2}\left(+e^{(2\mu_F + E_b - 2V_F(\mathbf{r}) - 2g_{BB}n_B(\mathbf{r}) - g_{FB}2n_F(\mathbf{r}))/k_BT}\right). \end{aligned} \tag{9.7}$$

Together with the constraint for the atom number per spin state $N_\sigma = N/2 = \int \mathrm{d}\mathbf{r}\, n_F(\mathbf{r}) + n_B(\mathbf{r})$, these coupled equations can be solved self-consistently for various temperatures and interactions.
This is done by iteratively calculating the density distributions, which depend

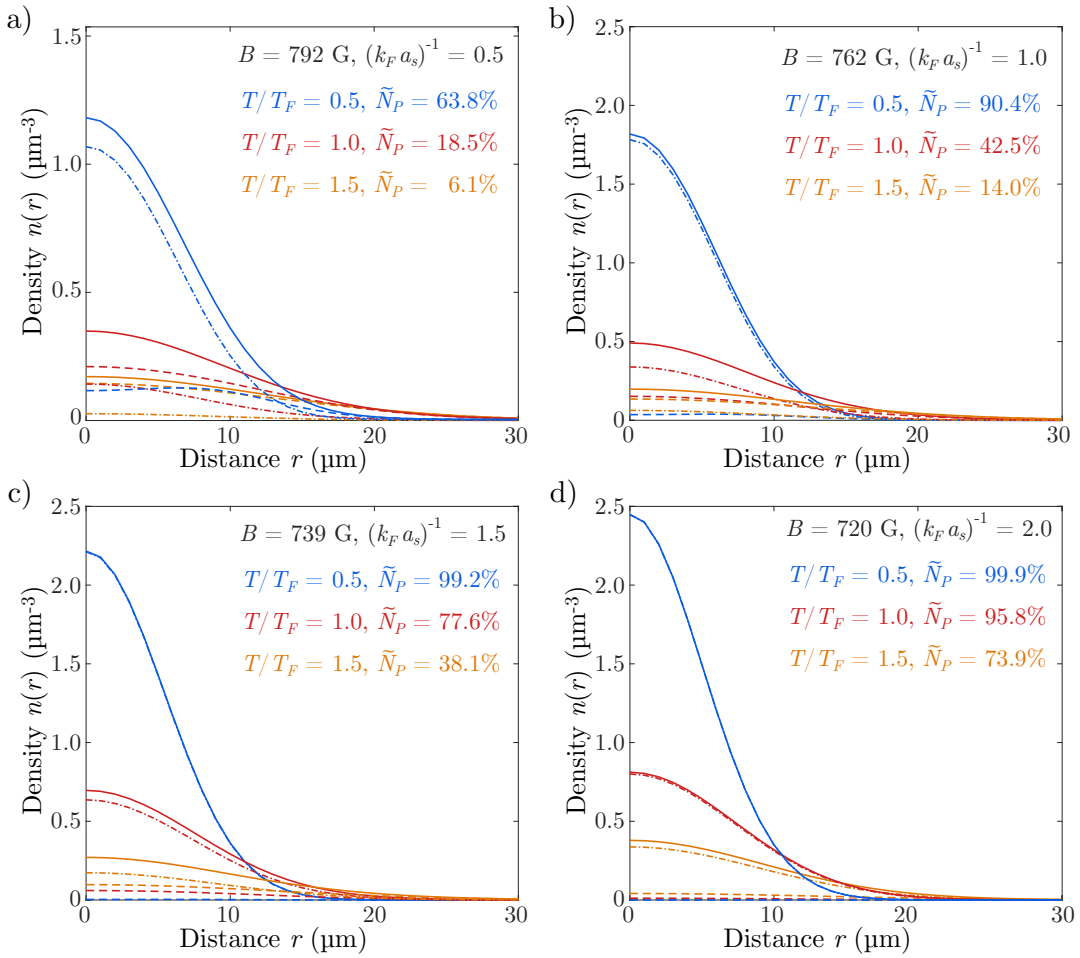

FIGURE 9.1: Density distributions $n(\mathbf{r})$ and pair fractions $\tilde{N}_P$ of a harmonically trapped Fermi gas on the BEC side of the BCS-BEC crossover at various temperatures T/T_F and interaction strengths $(k_F a_s)^{-1}$, as calculated within the mean-field model (see text). The solid line shows the radial density distributions of the total number of atoms per spin state, while the dashed (dashed-dotted) lines correspond to the free fermionic atoms (bosonic dimers). The calculations were carried out for $N_\sigma = 120\,000$ atoms per spin state, confined in an isotropic harmonic trap with trap frequency $\omega = 2\pi \times 500$ Hz. The magnetic fields $B = 792, 762, 739$ and 720 G were chosen to set interaction parameters of $(k_F a_s)^{-1} = 0.5, 1.0, 1.5$ and 2.0. These distributions can also be represented in reduced variables $\tilde{r}$ and $\tilde{n}(\tilde{r})$, where $\tilde{r} = r/R_{TF}$ and $\tilde{n} = nR_{TF}^3/N_\sigma$, where $R_{TF} = \sqrt{2E_F/(m\omega^2)}$ is the Thomas Fermi radius, see [204]. For the given parameters, we have $R_{TF} = 24.53$ μm.

on themselves[1] due to the mean-field interaction $\sim g\,n$, and using them in subsequent steps to update the distributions. After a number of iterations, the solutions typically converge. This number roughly depends on the interaction strength. For a larger mean-field energy, the step-to-step variations of the calculated density distributions are larger, which increases the number of steps to reach the convergence. We also employ a technique to prevent overshooting of

[1] In the first step, the density distribution is calculated without the mean-field interaction.

the density distributions. In this, the density distribution for the next iteration step is calculated as a weighted average of $b\%$ from the current step's distribution and $(100-b)\%$ from the previous step's distribution. We find that for large temperatures and small interaction strengths, a value of $b \approx 50-70$ results in a fast convergence. For $T \to T_C$ and $(k_F a_s)^{-1} \to 0$, b has to be chosen smaller ($\approx 2-10$) to ensure (fast) convergence.

The results for a few temperatures and interaction strengths are presented in Figure 9.1 and resolve the spatial density distributions of the unbound atoms and the dimers. As clearly visible, the fraction of dimers increases towards lower temperatures T/T_F and larger interaction parameters $(k_F a_s)^{-1}$, i.e. larger binding energies $E_B = \hbar^2/(m a_s)^2$. For large repulsive interactions and dimer fractions, the dimers even push out the unbound atoms from the center of the harmonic trap, as shown e.g. in Figure 9.1 a) for $T/T_F = 0.5$.

9.1.2 Pair fraction

As a result of the calculations, one not only obtains the density distributions, but also the number of unbound fermionic atoms (per spin state)

$$N_F = \int \mathrm{d}\mathbf{r}\, n_F(\mathbf{r}) \tag{9.8}$$

and bosonic dimers

$$N_B = \int \mathrm{d}\mathbf{r}\, n_B(\mathbf{r}) \tag{9.9}$$

and with this the pair fraction $\tilde{N}_P = \frac{N_B}{N_F+N_B}$. The contour lines for selected pair fractions are shown in Figure 9.2.

9.1.3 Critical temperature

Another important quantity that we obtain from the model is the critical temperature for condensation T_C. For this, one has to examine the effective chemical potential for the dimers in the center of the harmonic trap, given by

$$\mu_{B,\mathrm{eff}} = 2\mu_F + E_B - 2g_{BB}n_B(0) - g_{FB}2n_F(0). \tag{9.10}$$

When the effective chemical potential for the dimers becomes larger than zero, the model calculations fail, because the polylogarithm function in Equation (9.7) is not defined anymore. In a physical picture, this scenario corresponds to Bose-Einstein condensation of the dimers. One can then roughly find T_C at a fixed $(k_F a_s)^{-1}$, by starting the calculation at high temperatures (where $\mu_{B,\mathrm{eff}} < 0$) and slowly approaching smaller temperature (where $\mu_{B,\mathrm{eff}} \to 0$) until the calculation fails. The resulting curve for T_C on the BEC side is shown in Figure 9.2.
At $(k_F a_s)^{-1} = 0$ our model yields a value of $T_C/T_F = 0.2$. Interestingly, this coincides with the sophisticated result from the t-matrix calculation $T_C/T_F = 0.207$ [16], although the results for pair fraction deviate towards the Feshbach resonance.
The fundamental difference between the two models is the treatment of dimers

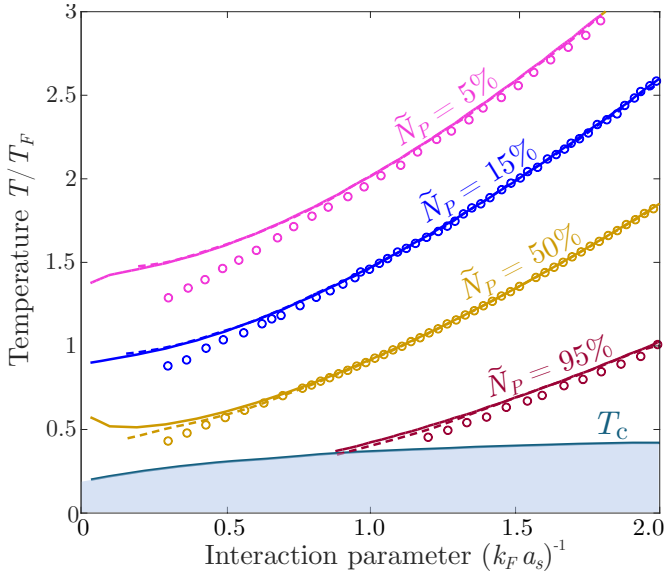

FIGURE 9.2: Critical temperature T_C and contour lines for the pair fractions of $\tilde{N}_P = 5\%, 15\%, 50\%$ and 95% for a harmonically trapped Fermi gas. The pair fraction was calculated from different approaches, namely the presented mean-field model (solid line), a t-matrix calculation (dots) [15, 16] and a classical calculation neglecting interactions (dashed line) [15, 97]. Data for the t-matrix and classical calculations are extracted from [15]. Further shown is the critical temperature T_C (green-grey solid line) obtained from the mean-field model as explained in Section 9.1.3.

and interactions towards the Feshbach resonance. Our model treats the dimers as purely bosonic entities, although their binding energy becomes comparable/smaller than the interaction and thermal energies scales towards the Feshbach resonance. The diagrammatic t-matrix calculation takes the intrinsic fermionic nature of the dimer constituents into account.
Additionally, the repulsive interaction within our mean-field model is linear in the scattering length a_s, leading to a nonphysical divergence of the mean-field energy $gn \propto a_s$ as the scattering length approaches $+\infty$. While the results for the pair fraction deviate, the effects seem to cancel each other out regarding the critical temperature.

9.1.4 Effective scattering length

One approach for avoiding a diverging mean-field interaction energy is by introducing an effective scattering length which does not diverge at the Feshbach resonance. As detailed in Section 2.2, the scattering cross section is a measure for the interparticle interactions and given by

$$\sigma_0(k) = \frac{4\pi a_s^2}{1 + k^2 a_s^2} \tag{9.11}$$

For small a_s, we recover $\sigma_0 = 4\pi a_s^2$ and for $|a_s| \to \infty$, it does not exceed the unitary limit $\sigma_u = 4\pi/k^2$, obtained for the largest possible scattering phase shift when $\sin^2(\delta_0) = 1$ (see Section 2.2).

One can therefore model an effective (local) scattering length of the form

$$a_{s,\text{eff}} = \frac{a_s}{\sqrt{1 + c(k_F^{\text{hom}})^2 a_s^2}} \tag{9.12}$$

which approaches a_s for $|(k_F a_s)^{-1}| \to \infty$ and $c^{-0.5}/k_F$ for $(k_F a_s)^{-1} \to 0$, as also discussed in Ref. [199].

The parameter c is a fudge factor which can be chosen to fulfill certain constraints. For example, the energy per particle in a unitary Fermi gas at zero temperature is given by $\xi \frac{3}{5} E_F^{\text{hom}} = \xi \frac{3}{5} \frac{(\hbar k_F^{\text{hom}})^2}{2m}$. If one sets this equal to the mean-field energy of the Fermions $\frac{4\pi\hbar}{m} a_s n$, one obtains $a_s = \xi \frac{18\pi}{40} \frac{1}{k_F} \approx 0.531/k_F$, which yields $c = 3.71$ for $\xi = 0.367$ [92, 93]. In [199], the energy was roughly assumed to be $\frac{3}{5} E_F^{\text{hom}}$, which yields $c = 0.5$.

In Figure 9.3, we compare the results for both values of c, together with the results for a diverging scattering length (i.e. $c = 0$). Already for $c = 0.5$ the results

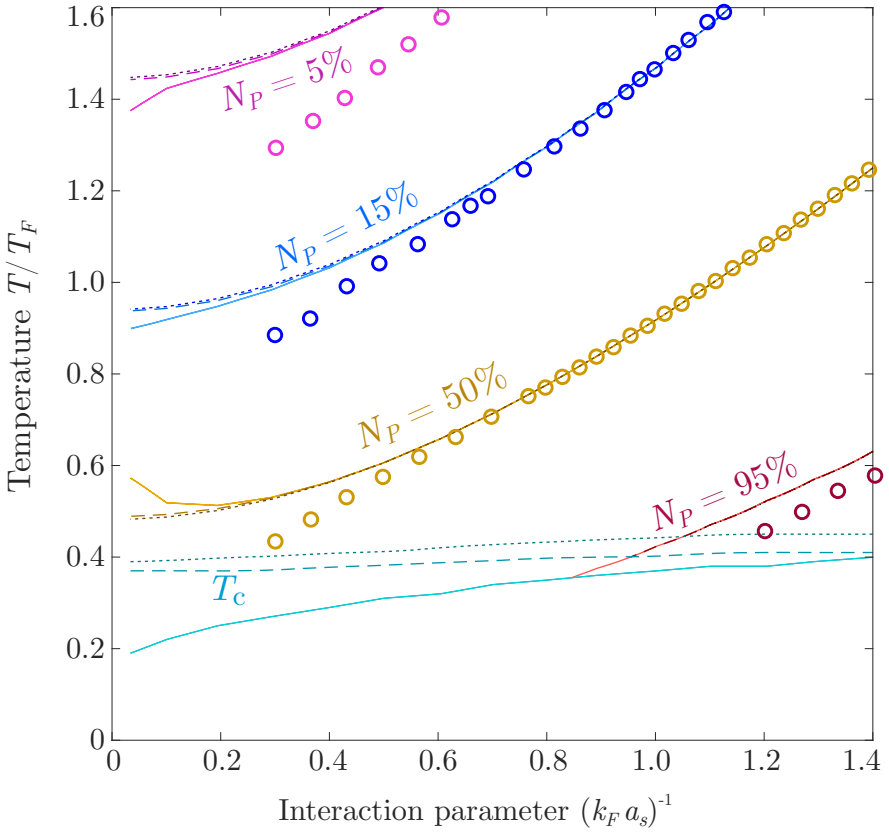

FIGURE 9.3: mean-field calculation of the critical temperature T_C and contour lines for the pair fractions of $\tilde{N}_P = 5\%, 15\%, 50\%$ and 95%. The results were obtained with an effective scattering length as parameterized by Equation (9.12) with $c = 0$ (solid lines), $c = 0.5$ (dashed lines) and $c = 3.71$ (dotted lines). Additionally, t-matrix calculations of the pair fraction are shown as dots [15].

for the pair fraction almost approach the classical limit ($c \to \infty$) and strongly deviate from the results obtained for a diverging scattering length ($c = 0$). For a larger value of c, corresponding to a smaller effective scattering length towards the Feshbach resonance, the critical temperature T_C within the model becomes quite insensitive to the interacting strength. For $c = 0.5$ ($c = 3.71$), we find $T_C = 0.37$ ($T_C = 0.39$) at $(k_F a_s)^{-1} \to 0$. This substantially differs from recent calculations of $T_C = 0.207$ [16]. In the BEC limit of $(k_F a_s)^{-1} \to \infty$, all calculations approach the expected value of $T_C = 0.5175\, T_F$ (see Section 2.1.3).

9.2 Partially condensed molecular Bose gas

Below the critical temperature T_C, the spin-balanced Fermi gas is in a superfluid state. For $0 < T < T_C$, the gas thereby consists of two phases, the superfluid and the normal fluid phase. In recent experiments, we investigated this state by exciting first and second sound waves via intensity modulation of a repulsive laser beam focused into the center of the harmonically trapped atom cloud [82]. While first sound is a density wave, second sound waves are essentially entropy waves and can only propagate in the presence of two different gas phases, as detailed in Refs. [82, 205–207]. With these experiments, we could, among other things, examine the superfluid phase in the BCS-BEC crossover.
To theoretically investigate the superfluid phase and its spatial extension at various interactions and temperatures $0 < T < T_C$, I implemented another model based on the local density approximation and the mean-field approach. With this model, we were able to locate the superfluid region of our cloud in the BEC regime very precisely and also make precise statements about the densities of the superfluid and normally fluid phases, see [82]. Within the model, the Fermi gas below T_C is assumed to consist purely of bosonic molecules which are partially condensed and partially thermal.

9.2.1 Non-interacting molecular Bose gas

For a non-interacting Bose gas, the ratio of condensed particles to the total number of particles is $N_0/N = 1 - (T/T_C^0)^3$. Such a gas is almost present in the deep BEC regime of a two-component Fermi gas when $(k_F a_s)^{-1} \to \infty$ and $T_C^0 \approx 0.5176\, T_F$ [115, 208], see also Section 2.1.3. In this case, fermions of opposite spin form bosonic molecules. The gas then consists of a condensed and a non-condensed, normal phase with density distribution functions

$$n_0(\mathbf{r}) = \frac{\mu_0 - V(\mathbf{r})}{g} \Theta\left[\mu_0 - V(\mathbf{r})\right] \tag{9.13}$$

$$n_B(\mathbf{r}) = \frac{1}{\lambda_{dB}^3} \mathrm{Li}_{3/2}\left(+e^{(\mu_B - V(\mathbf{r}))/k_B T}\right), \tag{9.14}$$

see Equations (2.19) and (2.30).
As the densities of these gas phases follow different distribution functions, the total density distribution of the atom cloud shows a characteristic bimodal feature, as also shown in experimental measurements of the density distributions in

Figure 1.1. This bimodal feature clearly indicates that the condensed molecules at high density accumulate in the center of the trap while the thermal ones surround them.

9.2.2 Model

To consider interparticle interactions, one can again make use of the mean-field approach, as in the previous section. With the coupling constant for dimer-dimer interaction

$$g_{BB} = \frac{2\pi\hbar^2}{m} 0.6\, a_s \tag{9.15}$$

one obtains a set of coupled equations for the density distributions [6, 82, 209]

$$n_0(\mathbf{r}) = \frac{\mu_0 - V(\mathbf{r}) - 2g_{BB}n_B(\mathbf{r}))}{g} \Theta\left[\mu_0 - V(\mathbf{r}) - 2g_{BB}n_B(\mathbf{r})\right] \tag{9.16}$$

$$n_B(\mathbf{r}) = \frac{1}{\lambda_{dB}^3} \mathrm{Li}_{3/2}\left(\exp\left[\frac{\mu_B - V(\mathbf{r}) - 2g_{BB}n_0(\mathbf{r}) - 2g_{BB}n_B(\mathbf{r})}{k_B T}\right]\right) \tag{9.17}$$

for a given temperature T, scattering length a_s and trapping potential $V(\mathbf{r})$ As $0 < T < T_C$, the thermal fraction has to reach the critical density $\mathrm{Li}_{3/2}(1)/\lambda_{dB}^3$ somewhere in the trap. Otherwise, the gas would be either not partially condensed or not be in thermal equilibrium. We can therefore set

$$\mu_B = \min\left[V(\mathbf{r}) + 2g_{BB}n_0(\mathbf{r}) + 2g_{BB}n_B(\mathbf{r})\right] \tag{9.18}$$

to fulfill this condition. This effectively fixes μ_B. To also fix μ_0, we have to again consider the constraint for the total particle number $N = \int \mathrm{d}\mathbf{r}\, n_0(\mathbf{r}, \mu_0) + n_B(\mathbf{r})$. With this, the set of coupled equations can be solved self-consistently to obtain the density distributions for the superfluid and thermal gas phases. The results for $(k_F a_s)^{-1} = (1,\ 1.5,\ 2)$ and $T/T_F = (0.05,\ 0.15,\ 0.25,\ 0.35)$ are presented in Figure 9.4.

9.2.3 Critical temperature

Another important quantity that the calculations reveal is the critical temperature T_C. In contrast to the previously presented mean-field model for the thermal Bose-Fermi mixture at $T > T_C$, the mean-field model for the partially condensed molecular Bose gas only works below T_C. In order to find T_C for a given interaction parameter $(k_F a_s)^{-1}$, one has therefore to start the model calculation at $T \ll T_C$ and gradually increase the temperature. The point, where the calculations run into numerical issues indicates the critical temperature.
From the calculations, we find $T_C/T_F \approx 0.415\ (0.44, 0.448)$ at $(k_F a_s)^{-1} = 2\ (3, 5)$ in agreement with calculations from [16] (see inset of Fig. 7) using the same mean-field approach. In [16], additional calculations for T_C using $a_{BB} = 0.75\, a_s$ $(1.16\, a_s, 2.00\, a_s)$ were carried out and compared to t-matrix calculations for T_C. The results are shown in Figure 9.5, together with the calculation using the established value $a_{BB} = 0.6\, a_s$ [94, 95].

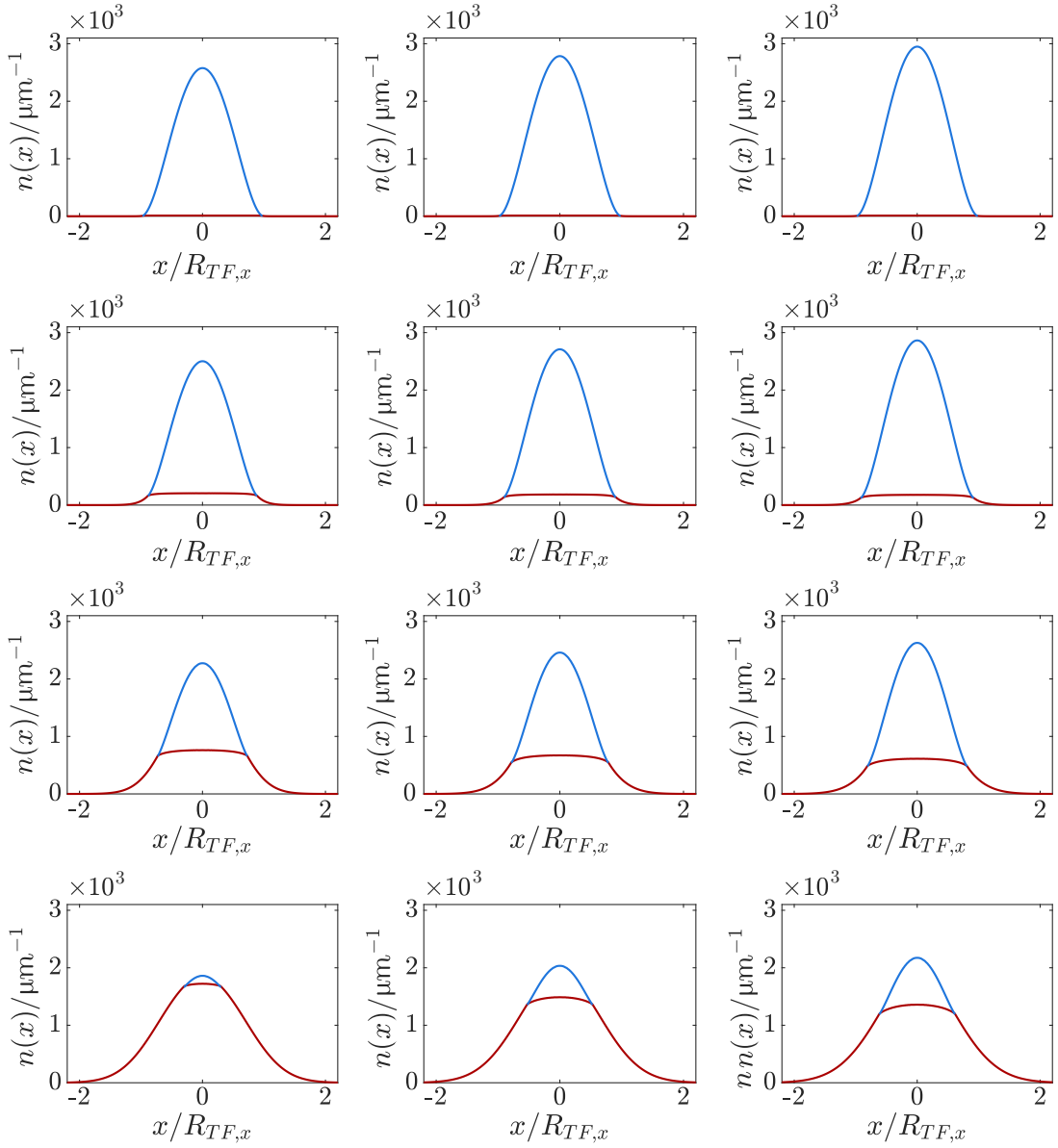

FIGURE 9.4: Line density distributions $n(x)$ of a partially condensed molecular Bose gas, calculated within a mean-field approach. From top to bottom, the rows correspond to temperatures of $T/T_F = (0.05,\ 0.15,\ 0.25,\ 0.35)$. From left to right, the columns correspond to $(k_F a_s)^{-1} = (1,\ 1.5,\ 2)$. The calculations were carried out for $N = 10^5$ atoms confined in an isotropic harmonic trap with trap frequencies $\omega_i = 2\pi \times 63\,\text{Hz}$ corresponding to a Thomas Fermi radius of $R_{TF,i} = 29.2\,\mu\text{m}$.

Interaction and harmonic trap effects

When approaching the Feshbach resonance, the critical temperature decreases due to the increasing repulsive interactions that prevent the gas from reaching the critical density required for condensation. This shifts the critical temperature from the critical temperature of a non-interacting Bose gas T_C^0. In Reference [71],

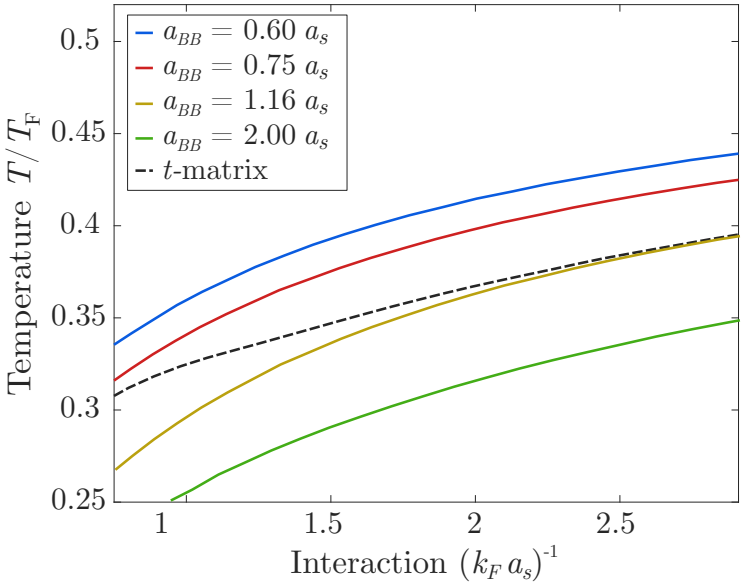

FIGURE 9.5: Critical temperature for condensation of a molecular Bose gas, taken from [16]. The solid lines are calculated with a mean-field approach for different dimer-dimer scattering lengths as indicated by the legend. As expected, T_C decreases with increasing interparticle interactions. Further shown is a t-matrix calculation (dashed line). It coincides with the mean-field result for a dimer-dimer scattering length of $a_{BB} = 1.16\, a_s$ [16] in the limit of $(k_F a_s)^{-1} \to \infty$. Precise calculations of the dimer-dimer problem yield $a_{BB} = 0.6\, a_s$ [94, 95].

the downshift for a harmonically trapped Bose gas was found to be

$$\frac{\Delta T_C^{\text{int}}}{T_C^0} = -1.33 \frac{a}{a_{HO}} N^{1/6} \tag{9.19}$$

where a is the scattering length, $a_{HO} = \sqrt{\frac{\hbar}{M\omega}}$ the harmonic oscillator length and N the atom number. In our scenario of a molecular Bose gas, $a = a_{BB} = 0.6 a_s$ and $M = 2m$. With $\hbar^2 k_F^2/2m = E_F = \hbar\omega(6N)^{1/3}$ and therefore $k_F = \sqrt{2m\omega/\hbar}(6N)^{1/6}$, one can then rewrite the shift in Equation (9.19) into

$$\frac{\Delta T_C^{\text{int}}}{T_C^0} = -0.592\, k_F a_s \tag{9.20}$$

with $T_C^0 = 0.5176\, T_F$ (see Section 2.1.3). At $(k_F a_s)^{-1} = 2\ (3, 5)$ this yields $\Delta T_C^{\text{int}}/T_C^0 = -0.296\ (-0.197, -0.118)$ and thus $T_C^{\text{int}}/T_F = 0.364\ (0.415, 0.456)$. Another effect that introduces a shift of the critical temperature is the harmonic trap itself. Condensation in the harmonic trap actually does not start when the effective chemical potential reaches zero, but when it approaches the energy of the ground state. For a three-dimensional isotropic trap, this energy is $\frac{3}{2}\hbar\omega$. For an isotropic harmonic trap with trap frequencies ω_x, ω_y and ω_z, the associated

shift is given by [71, 210]

$$\frac{\Delta T_C^{\mathrm{tr}}}{T_C^0} = -0.73 \frac{(\omega_x + \omega_y + \omega_z)/3}{(\omega_x\, \omega_y\, \omega_z)^{1/3}} N^{-1/3} \tag{9.21}$$

which is smallest for the isotropic case. For typical atom numbers of $N = 10^5$ (10^6) in an isotropic harmonic trap, the shift is $\Delta T_C^{\mathrm{tr}}/T_C^0 = -0.0157$ (-0.0073). For a cigar shaped atom cloud with aspect ratio of $1:10$, one obtains $\Delta T_C^{\mathrm{tr}}/T_C^0 = -0.0237$ (-0.0100) for the same atom numbers.

9.2.4 Condensate fraction

Another interesting quantity is the condensate fraction. For a non-interacting harmonically trapped Bose gas below T_C, the fraction of condensed particles scales as $N_0/N = 1 - (T/T_C^0)^3$. For a homogeneous Bose gas, one finds $n_0/n = N_0/N = 1 - (T/T_C^{0,\mathrm{hom}})^{3/2}$ as derived in Section 2.1.2.

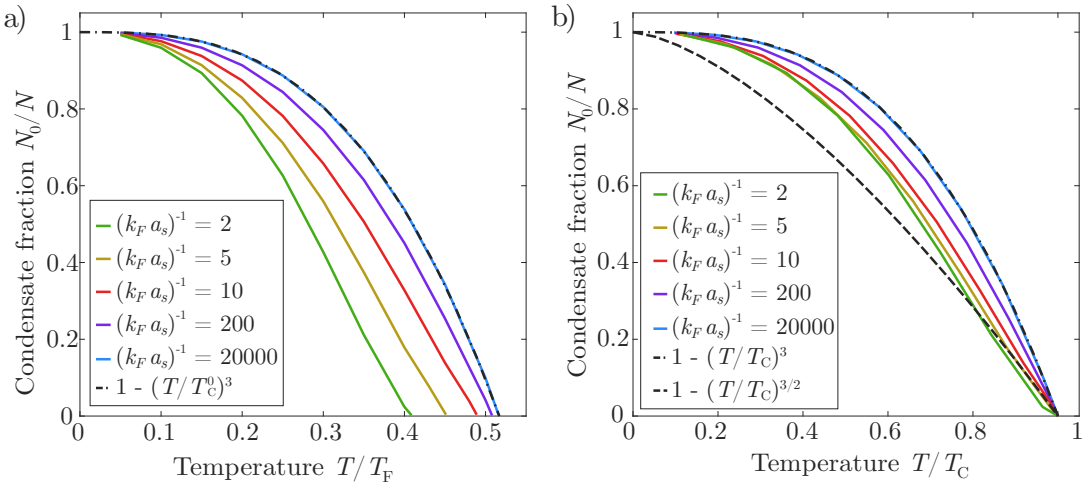

FIGURE 9.6: Condensate fraction of an interacting molecular Bose gas, as calculated with a mean-field approach. a) Shows the condensate fraction N_0/N as a function of the relative temperature T/T_F for various interaction parameters $(k_F a_s)^{-1}$ (solid lines), as well as for the non-interacting case (dash-dotted line). From the curves, we can infer the critical temperature T_C for each $(k_F a_s)^{-1}$. b) Shows the condensate fraction N_0/N as a function of the relative temperature T/T_C for same interaction parameters $(k_F a_s)^{-1}$ as in a). The critical temperature T_C at each $(k_F a_s)^{-1}$ was taken from [16] and agrees with the critical temperature inferred from our calculations shown in a). For comparison, the analytical results for a non-interacting harmonically trapped (dash-dotted line) and homogeneous Bose gas (dashed line) are shown. Note that the non-interacting harmonically trapped result almost coincides with the calculation for $(k_F a_s)^{-1} = 20000$ and is therefore difficult to recognize in a) and b). For a BEC of (bosonic) ^{87}Rb atoms with typical atom numbers of 10^5, trap frequencies of $\omega = 2\pi \times 100\,\mathrm{Hz}$ and a background scattering length of $\approx 100\, a_0$, one can associate an interaction parameter of $(k_F a_s)^{-1} \approx 15$.

Within our model, we can obtain the condensate fraction for various interaction parameters $(k_F a_s)^{-1}$. The results are shown in Figure 9.6 together with a comparison to the theoretical predictions for the non-interacting harmonically trapped and homogeneous Bose gas.

As expected, we recover the relation for the non-interacting harmonically trapped Bose gas in the limit of weak interactions, i.e. $(k_F a_s)^{-1} \to \infty$. For stronger interactions, the rise of the condensate fraction around T_C is flatter, compared to the non-interacting case. This was also observed in measurements [211] and model calculations presented in [71] (see Figs. 1 and 2) and can be explained by the fact that strong repulsive mean-field interactions result in a more homogeneous density distribution because the particles repel each other. The increase of the condensate fraction therefore approaches the relation for the homogeneous Bose gas. For further information, two comprehensive reviews on the effects of interactions in Bose gases below and above T_C can be found in References [6, 212].

9.3 The quantum virial expansion

Another framework to treat strongly-interacting Fermi gases is the quantum virial expansion. This expansion has proven to be a powerful tool for investigating strongly-interacting Fermi gases at high temperatures T [170] and was also frequently used within this thesis. In the high temperature limit, the chemical potential μ of a Fermi gas approaches $-\infty$ faster than T approaches ∞ [21, 22]. Therefore, the fugacity $z = \exp(\mu/k_B T)$ becomes a small parameter, even for strong interparticle interactions as present in the BCS-BEC crossover [174]. In this limit, any physical quantity of the Fermi gas can be expanded as a series expansion in the fugacity z with corresponding expansion coefficients b_n, the so-called virial coefficients.
One of those quantities is the grand canonical potential Ω_G. For the grand canonical Ω_G potential, the virial expansion reads

$$\Omega_G = -\frac{2k_B T V}{\lambda_{dB}^3}\left[z + b_2 z^2 + b_3 z^3 + \dots\right] \tag{9.22}$$

where b_n are the virial coefficients, V is the volume and λ_{dB} is the thermal de Broglie wavelength [170]. The factor of 2 accounts for the two spin components. The local interactions are determined by the ratio of the de Broglie wavelength λ_{dB} and the scattering length a_s. The virial coefficients are therefore dimensionless functions of $\frac{\lambda_{dB}}{a_s}$ [170, 176] and can all be expressed as the sum of two terms

$$b_n = b_n^{(0)} + b_n^{\text{int}}. \tag{9.23}$$

While the first term $b_n^{(0)} = \frac{(-1)^{n+1}}{n^{5/2}}$ accounts for the presence of n non-interacting fermions[2] in the grand canonical ensemble, the latter b_n^{int} considers their n-body interactions. These include scattering properties as well as possible n-body bound states. This becomes clear, when rewriting the grand canonical potential

$$\Omega_G = -\frac{2k_BTV}{\lambda_{dB}^3}\left[z + b_2 z^2 + b_3 z^3 + \dots\right] \tag{9.24}$$

$$= -\frac{2k_BTV}{\lambda_{dB}^3}\left[z + (b_2^{(0)} + b_2^{\text{int}})z^2 + (b_3^{(0)} + b_3^{\text{int}})z^3 + \dots\right] \tag{9.25}$$

$$= -\frac{2k_BTV}{\lambda_{dB}^3}\left[z + b_2^{(0)}z^2 + b_3^{(0)}z^3 + \dots + b_2^{\text{int}}z^2 + b_3^{\text{int}}z^3 + \dots\right] \tag{9.26}$$

$$= -\frac{2k_BTV}{\lambda_{dB}^3}\left[\frac{1}{1^{5/2}}z - \frac{1}{2^{5/2}}z^2 + \frac{1}{3^{5/2}}z^3 + \dots + b_2^{\text{int}}z^2 + b_3^{\text{int}}z^3 + \dots\right] \tag{9.27}$$

$$= -\frac{2k_BTV}{\lambda_{dB}^3}\left[-\text{Li}_{5/2}(-z) + b_2^{\text{int}}z^2 + b_3^{\text{int}}z^3 + \dots\right]. \tag{9.28}$$

We obtain as one term the polylogarithm function of order $5/2$ and argument $-z$, originating from the infinite sum over all terms $b_n^{(0)}\, z^n$. As detailed in Chapter 2, the polylogarithm arises from quantum statistics. This means even when there are no particle interactions involved (e.g. in a system with zero scattering length and zero bound states), the quantum virial expansion inherently accounts for quantum statistics - in this case, the Fermi-Dirac statistics.

The only virial coefficient which is (currently) known analytically in the entire phase space of the BCS-BEC crossover is the second order coefficient

$$\begin{aligned} b_2 &= b_2^{(0)} + b_2^{\text{int}} \\ &= \frac{-1}{2^{5/2}} + \sqrt{2}\Theta(a_s)\mathrm{e}^{\lambda_{dB}^2/2\pi a_s^2} - \frac{\sqrt{2}}{2}\text{sgn}(a_s)\left(1 - \text{erf}\left[\sqrt{\lambda_{dB}^2/2\pi a_s^2}\right]\right)\mathrm{e}^{\lambda_{dB}^2/2\pi a_s^2}. \end{aligned} \tag{9.29}$$

where $\lambda_{dB}^2/(2\pi a_s^2) = E_b/(k_BT)$. To obtain this result, one has to solve the two-body problem of two interacting Fermions with opposite spin. A detailed calculation can be found in [170, 175, 213] and in Appendix A.4. For a diagrammatic calculation of the third virial coefficient b_3, see Ref. [176].
With the grand canonical potential expressed within the quantum virial expansion, other key properties of the Fermi gas can be derived using fundamental thermodynamic relations [170]. As two important examples, the density distribution and Tan's contact are derived in the following sections.

[2]For a derivation, see Appendix A.4. For bosons one finds $b_n^{(0)} = \frac{1}{n^{5/2}}$, as expressed in Equation (A.39).

9.3.1 Density distribution from the quantum virial expansion

The density is related to the grand canonical potential via [166, 170, 214]

$$n = -\frac{1}{V}\frac{\partial \Omega_G}{\partial \mu}. \tag{9.30}$$

For a trapped, spin-balanced Fermi gas within the local density approximation, one obtains the total density distribution

$$n(\mathbf{r}) = \frac{2}{\lambda_{dB}^3}\left[e^{(\mu - V(\mathbf{r}))/k_BT)} + 2b_2 e^{2(\mu - V(\mathbf{r}))/k_BT)} + ...\right]. \tag{9.31}$$

The first two terms represent the sum of two thermal density distributions[3]. The first term can be associated with the free fermionic atoms with chemical potential μ and trapping potential $V(\mathbf{r})$, while the second term describes the dimers with chemical potential 2μ and trapping potential $2V(\mathbf{r})$. At first glance, it seems that the chemical potential for the dimers misses the term for the binding energy $\hbar^2/ma_s^2$. This term is, however, included in the b_2 coefficient as shown in Equation (9.29).
For a cigar shaped atom cloud with trap frequencies $\omega_y = \omega_z = \omega_r$, as usually present in our experiments, the result for the column density $n(x)$ along the axial direction is obtained by integration

$$n(x) = \int dy \int dz\, n(\mathbf{r}) = \frac{4\pi k_B T}{m\omega_r^2 \lambda_{dB}^3}\left[e^{(\mu - m\omega_x^2 x^2/2)/k_BT} + b_2 e^{(2\mu - m\omega_x^2 x^2)/k_BT} + ...\right]. \tag{9.32}$$

The density distribution is especially useful for thermometry. By fitting the calculated density distributions to the measured distributions, we can determine the temperature of our atomic clouds quite accurately. This is demonstrated in Appendix A.4.

9.3.2 Tan's contact from the virial expansion

The quantum virial expansion can also be used to obtain Tan's contact $\mathcal{I}$ [70]. In our work, we used this approach to calculate the contact in the entire BCS-BEC crossover of a harmonically trapped Fermi gas [13, 14]. The conceptual idea is briefly summarized and further detailed here. For more details, see [14, 70].
We start from Tan's adiabatic sweep theorem

$$\left(\frac{\partial E}{\partial(1/a_s)}\right)_{S,N,V} = -\frac{\hbar^2 \mathcal{I}}{4\pi m} \tag{9.33}$$

relating the total contact $\mathcal{I}$ to the change of the internal energy E with scattering length a_s at fixed entropy S, atom number N and volume V, see also Section 2.6.1.

[3] For simplicity, I do not split the virial coefficients into two terms in this calculation. If one does so and considers, as above, the infinite sum over $b_n^{(0)}$, one obtains the result $n(\mathbf{r}) \propto -\mathrm{Li}_{3/2}(-z) + 2b_2^{\mathrm{int}} z^2 + \ldots$, see Appendix A.4. This also accounts for the Fermi-Dirac statistics, in agreement with the result for the density distribution presented in Section 2.1.1.

The energy E can also be written in its differential form [170, 214] according to the first law of thermodynamics[4]

$$\mathrm{d}E = T\mathrm{d}S + \mu\mathrm{d}N - p\mathrm{d}V - \frac{\hbar^2\mathcal{I}}{4\pi m}\mathrm{d}(1/a_s) \tag{9.34}$$

where p is the pressure. Here, one can see that the total contact $\mathcal{I}$ and the scattering length a_s can be understood as a pair of conjugate variables with respect to the energy E, where $\mathcal{I}$ represents an extensive and a_s an intensive quantity. To make use of the virial expansion above, the energy E has to be expressed in terms of the grand canonical potential Ω_G. These quantities are related via [214]

$$\Omega_G = E - TS - \mu N. \tag{9.35}$$

Combining Equations (9.34) an (9.35), one obtains

$$\mathrm{d}\Omega_G = \mathrm{d}E - T\mathrm{d}S - S\mathrm{d}T - \mu\mathrm{d}N - N\mathrm{d}\mu \tag{9.36}$$

$$= -\frac{\hbar^2\mathcal{I}}{4\pi m}\mathrm{d}(1/a_s) - p\mathrm{d}V - S\mathrm{d}T - N\mathrm{d}\mu \tag{9.37}$$

and with this Tan's adiabatic sweep theorem for the grand canonical ensemble

$$\left(\frac{\partial\Omega_G}{\partial(1/a_s)}\right)_{T,\mu,V} = -\frac{\hbar^2\mathcal{I}}{4\pi m}. \tag{9.38}$$

Within the quantum virial expansion of the grand canonical potential, as given by Equation (9.22), the contact $\mathcal{I}$ is

$$\mathcal{I} = 16\pi^2\frac{V}{\lambda_{dB}^4}\left[c_2z^2 + c_3z^3 + \dots\right] \tag{9.39}$$

for a given chemical potential μ, temperature T and scattering length a_s, where $c_n = \partial b_n/\partial(\lambda_{dB}/a_s)$. Results of this calculation are shown in [13, 14, 170].

9.4 The Equations of State

In the years 2010-2012, the groups of M. Zwierlein and C. Salomon published measurements on the equations of state (EoS) of a strongly-interacting Fermi gas [88, 166, 203]. Their results are valid for Fermi gas on the Feshbach resonance at various temperatures [88, 203] or at zero temperature for various interaction strengths [166].
Within all these works, the gas pressure $P(\mu, T)$ of the Fermi gas was derived and related to the pressure of a non-interacting Fermi gas using multiplicative transfer functions. These are functions of μ and T for a gas on the Feshbach resonance [88, 203] or functions μ and a_s for the zero temperature Fermi gas [166].

[4] Note, that in thermodynamics the letter U is typically used for the systems internal energy E.

As a brief summary, this was achieved by precisely measuring the density distributions $n(\mathbf{r})$ of a unitary or $T \approx 0$ Fermi gas for a known trapping potential $V(\mathbf{r})$. Using the local density approximation, $n(V)$ was then obtained. From this, the pressure $P(\mu, T)$ (at $(k_F a_s)^{-1} = 0$) or $P(\mu, a_s)$ (at $T = 0$) was derived using fundamental thermodynamic relations (see [88, 166, 203] for more details). The conceptual idea follows a proposal by [215]. Although the measurements were carried out with harmonically trapped Fermi gases, the corresponding equations of state were deduced for homogeneous Fermi gases.
Since these works form an important basis for the description of strongly interacting Fermi gases and I have used their results frequently in the course of this thesis, I will briefly present the results below and explain how useful quantities can be derived from them.

9.4.1 The Equation of State of a Unitary Fermi gas

On the Feshbach resonance, the scattering length a_s diverges and drops out of the description of the Fermi gas. The properties of the gas are therefore determined by the chemical potential μ and the temperature T, only. The transfer function to translate properties of a non-interacting to the unitary Fermi gas must therefore be a function these two parameters.

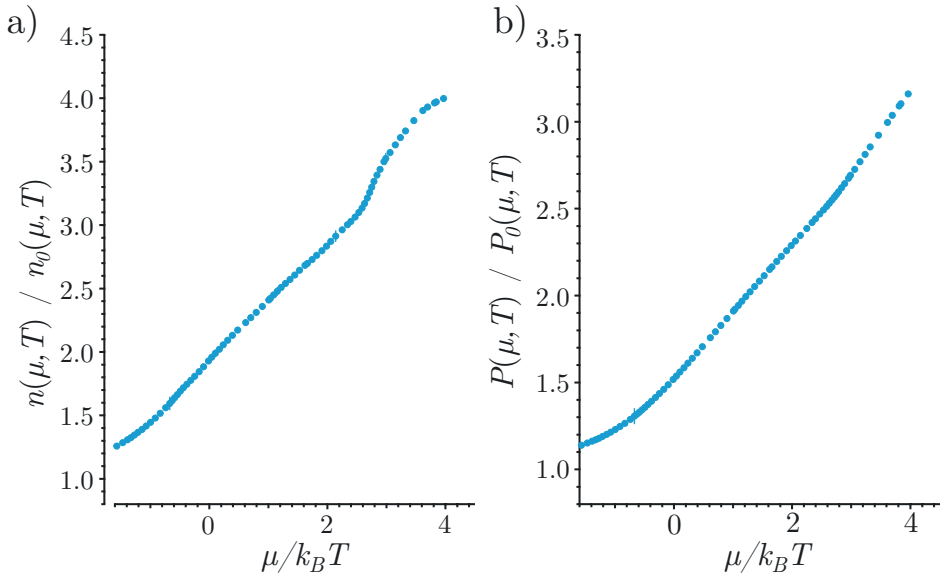

FIGURE 9.7: Measured equations of state for the unitary Fermi gas, taken and adapted from [88]. a) Shows the density and b) the pressure of a unitary Fermi gas, normalized by the corresponding density and pressure of a non-interacting Fermi gas as function of the ratio μ/k_BT.

In Reference [88], such functions were experimentally determined for the density $n(\mu, T)$ and the pressure $P(\mu, T)$ of the unitary Fermi gas. The derived functions relate these quantities to the ideal Fermi gas density (see Section 2.1.1)

$$n_0(\mu, T) = -\frac{1}{\lambda_{dB}^3} \mathrm{Li}_{3/2}\left(-e^{\mu/k_B T}\right) \tag{9.40}$$

and the ideal Fermi gas pressure

$$P_0(\mu, T) = -\frac{k_B T}{\lambda_{dB}^3} \mathrm{Li}_{5/2}\left(-e^{\mu/k_B T}\right). \tag{9.41}$$

The results are shown in Figure 9.7. Here, the transfer functions are the ratios $n(\mu, T)/n_0(\mu, T)$ and $P(\mu, T)/P_0(\mu, T)$ between the unitary and the ideal Fermi gas density and pressure. In the high temperature limit where $\mu/k_B T \to -\infty$ [21, 22], both transfer functions approach the value of 1. This behaviour is expected because, at high temperatures, the Fermi gas becomes dilute and the effects of strong interactions are negligible. Thus, with the thermal energy exceeding the energy of the many-body interactions, the unitary Fermi gas behaves like an ideal Fermi gas. For the zero temperature limit where $\mu/k_B T \to \infty$, the ratio for the density and the pressure approaches $\xi^{-3/2} \approx 4.5$ [88, 203]. This is in agreement[5] with the chemical potential of the unitary Fermi gas approaching $\mu \to \xi E_F$ for $T \to 0$.

With the density or the pressure EoS, other properties of the unitary Fermi gas

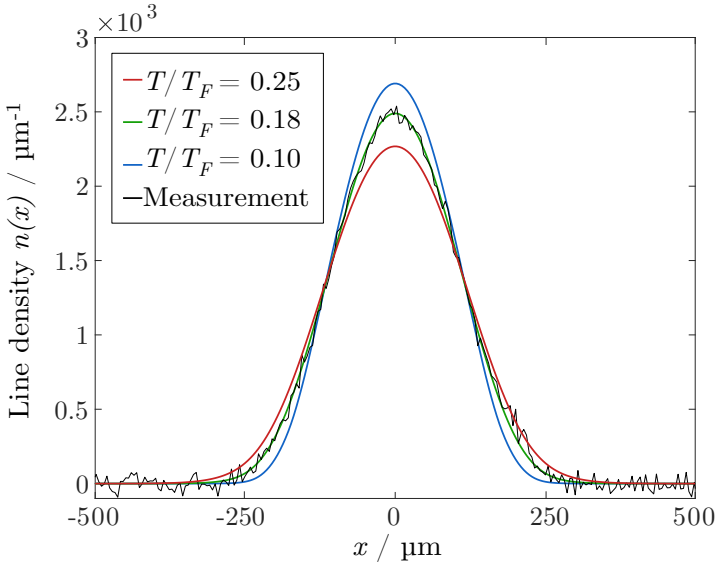

FIGURE 9.8: Measured and calculated line density distributions of a unitary Fermi gas for given atom numbers and trap frequencies. The red, green and blue solid show calculations based on the EoS measurements for $T/T_F = 0.25, 0.18$ and 0.10. The black solid line shows a measured density distribution, to which we assign a temperature of $T = 0.18\, T_F$.

can be calculated using fundamental thermodynamic relations [214]. As a first example, note that already n and P are related via $n = \left(\frac{\partial P}{\partial \mu}\right)_T$ [88]. Deriving a second time, yields the compressibility $k = \frac{1}{n^2}\left(\frac{\partial n}{\partial \mu}\right)_T$ [88]. Also, the local Fermi momentum $k_F^{\mathrm{hom}} = (6\pi^2 n)^{1/3}$ and the local Fermi energy $E_F^{\mathrm{hom}} = \hbar^2 (k_F^{\mathrm{hom}})^2/2m$

[5] The zero-temperature density of an ideal Fermi gas is given by $n_0 = \frac{k_F^3}{6\pi^2} = \frac{1}{6\pi^2}\left(\frac{2m}{\hbar}\right)^{3/2} E_F^{3/2} = \frac{1}{6\pi^2}\left(\frac{2m}{\hbar}\right)^{3/2} \mu^{3/2}$ at $T = 0$. As $\mu = \xi E_F$ for the unitary Fermi gas and $\mu = E_F$ for the ideal Fermi gas, the ratio of the densities at $T = 0$ is $n(\mu, 0)/n_0(\mu, 0) = \xi^{-3/2}$ [88].

are directly determined from the density.
The density distribution is especially useful for thermometry. By calculating $n(\mathbf{r})$ for different temperatures and fitting the calculations to measured density distributions, we can estimate the temperature of our atom cloud in the experiment. This is demonstrated as an example in Figure 9.8.

As a remark, note that the EoS results presented in [166] indicate a Bertsch parameter of $\xi = 0.42(1)$. This value is almost 15% larger than more recent results, which find an agreement on $\xi = 0.367$ [92, 93]. In Reference [88] a value of $0.376(4)$ was reported, which is closer to the recent predictions. For this reason, we consider the latter EoS measurements to be more reliable for the unitary Fermi gas and therefore typically use these results.

9.4.2 The Equation of State of a low temperature Fermi gas

At zero temperature, for varying interparticle interactions, the transfer functions are functions of μ and a_s. These have been determined in [166] for spin-balanced and imbalanced two-component Fermi gases. Figure 9.9 shows the function $h_S(\tilde{\delta})$ for the spin-balanced Fermi gas, which relates the gas pressure at zero temperature

$$P(\mu, a_s) = P_0(\mu) h_s(\tilde{\delta}) \tag{9.42}$$

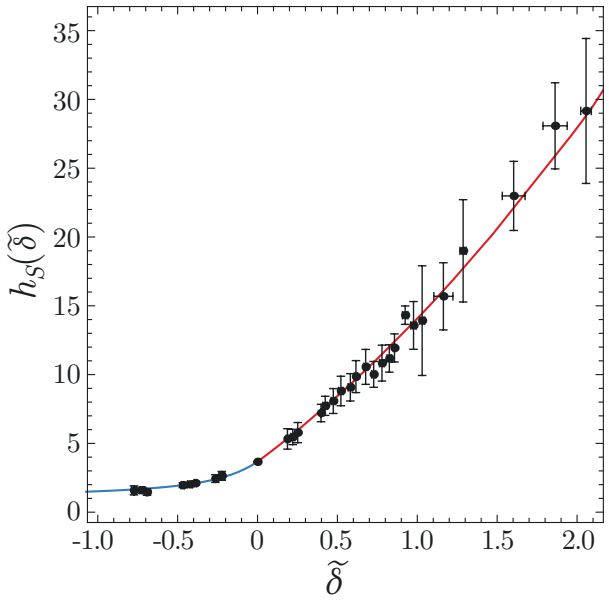

FIGURE 9.9: Measured equation of state for a spin-balanced zero temperature Fermi gas, taken and adapted from [166]. The figure shows the function $h_S(\tilde{\delta})$, as inferred from the measurements (black dots), as well as two Padé-approximations (solid blue and red lines) for the BCS ($\tilde{\delta} < 0$) and BEC regime ($\tilde{\delta} > 0$). This function relates the properties of a strongly-interacting, zero temperature Fermi gas to those of an ideal Fermi gas. Its argument $\tilde{\delta} = \frac{\hbar^2}{\sqrt{2m\mu}a_s}$ can be regarded as a dimensionless interacting parameter. For more details, see text and the Supplementary Material of [166] where also the parameters of the Padé-approximations are listed.

to the pressure of an ideal Fermi gas at $T = 0$, given by

$$P_0 = \frac{\partial n_0}{\partial \mu} = \frac{2}{15\pi^2}\left(\frac{2m}{\hbar}\right)^{3/2}\mu^{5/2} \tag{9.43}$$

where $\tilde{\delta} = \frac{\hbar^2}{\sqrt{2m\mu}a_s}$ can be seen as a normalized interaction parameter, expressed in terms of μ and a_s. For an ideal Fermi gas at zero temperature, $\mu = E_F$, so that $\frac{\hbar^2}{\sqrt{2m\mu}a_s} = (k_F a_s)^{-1}$. Both, $P(\mu, a_s)$ and $h_s(\tilde{\delta})$ again provide other Fermi gas properties, as outlined in the previous section.
As another important example, one can deduce the total energy E of the Fermi gas as a function of the scattering length a_s, as detailed in the Supplemental material of Reference [166]. Using Tan's adiabatic sweep theorem

$$\frac{\mathrm{d}E}{\mathrm{d}(-1/a_s)} = \frac{\hbar^2 C V}{4\pi m} \tag{9.44}$$

introduced in Section 2.6.1, this gives access to Tan's contact C for a homogeneous Fermi gas. From this, the total contact $\mathcal{I}$ for the harmonically trapped Fermi gas can be calculated by integration over the trap, as outlined in the Appendix of Reference [143]. The complete procedure is demonstrated in our work [14], which can also be found in Chapter 7.

Chapter 10

Conclusion and outlook

In my thesis, I have extensively investigated strongly interacting Fermi gases using an apparatus designed to generate ultracold, quantum degenerate clouds of ^{6}Li at high magnetic fields in the vicinity of the Feshbach resonance at 832.2 Gauss.
The main focus of this thesis is the experimental investigation of pair correlations in strongly interacting Fermi gases. Using a recently proposed photoexcitation scheme, I quite precisely measured short-range two-body correlations in a two-component Fermi gas for a wide range of interactions and temperatures. The central result was a comprehensive map of Tan's contact parameter in the entire phase diagram of the BCS-BEC crossover. This parameter not only quantifies the short-range two-body correlations in strongly interacting Fermi gases, but also appears in various fundamental relations describing such systems.
The experimental studies are complemented by a thorough theoretical investigation of the measured correlations based on various approaches. Together with our measurements, we were able to identify the validity ranges of the different established models to describe a Fermi gas in the BCS-BEC crossover. In addition, I have detailed our experimental methods and calibration techniques. Within this thesis, these methods have been both developed and significantly improved, enabling precise measurements with our experimental apparatus.
Moreover, I have detailed the technical implementations and experimental steps necessary for the preparation, manipulation, and detection of quantum degenerate, strongly interacting fermionic ^{6}Li gases.
I have described the improvement and integration of our high-power solid-state laser system into the experimental setup, providing the optical power needed for laser cooling. Along with a newly designed lithium oven, these enhancements have significantly improved the durability and robustness of our apparatus.
Furthermore, I have presented the test of our recently proposed holographic imaging scheme for atoms in optical lattices. In the test setup, atoms in an optical lattice are imitated by submicron holes in an opaque mask. Our results indicate that with a few hundred photons scattered per hole, high-fidelity single-site detection might be achievable.
And finally, I have detailed and compared four different approaches for theoretically modeling strongly interacting Fermi gases. These models have been tested against experimental data, used to extract key properties and to understand the underlying physics governing these complex quantum systems.

Outlook for future experiments

For future experiments, implementing our newly developed optical trapping potential for creating homogeneous Fermi gases can complement our previous work. This includes measurements of the pair fraction [15], first and second sound measurements [82], and measurements of two-body correlations using photoexcitation [13, 14]. All these aspects can then also be investigated in homogeneous systems, which are easier accessible from a theoretical perspective and therefore better suited for testing theoretical predictions.
By measuring the pair fraction and the underlying two-body correlations, we expect to observe a clear signature of superfluidity in the signals as the temperature of the atomic gas is lowered below the critical temperature for superfluidity [171]. This should enable us to determine this temperature and the underlying evolution of pair correlations. To this end, the critical temperature has not been experimentally determined precisely in the entire range of interactions in the BCS-BEC crossover.
This progression can also provide a pathway to experimentally observe the elusive Fulde–Ferrell–Larkin–Ovchinnikov (FFLO) phase for the first time in a three-dimensional Fermi gas. The FFLO phase is characterized by Cooper pairs with nonzero total momentum and a spatially non-uniform order parameter [133]. So far, the phase has only been observed in one-dimensional gases [216]. Observing the phase of a harmonically confined Fermi gas is particularly challenging. The reason for this is that the gas properties change locally due to the inhomogeneous density distribution. As a consequence, only small regions of the gas cloud can meet the requirements for temperature, spin polarization and interaction necessary for the FFLO phase [217, 218]. Using a homogeneous Fermi gas can therefore strongly enhance the signal. As the Fermi gas transitions into the FFLO phase, a change in the pair correlations might become evident in the photoexcitation rate.
In our previous work, we developed knowledge about excitation protocols for first and second sound excitations [82]. In the reported studies, second sound was excited in the center of a cigar shaped, harmonically trapped atom cloud. When exciting first and second sound in the center of the homogeneous atom cloud, density waves should become visible as concentric rings traveling to the outer region of the gas. Measuring the diameter of the rings as a function of the sound wave propagation time reveals the speeds of sound. Since these are directly linked to the normal fluid and superfluid densities [82], these experiments should enable us to determine the superfluid fraction in the BCS-BEC crossover. Having rings traveling at constant speed in the homogeneous system, instead of small localized wave packets in the previously used cigar shaped atom cloud configuration, could thereby enhance the precision for determining the speeds of sound. However, note that the strength of the rings should decrease as the diameter of the ring increases.
Additionally, after having successfully tested our proposed holographic imaging scheme [50] on idealized hole masks [17], our experimental and theoretical insights enable us to adapt this technique to real atomic systems in optical lattices or optical tweezer arrays.

Appendix A

Appendix

A.1 Technical drawing of the lithium oven

Figure A.1 shows a technical drawing of our lithium oven, which is described in Section 3.2.

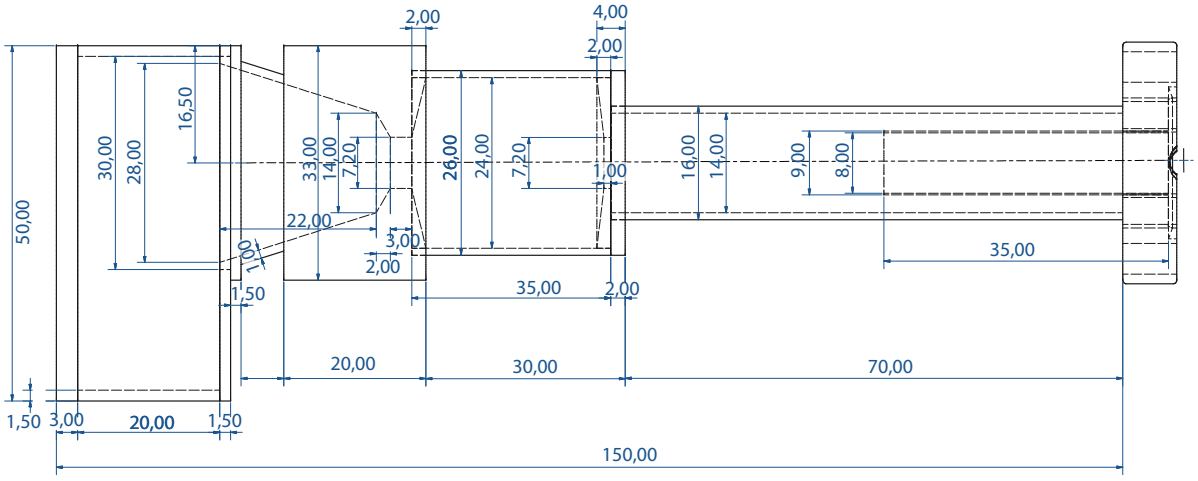

FIGURE A.1: Technical drawing of our Lithium oven, described in Section 3.2. All units are in millimeters. The oven is made of solid steel (AISI 316L).

A.2 Level scheme with relevant transitions

Figure A.2 shows a level scheme of ^{6}Li with all relevant optical laser transitions for cooling in the zero field and imaging in the high field as presented in Section 3.4. In addition, the radio frequency and microwave transitions are shown, that can be driven with the implemented antennas (see Section 3.7). The presented term scheme combines the term scheme shown in Figure 2.5 and the Zeeman splitting of the $S_{1/2}$ ground state shown in Figure 2.6. Additionally, the Zeeman splitting for the $P_{3/2}$ excited state is shown.

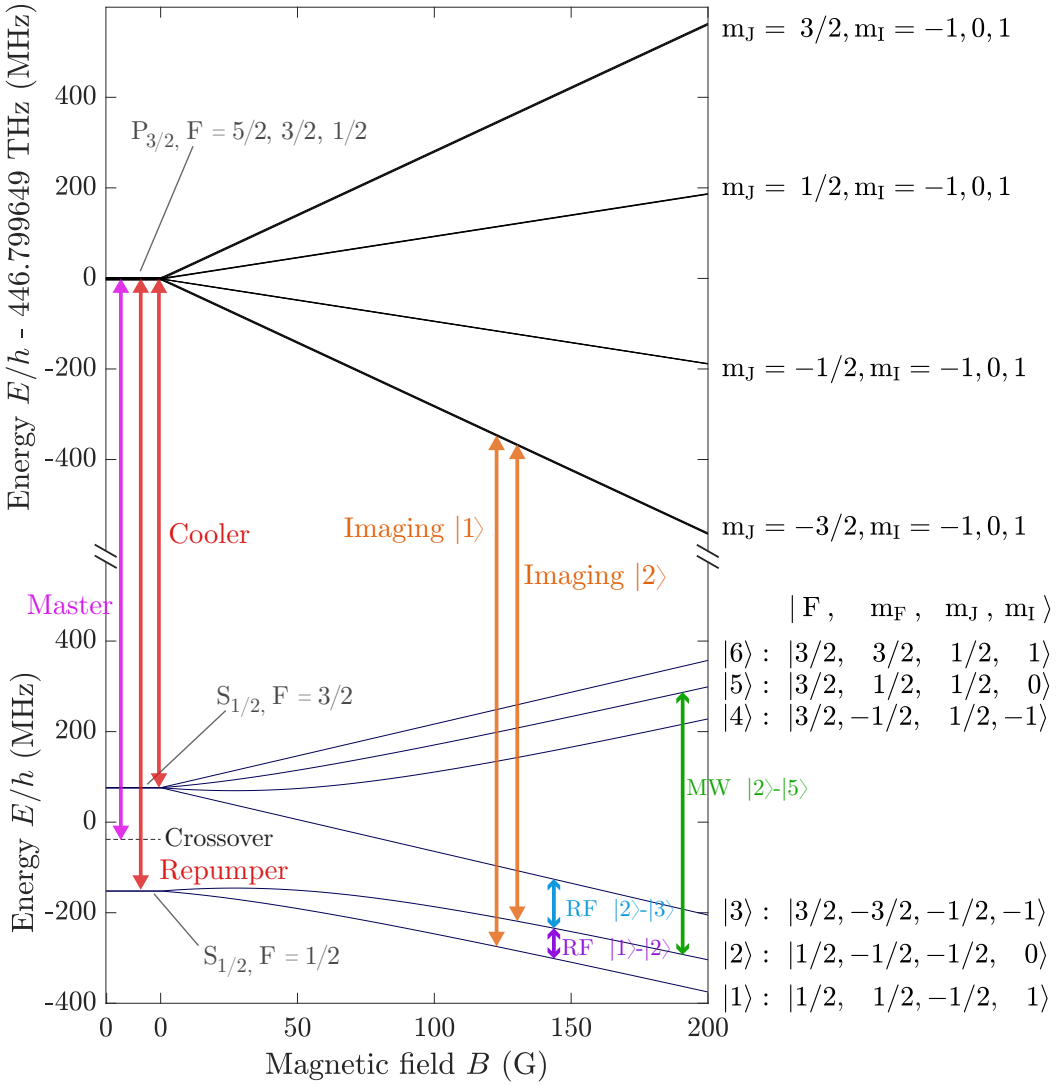

FIGURE A.2: Level scheme of ^{6}Li with all relevant laser transitions used in the experiment for atom preparation and imaging. These include the master laser (pink), which is spectroscopically stabilized to the transition from the $S_{1/2}$, $F_{1/2} - S_{1/2}$, $F_{3/2}$ crossover to the $P_{3/2}$ state, the cooler and repumper lasers (red) and the imaging laser (orange) for high field absorption imaging. The cooler/repumper and imaging lasers are stabilized to the master laser by means of a frequency offset locking scheme, as presented in Section 3.4. In addition, the radio frequency and microwave (MW) transitions are shown, that can be driven with the implemented antennas. For illustrative reasons, we only show the MW transition from $|2\rangle$ to $|5\rangle$. However, also transitions between $|1\rangle$ and $|6\rangle$, as well as $|3\rangle$ and $|4\rangle$ are possible with the MW antenna. The frequency of 446.799649 THz for the $S_{1/2}$−$P_{3/2}$ splitting is taken from [76].

A.3 Fundamental 1342 nm laser cleaning and alignment guide

In this appendix, the procedure to clean and realign the 1342 nm solid state laser, presented in Chapter 5, is explained. Due to the accumulation of dust on the optical elements in the fundamental cavity, this should be done approximately once a year wearing protective laser goggles for both the pump laser wavelength at 888 nm and the fundamental laser wavelength at 1342 nm.

- First, the laser has to be switched off by slowly turning the current of the pump diode laser to zero. At the same time, the Peltier element based temperature stabilization of the etalon and the laser crystal have to be switched off and the water temperature for the crystal chiller should be changed to the ambient temperature which is about 20°C. Note, that one should keep the crystal chiller always running to prevent clogging of the water pipes due to corrosion.

- Once the laser is switched off, both etalons have to be removed for cleaning. To later speed up the realignment process, their angles with respect to the optical axis should be noted roughly. Removing the etalons also gives access to the terbium gallium garnet (TGG) crystal which is mounted on a cylindrical metal rod (see [65]), that can then be removed from the Faraday rotator magnet housing.

- Next, all optical elements in the cavity have to be cleaned carefully. For cleaning, I made good experience with a mixture of methanol and acetone. This combines the good dust-dissolving properties of acetone with the good non-staining evaporation properties of methanol. The cleaning includes both surfaces of the laser crystal and the etalons, the wave plate and the TGG crystal. Due to the mounting of the TGG crystal and the wave plate, only one surface can be easily cleaned, which is sufficient to restore proper output power and stable operation. In addition, all four cavity mirrors have to be cleaned. Care has to be taken when cleaning the piezo-actuated mirror, as its surface is not easily accessible. For the incoupling and outcoupling mirrors, both sides should be cleaned.

- After cleaning, the TGG crystal can be reinserted and the laser can be started for a quick performance test without the two etalons. For this, the current of the diode pump laser has to be slowly increased to approximately 52 A. Simultaneously, the crystal chiller temperature should be set to $8 - 9$°C. The Peltier regulator for the crystal can stay switched off until the very last step of the alignment process where the laser is tuned to its target frequency. Lasing at 1342 nm typically starts at a pump current of 50 A.

- The laser now needs approximately 10-20 minutes to thermalize. After that, it should now reach an output power of $5.1 - 5.2$ W at 52 A of pump laser current. The laser frequency should then be around 223.355 THz, corresponding to the highest gain of the laser crystal (see Figure 5.3). This

can be measured with the infrared wavelength meter (see Figure 5.7). If the output power is not reached, optimize the power by rotating the TGG crystal mount around its symmetry axis. Additionally, beam walking can be done with the outcoupling mirror and the curved mirror which is not mounted to the piezo actuator (top right and bottom left mirrors in Figure 5.2).

- If the output power of $5.1 - 5.2\,\mathrm{W}$ is reached, switch off the laser again (see steps above), carefully re-insert the thin etalon (E_1) and start the laser again. It will typically now operate at a different wavelength and output power.

- While the laser is running, tilt the thin etalon around the vertical axis to optimize for the highest output power. When tilting the etalon, the output power changes almost periodically. Typically, a global maximum at $4.8 - 4.9\,\mathrm{W}$ of output power can be found, corresponding to a frequency of $223.355\,\mathrm{THz}$. If the output power is optimized, switch off the laser again (see steps above). Note, that the etalon's angle is now optimized for the highest output power, which does not correspond to the desired output frequency. Frequency tuning is done in the very last step.

- Reinsert the thick etalon (E_2) at about the same angle as before the optical cleaning and stabilize its temperature to $\approx 40°\mathrm{C}$. This will later provide a large bandwidth for temperature tuning. Then start the laser again, and carefully tilt the thick etalon horizontally to optimize for the highest output power. This should be found at $4.2 - 4.3\,\mathrm{W}$ and a frequency of $223.355\,\mathrm{THz}$.

When this power is reached, the cleaning and alignment was done properly and the laser can be tuned to the target frequency of $223.400\,\mathrm{THz}$.

- As a first test, change the temperature of etalon E_2 by $\pm 8°\mathrm{C}$. The laser frequency should now change by about $\mp 12\,\mathrm{GHz}$. This corresponds to an operation range of $223.355 \pm 12\,\mathrm{GHz}$. With this, one can verify that the transmission function of the thin etalon is centered around $223.355\,\mathrm{THz}$.

- Now, tilt E_1 around the vertical axis towards an increasing angle between its surface normal and the cavity beam propagation direction. If E_1 was inserted as before (see Figure 5.3), this corresponds to a clockwise rotation of the horizontal adjuster screw. This changes the effective optical path length of the etalon and consequently shifts its transmission function. A $180°$ clockwise rotation of the screw shifts the transmission function up by about $+20\,\mathrm{GHz}$. To confirm, perform a $180°$ rotation clockwise and probe again the lasers frequency windows by changing the temperature of E_2. The laser should now operate at approximately $223.375 \pm 12\,\mathrm{GHz}$.

- Finally, rotate the adjuster screw for E_1 clockwise by another $180 - 225°$ until the frequency range of the laser is centered around the desired frequency of $223.400\,\mathrm{THz}$. The laser should now have an output power of $3.5 - 3.8\,\mathrm{W}$.

If all these steps are done correctly, the laser now operates stable at the desired frequency. The Peltier regulator for the crystal can then be activated to further stabilize the crystal temperature.
After a few weeks, the laser operation may become slightly unstable again due to dust accumulating on the surface of the thin etalon which causes heating and a corresponding downshift of its transmission function. In this case, turning the etalon adjuster screw clockwise will shift the transmission function towards a higher central frequency (see above) and restore a stable operation.

A.4 Details on the quantum virial expansion and thermometry

For calculating important properties of strongly-interacting Fermi gases, the quantum virial expansion is usually done for the grand canonical potential [170]

$$\Omega_G = -k_B T \ln(\mathcal{Z}) = -k_B T \ln\left(\sum_N \mathcal{Z}_N z^N\right) = -k_B T \ln\left(1 + \mathcal{Z}_1 z + \mathcal{Z}_2 z^2 + \mathcal{Z}_3 z^3 + \dots\right) \tag{A.1}$$

where $\mathcal{Z}$ is the grand canonical partition function and

$$\mathcal{Z}_N = \frac{1}{h^{3N} N!} \int dr^{3N} \int dp^{3N} e^{-H_N(r,p)/k_B T} \tag{A.2}$$

are the canonical partition functions, where $H_N(r,p)$ is the N-body Hamiltonian [213, 214].
Expanding the logarithm in Equation (A.1) for $z \ll 1$ leads to

$$\begin{aligned}
\Omega_G &\approx -k_B T \left[\mathcal{Z}_1 z + \left(\mathcal{Z}_2 - \frac{\mathcal{Z}_1^2}{2}\right) z^2 + \left(\frac{\mathcal{Z}_1^3}{3} - \mathcal{Z}_1 \mathcal{Z}_2 + \mathcal{Z}_3\right) z^3 + \dots\right] \\
&= -k_B T \mathcal{Z}_1 \left[z + \left(\frac{\mathcal{Z}_2}{\mathcal{Z}_1} - \frac{\mathcal{Z}_1}{2}\right) z^2 + \left(\frac{\mathcal{Z}_1^2}{3} - \mathcal{Z}_2 + \frac{\mathcal{Z}_3}{\mathcal{Z}_1}\right) z^3 + \dots\right] \\
&= -k_B T \mathcal{Z}_1 \left[z + b_2 z^2 + b_3 z^3 + \dots\right].
\end{aligned} \tag{A.3}$$

With $\mathcal{Z}_1 = \frac{2S+1}{h^3} \int dr^3 \int dp^3 e^{-p^2/2mk_B T} = \frac{2V}{\lambda_{dB}^3}$ this becomes

$$\Omega_G = -\frac{2V k_B T}{\lambda_{dB}^3} \left[z + b_2 z^2 + b_3 z^3 + \dots\right] \tag{A.4}$$

where V is the volume of the system and the factor of 2 accounts the two different spin components.

A.4.1 Analytical calculation of b_2

The following considerations can be in detail found in [170, 175, 213]. For the second order virial coefficient

$$b_2 = \frac{\mathcal{Z}_2}{\mathcal{Z}_1} - \frac{\mathcal{Z}_1}{2} = \frac{1}{\mathcal{Z}_1}\left(\mathcal{Z}_2 - \frac{\mathcal{Z}_1^2}{2}\right) \tag{A.5}$$

one has to calculate $\mathcal{Z}_2$. While calculating the interactionless single particle partition function $\mathcal{Z}_1$ is rather simple, calculating $\mathcal{Z}_2$ also involves the 2-body scattering problem as well as the presence of bound states. The calculations simplify if we, for now, just calculate the difference between the interacting and non-interacting second order virial coefficient [175]

$$\begin{aligned} b_2^{\text{int}} = b_2 - b_2^{(0)} &= \frac{1}{\mathcal{Z}_1}\left(\mathcal{Z}_2 - \frac{\mathcal{Z}_1^2}{2}\right) - \frac{1}{\mathcal{Z}_1^{(0)}}\left(\mathcal{Z}_2^{(0)} - \frac{\left(\mathcal{Z}_1^{(0)}\right)^2}{2}\right) = \frac{1}{\mathcal{Z}_1}\left(\mathcal{Z}_2 - \mathcal{Z}_2^{(0)}\right) \\ &= \frac{\lambda_{dB}^3}{2V}\left(\mathcal{Z}_2 - \mathcal{Z}_2^{(0)}\right) = \frac{\lambda_{dB}^3}{2V}\,\text{Tr}\left(e^{-\beta\hat{H}_2} - e^{-\beta\hat{H}_2^{(0)}}\right) \end{aligned} \tag{A.6}$$

where the superscript $^{(0)}$ denotes the non-interacting quantities and $\mathcal{Z}_1^{(0)} \equiv \mathcal{Z}_1$. Later $b_2^{(0)}$ can be simply added to obtain b_2. The operator $\hat{H}_2$ over which the trace $\text{Tr}[\dots]$ is performed is the Hamilton operator of the two particle Schrödinger equation

$$\hat{H}_2\Psi_\alpha(r_1, r_2) = E_\alpha\Psi_\alpha(r_1, r_2) \tag{A.7}$$

and given by

$$\hat{H}_2 = -\frac{\hbar^2}{2m}\left(\bigtriangledown_1^2 + \bigtriangledown_2^2\right) + V(r_{12}) \tag{A.8}$$

with the central interaction potential $V(r_{12})$ and the two-particle wave function $\Psi_\alpha(r_1, r_2)$, where r_i is the position of the particles and $r_{12} = |r_2 - r_1|$ their distance.

Solving the Schrödinger equation

To solve this, a transformation to the center-of-mass coordinates $R = \frac{1}{2}(r_1 + r_2)$ and relative coordinates $r = r_2 - r_1$ of the two particles is performed [175, 213]. With that, the wave function $\Psi_\alpha(r_1, r_2)$ can be separated into two parts

$$\Psi_\alpha(r_1, r_2) = \Psi_\alpha(R, r) = \Psi_j(R)\Psi_n(r) = \left(\frac{1}{\sqrt{V}}e^{iP_jR/\hbar}\right)\Psi_n(r) \tag{A.9}$$

with the assumption of a simple plane wave for the center of mass wavefunction. The energy eigenvalues E_α are then given by

$$E_\alpha = \frac{P_j^2}{2(2m)} + \epsilon_n \tag{A.10}$$

and consist of the kinetic energy of center of mass and the relative kinetic energies ϵ_n of the two particles, where P_j denotes the center of mass momentum. With

that Eq. (A.6) becomes

$$\begin{aligned} b_2 - b_2^{(0)} &= \frac{\lambda_{dB}^3}{2V} \sum_{\alpha} \left(e^{-\beta E_\alpha} - e^{-\beta E_\alpha^{(0)}} \right) \\ &= \frac{\lambda_{dB}^3}{2V} \sum_{j} e^{-\beta P_j/4m} \sum_{n} \left(e^{-\beta \epsilon_n} - e^{-\beta \epsilon_n^{(0)}} \right) \end{aligned} \tag{A.11}$$

since the center of mass energies $P_j/4m$ are the same for interacting and non-interacting particles. The first sum over j is simply

$$\sum_j e^{-\beta P_j^2/4m} = \frac{V}{h^3} \int_0^\infty 4\pi e^{-\beta P^2/4m} P^2 dP = \sqrt{8} \frac{V}{\lambda_{dB}^3} \tag{A.12}$$

which is equal to the single particle partition function of an atom with mass $2m$. This leads to

$$b_2 - b_2^{(0)} = \frac{\lambda_{dB}^3}{2V} \sqrt{8} \frac{V}{\lambda_{dB}^3} \sum_n \left(e^{-\beta \epsilon_n} - e^{-\beta \epsilon_n^{(0)}} \right) = \sqrt{2} \sum_n \left(e^{-\beta \epsilon_n} - e^{-\beta \epsilon_n^{(0)}} \right). \tag{A.13}$$

For the further calculation one has to consider the energy spectra of ϵ_n and $\epsilon_n^{(0)}$.

Calculating the density of states $g(k)$ of ϵ_n and $\epsilon_n^{(0)}$

For the non-interacting system, the energies are given by a simple continuum $\epsilon_n^{(0)} = \frac{\hbar^2 k_n^2}{2(1/2)m}$ with a density states $g^{(0)}(k)$. In the interacting system, the density of states is $g(k)$. Additionally, bound states with energies ϵ_B may exist[1]. By rewriting the sum over n as an integral, Equation (A.13) becomes

$$b_2 - b_2^{(0)} = \sqrt{2}\Theta(a_s) \sum_B e^{\beta \epsilon_B} + \sqrt{2} \int_0^\infty dk\, e^{-\beta \hbar^2 k^2/m} \left[g(k) - g^{(0)}(k) \right]. \tag{A.14}$$

To find the densities of states $g(k)$ and $g^{(0)}(k)$ one can examine the corresponding wavefunction of the relative motion. Since a central interaction potential $V(r)$ was assumed, the wave function can be written as a product of a radial function $\chi_{kl}(r)$ and a spherical harmonic $Y_{lm}(\theta, \psi)$

$$\Psi_{klm}(r) = A_{klm} \frac{\chi_{kl}(r)}{r} Y_{lm}(\theta, \psi) \tag{A.15}$$

with $\Psi_{klm}(-r) = \Psi_{klm}(r)$ for bosons and $\Psi_{klm}(-r) = -\Psi_{klm}(r)$ for fermions. The radial function $\chi_{kl}(r)$ has to fulfill the boundary condition

$$\chi_{kl}(R_0) = 0 \tag{A.16}$$

[1] In our systems, the only bound state involved in the scattering process and in the description of the Fermi gas is the Feshbach bound state with $e_B = \hbar^2/(m a_s^2)$ for $a_s > 0$. Therefore $\sum_B e^{\beta \epsilon_B} = e^{\hbar^2/(m a_s^2 k_B T)} = e^{\lambda_{dB}^2/(2\pi a_s^2)}$

at a very large distance R_0 between the two atoms. The asymptotic form of $\chi_{kl}(r)$ is then

$$\chi_{kl}(r) \propto \sin\left(kr - \frac{l\pi}{2} + \delta_l(k)\right) \tag{A.17}$$

with the scattering phase shift $\delta_l(k)$. Combining the last two equations, the condition

$$kR_0 - \frac{l\pi}{2} + \delta_l(k) = n\pi, \qquad n = 0, 1, 2, \ldots \tag{A.18}$$

arises which leads to an expression for the wave number difference Δk for two consecutive states n and $n+1$ (see also [213])

$$\left(R_0 + \frac{\mathrm{d}\delta_l(k)}{\mathrm{d}k}\right)\Delta k = \pi. \tag{A.19}$$

With that the density of states $g_l(k)$ for the l'th partial wave is then given by

$$g_l(k) = \frac{2l+1}{\Delta k} = \frac{2l+1}{\pi}\left(R_0 + \frac{\mathrm{d}\delta_l(k)}{\mathrm{d}k}\right) \tag{A.20}$$

The factor $2l+1$ arises from the fact that each k that belongs to an l'th partial wave, the magnetic quantum numbers m can take the values $-l, (-l+1), .., l$. The total density of states for all the partial waves is thus given by

$$g(k) = \sum_l g_l(k) = \sum_l \frac{2l+1}{\pi}\left(R_0 + \frac{\mathrm{d}\delta_l(k)}{dk}\right). \tag{A.21}$$

For the non-interacting case $\frac{\mathrm{d}\delta_l(k)}{\mathrm{d}k} = 0$ and therefore

$$g(k) - g^{(0)}(k) = \sum_l \frac{2l+1}{\pi}\frac{\mathrm{d}\delta_l(k)}{\mathrm{d}k}. \tag{A.22}$$

This leads to

$$b_2 - b_2^{(0)} = \sqrt{2}\Theta(a_s)\sum_B e^{\beta\epsilon_B} + \sqrt{2}\sum_l \frac{2l+1}{\pi}\int_0^\infty dk\, e^{-\beta\hbar^2k^2/m}\frac{\mathrm{d}\delta_l(k)}{\mathrm{d}k}. \tag{A.23}$$

To get the full expression, the scattering phase shift $\delta_l(k)$ has to be calculated. At ultracold temperatures, fermions in different spin states only scatter in s-wave collisions ($l = 0$), see Section 2.2. For the s-wave Feshbach resonance, the phase shift is given by the expression

$$k\cot[\delta_0(k)] = -\frac{1}{a_s} + \frac{1}{2}r_0k^2 + \ldots \tag{A.24}$$

where r_0 is the effective range of the scattering potential[2]. This results in

$$\frac{\mathrm{d}\delta_0(k)}{\mathrm{d}k} = -\left(\frac{1}{a_s} + \frac{r_0 k^2}{2}\right) \times \left[\left(\frac{1}{a_s} - \frac{r_0 k^2}{2}\right)^2 + k^2\right]^{-1}. \tag{A.25}$$

With this result and the substitution $y = k|a_s|$ the integral in Eq. (A.23) becomes

$$\int_0^\infty dk\, \frac{d\eta_0(k)}{dk} e^{-\beta\hbar^2 k^2/m} = -\mathrm{sgn}(a_s) \int_0^\infty dy \frac{1 + y^2 r_0/(2a_s)}{[1 - y^2 r_0/(2a_s)]^2 + y^2} \exp\left(-\frac{\lambda_{dB}^2}{2\pi a_s^2} y^2\right). \tag{A.26}$$

For zero-range interaction ($r_0 \to 0$), the integral has the simple solution [170]

$$\int_0^\infty dk\, \frac{d\eta_0(k)}{dk} e^{-\beta\hbar^2 k^2/m} = -\mathrm{sgn}(a) \frac{\pi}{2} \left[1 - \mathrm{erf}\left(\frac{\lambda_{dB}}{\sqrt{2\pi}|a_s|}\right)\right] \exp\left(\frac{\lambda_{dB}^2}{2\pi a_s^2}\right) \tag{A.27}$$

which leads to the expression

$$b_2 = b_2^{(0)} + \sqrt{2}\Theta(a_s) \sum_B e^{\beta\epsilon_B} - \frac{\sqrt{2}}{2} \mathrm{sgn}(a_s) \left[1 - \mathrm{erf}\left(\frac{\lambda_{dB}}{\sqrt{2\pi}|a_s|}\right)\right] \exp\left(\frac{\lambda_{dB}^2}{2\pi a_s^2}\right) \tag{A.28}$$

for the second order virial coefficient b_2. The zero-range approximation also holds for a contact interaction where $r_0 \ll a_s$ [170].

Calculating $b_2^{(0)}$

The last thing to consider is the 2nd order virial coefficient $b_2^{(0)}$ for the non-interacting system. To calculate all the interactionless virial coefficients $b_n^{(0)}$ one can look again into the grand canonical partition function which can be written as

$$\begin{aligned} \mathcal{Z}^{(0)}(\mu, V, T) &= \sum_N \mathcal{Z}_N^{(0)}(N, V, T) z^N = \sum_N \sum_{\{n_i\}}^{\sum n_i = N} \prod_i \left(e^{-\beta(\epsilon_i - \mu)}\right)^{n_i} \\ &= \sum_{n_1} \sum_{n_2} \cdots \sum_{n_i} \prod_i \left(e^{-\beta(\epsilon_i - \mu)}\right)^{n_i} = \prod_i \sum_{n_i} \left(e^{-\beta(\epsilon_i - \mu)}\right)^{n_i}. \end{aligned} \tag{A.29}$$

Where n_i are the occupation numbers for the states i. For fermions, the sum over the occupation numbers n_i runs just from 0 to 1 due to the Pauli exclusion principle [25], which simplifies the partition function to

$$\mathcal{Z}_F^{(0)}(\mu, V, T) = \prod_i \left(1 + e^{-\beta(\epsilon_i - \mu)}\right) \tag{A.30}$$

[2] As explained in Chapter 2, this range has a value of $r_0 = (mC_6/\hbar^2)^{1/4} \approx 62.5\, a_0$ for ^{6}Li with $C_6 = 1.333 \times 10^{-76}\,\mathrm{Jm}^6$ [73].

and leads to a grand canonical potential given by

$$\begin{aligned}\Omega_F^{(0)} &= -k_B T \ln(\mathcal{Z}_F^{(0)}) = -k_B T \sum_i \ln\left(1 + e^{-\beta(\epsilon_i - \mu)}\right) \\ &= -k_B T \sum_i \ln\left(1 + z e^{-\beta\epsilon_i}\right). \end{aligned} \tag{A.31}$$

With the energies that now just account for single particle motions without interaction, the kinetic energy $\epsilon_i = \hbar^2 k^2/2m$, the relation$\sum_i = 2V/(2\pi)^3 \int_0^\infty 4\pi k^2 dk$ (factor of 2 for the two spin states) and the substitution $t = \beta\epsilon_i$ this is

$$\begin{aligned}\Omega_F^{(0)} &= -\frac{2Vk_BT}{\lambda_{dB}^3}\frac{2}{\sqrt{\pi}}\int_0^\infty dt\sqrt{t}\ln\left(1 + ze^{-t}\right) \\ &= -\frac{2Vk_BT}{\lambda_{dB}^3}\frac{2}{\sqrt{\pi}}\int_0^\infty dt\sqrt{t}\left[ze^{-t} - \frac{1}{2}z^2e^{-2t} + \frac{1}{3}z^3e^{-3t} - \dots\right] \\ &= -\frac{2Vk_BT}{\lambda_{dB}^3}\frac{2}{\sqrt{\pi}}\left[\frac{\sqrt{\pi}}{2}z - \frac{1}{2}\sqrt{\frac{\pi}{32}}z^2 + \frac{1}{3}\sqrt{\frac{\pi}{108}}z^3 - \dots\right] \\ &= -\frac{2Vk_BT}{\lambda_{dB}^3}\left[z - \sqrt{\frac{1}{32}}z^2 + \sqrt{\frac{1}{243}}z^3 - \dots\right] \\ &= -\frac{2Vk_BT}{\lambda_{dB}^3}\left[-\mathrm{Li}_{5/2}(-z)\right]. \end{aligned} \tag{A.32}$$

Comparing this to the previous result of the grand canonical potential from Eq. (A.4) namely

$$\Omega_G = -\frac{2Vk_BT}{\lambda_{dB}^3}\left[z + b_2z^2 + b_3z^3 + ...\right] \tag{A.33}$$

one can directly identify

$$b_n^{(0)} = \frac{(-1)^{n+1}}{n^{5/2}}. \tag{A.34}$$

With that, the 2nd order virial coefficient is given by

$$\begin{aligned} b_2 &= b_2^{(0)} + b_2^{\mathrm{int}} \\ &= -\frac{1}{\sqrt{32}} + \sqrt{2}\Theta(a_s)\sum_B e^{\beta\epsilon_B} - \frac{\sqrt{2}}{2}\mathrm{sgn}(a_s)\left[1 - \mathrm{erf}\left(\frac{\lambda_{dB}}{\sqrt{2\pi}|a_s|}\right)\right]\exp\left(\frac{\lambda_{dB}^2}{2\pi a_s^2}\right) \\ &= \sqrt{2}\left[-\frac{1}{8} + \Theta(a_s)\sum_B e^{\beta\epsilon_B} - \frac{1}{2}\mathrm{sgn}(a_s)\left[1 - \mathrm{erf}\left(\frac{\lambda_{dB}}{\sqrt{2\pi}|a_s|}\right)\right]\exp\left(\frac{\lambda_{dB}^2}{2\pi a_s^2}\right)\right]. \end{aligned} \tag{A.35}$$

Non-interacting virial coefficients for bosons

For bosons, the sum over n_i in Equation (A.29) runs to infinity. Using the geometric series, we find

$$\mathcal{Z}_B^{(0)}(\mu, V, T) = \prod_i \frac{1}{1 - e^{-\beta(\epsilon_i - \mu)}} \tag{A.36}$$

and therefore

$$\Omega_B^{(0)} = -k_B T \ln(\mathcal{Z}_B^{(0)}) = k_B T \sum_i \ln\left(1 - z e^{-\beta\epsilon_i}\right). \tag{A.37}$$

Equation (A.32) for bosons then reads

$$\begin{aligned}
\Omega^{(0)} &= \frac{2Vk_BT}{\lambda_{dB}^3}\frac{2}{\sqrt{\pi}}\int_0^\infty dt\sqrt{t}\ln\left(1 - ze^{-t}\right) \\
&= \frac{2Vk_BT}{\lambda_{dB}^3}\frac{2}{\sqrt{\pi}}\int_0^\infty dt\sqrt{t}\left[-ze^{-t} - \frac{1}{2}z^2e^{-2t} - \frac{1}{3}z^3e^{-3t} - \dots\right] \\
&= \frac{2Vk_BT}{\lambda_{dB}^3}\frac{2}{\sqrt{\pi}}\left[-\frac{\sqrt{\pi}}{2}z - \frac{1}{2}\sqrt{\frac{\pi}{32}}z^2 - \frac{1}{3}\sqrt{\frac{\pi}{108}}z^3 - \dots\right] \\
&= -\frac{2Vk_BT}{\lambda_{dB}^3}\left[z + \sqrt{\frac{1}{32}}z^2 + \sqrt{\frac{1}{243}}z^3 + \dots\right] = -\frac{2Vk_BT}{\lambda_{dB}^3}\mathrm{Li}_{5/2}(z) \\
&= -\frac{2Vk_BT}{\lambda_{dB}^3}\left[b_1^{(0)}z + b_2^{(0)}z^2 + b_3^{(0)}z^3 + \dots\right]
\end{aligned} \tag{A.38}$$

with

$$b_n^{(0)} = \frac{1}{n^{5/2}} \tag{A.39}$$

being the virial coefficients for non-interacting bosons.

A.4.2 Thermometry

The quantum virial expansion is useful for determining the temperature of a strongly-interacting, harmonically trapped Fermi gas. This method involves fitting theoretically calculated, temperature-dependent density distributions to experimentally measured ones and identifying the temperature that minimizes the deviation.
The total density distribution of a two-component, spin-balanced Fermi gas within the quantum virial expansion is given by (see Section 9.3.1)

$$n(\mathbf{r}) = \frac{2}{\lambda_{dB}^3}\left[-\mathrm{Li}_{3/2}\left(-e^{(\mu - V(\mathbf{r}))/k_BT}\right) + 2b_2^{\mathrm{int}}e^{2(\mu - V(\mathbf{r}))/k_BT} + ...\right]. \tag{A.40}$$

In our experiments, we typically determine the (two-dimensional) column density $n_{2D}(x,y) = \int \mathrm{d}z\, n(\mathbf{r})$ via absorption imaging. We calculate from this the one-dimensional line density $n(x) = \int \mathrm{d}y\, n_{2D}(x,y) = \int\int \mathrm{d}z\mathrm{d}y\, n(\mathbf{r})$, which additionally reduces noise. For a cigar shaped cloud with trap frequency $\omega_y = \omega_z = \omega_r$ this yields

$$\begin{aligned} n(x) &= \int\int \mathrm{d}y\mathrm{d}z\, n(\mathbf{r}) \\ &= \frac{4\pi k_B T}{m\omega_r^2 \lambda_{dB}^3} \left[-\mathrm{Li}_{5/2}\left(-e^{(\mu - m\omega_x^2 x^2/2)/k_B T}\right) + b_2^{\mathrm{int}} e^{(2\mu - m\omega_x^2 x^2)/k_B T} \right]. \end{aligned} \tag{A.41}$$

within the second order quantum virial expansion. For given trap frequencies ω_r, ω_x and scattering length a_s, we can fit this function to the measured density distribution to determine the (absolute) temperature T of the atom cloud as well as the chemical potential μ. By further determining the total atom number N from the absorption image (see Section 4.6), we can express the temperature in units of $T_F = E_F/k_B = \hbar(3N\omega_r^2\omega_x)^{1/3}/k_B$.

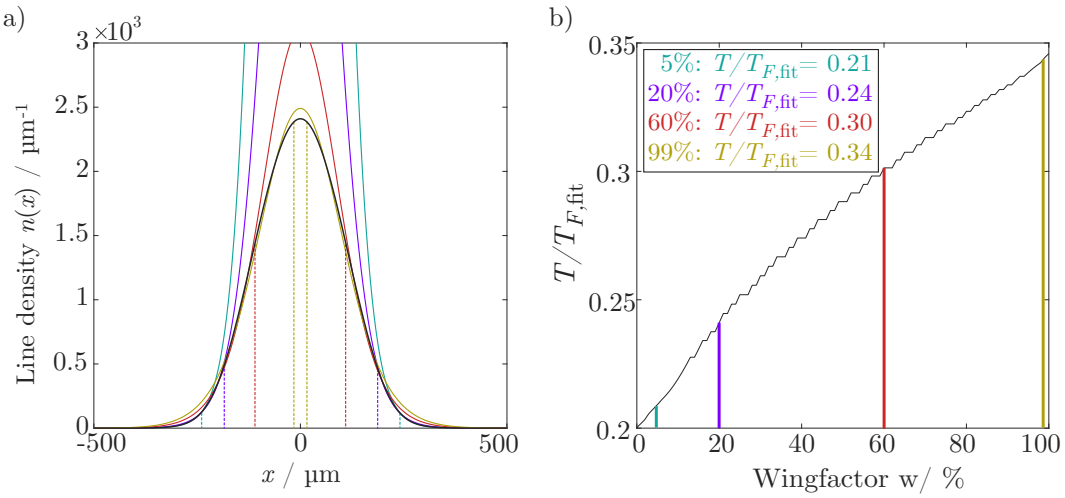

FIGURE A.3: Thermometry of a unitary Fermi gas. a) Calculated (black solid line) and fitted (colored solid lines) density distributions. The calculation is based on the EoS from Ku *et al.* [88], while the fit employs the quantum virial expansion according to Equation (A.41). The yellow (red, purple, turquoise) colors indicate the excluded regions of the line density distribution $n(x)$ where the density exceeds $w = 99\%$ (60%, 20%, 5%) of the peak density, where w is the wing factor. b) Extracted temperature as a function of the wing factor w. For $w \to 0\%$, we recover the correct temperature of $0.20\,T_F$.

Since the quantum virial expansion is only valid for a small fugacity $z \ll 1$, we have to restrict the fit to the outer tails of the line density distribution, where the local fugacity $z(x) = \exp\left[(\mu - m\omega_x^2 x^2/2)/k_B T\right]$ is small. We typically observe a tendency towards higher fit temperatures, when allowing the fit to include more data points from the inner regions of the density distribution where the fugacity is larger. However, the more we restrict the fit to the outer regions of smaller density (the *wings* of the cloud), the more the fitted temperature convergences

towards the true temperature.
We confirm this behaviour with calculations of the density distributions based on the EoS (see Section 9.4.1 for a unitary Fermi gas and based on a mean-field approach (see Sections 9.1 and 9.2). This is shown as an example in Figure A.3 for a unitary Fermi gas with $T = 0.2\,T_F$. Here, we introduce the quantity w, referred to as the wing factor, which determines the regions of the density included in the fit. Specifically, for a wing factor w, we only include regions, where $n(x) < w\,n_{\mathrm{peak}}$, where n_{peak} is the central peak density. For $w \to 0\%$, the extracted temperatures approach the correct temperature of $0.20\,T_F$.
In our experiments, the density distributions typically exhibit noise, which complicates the fitting process in regions of low density. The correct temperature can then be determined from an extrapolation of the fitted temperatures towards $w = 0\%$. Based on numerical calculations incorporating noise levels comparable to those in our experiments, we estimate an accuracy of $\approx 0.04\ T/T_F$ at small temperatures ($T < 0.5T_F$) and up to $0.08\ T/T_F$ at high temperatures ($T \gtrsim 1\,T_F$). These values hold for thermometry on a density distribution determined from a single absorption image of the atomic cloud. Averaging over 5 absorption images of identically prepared atom clouds increases the precision to $\approx 0.02\,T/T_F$ at small temperatures ($T < 0.5T_F$) and up to $0.05\ T/T_F$ at high temperatures ($T \gtrsim 1\,T_F$). The high stability of our system helps significantly in this process.

Appendix B

Additional publication reprints

This appendix contains original reprints of other publications to which I contributed during this thesis.

B.1 Pair fraction in a finite-temperature Fermi gas on the BEC side of the BCS-BEC crossover.

Note that the information shown is published in Reference [15].

Thomas Paintner, Daniel K. Hoffmann, Manuel Jäger, Wolfgang Limmer, Wladimir Schoch, Benjamin Deissler, Michele Pini, Pierbiagio Pieri, Giancarlo Calvanese Strinati, Cheng Chin, and Johannes Hecker Denschlag

"Pair fraction in a finite-temperature Fermi gas on the BEC side of the BCS-BEC crossover", *Physical Review A* **99**, 053617 (2019)

PHYSICAL REVIEW A **99**, 053617 (2019)

Pair fraction in a finite-temperature Fermi gas on the BEC side of the BCS-BEC crossover

Thomas Paintner,[1] Daniel K. Hoffmann,[1] Manuel Jäger,[1] Wolfgang Limmer,[1] Wladimir Schoch,[1] Benjamin Deissler,[1] Michele Pini,[2] Pierbiagio Pieri,[2,3] Giancarlo Calvanese Strinati,[2,3,4] Cheng Chin,[5] and Johannes Hecker Denschlag[1,*]

[1]*Institut für Quantenmaterie and Center for Integrated Quantum Science and Technology (IQ^{ST}), Universität Ulm, D-89069 Ulm, Germany*

[2]*School of Science and Technology, Physics Division, Università di Camerino, I-62032 Camerino (MC), Italy*

[3]*INFN, Sezione di Perugia, I-06123 Perugia (PG), Italy*

[4]*CNR-INO, Istituto Nazionale di Ottica, Sede di Firenze, I-50125 Firenze (FI), Italy*

[5]*James Franck Institute, Enrico Fermi Institute, and Department of Physics, The University of Chicago, Chicago, Illinois, USA*

(Received 23 February 2019; published 28 May 2019)

We investigate pairing in a strongly interacting two-component Fermi gas with positive scattering length. In this regime, pairing occurs at temperatures above the superfluid critical temperature; unbound fermions and pairs coexist in thermal equilibrium. Measuring the total number of these fermion pairs in the gas we systematically investigate the phases in the sectors of pseudogap and preformed pair. Our measurements quantitatively test predictions from two theoretical models. Interestingly, we find that already a model based on classical atom-molecule equilibrium describes our data quite well.

DOI: 10.1103/PhysRevA.99.053617

I. INTRODUCTION

A unique feature of fermionic superfluids is the pairing. For a weakly interacting Bardeen-Cooper-Schrieffer (BCS) superfluid pairing occurs directly at the critical temperature for superfluidity T_c [1]. This pairing is accompanied with the emergence of an excitation gap Δ_{sc} which is identified with the superfluid order parameter and Δ_{sc}^2 is proportional to the density of condensed pairs [2]. For fermions with strong coupling, an excitation gap already emerges at a temperature above T_c. This is referred to as the pseudogap regime [3]. The existence of the pseudogap has been observed early on, e.g., in underdoped high-T_c superconductors [4,5]. While its nature has been intensely studied, it is still not fully understood. Understanding the pseudogap is expected to be the key for revealing the mechanism behind high-T_c superconductivity [6,7]. One interpretation of the pseudogap is based on the presence of noncondensed pairs with nonvanishing momentum [8].

Ultracold Fermi gases are an excellent system for investigating the gap and pseudogap physics from the BCS to Bose-Einstein condensate (BEC) regimes [9]. Using radio-frequency (RF) spectroscopy in various forms, e.g., [10–13], the excitation gap has been studied in the way similar to angle-resolved photoemission spectroscopy (ARPES) of solid-state systems [14]. Evidence for pairing above T_c was found in the RF experiments, as well as in other physical quantities, such as viscosity [15], heat capacity [16], and Tan's contact [17,18].

In this article, we investigate pairing of fermions for various temperatures and interaction strengths on the BEC side of the BEC-BCS crossover. For this, we measure the total number of bound fermion pairs N_p in our sample for $T > T_c$. Such counting of fermion pairs is in general not possible for solid-state systems and therefore complements existing methods. We determine the fermion pair number by converting all atom pairs to tightly bound diatomic molecules, either by photoexcitation [19] or by a fast magnetic-field ramp [20,21] and measuring the decrease in atom number of the cloud. When we compare the measured and calculated pair numbers we find quite good agreement with two models: an *ab initio* t-matrix approach and a classical statistical model of atom-molecule equilibrium [22]. We provide an explanation why the classical model achieves good results, despite the fact that strong interactions and quantum statistics play an important role in our system.

In the following, we consider an ultracold, spin-balanced, strongly interacting two-component Fermi gas in a harmonic trap. Collisions lead to pairing of atoms with opposite spins, $|\uparrow\rangle$, $|\downarrow\rangle$. For a given temperature and interaction strength well-defined fractions of pairs and atoms are established at thermal equilibrium, as long as collisional losses are negligible. Figure 1 shows the phase diagram of such a system in the vicinity of a Feshbach resonance at $(k_F a)^{-1} = 0$. Here, a is the s-wave scattering length, $k_F = \sqrt{2mE_F}/\hbar$ denotes the norm of the Fermi wave vector, m is the atomic mass, and $E_F = k_B T_F$ is the Fermi energy in the trap center with k_B the Boltzmann constant. The dash-dotted and solid lines are contours of constant molecular fractions N_p/N_σ for two different approaches. Here, $N_\sigma = N_p + N_a$ is the number of all atoms per spin state regardless of whether they are bound in pairs (N_p) or free (N_a). The dotted lines are calculations based on a self-consistent t-matrix approach [23], while the solid lines correspond to a statistical mechanics approach treating the particles as a canonical ensemble of noninteracting molecules and atoms in chemical equilibrium (see [22] and Appendix A). Here, the molecules have a binding energy of $E_b = -\hbar^2/(ma^2)$. Also shown is a calculation (cyan dash-dotted line) by Perali *et al.* [24] of the BCS mean-field critical temperature which provides an approximate estimate of the pair breaking temperature. It partially coincides

*Corresponding author: johannes.denschlag@uni-ulm.de

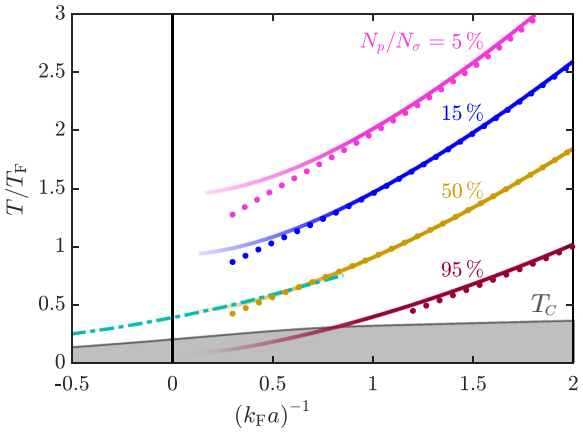

FIG. 1. Theoretical phase diagram for a balanced two-component harmonically trapped ultracold Fermi gas in the vicinity of a Feshbach resonance (vertical line) where k_F and T_F are determined in the trap center. Shown are calculated contours for various pair fractions. Dotted lines are based on a self-consistent t-matrix approach [23], while solid lines are based on a classical model of noninteracting atoms and molecules (see text) [22]. Close to the Feshbach resonance the solid lines are blurred because the classical model is expected to lose its validity. The cyan dash-dotted line marks a pair breaking temperature, as calculated by [24] with a BCS mean-field model that was extended to the near-BEC regime. The gray shaded area marks the superfluid phase below the critical temperature T_c which was calculated within the self-consistent t-matrix approach [25].

with the 50 % pair fraction line of the statistical mechanics approach.

We carry out our experiments with a spin-balanced two-component Fermi gas of ^{6}Li atoms which is initially prepared at a magnetic field of 780 G. The atoms have magnetic quantum numbers $m_F = +1/2$ ($|\uparrow\rangle$) and $m_F = -1/2$ ($|\downarrow\rangle$) and correlate to the $F = 1/2$ hyperfine level of the ground state at 0 G. They are confined in a harmonic three-dimensional cigar-shaped trapping potential which is generated in radial direction mainly by a focused 1070-nm dipole trap laser beam and along the axial direction mainly by a magnetic field gradient. The temperature T is set via evaporative cooling and is measured by fitting a distribution obtained from the second-order quantum virial expansion to the outer wings of the density profile [26]. The particle number N_σ per spin state ranges from 3×10^4 for the lowest temperature of about $0.3\,T_F$ to 3×10^5 for the highest temperature of about $3\,T_F$. The population balance of the two spin states is assured by means of a 100-ms-long resonant RF pulse that mixes the two Zeeman states $|\uparrow\rangle$ and $|\downarrow\rangle$. For a spin-balanced system the Fermi energy is given by $E_F = \hbar(6N_\sigma\omega_r^2\omega_a)^{1/3}$, where ω_r and ω_a denote the radial and axial trapping frequency, respectively. In our experiment ω_r ranges from about $2\pi \times 300$ Hz to $2\pi \times 1.6$ kHz while $\omega_a = 2\pi \times 21$ Hz is almost constant as it is dominated by the magnetic confinement. The interaction parameter $(k_F a)^{-1}$ can be tuned by changing either the scattering length a via the broad magnetic Feshbach resonance located at 832 G [27,28], or by adjusting the Fermi energy E_F.

II. MEASURING THE PAIR FRACTION

In order to determine the pair fraction N_p/N_σ we measure the particle numbers N_p and N_σ separately. N_σ is obtained by means of spin-selective absorption imaging of the $|\uparrow\rangle$ component using a σ^--polarized 671-nm laser beam resonant with the D_2 transition of ^{6}Li [29]. This transition is essentially closed due to a decoupling of the nuclear spin and the total electronic angular momentum in the Paschen-Back regime of the hyperfine structure [30]. All $|\uparrow\rangle$ atoms will be counted regardless of whether they are free or bound in the weakly bound pairs. Since the binding energy E_b of these pairs is always less than $h \times 1$ MHz in our experiments, the imaging laser is resonant with both free atoms and bound pairs. In order to determine the number of bound pairs N_p, we transfer all pairs to states that are invisible in our detection scheme and measure again the remaining $|\uparrow\rangle$ state atom number via absorption imaging. We use two different bound-state transfer methods which produce consistent results. They are briefly described in the following.

A. Optical transfer (OT) method

This transfer method is based on resonant excitation of fermion pairs to a more strongly bound molecular state ($A^1\Sigma_u^+$, $v' = 68$) with a laser ($\lambda = 673$ nm) which is detuned by 2 nm from the atomic transition; see also [19]. Subsequently, the excited molecules quickly decay to undetected atomic or molecular states; see Fig. 2(a). This optical excitation of the fermion pairs occurs via an admixture of the molecular bound state $X^1\Sigma_g^+$, $v = 38$ to the fermion pair wave function [19].

If, for now, we ignore other loss processes, the number of fermion pairs decays exponentially as a function of the laser pulse length Δt such that the measured total number $N_\sigma(\Delta t)$ of $m_F = +1/2$ atoms as a function of time is given by

$$N_\sigma(\Delta t) = N_\sigma(0) - N_p(1 - e^{-k_1 \Delta t}), \tag{1}$$

where $1/k_1$ is the time constant for the optical excitation. Figure 2(b) shows this decay for five different initial temperatures T/T_F at a magnetic field of 726 G. By fitting Eq. (1) to the measured data (see fit curves) we are able to extract the pair number N_p. Besides the photoexcitation of pairs a loss in N_σ could in principle also be induced by photoassociation of two free atoms. However, we made sure that within our field range its rate is negligible. The photoassociation rate constants range between 1×10^{-9} and 3×10^{-9} cm^5(W s)$^{-1}$ for magnetic fields between 726 and 820 G. We work with low particle densities of at most 10^{11} cm^{-3} and a maximum laser intensity of about 1.9 W/cm^2.

For the data shown in Fig. 2(b) the laser intensity is 0.22 W/cm^2 and the peak density for the lowest temperature of $T/T_F = 0.64$ is 1.4×10^{11} cm^{-3} which corresponds to an initial photoassociation time constant of about 33 ms. This is much longer than the loss dynamics observed in Fig. 2(b). Indeed, the fact that the curves in Fig. 2(b) approach constant values for pulse times $t \gtrsim 0.3$ ms already suggests that the photoassociation of free atoms is negligible.

However, closer to resonance the time constants for photoassociation and pair excitation become more comparable.

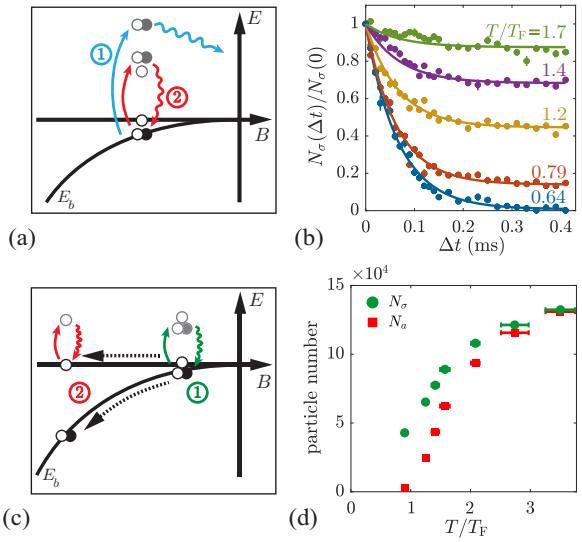

FIG. 2. Measurement of the number of fermion pairs. (a) and (b) Optical transfer method. A resonant laser pulse transfers pairs to states which are invisible to our detection scheme [blue arrows (1)]. The total number $N_\sigma(\Delta t)$ of remaining fermion pairs and single atoms is measured by absorption imaging [red arrows (2)]. (b) $N_\sigma(\Delta t)/N_\sigma(0)$ as a function of the pulse width Δt at a magnetic field of 726 G for various temperatures $T/T_F = \{0.64, 0.79, 1.2, 1.4, 1.7\}$. The solid lines are fit curves using Eq. (1). (c) and (d) Magnetic transfer method. Using absorption imaging, the particle number $N_\sigma = N_a + N_p$ is measured at the magnetic field (1) and the number of unbound atoms N_a is measured after a fast ramp to (2). (d) The measured particle numbers at (1) ($B = 726$ G, green solid circles) and at (2) ($B = 550$ G, red solid squares) for various temperatures T/T_F.

Therefore, we generally release the particles from the trap 0.3 ms before applying the laser pulse. The subsequent expansion lowers the cloud density by about a factor of 4 and assures additionally that photoassociation is negligible. Furthermore, lowering the density also strongly suppresses regeneration of depleted Fermi pairs during the laser pulse, since pair regeneration mainly occurs via three-body recombination. We have checked that during the expansion the fermion pairs do not break up. For this, we carried out measurements at a magnetic field of 780 G, working at the lowest temperatures of about 0.3 T_F, where only about 10%−15% of the atoms are unbound and thus photoassociation does not play a significant role. We measured the same pair numbers with and without expansion.

In general the OT method works very well up to magnetic fields of about $B = 820$ G, close to the Feshbach resonance. There, we observe marked deviations from the exponential decay in Eq. (1), a behavior that also had been reported earlier by the Rice group [19]. An analysis of these signals would require a better understanding of the nature of strongly interacting pairs. For this reason, we decide to stay below magnetic fields of 820 G for the present investigations where the analysis is unequivocal.

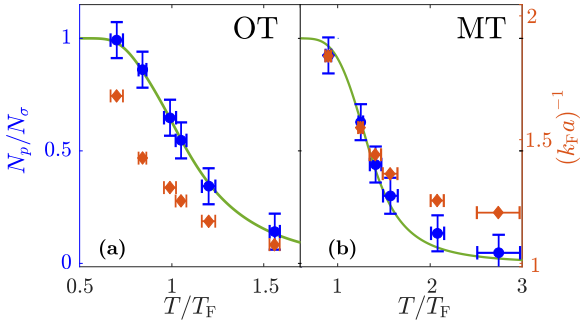

FIG. 3. Measured pair fractions N_p/N_σ (blue circles) at 726 G for various temperatures T/T_F. (a) Optical transfer (OT) method; (b) magnetic transfer (MT) method (see Fig. 2). We note that due to evaporative cooling $(k_F a)^{-1}$ also changes with T/T_F (orange diamonds). The green curves are calculations based on the classical model.

B. Magnetic transfer (MT) method

Here, we increase the binding energy of the pairs to $h \times 80.6$ MHz by quickly ramping the magnetic field at 20 G/ms down to 550 G; see Fig. 2(c). This works very efficiently without breaking up the molecules as previously shown in [20,21]. At 550 G the fermion pairs cannot be resonantly excited anymore by the imaging laser and become invisible to our detection scheme; see [31]. N_p is determined as the difference of the numbers for atoms and pairs (N_σ) measured before the ramp and unbound atoms (N_a) obtained after the ramp. Figure 2(d) shows these particle numbers for different temperatures at a magnetic field of 726 G.

We did not perform measurements with the MT method for magnetic fields higher than 750 G because of technical limitations for the ramping speed. If the field ramp duration (≈10 ms for the case of 750 G) becomes comparable to the equilibration time for the atom-molecule mixture (a few milliseconds at 750 G) the measurement does not yield the correct molecule number anymore. This restriction of the magnetic field ramp implies that we cannot use the MT method in the strong interaction crossover regime, but only in the far BEC regime. There, however, the MT method is quite useful to check for consistency with the OT method. This consistency is shown in Fig. 3 where we plot the pair fractions N_p/N_σ obtained at 726 G from both methods as a function of the temperature (blue circles). Since the temperature was adjusted by varying the evaporative cooling, different temperatures correspond to different particle numbers N_σ and thus to different interaction parameters $(k_F a)^{-1}$(orange diamonds). The green lines are calculated pair fractions using the classical model. In general, we find good agreement between the experimental data and the theoretical prediction, which also indicates consistency between the OT and MT methods.

III. RESULTS

We now apply the OT and MT methods to map out the fraction of pairs on the BEC side. For this, we perform measurements for a variety of magnetic fields and temperatures. The pair fractions N_p/N_σ obtained from both experimental

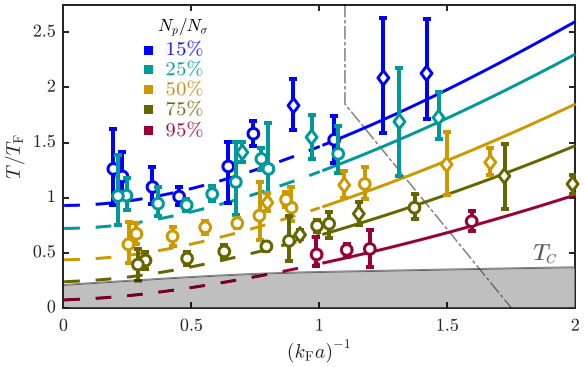

FIG. 4. Map of the pair fraction N_p/N_σ as a function of temperature and interaction strength on the BEC side of the Feshbach resonance. The circles (diamonds) are measurements obtained with the OT (MT) method. The thick solid and dashed lines are classical model calculations (cf. Fig. 1). They are dashed in the strong-interaction regime where the classical model is expected to be no longer valid. The error bars include both a statistical and a systematic part, i.e., the standard deviation of the mean of 10 temperature measurements and the uncertainty in determining the molecule fraction from the fit, respectively. The upper-right area bounded by the gray dash-dotted line exhibits >5 % particle loss due to inelastic collisions on the time scale of a measurement. The gray shaded area indicates the superfluid phase below T_c, as in Fig. 1.

methods are shown in Fig. 4 (circles, OT method; diamonds, MT method). The area on the right-hand side of Fig. 4, as bounded by the thin dash-dotted line, marks a region where we observe non-negligible loss of particles (>5 %) during our measurements due to inelastic collisions of bound pairs. This loss increases with $(k_F a)^{-1}$; see, e.g., [32,33]. In order to simplify our discussion we only consider data points outside this area.

The solid and dashed lines in Fig. 4 represent the statistical mechanics model without any adjustable parameters. For higher temperatures we generally observe larger fluctuations and thus larger error bars, because of the larger atom cloud within a limited field of view. Overall, we find that the agreement between measurement and model remains quite good even in the crossover regime where this model of classical particles with no interaction energy should be expected to break down. In fact, the model could be expected to work to the extent that the internal degrees of freedom of the fermion pairs are frozen and only the degrees of freedom associated with the center of mass of the pair remain active. This approximately occurs when the fermionic chemical potential changes sign which, using a t-matrix approach, we estimate to occur at a coupling value of about $(k_F a)^{-1} = 0.5$ at T_c. This might explain the good agreement found between the model and the experimental data when $(k_F a)^{-1} \gtrsim 0.5$ as well as with the theoretical calculation based on a self-consistent t-matrix approach.

IV. CONCLUSION

To conclude, we have systematically mapped out the fermion pair fraction in a strongly interacting Fermi gas as a function of both temperature and coupling strength. Our measurements show how pairing of ultracold fermions changes as we move from the BEC regime into the strong interaction regime. We demonstrate a novel method to measure the pair fractions from the near-BEC limit to the pseudogap regime, which is based on a number measurement of fermion pairs. This method is complementary to existing excitation-gap measurements and has no counterpart in conventional condensed matter systems. We find that a statistical mechanics model treating the fermions and pairs as classical particles describes the measured data quite well in the investigated range, as we have also confirmed through an advanced many-body calculation based on a t-matrix approach. In the future, we plan to extend our measurements and investigate more in detail the coupling region $[0.1 \lesssim (k_F a)^{-1} \lesssim 0.5]$ where the preformed-pair and the pseudogap regimes overlap with each other.

ACKNOWLEDGMENTS

We gratefully acknowledge discussions with Q. Chen and K. Levin and support from the Deutsche Forschungsgemeinschaft within SFB/TRR 21 (project part B4) and project LI 988/6-1, the Baden-Württemberg Foundation, and the Center for Integrated Quantum Science and Technology (IQ^{ST}). C.C. acknowledges support from the Alexander v. Humboldt fellowship, the Chicago Materials Research Science and Engineering Center by the National Science Foundation (Grant No. DMR-1420709), and the Army Research Office (Grant No. W911NF-14-1-0003).

APPENDIX A: MODEL OF A CANONICAL ENSEMBLE OF NONINTERACTING ATOMS AND MOLECULES

In our simple statistical mechanics model we treat the cold gas of fermions and fermion pairs as a classical canonical ensemble of atoms and molecules, respectively, with negligible interaction energy among each other. In collisions a pair of $|\uparrow\rangle$ and $|\downarrow\rangle$ atoms can combine to form a molecule, and vice versa a molecule can break up into an unbound pair of $|\uparrow\rangle, |\downarrow\rangle$ atoms. At a given temperature the atom and molecule numbers are in chemical equilibrium. Following [22], the equilibrium condition is derived by minimizing the Helmholtz free energy $F = k_B T \ln Z$, subject to the constraint of particle number conservation. Here

$$Z = \frac{Z_s^{2N_a} Z_s^{N_p} \mathrm{e}^{N_p E_b/k_B T}}{N_a! N_a! N_p!}$$

is the partition function of the system and Z_s and $Z_s e^{-E_b/k_B T}$ are the single-particle partition functions for atoms and molecules, respectively. $\overline{\omega} = \sqrt[3]{\omega_r^2 \omega_a}$ is the geometric mean of the trapping frequencies ω_a, ω_r in axial and in radial direction, respectively. Using Stirling's formula to approximate the factorials a minimum in the free energy is found at a molecule (pair) number,

$$N_p = \frac{1}{Z_s} {N_a}^2 \, \mathrm{e}^{-E_b/k_B T},$$

for a given temperature T and binding energy $E_b = -\hbar^2/(ma^2)$. Using the partition function $Z_s = (k_B T/\hbar\,\overline{\omega})^3$,

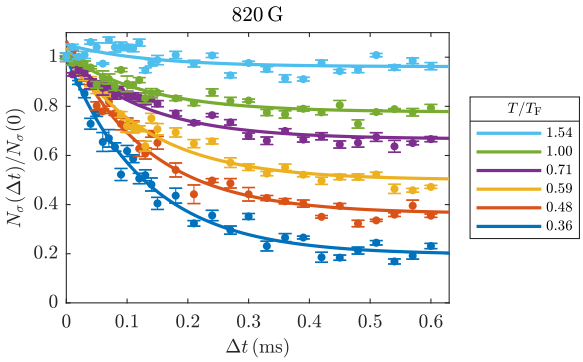

FIG. 5. Ratio $N_\sigma(\Delta t)/N_\sigma(0)$ after an optical transfer pulse of length Δt at a magnetic field of 820 G for various temperatures (see legend). The solid lines are fits of an exponential decay towards a constant offset.

the Fermi energy $E_F = k_B T_F = \hbar\bar{\omega}\sqrt[3]{6N_\sigma}$, and the total pair fraction per spin state $N_\sigma = N_a + N_p$ we obtain the following implicit expression for the pair fraction N_p/N_σ in thermal equilibrium:

$$\frac{(1 - N_p/N_\sigma)^2}{N_p/N_\sigma} = 6\left(\frac{T}{T_F}\right)^3 \exp\left[\frac{E_b}{k_B T}\right].$$

APPENDIX B: MEASUREMENTS CLOSE TO UNITARITY

As pointed out in the main text we only carry out measurements at magnetic fields of up to 820 G because for higher magnetic fields we observe deviations from an exponential decay during the optical excitation of the pairs towards deeply bound molecules. Such deviations are indeed expected close to resonance as a result of many-body effects [34]. In addition, as the optical excitation cross section decreases towards the resonance its rate becomes increasingly comparable to the one of photoassociation. In order to clarify that an exponential fit towards a constant value is still a good description at 820 G, we show corresponding decay curves in Fig. 5. A slight nonexponential behavior of the measured decay will increase the uncertainty in the measured equilibrium pair fraction.

[1] J. Bardeen, L. N. Cooper, and J. R. Schrieffer, Phys. Rev. **108**, 1175 (1957).
[2] J. Bardeen, L. N. Cooper, and J. R. Schrieffer, Phys. Rev. **106**, 162 (1957).
[3] Q. Chen, J. Stajic, S. Tan, and K. Levin, Phys. Rep. **412**, 1 (2005).
[4] H. Ding, T. Yokoya, J. C. Campuzano, T. Takahashi, M. Randeria, M. R. Norman, T. Mochiku, K. Kadowaki, and J. Giapintzakis, Nature (London) **382**, 51 (1996).
[5] A. G. Loeser, Z.-X. Shen, D. S. Dessau, D. S. Marshall, C. H. Park, P. Fournier, and A. Kapitulnik, Science **273**, 325 (1996).
[6] J. Stajic, Science **357**, 561 (2017).
[7] E. J. Mueller, Rep. Prog. Phys. **80**, 104401 (2017).
[8] Q. Chen and K. Levin, Phys. Rev. Lett. **95**, 260406 (2005).
[9] J. Stajic, J. N. Milstein, Q. Chen, M. L. Chiofalo, M. J. Holland, and K. Levin, Phys. Rev. A **69**, 063610 (2004).
[10] C. Chin, M. Bartenstein, A. Altmeyer, S. Riedl, S. Jochim, J. Hecker Denschlag, and R. Grimm, Science **305**, 1128 (2004).
[11] A. Schirotzek, Y.-i. Shin, C. H. Schunck, and W. Ketterle, Phys. Rev. Lett. **101**, 140403 (2008).
[12] J. P. Gaebler, J. T. Stewart, T. E. Drake, D. S. Jin, A. Perali, P. Pieri, and G. C. Strinati, Nat. Phys. **6**, 569 (2010).
[13] Y. Sagi, T. E. Drake, R. Paudel, R. Chapurin, and D. S. Jin, Phys. Rev. Lett. **114**, 075301 (2015).
[14] M. Hashimoto, I. M. Vishik, R.-H. He, T. P. Devereaux, and Z.-X. Shen, Nat. Phys. **10**, 483 (2014).
[15] E. Elliott, J. A. Joseph, and J. E. Thomas, Phys. Rev. Lett. **113**, 020406 (2014).
[16] J. Kinast, A. Turlapov, J. E. Thomas, Q. Chen, J. Stajic, and K. Levin, Science **307**, 1296 (2005).
[17] F. Palestini, A. Perali, P. Pieri, and G. C. Strinati, Phys. Rev. A **82**, 021605(R) (2010).
[18] E. D. Kuhnle, S. Hoinka, P. Dyke, H. Hu, P. Hannaford, and C. J. Vale, Phys. Rev. Lett. **106**, 170402 (2011).
[19] G. B. Partridge, K. E. Strecker, R. I. Kamar, M. W. Jack, and R. G. Hulet, Phys. Rev. Lett. **95**, 020404 (2005).
[20] C. A. Regal, M. Greiner, and D. S. Jin, Phys. Rev. Lett. **92**, 040403 (2004).
[21] M. W. Zwierlein, C. A. Stan, C. H. Schunck, S. M. F. Raupach, A. J. Kerman, and W. Ketterle, Phys. Rev. Lett. **92**, 120403 (2004).
[22] C. Chin and R. Grimm, Phys. Rev. A **69**, 033612 (2004).
[23] M. Pini, P. Pieri, and G. C. Strinati, Phys. Rev. B **99**, 094502 (2019).
[24] A. Perali, P. Pieri, L. Pisani, and G. C. Strinati, Phys. Rev. Lett. **92**, 220404 (2004).
[25] M. Pini *et al.* (unpublished).
[26] X.-J. Liu, Phys. Rep. **524**, 37 (2013).
[27] G. Zürn, T. Lompe, A. N. Wenz, S. Jochim, P. S. Julienne, and J. M. Hutson, Phys. Rev. Lett. **110**, 135301 (2013).
[28] M. Bartenstein, A. Altmeyer, S. Riedl, R. Geursen, S. Jochim, C. Chin, J. H. Denschlag, R. Grimm, A. Simoni, E. Tiesinga, C. J. Williams, and P. S. Julienne, Phys. Rev. Lett. **94**, 103201 (2005).
[29] W. Ketterle and M. Zwierlein, in *Ultra-Cold Fermi Gases*, International School of Physics Enrico Fermi, Vol. Course CLXIV, edited by M. Inguscio, W. Ketterle, and C. Salomon (IOS Press, Amsterdam, 2008).
[30] S. Jochim, *Bose Einstein Condensation of Molecules* (Fraunhofer-IRB-Verlag, Stuttgart, 2005).
[31] S. Jochim, M. Bartenstein, A. Altmeyer, G. Hendl, C. Chin, J. H. Denschlag, and R. Grimm, Phys. Rev. Lett. **91**, 240402 (2003).
[32] T. Bourdel, L. Khaykovich, J. Cubizolles, J. Zhang, F. Chevy, M. Teichmann, L. Tarruell, S. J. J. M. F. Kokkelmans, and C. Salomon, Phys. Rev. Lett. **93**, 050401 (2004).
[33] D. S. Petrov, C. Salomon, and G. V. Shlyapnikov, Phys. Rev. Lett. **93**, 090404 (2004).
[34] F. Werner, L. Tarruell, and Y. Castin, Eur. Phys. J. B **68**, 401 (2009).

B.2 Second sound in the crossover from the Bose-Einstein condensate to the Bardeen-Cooper-Schrieffer superfluid.

Note that the information shown is published in Reference [82].

Daniel K. Hoffmann, Vijay Pal Singh, Thomas Paintner, Manuel Jäger, Wolfgang Limmer, Ludwig Mathey, and Johannes Hecker Denschlag

"Second sound in the crossover from the Bose- Einstein condensate to the Bardeen-Cooper- Schrieffer superfluid", *Nature Communications* **12**, 7074 (2021)

nature COMMUNICATIONS

ARTICLE

https://doi.org/10.1038/s41467-021-27149-z OPEN

Second sound in the crossover from the Bose-Einstein condensate to the Bardeen-Cooper-Schrieffer superfluid

Daniel K. Hoffmann[1], Vijay Pal Singh[2,3], Thomas Paintner[1], Manuel Jäger[1], Wolfgang Limmer[1], Ludwig Mathey[3,4] & Johannes Hecker Denschlag[1✉]

Second sound is an entropy wave which propagates in the superfluid component of a quantum liquid. Because it is an entropy wave, it probes the thermodynamic properties of the quantum liquid. Here, we study second sound propagation for a large range of interaction strengths within the crossover between a Bose-Einstein condensate (BEC) and the Bardeen-Cooper-Schrieffer (BCS) superfluid, extending previous work at unitarity. In particular, we investigate the strongly-interacting regime where currently theoretical predictions only exist in terms of an interpolation in the crossover. Working with a quantum gas of ultracold fermionic ^{6}Li atoms with tunable interactions, we show that the second sound speed varies only slightly in the crossover regime. By varying the excitation procedure, we gain deeper insight on sound propagation. We compare our measurement results with classical-field simulations, which help with the interpretation of our experiments.

[1] Institut für Quantenmaterie and Center for Integrated Quantum Science and Technology (IQST), Universität Ulm, D-89069 Ulm, Germany. [2] Institut für Theoretische Physik, Leibniz Universität Hannover, Appelstraße 2, 30167 Hannover, Germany. [3] Institut für Laserphysik, Zentrum für Optische Quantentechnologien, Universität Hamburg, 22761 Hamburg, Germany. [4] The Hamburg center for Ultrafast Imaging, Universität Hamburg, Luruper Chaussee 149, 22761 Hamburg, Germany. ✉email: johannes.denschlag@uni-ulm.de

Second sound is a transport phenomenon of quantum liquids that emerges below the critical temperature for superfluidity T_c.[1–3] It was experimentally discovered[4] in 1944 in He II[5] and was described with a hydrodynamic two-fluid model[2,6–8] which treats He II as a mixture of a superfluid (SF) and a normal fluid (NF). The SF component has no entropy and flows without dissipation. The NF component carries all the entropy and has non-zero viscosity. In the limit of vanishing temperature $T \to 0$, the two-fluid model predicts that first sound (i.e., standard sound waves) corresponds to a propagating pressure oscillation with constant entropy, while second sound is an entropy oscillation propagating at constant pressure[8].

The properties of a SF naturally depend on parameters such as its temperature and the interaction strength between its particles. With the advent of ultracold quantum gases, with tunable interactions, these dependencies can now be studied. In particular, an ultracold fermionic quantum gas with a tunable Feshbach resonance offers a unique opportunity to access various sorts of superfluidity in one system, ranging continuously between a Bose-Einstein condensate (BEC) of bosonic molecules, a resonant SF, and a SF gas of Cooper pairs (BCS superfluid)[9–11]. In the experiment, this is done by tuning the interaction parameter $(k_F a)^{-1}$, where a is the scattering length, $k_F = \sqrt{2mE_F}/\hbar$ the Fermi wavenumber, E_F is the Fermi energy, and m the atomic mass.

A large range of thermodynamical properties of the BEC-BCS crossover has been studied, e.g., in refs. [11–19]. This includes experiments on first sound (see e.g., ref. [16]) and second sound. Second sound has recently been observed by Sidorenkov et al.[20] in a unitary Fermi gas and by Ville et al.[21] and Christodoulou et al.[22] in a two-dimensional bosonic SF. Second sound was also possibly present in an experiment by Meppelink et al.[23] as pointed out in ref. [3].

Here, we experimentally investigate how second sound changes across the BEC–BCS crossover. This is important, because full theoretical calculations are not yet available for the entire strongly interacting regime. Nevertheless, comparing our measurements to existing calculations and interpolations we find reasonable agreement. In particular, c-field simulations in the BEC regime match quite well the observed wave dynamics in experiments at interaction strengths of up to $(k_F a)^{-1} = 1$. In addition, we investigate experimentally and theoretically the system response when modifying the excitation scheme. As second sound is mainly an entropy wave and first sound is mainly a pressure wave, different excitation schemes give rise to different responses for first and second sound. This helps for separating the generally weak second sound signals from the first sound ones. We find that this separation works especially well when first sound is excited as a density dip wave packet. For this case, we were able to quantitatively compare the amplitudes of first and second sound and compare the results with a prediction.

Results

Experimental details. Our experiments are carried out with a balanced, two-component ultracold gas of fermionic ^{6}Li atoms in the two lowest hyperfine states $|F, m_F\rangle = |1/2, \pm 1/2\rangle$ of the electronic ground state. The gas is confined by a combined magnetic and optical dipole trap with a trap depth of $U_0 \approx 1\,\mu\mathrm{K} \times k_B$, for details see ref. [24,25]. The trap is nearly harmonic and cylindrically symmetric with trapping frequencies $\omega_r = 2\pi \times 305$ Hz and $\omega_x = 2\pi \times 21$ Hz. The temperature and the particle density are controlled by evaporative cooling. In the experiments the temperature ranges approximately from $0.13\,T_F$ to $0.30\,T_F$, where $T_F = E_F/k_B = \hbar\bar{\omega}(3N)^{1/3}/k_B$ is the Fermi temperature, $\bar{\omega} = \left(\omega_x \omega_r^2\right)^{1/3}$ is the geometric mean of the trapping frequencies and N is the total number of atoms. The scattering length a is tunable with an external magnetic field B via a magnetic Feshbach resonance at 832 G[26].

To excite sound modes in the system, we focus a blue-detuned 532 nm laser onto the trap center following the approaches introduced in refs. [16,20,27] (Fig. 1a). The laser beam is aligned perpendicularly to the optical dipole trap and produces a repulsive potential barrier of $U_{ex} \approx 0.2\,U_0$. At its focus, the beam has a waist of about 20 μm, which is comparable to the cloud size in the radial direction. To excite sound waves, the height of this additional potential is modulated. The excited sound modes generally exhibit contributions from both first and second sound[28–30]. However, it is possible to generate preferentially either one of the two sound modes by adapting the excitation method.

To excite primarily first sound, we abruptly switch on the excitation laser beam (Fig. 1b), similarly as for the first experiments on sound propagation in a dilute BEC[27]. This applies pressure on the cold cloud on both sides of the laser beam and creates two density wave packets (Fig. 1c) which propagate out in opposite directions along the axial trap axis with the speed u_1. In the experiments, we detect these waves with the help of absorption imaging by measuring the density distribution of the atomic cloud as a function of time.

Figure 1d shows such density waves for an experiment at $(k_F a)^{-1} \approx (1.61 \pm 0.05)$, $B = 735$ G and a temperature of $T = (220 \pm 30)$ nK $= (0.30 \pm 0.06)\,T_F$, which corresponds to $T = (0.80 \pm 0.15)\,T_c$, where T_c is the critical temperature. For the given interaction strength, we used $T_c = 0.37\,T_F$ (see Supplementary Note 1).

Figure 1d is a time-ordered stack of one-dimensional line density profiles of the atom cloud[31]. Each profile was obtained by integrating the measured column density of the atomic cloud along the transverse (i.e., y-) direction (see "Methods" for details). The time-ordered stack shows the propagation of the sound waves along the axial direction x as a function of time. We observe two density wave packets which propagate with first sound velocity from the trap center towards the edge of the cloud (two bright traces, marked with red arrows). The propagating waves produce a density modulation of only a few percent of the peak density and can be considered as a weak perturbation of the system. To obtain the speed of sound, we examine how the center position of each wave packet changes with time. The center positions are determined via a Gaussian fit. Please note that the central sound speed is determined over a local area of the cloud where the density varies by about 30%. As a consequence, the measured sound speed should be considered a mean value. From Fig. 1d we obtain $u_1 = (17.2 \pm 3)$ mm/s near the trap center. Our analysis shows that the sound propagation slows down as the pulse approaches the edge of the cloud where the particle density decreases. In the following, we focus on the sound speed close to the trap center.

To primarily excite second sound, we sinusoidally modulate the intensity of the excitation beam for 7 ms with a modulation frequency of $\omega_{ex} = 2\pi \times 570\,\mathrm{Hz} \approx 2\omega_r$ and a modulation amplitude of $\Delta U \approx 0.2\,U_0$. This parametrically heats the gas in radial direction (Fig. 1b). Subsequent thermalization via collisions occurs within a few milliseconds. As a consequence a local depletion of the SF density is created, which is filled with normal gas, forming a region of increased entropy (Fig. 1c). This gives rise to two wave packets which propagate outwards along the axial direction with the speed of second sound. Figure 1e shows corresponding experimental data where we measure the local density distribution as in Fig. 1d. The second sound wave appears here as a density dip (dark traces, marked with orange arrows). A clear indication that the dark trace corresponds to second sound is the fact that it vanishes at the Thomas-Fermi radius $R_{TF} \approx 110\,\mu$m where the SF fraction vanishes. Second sound only propagates inside the SF phase.

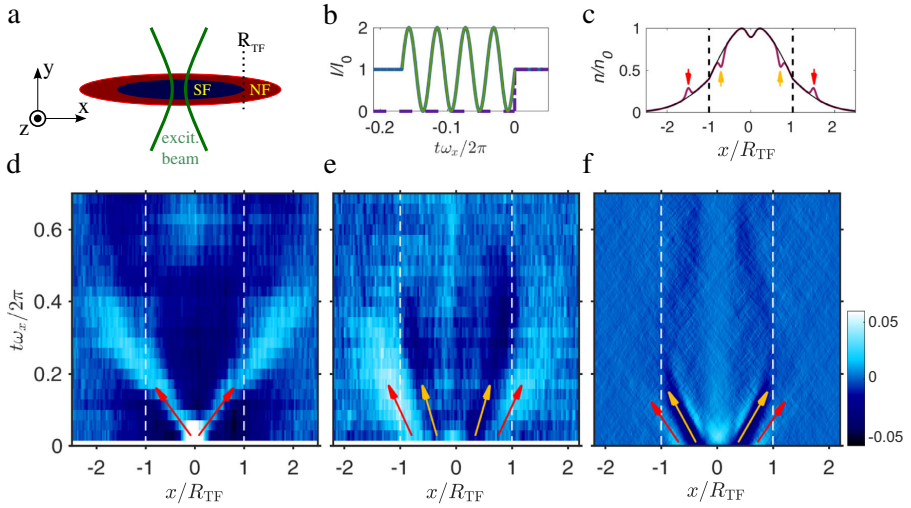

Fig. 1 Sound excitation in a trapped superfluid Fermi gas in the vicinity of the BEC-BCS crossover. a Set-up: A focussed, intensity-modulated, blue-detuned laser beam excites sound waves in the cigar-shaped atom cloud. **b** Two different modulation sequences of the laser intensity. Purple dashed line: step excitation. Green solid line: heat pulse. The time t is given in units of the axial trapping period $2\pi/\omega_x$. **c** Sketch of a bimodal density distribution of a trapped BEC (purple line) at $y = z = 0$. At the center of the trap a blue detuned beam produces a dimple in the potential. Modulating the beam intensity produces first sound waves (red arrows) and second sound (orange arrows) waves. Second sound reduces the local density of the cloud, while for first sound a density peak emerges. The thin black line shows the profile of the unperturbed cloud. Please note that the crests and troughs of the waves are shown in an exaggerated way for better visibility. **d** The false color plot shows the measured local change in the density $\Delta\tilde{n}(x,t)$ as a function of axial position x and time t. Here, $(k_F a)^{-1} = (1.61 \pm 0.05)$ at $B = 735$ G and $T/T_c = (0.80 \pm 0.15)$. After excitation, two wave packets (bright traces, marked with red arrows) propagate with first sound velocity u_1 towards the edges of the cloud. The excitation method predominantly excites first sound. Second sound is present as well but is barely discernible here. **e** Propagation of first sound waves (bright traces, marked with red arrow) and second sound waves (dark traces, marked with orange arrows) after excitation with sinusoidal pulse of (**b**). All other settings are the same as in (**d**). **f** Simulated sound propagation for the same parameters as in (**e**). The orange arrows mark the propagating second sound and the red arrows the first sound, respectively.

Besides a second sound wave, the excitation also produces a first sound wave (bright traces, marked with red arrows) which propagates faster than the second sound wave and travels beyond the Thomas-Fermi radius. The first sound wave is broader than in Fig. 1d, which can be mainly explained by the longer excitation pulse. To obtain u_2 we measure the time-dependent position of the minimum of each dark trace, which is again determined via a Gaussian fit. For Fig. 1e we obtain $u_2 = (5.1 \pm 1.1)$ mm/s. We note that for the small excitation amplitudes in our experiments (see colorbar in Fig. 1d–e), we do not observe the asymmetric sound wave distortions reported in ref. [23]. These distortions were also absent in ref. [20].

Figure 1f shows numerical simulations of our experiment applying a dynamical c-field method[32] (see Supplementary Note 2 for detailed information on the method). The dimer scattering length[33] is $a_{dd} = 0.6a$ and we assume all fermionic atoms to be paired up in molecules. To compare the simulations with the experimental results we choose the same values of $(k_F a)^{-1}$ and the same central density of the trapped gas as in the experiment. The theory value for u_2 is (5.7 ± 0.05) mm/s in agreement with the experimental value (5.1 ± 1.1) mm/s.

Interaction strength dependence of second sound. We now perform measurements of second sound speed in the region $(-0.22 \pm 0.04) < (k_F a)^{-1} < (1.61 \pm 0.05)$ of the BCS-BEC crossover. These are shown in Fig. 2 along with theoretical predictions. The second sound velocity u_2 is given in units of the Fermi velocity $v_F = \hbar k_F^{hom}/m$. Here, the Fermi wavenumber $k_F^{hom} = (3\pi^2 n_0)^{1/3}$ is determined from the 3D peak density close to the trap center. The peak density is deduced using the inverse Abel transformation[34] and a self-consistent mean field calculation (see Supplementary Note 4). We have verified that in the BEC regime our mean field calculation gives similar results for the peak density when we input the trapping frequencies, the temperature, the scattering length and the total number of particles. The blue dash-dotted line is a calculation from ref. [28], based on a hydrodynamic description in a homogeneous gas for the limiting cases of the BEC and the BCS regime and unitarity. To connect these regimes, the results are interpolated across the crossover, bridging the range $|(k_F a)^{-1}| < 1$. The blue solid and the brown solid lines are our analytic hydrodynamic calculations which are valid in the BCS and BEC limit, respectively (see Supplementary Note 3). For comparison, we show the results of the numerical c-field simulations (green squares), which agree with both, analytic description and experimental results. Despite the large error bars the measurements indicate an increase of u_2 when approaching unitarity from the BEC side, in agreement with the theoretical results.

In general, second sound can only propagate in the SF phase of the gas. It is therefore natural to ask how the SF density n_s and the speed of second sound u_2 are related. Using our measurements for u_2 we can roughly determine the relationship between n_s and u_2 for our temperature T and $(k_F a)^{-1} > 1.5$, since in this regime the SF density can be estimated. For this, we carry out self-consistent mean field calculations to determine the density distributions of the SF and the NF for an interacting BEC in the

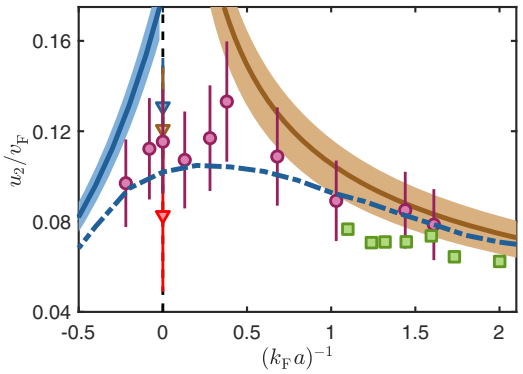

Fig. 2 Second sound velocity u_2 as a function of interaction strength. The purple circles depict measured data for temperatures in the range $T = 105-230$ nK which corresponds to $T/T_c = 0.66-0.84$ (see Supplementary Note 1). The error bars are due to statistical uncertainties. The brown and blue solid line show hydrodynamic predictions for the BEC and BCS regime at $T = 0.75T_c$, respectively (see Supplementary Note 3). The shaded areas mark the second sound velocity in the temperature range of the experiments. The blue dash-dotted line shows a theoretical prediction of second sound in the crossover[28] for a homogeneous gas at $T/T_c = 0.75$. It interpolates between the results from hydrodynamic theory in the BEC and BCS regime. The green squares are results of our numerical c-field simulations which are consistent with both, analytic and experimental results. For comparison we also show the second sound velocity on the resonance measured in ref. [20] at the temperatures $T/T_c = 0.65$ (blue triangle), $T/T_c = 0.75$ (brown triangle), and $T/T_c = 0.85$ (red triangle).

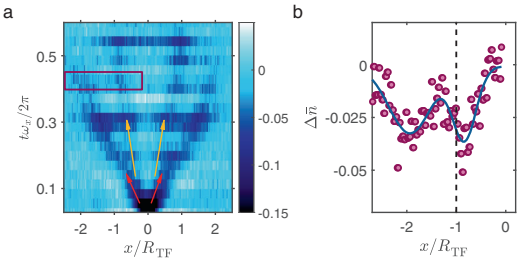

Fig. 3 Comparing signal strength of first and second sound. a Sound excitation experiment at $(k_F a)^{-1} = (1.61 \pm 0.05)$ and at a temperature of $T/T_c = (0.80 \pm 0.15)$. In contrast to Fig. 1d, first sound (red arrows) and second sound (orange arrows) are now visible simultaneously. For $t\omega_x/2\pi < 0.15$ first and second sound waves overlap and therefore cannot be distinguished from each other. **b** shows $\Delta\bar{n}$ for $t\omega_x/2\pi = 0.43$. We fit the center position of each of the two sound waves using a Gaussian function (solid line).

trap (see Supplementary Note 4). As an important input into these calculations we make use of the Thomas-Fermi radius which we have measured in the second sound experiments (the measured Thomas-Fermi radii can be found in Supplementary Note 1). As an example, from the measurement at $(k_F a)^{-1} = (1.61 \pm 0.05)$ we determine the peak SF fraction to be $n_{s0}/n_0 = 0.98$ close to the trap center at maximum density (see Supplementary Note 4), where the local $(k_F^{hom} a)^{-1} = (1.06 \pm 0.05)$ and $T/T_c^{hom} = (0.40 \pm 0.15)$, with $T_c^{hom} = 0.21 T_F^{hom}$ and $T_F^{hom} = \hbar^2 (k_F^{hom})^2 / 2mk_B$. For comparison, for a homogeneous weakly interacting BEC with a SF fraction close to unity the temperature would need to be $T \ll T_c^{hom}$, according to $n_s/n = 1 - (T/T_c^{hom})^{3/2}$. At unitarity, by contrast, the SF fraction reaches unity already at $T/T_c^{hom} \approx 0.55$, as shown by Sidorenkov et al.[20]. As expected, this comparison shows that for a given T/T_c^{hom} the SF fraction grows with interaction strength.

Tuning the sound mode excitation. In the following we investigate how the SF gas responds to different excitation protocols[28–30]. For this, we vary the excitation scheme, the excitation frequency and amplitude. By observing the corresponding response of the system we gain additional insights into the nature of first and second sound.

In Fig. 3a we show the evolution of the system after a step pulse excitation at $B = 735$ G and $\Delta U = 0.3U_0$, in which both, first and second sound are excited. In contrast to the experiment in Fig. 1d, the laser beam is abruptly switched off - not on. As a consequence, the wave packets of both first and second sound now correspond to dips in the particle density. In Fig. 3b we show the density distribution for the time and position range indicated by the purple rectangle in Fig. 3a. From a fit of two Gaussian dips to the two wave packets, we determine an amplitude ratio of $W_2/W_1 \approx 1.1$. This result approximately matches the predictions of refs. [29,30] (see also Supplementary Note 3), where the response of both, a weakly and a strongly interacting molecular Bose gas has been studied. For an interaction parameter of $(k_F a)^{-1} = 2$, the prediction yields $W_2/W_1 = 0.9$, which is of similar magnitude as our result.

Next, we study the system response when modifying the excitation scheme. For this, we vary the excitation frequency and the number of modulation cycles. Figure 4a–d shows the system response for a modulation frequency of $\omega_{ex} = 0.61\omega_r$, so that parametric heating is rather suppressed and coupling to first sound is enhanced as compared to the measurement shown in Fig. 1e. While Fig. 4a, b corresponds to a 1.5 cycle modulation, Fig. 4c, d corresponds to a 1 cycle modulation.

The numerical simulations in Fig. 4b, d demonstrate how the excitation pattern produces a corresponding wave train of first sound. Once the simulated waves of first sound have propagated beyond the Thomas-Fermi radius, they diffuse out and lose signal strength. In the simulation, the diffusion of the first sound wave train is stronger than in the experiment. This might be explained by the choice of the discretization length which was used in the simulations (see Supplementary Note 2B). The first sound wave train is always followed by a single dark second sound wave packet.

The experimental data in Fig. 4a agree reasonably well with the simulation in Fig. 4b. Comparing Fig. 4c and d, there seems to be a discrepancy. In the experiment clearly a first sound wave train, consisting of two bright traces and one dark trace, propagates beyond the Thomas-Fermi radius. In the simulation, however, the second bright trace of the wave train, which is clearly visible in the center, disappears before it reaches the Thomas-Fermi radius (black arrow). The corresponding damping happens when the bright sound trace crosses the dark second sound trace (see also insert in Fig. 4d). The reason for the damping is that first sound waves diffuse in a thermal environment. This diffusion, however, is apparently too strong in the simulation results, which is probably a consequence of constraints in the numerical resolution (for more details see Supplementary Note 2B).

In conclusion, we have studied second sound propagation in an ultracold Fermi gas of ^{6}Li atoms throughout the BEC-BCS

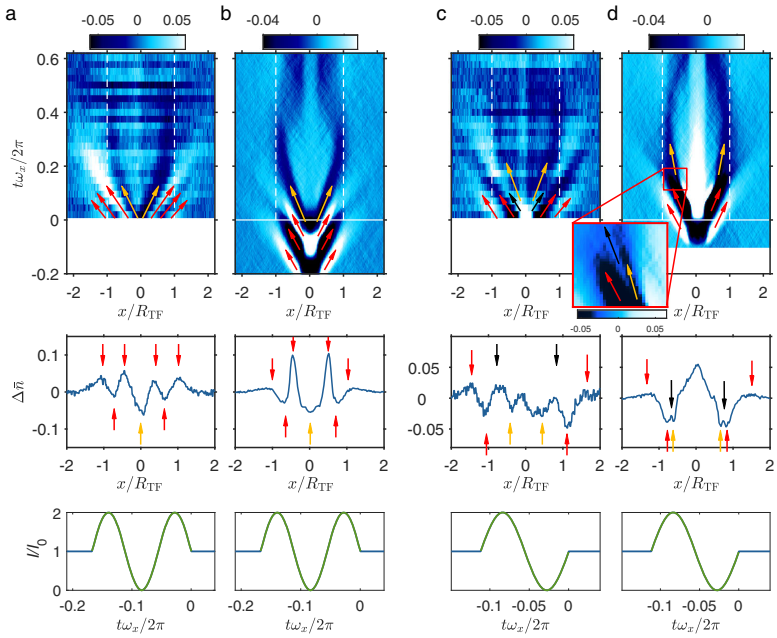

Fig. 4 Sound excitation with different modulation sequences. a, **c** $\Delta\bar{n}(x,t)$ data at $\omega_{\rm ex} = 0.61\omega_r$, $\Delta U = 0.3U_0$ and $(k_{\rm F}a)^{-1} = (1.61 \pm 0.05)$ for a modulation of 1.5 cycles and of 1 cycle, respectively. The excitation pulse excites both, first and second sound waves. **b**, **d** $\Delta\bar{n}(x,t)$ from numerical c-field simulations. Top row: False color images of $\Delta\bar{n}(x,t)$. First and second sound waves are marked with red and orange arrows, respectively. The inset in (**d**) is an enlargement, showing how the calculated bright first sound wave (black arrow) is damped when it crosses the second sound wave (orange arrow). Mid row: Shown is $\Delta\bar{n}$ for $t\omega_x/2\pi = 0$ (**a**, **b**) and for $t\omega_x/2\pi = 0.15$ (**c**, **d**). Bottom row: Applied excitation scheme.

crossover for a finite temperature of $T \approx 0.75\,T_c$. We find the second sound velocity to vary only slightly across the BCS-BEC crossover, which is in agreement with an interpolation of hydrodynamic theory[28]. In the BEC regime, the results match numerical predictions based on c-field simulations.

In addition, we investigate the response of the SF gas on various excitation pulse shapes, ranging from gentle local heating to an abrupt kick. While a sinusoidal excitation pulse leads to a corresponding wave train for the first sound, it only produces a single pulse for the second sound. In the future, it will be useful to extend our measurements in the strongly interacting regime to a larger range of temperatures below T_c. Since the second sound velocity is related to the local SF density, these measurements can help to determine the correlation between the SF density and the temperature in the strongly interacting regime.

Methods

Calculating $\Delta\bar{n}$ from the density profiles. Each of the experimental sound propagation images in Figs. 1d–e, 3a, 4a and c is a time-ordered stack of one-dimensional line density profiles $\Delta\bar{n}(x,t)$ of the atom cloud. A one-dimensional line density profile $n(x,t)$ is produced as follows: After sound excitation has ended and after an additional propagation time t, we take an absorption image of the atom cloud to obtain the column density distribution $n_{\rm ex}(x,y,t)$. Next, we integrate the absorption image along the y-axis (which is perpendicular to the symmetry axis of the cigar-shaped atom cloud) to obtain a one-dimensional line density profile $n_{\rm ex}(x,t)$. To reduce noise, we average 15 density profiles and obtain $\bar{n}_{\rm ex}(x,t)$. We repeat this procedure for an unperturbed cloud to obtain $\bar{n}(x)$. By subtracting the two density profiles from each other we obtain $\Delta\bar{n}(x,t) = (\bar{n}_{\rm ex}(x,t) - \bar{n}(x))/\bar{n}(0)$.

Data availability

The data for the measured temperatures and Thomas-Fermi radii are provided in Supplementary Note 1.

Code availability

The simulation codes and simulated data are available at https://zenodo.org/record/5572570[35].

Received: 19 March 2020; Accepted: 26 October 2021;
Published online: 06 December 2021

References

1. Halperin, W. P. Eighty years of superfluidity. *Nature* **553**, 413–414 (2018).
2. Donnelly, R. J. The two-fluid theory and second sound in liquid helium. *Physics Today*, 34–39 (October 2009).
3. Pitaevskii, L. & Stringari, S. *Second Sound in Ultracold Atomic Gases. Universal Themes of Bose-Einstein Condensation* (pp. 322–347) (Cambridge University Press, 2015).
4. Peshkov, V. P. Second sound in helium II. *Sov. Phys. JETP* **11**, 580 (1960).
5. Griffin, A. New light on the intriguing history of superfluidity in liquid ^{4}He. *J. Phys.: Condens. Matter* **21**, 164220 (2009).
6. Tisza, L. Transport phenomena in helium II. *Nature* **141**, 913 (1938).
7. Landau, L. D. The theory of superfluidity of helium II. *J. Phys. USSR* **5**, 71 (1941).
8. Putterman, S. J. *Superfluid Hydrodynamics* (North Holland, Amsterdam, 1974).
9. Giorgini, S., Pitaevskii, L. P. & Stringari, S. Theory of ultracold atomic Fermi gases. *Rev. Mod. Phys.* **80**, 1215–1275 (2008).
10. Ketterle, W. & Zwierlein, M. W. In *Ultra-cold Fermi Gases*, International School of Physics "Enrico Fermi", Vol. Course CLXIV, (eds Inguscio, M., Ketterle, W. & Salomon, C.) (IOS Press, 2008).
11. Zwerger, W. *The BCS-BEC Crossover and the Unitary Fermi Gas* (Lecture Notes in Physics, Springer Science & Business Media, Berlin Heidelberg, 2011).
12. Nascimbène, S., Navon, N., Jiang, K. J., Chevy, F. & Salomon, C. Exploring the thermodynamics of a universal Fermi gas. *Nature* **463**, 1057–1060 (2010).

13. Ku, M. J. H., Sommer, A. T., Cheuk, L. W. & Zwierlein, M. W. Revealing the superfluid lambda transition in the universal thermodynamics of a unitary Fermi gas. *Science* **335**, 563 (2012).
14. Shin, Y., Schunck, C. H., Schirotzek, A. & Ketterle, W. Phase diagram of a two-component Fermi gas with resonant interactions. *Nature* **451**, 689–693 (2008).
15. Sagi, Y., Drake, T. E., Paudel, R., Chapurin, R. & Jin, D. S. Breakdown of the Fermi liquid description for strongly interacting fermions. *Phys. Rev. Lett.* **114**, 075301 (2015).
16. Joseph, J. et al. Measurement of Sound Velocity in a Fermi Gas near a Feshbach Resonance. *Phys. Rev. Lett.* **98**, 170401 (2007).
17. Taylor, E. et al. First and second sound in a strongly interacting Fermi gas. *Phys. Rev. A* **80**, 053601 (2009).
18. Perali, A., Pieri., P., Pisani., L. & Calvanese Strinati, G. BCS-BEC crossover at finite temperature for superfluid trapped Fermi atoms. *Phys. Rev. Lett.* **92**, 220404 (2004).
19. Navon, N., Nascimbène, S., Chevy, S. & Salomon, C. The equation of state of a low-temperature Fermi gas with tunable interactions. *Science* **328**, 729–732 (2010).
20. Sidorenkov, L. et al. Second sound and the superfluid fraction in a Fermi gas with resonant interactions. *Nature* **498**, 78–82 (2013).
21. Ville, J. L. et al. Sound propagation in a uniform superfluid two-dimensional Bose gas. *Phys. Rev. Lett.* **121**, 145301 (2018).
22. Christodoulou, P. et al. Observation of first and second sound in a BKT superfluid. *Nature* **594**, 191–194 (2021).
23. Meppelink, R., Koller, S. B. & van der Straten, P. Sound propagation in a Bose-Einstein condensate at finite temperatures. *Phys. Rev. A* **80**, 043605 (2009).
24. Paintner, T. et al. Pair fraction in a finite-temperature Fermi gas on the BEC side of the BCS-BEC crossover. *Phys. Rev. A* **99**, 053617 (2019).
25. Hoffmann, D. K., Paintner, T., Limmer, W., Petrov, D. S. & Hecker Denschlag, J. Reaction kinetics of ultracold molecule-molecule collisions. *Nat. Commun.* **9**, 5244 (2018).
26. Zürn, G. et al. Precise characterization of ^{6}Li Feshbach resonances using trap-sideband-resolved RF spectroscopy of weakly bound molecules. *Phys. Rev. Lett.* **110**, 135301 (2013).
27. Andrews, M. R. et al. Propagation of sound in a Bose-Einstein condensate. *Phys. Rev. Lett.* **79**, 553 (1997).
28. Heiselberg, H. Sound modes at the BCS-BEC crossover. *Phys. Rev. A* **73**, 013607 (2006).
29. Arahata, E. & Nikuni, T. Propagation of second sound in a superfluid Fermi gas in the unitary limit. *Phys. Rev. A* **80**, 043613 (2009).
30. Hu, H., Taylor, E., Liu, X.-J., Stringari, S. & Griffin, A. Second sound and the density response function in uniform superfluid atomic gases. *N. J. Phys.* **12**, 043040 (2010).
31. Capuzzi, P., Vignolo, P., Federici, F. & Tosi, M. P. Sound propagation in elongated superfluid fermion.ic clouds. *Phys. Rev. A* **73**, 021603 (2006).
32. Singh, V. P. et al. Probing superfluidity of Bose-Einstein condensates via laser stirring. *Phys. Rev. A* **93**, 023634 (2016).
33. Petrov, D. S., Salomon, C. & Shlyapnikov, G. V. Weakly bound dimers of fermionic atoms. *Phys. Rev. Lett.* **93**, 090404 (2004).
34. Partridge, G. B. et al. Deformation of a trapped Fermi gas with unequal spin populations. *Phys. Rev. Lett.* **97**, 190407 (2006).
35. Hoffmann, D. K. et al. Simulation script and data for "Second sound in the crossover from the Bose-Einstein condensate to the Bardeen-Cooper-Schrieffer superfluid". *Zenodo*. https://doi.org/10.5281/zenodo.5572570 (2021).

Acknowledgements

The authors thank Benjamin Deissler and Wladimir Schoch for the support in the stages of the experiment. In addition, the authors thank Sandro Stringari, Hui Hu, Xia-Ji Liu, and Jia Wang for encouraging and illuminating discussions. V.P.S. and L.M. acknowledge the support from the DFG in the framework of SFB 925 and the excellence clusters 'The Hamburg Centre for Ultrafast Imaging'- EXC 1074 - project ID 194651731, 'Advanced Imaging of Matter' - EXC 2056 - project ID 390715994 and Germany's Excellence Strategy, EXC-2123 QuantumFrontiers, Project No. 390837967. D.K.H., T.P., M.J., W.L., and J.H.D. acknowledge support from the Deutsche Forschungsgemeinschaft within SFB/TRR 21 (project part B4) and project LI988/6-1, the Baden-Württemberg Foundation, and the Center for Integrated Quantum Science and Technology (IQST).

Author contributions

D.K.H. and T.P. performed the experiments. D.K.H. and M.J. performed the data analysis, V.P.S. carried out analytic and numerical simulations. J.H.D and L.M. supervised the project. The manuscript was written by D.K.H., W.L., M.J., V.P.S., L.M., and J.H.D.

Funding

Open Access funding enabled and organized by Projekt DEAL.

Competing interests

The authors declare no competing interests.

Additional information

Supplementary information The online version contains supplementary material available at https://doi.org/10.1038/s41467-021-27149-z.

Correspondence and requests for materials should be addressed to Johannes Hecker Denschlag.

Peer review information *Nature Communications* thanks Xia-Ji Liu, Florian Schreck, and the other, anonymous, reviewer(s) for their contribution to the peer review of this work.

Reprints and permission information is available at http://www.nature.com/reprints

Publisher's note Springer Nature remains neutral with regard to jurisdictional claims in published maps and institutional affiliations.

SUPPLEMENTARY INFORMATION

Supplementary Note 1: Temperatures to the measurements in Fig. 1 and Fig. 2

In this section we present the temperatures to the measurements shown in Fig. 1 and Fig. 2 (see Supp. Table 1). We determine the temperatures by fitting a second order virial expansion of the density distribution at the wings of the cloud[1]. To compare the absolute temperature with T_c for various interaction strengths we use values for T_c as shown in Supp. Figure 1.

T_c is not precisely known yet in the strongly interacting regime. In the limit of the BEC regime the BEC mean-field model should give accurate values for critical temperature. Closer towards the resonance we expect the diagrammatic t-matrix calculation to provide quite good values[2]. For the range in between $(0.5 < (k_F a)^{-1} < 3)$ we linearly interpolate between both T_c curves.

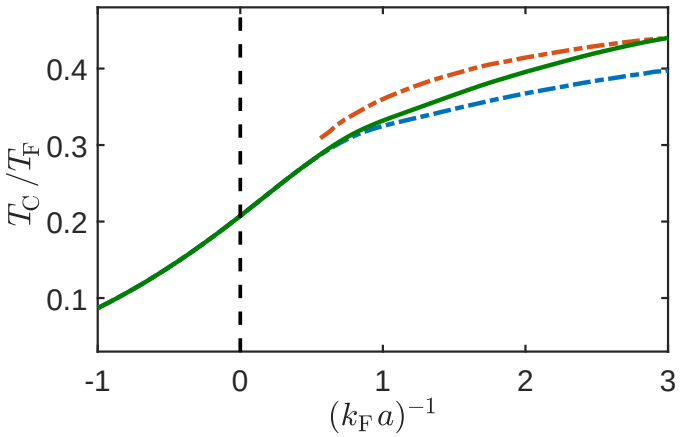

Supplementary Figure 1. **Critical temperature T_c in units of T_F as a function of $(k_F a)^{-1}$ for a harmonically trapped Fermi gas.** The blue dash-dotted line shows a diagrammatic t-matrix calculation and the orange dash-dotted line a calculation based on a BEC mean-field model[2]. The green straight line interpolates linearly between the two approaches. In the BEC limit of noninteracting molecules T_c is given by $T_c = 0.94\hbar(\omega_x\omega_r^2 N)^{1/3}$ and therefore $T_c/T_F = 0.517$.

For the measurements on the resonance we compared our result with the temperature determined using the equation of state from Ref.[3]. We find reasonable agreement between

the temperatures obtained from the two approaches with deviations on the order of $5-10\%$.

$(k_\mathrm{F}a)^{-1}$	T [nK]	T/T_F	$T_\mathrm{c}/T_\mathrm{F}$	T/T_c	R_TF [μm]
-0.22 ± 0.04	105 ± 23	0.13 ± 0.04	0.176	0.74 ± 0.24	96 ± 5
-0.08 ± 0.03	106 ± 22	0.13 ± 0.04	0.196	0.66 ± 0.21	107 ± 5
0 ± 0.02	158 ± 28	0.17 ± 0.05	0.207	0.82 ± 0.24	108 ± 5
0.13 ± 0.03	140 ± 30	0.18 ± 0.05	0.226	0.80 ± 0.22	121 ± 5
0.28 ± 0.04	140 ± 30	0.19 ± 0.05	0.249	0.76 ± 0.20	156 ± 5
0.38 ± 0.04	190 ± 30	0.22 ± 0.06	0.263	0.84 ± 0.22	153 ± 5
0.68 ± 0.05	190 ± 30	0.24 ± 0.06	0.302	0.79 ± 0.19	139 ± 5
1.03 ± 0.05	200 ± 30	0.25 ± 0.06	0.334	0.75 ± 0.17	124 ± 5
1.44 ± 0.05	230 ± 30	0.29 ± 0.06	0.361	0.80 ± 0.16	115 ± 5
1.61 ± 0.05	220 ± 30	0.30 ± 0.06	0.373	0.80 ± 0.15	110 ± 5

Supplementary Table 1. **Temperatures and Thomas-Fermi radii to the measurements presented in Fig. 2 (main text).** The temperatures are given in nK as well as units of T_F and T_c. For expressing the temperature in units of T_c we use an interpolated critical temperature curve (see Supp. Fig. 1).

Supplementary Note 2: C-field simulation method

Here we present our simulation method that is used to simulate sound mode dynamics in a condensate of ^{6}Li molecules on the BEC side. The system is described by the Hamiltonian

$$\hat{H}_0 = \int \mathrm{d}\mathbf{r}\Big[\frac{\hbar^2}{2M}\nabla\hat{\psi}^\dagger(\mathbf{r})\cdot\nabla\hat{\psi}(\mathbf{r}) + V(\mathbf{r})\hat{\psi}^\dagger(\mathbf{r})\hat{\psi}(\mathbf{r}) + \frac{g}{2}\hat{\psi}^\dagger(\mathbf{r})\hat{\psi}^\dagger(\mathbf{r})\hat{\psi}(\mathbf{r})\hat{\psi}(\mathbf{r})\Big]. \tag{1}$$

$\hat{\psi}$ and $\hat{\psi}^\dagger$ are the bosonic annihilation and creation operator, respectively. The 3D interaction parameter is given by $g = 4\pi a_\mathrm{dd}\hbar^2/M$, where a_dd is the dimer-dimer scattering length and M the dimer mass. The external potential $V(\mathbf{r})$ represents the cigar-shaped trap $V_\mathrm{trap}(\mathbf{r}) = M(\omega_x^2x^2 + \omega_r^2r^2)/2$. ω_x and ω_r are the axial and radial trapping frequencies, respectively. $r = (y^2+z^2)^{1/2}$ is the radial coordinate.

To perform numerical simulations we discretize space with the lattice of $180\times35\times35$ sites and the discretization length $l = 0.5\,\mu$m, where l is chosen to be smaller than or comparable

to the healing length $\xi > 0.5\,\mu$m and the thermal de Broglie wavelength $\lambda_{\rm dB} \approx 1 - 1.5\,\mu$m. Since $\lambda_{\rm dB}$ determines the scale for thermal fluctuations, the associated thermal energy should always be below the cutoff energy introduced by the discretization length. We also note that in the opposite limit $l > \xi$, $\lambda_{\rm dB}$ the simulation method would be inadequate to capture small-distance excitations, such as vortices. In our c-field representation we replace in Eq. 1 and in the equations of motion the operators $\hat{\psi}$ by complex numbers ψ, see Ref.[4]. We sample the initial states in a grand-canonical ensemble of temperature T and chemical potential μ via a classical Metropolis algorithm. We obtain the time evolution of $\psi(t)$ using the classical equations of motion. As our key observable, we calculate the density $n(\mathbf{r}, t) = |\psi(\mathbf{r}, t)|^2$ and average it over the thermal ensemble. For our simulations we use the trapping frequencies $(\omega_x, \omega_r) = 2\pi \times (70\,\text{Hz}, 780\,\text{Hz})$ that are higher than the experimental trap values. This is because the size of the simulation lattice is needed to be small in order to have a reasonable calculation time. We show below that this larger value of the trapping frequency does not affect our results of the sound velocity, which is determined from the sound propagation near the trap center. We choose the scattering length $a_{\rm dd}$ and the trap central density n_0 according to the experiment. $a_{\rm dd}$ varies in the range $a_{\rm dd} = 720 - 1650 a_0$, where a_0 is the Bohr radius, and n_0 in the range $n_0 = 5.5 - 11.2\,\mu\text{m}^{-3}$. Together with the trapping frequencies $(\omega_x, \omega_r) = 2\pi \times (70\,\text{Hz}, 780\,\text{Hz})$ these parameters result in a cigar-shaped cloud of $N = 4.0 \times 10^4 - 4.5 \times 10^4$ ^{6}Li molecules. The temperature varies in the range $T = 240 - 280\,$nK or $T/T_{\rm c} = 0.5 - 0.8$.

To excite sound modes we add the perturbation $\mathcal{H}_{ex}(t) = \int \mathrm{d}\mathbf{r}\, V(\mathbf{r}, t) n(\mathbf{r})$, where $n(\mathbf{r})$ is the density at the location $\mathbf{r} = (x, y, z)$. The excitation potential $V(\mathbf{r}, t)$ is given by

$$V(\mathbf{r}, t) = V_0(t) \exp\Big(-\frac{(x - x_0)^2 + (z - z_0)^2}{2\sigma^2}\Big), \tag{2}$$

where $V_0(t)$ is the time-dependent strength and σ is the width. The locations x_0, z_0 are chosen to be the trap center. We excite sound modes following the scheme used in the experiment, where σ and V_0 are chosen such that the changes in the local density due to the excitation potential are consistent with the experiment. We calculate the density profile $\bar{n}_{ex}(x, t)$, which is integrated along the radial direction. For sound propagation we examine $\Delta\bar{n}(x, t) = \big(\bar{n}_{ex}(x, t) - \bar{n}(x)\big)/\bar{n}(0)$, where $\bar{n}(x)$ is the density profile of the unperturbed cloud integrated in the radial direction and $\bar{n}(0)$ is the maximum density. As we show in the main text, the time evolution of $\Delta\bar{n}(x, t)$ displays excitation of second sound, which is identified

by a vanishing sound velocity at R_{TF}. We note that solitonic excitations are not expected as they involve a steep change of the local phase, whereas our excitation protocol modifies the local density. Furthermore the size of solitonic wave features is on the order of the healing length of 0.5 µm whereas the first and second sound features we observe have a width of a few tens of micrometers. We fit $\Delta\bar{n}(x,t)$ with a Gaussian to determine the second sound velocity u_2 at the trap center. We note that within the range of $T/T_{\mathrm{c}} = 0.5-0.7$ the velocity u_2 changes only negligibly with temperature compared to the experimental errorbars.

A. Low versus strong transverse trapping frequency

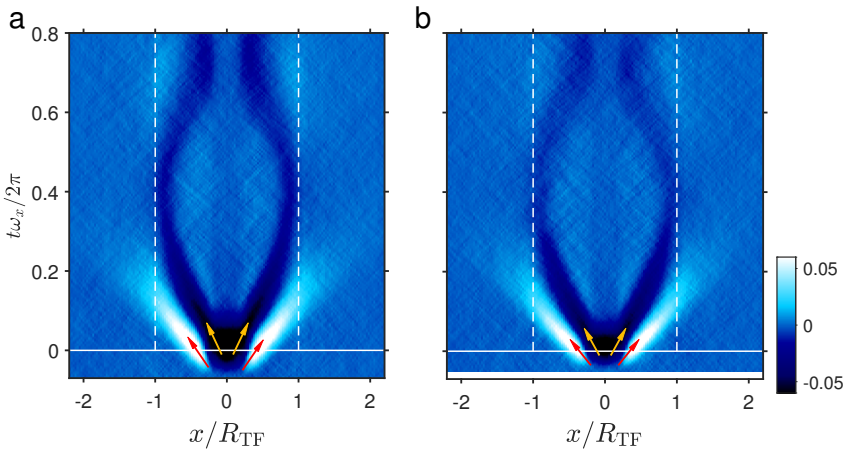

Supplementary Figure 2. **Low versus strong transverse trapping frequency. a,** Time evolution of $\Delta\bar{n}(x,t)$ as a function of axial position x and time t for $\omega_r = 2\pi \times 546\,\mathrm{Hz}$, where sound excitations are created using the excitation frequency $\omega_{\mathrm{ex}}/\omega_r = 0.61$ and a half-cycle modulation. **b,** $\Delta\bar{n}(x,t)$ for $\omega_r = 2\pi \times 780\,\mathrm{Hz}$, where we used the same relative value of $\omega_{\mathrm{ex}}/\omega_r = 0.61$ and the same half-cycle modulation as in the case of **a**. The red and orange arrows indicate the propagation of first and second sound, respectively. The determined values of the second sound velocity u_2 are $(4.74 \pm 0.15)\,\mathrm{mm/s}$ and $(4.5 \pm 0.10)\,\mathrm{mm/s}$ for the systems of low and high trapping frequency, respectively. Consequently, there is at most a weak dependence of the second sound velocity u_2 on the confinement in the transverse direction.

To examine whether a stronger confinement in the transverse direction affects the sim-

ulation result of the sound velocity, we choose a lower transverse trapping frequency of $\omega_r = 2\pi \times 546\,\mathrm{Hz}$ and compare its result with that of $\omega_r = 2\pi \times 780\,\mathrm{Hz}$, while we use the same axial trapping frequency $\omega_x = 2\pi \times 70\,\mathrm{Hz}$ and the same scattering length $a_{\mathrm{dd}} = 840 a_0$. The simulated cloud consists of $N \approx 66,000$ and $55,000$ molecules for the systems of low and high trapping frequency, respectively. To excite sound modes we use the excitation frequency $\omega_{\mathrm{ex}}/\omega_r = 0.61$ and a half-cycle modulation, which are the same as in the case of high frequency simulation. In Supp. Fig. 2 we show the time evolution of the density profile for both the systems of low and high trapping frequency. Both simulations show excitation of first and second sound pulses, as indicated by the red and orange arrows in Supp. Fig. 2. The propagation of two sound modes seems similar to the case of high frequency. For a quantitative comparison we determine the second sound velocity u_2, following the procedure described above. We obtain $u_2 = (4.74 \pm 0.15)\,\mathrm{mm/s}$ and $(4.5 \pm 0.10)\,\mathrm{mm/s}$ for the systems of low and high trapping frequency, respectively. This ensures that within the numerical error both systems give a consistent result of the sound velocity.

B. Influence of temperature on the propagation of sound modes

To examine the influence of temperature on sound propagation, we simulate the system at four different temperatures: $T = 120$, 180, 210, and 240 nK, while the trapping frequencies, the scattering length and the central density were kept fixed. This resulted in the number of molecules $N \approx 43000$, 56000, 64000, and 72000 for $T = 120$, 180, 210, and 240 nK, respectively. The healing length at the trap center is around $\xi \approx 0.5\,\mu\mathrm{m}$ and the thermal de Broglie wavelength is in the range $1.0 - 1.5\,\mu\mathrm{m}$, which fulfills the continuum limit assumed in our simulation approach. For all simulations we excite sound modes using one cycle of modulation and the excitation frequency $\omega_{\mathrm{ex}}/\omega_r = 0.61$. In Supp. Fig. 3 we show the time evolution of the density profile $\Delta\bar{n}(x,t)$ for $T = 120$, 180, 210, and 240 nK. At $T = 120 - 210\,\mathrm{nK}$, the time evolution shows multiple sound excitations. We observe two first sound pulses (a bright pulse followed by a dark pulse) that propagate outside the superfluid region. These are created while the excitation scheme is carried out as we discussed in the main text. Following the excitation scheme, also a pulse of second sound is created, which propagates only within the superfluid region and has a vanishing velocity at the Thomas-Fermi radius. In Supp. Fig. 3 a-c (upper row) an additional bright first sound wave

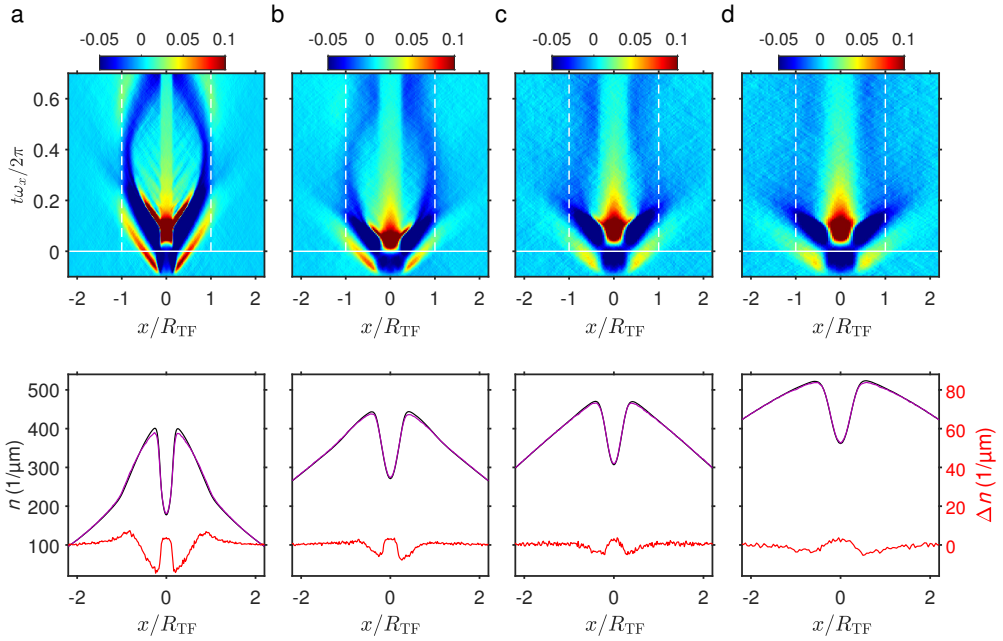

Supplementary Figure 3. **Influence of temperature on the propagation of sound modes. a-d,** Sound excitations created using one cycle of modulation and excitation frequency $\omega_{\mathrm{ex}}/\omega_r = 0.61$ for the temperatures of $T = 120$, 180, 210, and 240 nK, respectively. The bottom row shows the 1D line density profile of the perturbed cloud (purple) at time $t\omega_x/(2\pi) = 0.6$ and the corresponding background density profile (black) as well as their difference Δn (red).

appears which diffuses after a short propagation time. This happens due to the fact that this first sound wave is created after the dark second sound wave but propagates with higher velocity within the superfluid region. When it crosses the second sound wave it fades out in the simulation because mixing of first and second sound leads to diffusion. In addition, second sound signal seems to wash out for increasing temperatures. In fact, at a temperature near the transition temperature second sound becomes a diffusive sound mode as discussed in Ref.[11]. This seems to also increase the diffusion of first sound, leading e.g. to the suppression of the additional bright first sound in Supp. Fig. 3 d.

Although predicted in the simulations the diffusion of first sound is not observed in the experiment (see Fig. 4) as its wave is still clearly visible even beyond the Thomas-Fermi radius. The discrepancy between experiment and theory could be due to the inherent discrete

nature of the simulation method, where the variation in the density and the phase is not smooth on the scale of the discretization length, causing an additional dispersion of the sound wave.

To understand the long time behavior we show in the lower row of Supp. Fig. 3 the 1D density profiles at $t\omega_x/(2\pi) = 0.6$. The purple line corresponds to the cloud where sound was excited. The black line corresponds to the cloud without sound excitation. The red curve is the difference. The peak in the center of the second sound dips is due to the fact that very little or no superfluid phase is present (because the repulsive dipole potential prevents the gas from reaching the critical density in the center, see Supp. Fig. 5) and therefore second sound cannot enter the central region after it gets reflected at the Thomas-Fermi radius. This reflection is strongly visible for the lowest temperature of $T = 120$ nK in Supp. Fig. 3 a (upper row).

Supplementary Note 3: Analytic description of the sound modes

In the following we present an analytic description of first and second sound based on the two-fluid hydrodynamic model for a uniform gas. The total density n of the gas is a sum of the superfluid n_s and normal fluid density n_n. The first and second sound mode squared velocities are given by[5]

$$u_{1/2}^2 = \frac{1}{2}(c_T^2 + c_2^2 + c_3^2) \pm \left[\frac{1}{4}(c_T^2 + c_2^2 + c_3^2)^2 - c_T^2 c_2^2\right]^{1/2}, \tag{3}$$

where $c_T^2 = 1/M(\partial p/\partial n)_T$ and $c_2^2 = n_\mathrm{s} s^2 T/(n_\mathrm{n} c_\mathrm{V})$ representing the isothermal and entropic sound velocities, respectively. p is the pressure, s the entropy per unit mass, T the temperature, and $c_V = T(\partial s/\partial T)_n$ the heat capacity per unit mass. The quantity $c_3^2 \equiv c_S^2 - c_T^2 = (\partial s/\partial n)_T^2 (n^2 T/c_V)$ couples the sound velocities c_2 and c_T, where $c_S^2 = 1/M(\partial p/\partial n)_s$ corresponds to the adiabatic sound velocity. The decoupled sound modes in the limit of vanishing T are

$$u_1^2 = c_T^2 = \frac{1}{M}\Big(\frac{\partial p}{\partial n}\Big)_T \quad \text{and} \quad u_2^2 = c_2^2 = \frac{n_\mathrm{s}}{n_\mathrm{n}}\frac{s^2 T}{c_V}. \tag{4}$$

Here, first and second sound can be described as a pressure and entropy wave, respectively. To determine the second sound velocity u_2, we calculate the entropy and the normal fluid density defined as

$$S = \sum_{\mathbf{k}} \Big(- f_k \log f_k \pm (1 \pm f_k) \log(1 \pm f_k) \Big) \tag{5}$$

and

$$n_{\rm n} = \frac{1}{M} \int \frac{d\mathbf{k}^3}{(2\pi)^3} \frac{\hbar^2 k^2}{3} \Big(- \frac{\partial f_k}{\partial E_k} \Big), \tag{6}$$

respectively[5]. $f_k = 1/\big(\exp(E_k/k_{\rm B}T) \mp 1\big)$ is the thermal occupation number, where E_k is the excitation energy and $\mathbf{k}$ the wavevector. The upper and lower sign correspond to a Bose and Fermi gas, respectively.

A. BEC

We use the Bogoliubov theory, valid in the dilute limit, to analyze the regime $k_{\rm B}T < gn$, where gn is the mean-field energy. The Bogoliubov spectrum is given by $E_k = \sqrt{\epsilon_k(\epsilon_k + 2gn)}$, where $\epsilon_k = \hbar^2 k^2/(2M)$ is the free-particle spectrum. M is the molecular mass. To examine the decoupled modes in Eq. 4 we approximate E_k by the linear spectrum $E_k \approx \hbar c k$, where $c = \sqrt{gn/M}$ is the Bogoliubov sound velocity. We obtain the entropy and the normal fluid density, respectively,

$$S = V \frac{2\pi^2}{45\hbar^3} (k_{\rm B}T)^3 \Big(\frac{M}{gn} \Big)^{3/2} \quad \text{and} \quad n_{\rm n} = \frac{2\pi^2}{45} \frac{(k_{\rm B}T)^4}{\hbar^3} \frac{M^{3/2}}{(gn)^{5/2}}. \tag{7}$$

The entropy per unit mass is $s = S/(NM) = gn_{\rm n}/(MT)$ and the heat capacity per unit mass is $c_V = 3s$.

Within upper description we can deduce following sound speeds

$$u_1 = \sqrt{\frac{gn}{M}} \quad \text{and} \quad u_2 = \sqrt{\frac{1}{3}\frac{gn}{M}}. \tag{8}$$

Here, u_2 is $u_1/\sqrt{3}$. This result is only valid at zero temperature, see Supp. Fig. 4a, where we show the full numerical solutions of Eq. 3 using the Bogoliubov description.

For $k_{\rm B}T > gn$ instead we make use of a thermal gas description to determine s, c_V, and $n_{\rm n}$, which are given by $s = 2.568 k_{\rm B} n_{\rm n}/(2Mn)$, $c_V = 3s/2$, and $n_{\rm n} = n(T/T_{\rm c})^{3/2}$, respectively[5]. In this regime, solving Eq. 3 the sound velocities read,

$$u_1 = \sqrt{\frac{gn}{M} + \frac{0.856 k_{\rm B}T}{M}} \quad \text{and} \quad u_2 = \sqrt{\frac{n_{\rm s}}{n}\frac{gn}{M}}. \tag{9}$$

u_2 is proportional to $\sqrt{n_s/n}$ and can be approximated by $u_2 = \sqrt{\left(1-(T/T_c)^{3/2}\right)gn/M}$ (see Supp. Fig. 4a).

Sound amplitudes

Besides the sound velocity, our analytic description can be used to determine the amplitudes of the propagating sound modes, described as[6]

$$\delta n(x,t) = W_1 \delta\tilde{n}(x \pm u_1 t) + W_2 \delta\tilde{n}(x \pm u_2 t). \tag{10}$$

where $\delta\tilde{n}(x,t)$ is the density variation created by the excitation potential. $\delta\tilde{n}(x \pm u_{1/2}t)$ represent wave packets of first and second sound with weights $W_{1/2}$. The relative weight is given by[6]

$$\frac{W_2}{W_1} = \frac{c_2^2 - u_2^2}{u_1^2 - c_2^2}\frac{u_1^2}{u_2^2} \tag{11}$$

We determine W_2/W_1 by numerically solving Eq. 3 for the regimes $k_B T < gn$ and $k_B T > gn$ using the Bogoliubov and thermal gas description, respectively.

We show these results in Supp. Fig. 4b. The Bogoliubov description of the weight works only for $k_B T \ll gn$. We note that at higher temperatures terms beyond Bogoliubov are needed to account for the thermal damping of the modes. The Bogoliubov description thus leads to an overestimation of the weight at high temperatures. For temperatures above the mean-field energy the weight is described by the thermal gas description, which we use to estimate the relative weight of the two modes in the main text. Please note that the thermal description gives unphysical solutions for $k_B T/gn \to 1$. In the experiment presented in fig. 3 of the main text $k_B T/gn \approx 0.8$ in the central region and therefore the Bogoliubov description should be valid.

B. BCS

A condensate of an interacting Fermi gas is described by the BCS spectrum $E_k = \sqrt{\xi_k^2 + \Delta^2}$, with $\xi_k = \hbar^2 k^2/(2m) - \mu$, where μ is the chemical potential and $\Delta(T)$ the gap. At low $k_B T \ll \Delta$, we use $\mu \approx E_F$ and expand ξ_k near the Fermi surface, i.e.

10

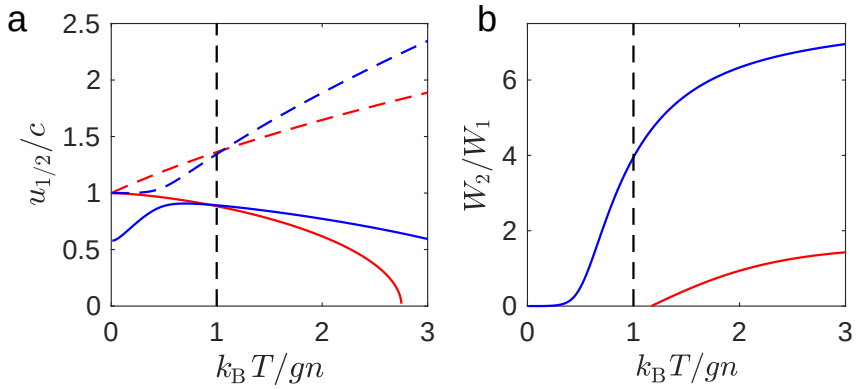

Supplementary Figure 4. **Sound velocities and amplitudes.** **a,** Sound velocities $u_{1/2}$ are determined from Eq. 3 and are shown as a function of $k_B T/gn$ using the Bogoliubov (blue lines) and thermal gas description (red lines). Here, c is the Bogoliubov sound speed introduced in the text. **b,** shows the relative weight W_2/W_1 for $k_B T < gn$ (blue line) and $k_B T > gn$ (red line). In the experiment in fig. 3 of the main text $k_B T/gn \approx 0.8$ in the central region.

$\xi_k = \hbar^2 k^2/(2m) - E_F \approx \hbar v_F |k - k_F|$ (see Ref.[7]). The entropy in Eq. 5 results in

$$S = \frac{3N_{tot}}{E_F} \int_0^\infty d\xi_k \, \frac{E_k}{k_B T} \exp\Big(-\frac{E_k}{k_B T}\Big) = 3N_{tot} \frac{\Delta_0}{E_F} \sqrt{\frac{\pi \Delta_0}{2k_B T}} \exp\Big(-\frac{\Delta_0}{k_B T}\Big), \tag{12}$$

with

$$\Delta_0 = (2/e)^{7/3} E_F \exp\big(\pi/(2k_F a)\big) \tag{13}$$

which is the gap at zero temperature[8]. With Eq. 12 we determine $s = S/(mN_{tot})$ and c_V. The normal fluid density in Eq. 6 gives

$$\frac{n_n}{n_{tot}} = 2 \int_0^\infty d\xi_k \Big(-\frac{\partial f_k}{\partial E_k}\Big) = \sqrt{\frac{2\pi\Delta_0}{k_B T}} \exp\Big(-\frac{\Delta_0}{k_B T}\Big). \tag{14}$$

Using s, c_V, and n_n in Eq. 4 we obtain the second sound velocity

$$u_2 = \frac{\sqrt{3}}{2} \frac{k_B T}{E_F} v_F, \tag{15}$$

which is valid for $T < T_c$. The BCS critical temperature is given by $k_B T_c = (\gamma/\pi)\Delta_0 = 0.567\Delta_0$, which depends on the interaction parameter $(k_F a)^{-1}$. We show in the main text the result u_2 at various interactions on the BCS side (see Fig. 2). u_2 vanishes at zero

temperature contrary to the BEC superfluids. We note that this result is consistent with Ref.[9].

Supplementary Note 4: BEC mean-field model

To estimate the density distribution of a partially Bose condensed cloud in the BEC regime we carry out a self-consistent calculation where the condensate phase is treated within the Thomas-Fermi approximation and for the normal phase we use a standard thermodynamical approach. Specifically, we solve the following set of coupled equations[10]

$$n_{\mathrm{s}}(\mathbf{r}) = \frac{\mu_{\mathrm{s}} - V_{\mathrm{ext}}(\mathbf{r}) - 2gn_{\mathrm{n}}(\mathbf{r})}{g}\Theta\left(\mu_{\mathrm{s}} - V_{\mathrm{ext}}(\mathbf{r}) - 2gn_{\mathrm{n}}(\mathbf{r})\right) \tag{16}$$

$$n_{\mathrm{n}}(\mathbf{r}) = \frac{1}{\lambda_{\mathrm{dB}}^3}\mathrm{Li}_{3/2}\left(\exp\left\{\frac{\mu_{\mathrm{n}} - V_{\mathrm{ext}}(\mathbf{r}) - 2gn_{\mathrm{s}}(\mathbf{r}) - 2gn_{\mathrm{n}}(\mathbf{r})}{k_B T}\right\}\right). \tag{17}$$

Here, λ_{dB} is the thermal de Broglie wavelength, $g = 4\pi\hbar^2 a_{\mathrm{dd}}/M$ is the coupling constant, T is the temperature and $V_{\mathrm{ext}}(\mathbf{r})$ is the external potential consisting of the harmonic trapping potential and the repulsive potential of the excitation beam, μ_{s} and μ_{n} are the chemical potentials of the superfluid and the normal fluid part, respectively. For the calculation we set $\mu_{\mathrm{n}} = \min[V_{\mathrm{ext}}(\mathbf{r}) + 2gn_{\mathrm{s}}(\mathbf{r}) + 2gn_{\mathrm{n}}(\mathbf{r})]$ which ensures that the normal gas reaches the critical density $n_{\mathrm{n,crit}} = \mathrm{Li}_{3/2}(1)/\lambda_{\mathrm{dB}}^3$ at the Thomas-Fermi radius. This way, the number of normal fluid atoms is fixed. μ_{s} is chosen such that the total atom number matches the experimental value.

Equation 16 represents the Thomas-Fermi approximation where we take into account the repulsive mean-field potential of the normal fluid part. Equation 17 is the density distribution of a thermal bosonic cloud, again including the additional mean-field potential produced by the atoms. By self-consistently solving the coupled equations we obtain the density distributions of the superfluid and the normal fluid gas as shown in Supp. Fig. 5. The repulsive excitation beam pushes the atoms away from the trap center which creates a density profile with two peaks of the same height. Interestingly in our self-consistent calculations we find that the peak density with and without the excitation beam is almost the same. This holds both for the line density and the 3D density. This allows for extracing the peak density in our experiments, when the excitation laser is present, from reference absorption images of an unperturbed cloud when no excitation laser is present. To do this,

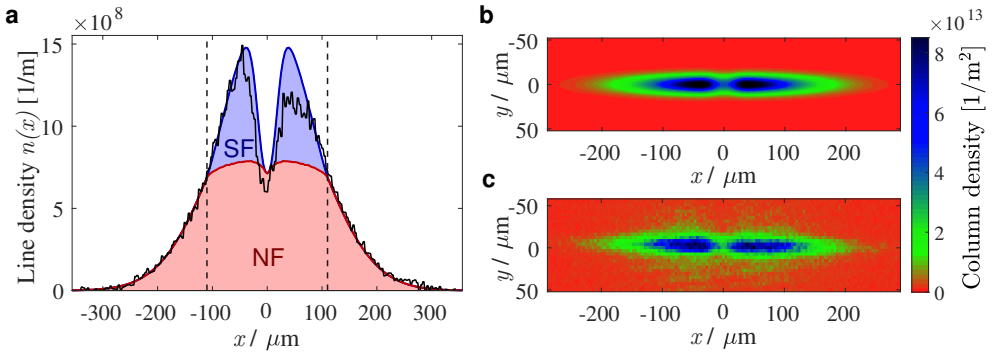

Supplementary Figure 5. **Calculated and measured atom densities at $(k_\mathrm{F}a)^{-1} = 1.61$ and a temperature of $T = 220\,\mathrm{nK}$. The repulsive excitation laser beam in the trap center locally reduces the atom density. The shown density distributions correspond to the state just before modulation starts.** **a**, The blue and red line show the line densities of the superfluid and the normal phase obtained from a self-consistent calculation, the measured total line density is shown is black. The vertical dotted lines indicate the Thomas-Fermi radius at $x = \pm 110\,\mu\mathrm{m}$. **b**, Calculated absorption image of the atom cloud. **c**, Measured absorption image of the atom cloud.

we apply the inverse Abel transformation to the reference absorption images to reconstruct the 3D density profile. Note that this transformation is in generally valid only for rotationally symmetric clouds, which is the case when no exciation beam is present. We have verified that we obtain the same density using our self-consistent calculations where we input the temperature, the total number of atoms, the trapping frequencies and the scattering length. This is possible since the interaction parameter of $(k_\mathrm{F}a)^{-1} = 1.61$ is still close to the BEC regime. Supplementary Figure 5 a-c shows there is good agreement for the calculated and measured density distributions, which validates this approach.

SUPPLEMENTARY REFERENCES

[1] Paintner, T. et al. Pair fraction in a finite-temperature Fermi gas on the BEC side of the BCS-BEC crossover. *Phys. Rev. A* **99**, 053617 (2019).

[2] Pini, M., Pieri, P., Jäger, M., Hecker Denschlag J., and Calvanese Strinati, G. Pair correlations in the normal phase of an attractive Fermi gas. *New J. Phys.* **22** 083008 (2019).

[3] Ku, M. J. H., Sommer, A. T., Cheuk, L. W. and Zwierlein, M. W. Revealing the Superfluid Lambda Transition in the Universal Thermodynamics of a Unitary Fermi Gas. *Science* **335**, 563 (2012).

[4] Singh, V. P. et al. Probing superfluidity of Bose-Einstein condensates via laser stirring. *Phys. Rev. A* **93**, 023634 (2016).

[5] Pethick, C. J. and Smith, H. *Bose-Einstein Condensation in Dilute Gases.* (Cambridge University Press, Cambridge, 2008)

[6] Arahata, E. and Nikuni, T. Propagation of second sound in a superfluid Fermi gas in the unitary limit. *Phys. Rev. A* **80**, 043613 (2009).

[7] Lifshitz, E.M. and Pitaevskii, L.P. *Statistical Physics, Part 2, Theory of the Condensed State.* (Butterworth-Heinemann, Oxford, 1980).

[8] Gor'kov, L.P. and Melik-Barkhudarov, T.K. Contribution to the Theory of Superfluidity in an Imperfect Fermi Gas. *Sov. Phys. JETP* **13**, 1018 (1961).

[9] Heiselberg, H. Sound modes at the BCS-BEC crossover. *Phys. Rev. A* **73**, 013607 (2006).

[10] Pitaevskii, L. and Stringari, S. *Bose-Einstein Condensation.* (Oxford University Press, Oxford, 2003).

[11] Singh, V. P. and Mathey, L. Sound propagation in a two-dimensional Bose gas across the superfluid transition. *Phys. Rev. Research* **2** 023336 (2020).

B.3 Pair correlations in the normal phase of an attractive Fermi gas.

Note that the information shown is published in Reference [16].

Michele Pini, Pierbiagio Pieri, Manuel Jäger, Johannes Hecker Denschlag, and Giancarlo Calvanese Strinati

"Pair correlations in the normal phase of an attractive Fermi gas", *New Journal of Phyiscs* **22**, 083008 (2020)

IOP Publishing New J. Phys. 22 (2020) 083008 https://doi.org/10.1088/1367-2630/ab9ee3

New Journal of Physics
The open access journal at the forefront of physics

Deutsche Physikalische Gesellschaft DPG
IOP Institute of Physics
Published in partnership with: Deutsche Physikalische Gesellschaft and the Institute of Physics

OPEN ACCESS

RECEIVED
27 November 2019

REVISED
28 May 2020

ACCEPTED FOR PUBLICATION
22 June 2020

PUBLISHED
5 August 2020

PAPER

Pair correlations in the normal phase of an attractive Fermi gas

M Pini[1], **P Pieri**[1,2], **M Jäger**[3], **J Hecker Denschlag**[3] and **G Calvanese Strinati**[1,2,4,5]

[1] School of Science and Technology, Physics Division, Università di Camerino, 62032 Camerino (MC), Italy
[2] INFN, Sezione di Perugia, 06123 Perugia (PG), Italy
[3] Institut für Quantenmaterie and Center for Integrated Quantum Science and Technology (IQST), Universität Ulm, 89069 Ulm, Germany
[4] CNR-INO, Istituto Nazionale di Ottica, Sede di Firenze, 50125 (FI), Italy
[5] Author to whom any correspondence should be addressed.

E-mail: giancarlo.strinati@unicam.it

Keywords: superfluid Fermi gases, pairing correlations, preformed pairs

Abstract

In a recent paper (2019 *Phys. Rev. A* **99**, 053617), the total number of fermion pairs in a spin-balanced two-component Fermi gas of ^{6}Li atoms was experimentally probed in the normal phase above the superfluid critical temperature, in order to investigate the sectors of pseudogap and preformed-pair in the temperature–coupling phase diagram. Here, we present a theoretical account of these experimental results in terms of an *ab initio* self-consistent *t*-matrix calculation, which emphasizes the role of the pair-correlation function between opposite-spin fermions at equilibrium. Good agreement is found between the available experimental data and the theoretical results obtained with no adjustable parameter.

1. Introduction

Preformed pairs are meant to be bound states which form above the critical temperature of a fermionic superfluid [1, 2]. They are usually associated with the occurrence of a pseudo-gap which can be viewed as a carry-over of the pairing gap in the superfluid phase to the normal phase [3]. Although in the limit of low density and strong fermionic attraction, a preformed pair can be approximately described by a bound state of two fermions of opposite spin, in general it has intrinsically a many-body nature. In order to take into account the many-body character of a pair, it is convenient to describe the pair problem in terms of correlations between the fermions. These correlations are a non-trivial function of temperature, particle density, and the inter-particle coupling.

Preformed pairs were recently studied in an experiment with a spin-balanced two-component Fermi gas of ^{6}Li in the normal phase [4], where the number of fermion pairs N_p was determined by converting all atom pairs to tightly-bound diatomic molecules which afterward were detected. The pairing fraction N_p/N_σ (where N_σ is the number of all atoms per spin-state) was reported for various temperatures and couplings on the BEC side of the BCS–BEC crossover.

A preliminary theoretical account of the pairing fractions was already presented in reference [4], which was obtained by a statistical model of non-interacting atoms and molecules at equilibrium [5, 6] as well as by an *ab initio* diagrammatic *t*-matrix approach [7]. However, the comparison between experiment and theory presented in reference [4] called for further improvements, because the statistical model could not be confidently extended to the crossover region and the *t*-matrix calculation was lacking refinements which turned out to be important for the crossover region.

Here, we present an improved account of the theoretical approach. We investigate correlations between spin-up and spin-down fermions at thermal equilibrium. On the basis of this, we derive a meaningful definition and measure for preformed pairs. We calculate thermodynamic quantities such as the pairing fraction, rather than dynamical quantities such as the pseudo-gap. Nevertheless, the pseudo-gap physics is well contained in our approach. As a consequence, the results of our quantum many-body approach in the crossover region differ significantly from the ones of the statistical atom–molecule model where the

fermionic character of the pairs is neglected. In general, we find good agreement between theory and experiment, giving us confidence on the validity of our approach.

Our detailed theoretical interpretation of the experimental data of reference [4] and new insights on the separation between the molecular and pseudo-gap regimes are the main results of this paper. In addition, we calculate for a homogeneous Fermi gas (i) the pair correlation function, (ii) Tan's contact (a quantity that sets the overall scale of the pair correlation function), and (iii) the pairing fraction. These three quantities are calculated for different temperatures and couplings across the BCS–BEC crossover. For a trapped system, we also report density profiles and compare them to experimental measurements, and we provide the superfluid critical temperature across the BCS–BEC crossover.

It should be mentioned that the temperature dependence of the contact in the homogeneous case and of the density profiles in the trapped case were already reported in references [8, 9] within the same self-consistent t-matrix approach of our work, albeit only for the unitary case. We have verified that for this case our results fully agree with the published ones.

The paper is organized as follows. Section 2 describes the theoretical approach. Section 3 presents calculated pair fractions $N_{\rm p}/N_\sigma$ for the homogeneous system. Section 4 compares these results to the experimental data of reference [4] after suitable averaging for the trap. Section 5 presents our conclusions. Appendix A discusses the use of conserving approximations for the many-body structure of the pair fraction. Appendix B highlights the circumstances under which the many-body approach to the pair fraction reduces to that of the statistical model. Finally, appendix C obtains the critical temperature of a trapped low-density Bose gas. Throughout the paper, we set $\hbar = 1$.

2. Theoretical approach

The theoretical approach that we set up to account for the experimental results of reference [4] on the pair fraction builds on the following ingredients: (i) the definition of the many-body propagator for composite bosons introduced in appendix A of reference [10]; (ii) the formalism developed in reference [11] to calculate the pair correlation function of opposite-spin fermions also in the normal phase; (iii) the experience recently nurtured in reference [7] on the fully self-consistent solution of the t-matrix approach to a Fermi gas with an attractive inter-particle interaction.

This Fermi gas is made to span the BCS–BEC crossover by varying the (dimensionless) coupling parameter $(k_{\rm F}a_{\rm F})^{-1}$, where $k_{\rm F} = (3\pi^2 n)^{1/3}$ is the Fermi wave vector associated with the number density n and $a_{\rm F}$ is the scattering length of the two-fermion problem [12]. In practice, the crossover between the BCS and BEC regimes is exhausted within the range $-1 \lesssim (k_{\rm F}a_{\rm F})^{-1} \lesssim +1$ about unitarity where $(k_{\rm F}a_{\rm F})^{-1} = 0$. In the following, we shall mostly be interested in the coupling region $0 \lesssim (k_{\rm F}a_{\rm F})^{-1} \lesssim +1.5$ on the BEC side of unitarity for which the experimental data of reference [4] are available.

2.1. Outline of the theoretical expressions to be related with the experimental data

Strictly speaking, a pair of spin-up and spin-down fermions can be regarded as a purely bosonic entity only in the BEC regime and at sufficiently low temperatures. In all other cases, one should search for *correlations* between fermions and define the occurrence of pairing accordingly. Adopting this point of view, which applies also to the so-called Cooper pairs in the BCS regime, is definitely required on the BEC side of unitarity in the normal phase, where the experimental data reported in reference [4] were collected. To this end, a suitable definition is needed of what would loosely speaking be referred to as a 'preformed pair' in the normal phase of a fermionic superfluid. This definition should be based on a quantum many-body approach where fermions are the elementary constituents of the theory, with no *a priori* reference to the preformed pairs themselves.

We begin by introducing the bosonic propagator

$$\mathcal{G}_{\rm B}(x,x') = -\langle T_\tau[\Psi_{\rm B}(x)\Psi_{\rm B}^\dagger(x')]\rangle, \tag{1}$$

where $x = (\mathbf{r},\tau)$ groups the spatial position $\mathbf{r}$ and imaginary time τ, $\Psi_{\rm B}(\mathbf{r})$ is a bosonic field operator, T_τ the time-ordered operator, and $\langle\cdots\rangle$ a thermal average taken at temperature T [13]. In terms of this propagator, the total number of bosons is given by

$$\begin{aligned} N_{\rm p} &= -\int {\rm d}\mathbf{r}\, \mathcal{G}_{\rm B}(x,x^+) \\ &= -\int {\rm d}\mathbf{r} \int \frac{{\rm d}\mathbf{q}}{(2\pi)^3} \frac{1}{\beta} \sum_\nu {\rm e}^{{\rm i}\Omega_\nu \eta}\, \mathcal{G}_{\rm B}(\mathbf{q},\Omega_\nu), \end{aligned} \tag{2}$$

where $\mathbf{q}$ is a wave vector, $\Omega_\nu = 2\pi\nu/\beta$ (ν integer) a bosonic Matsubara frequency with $\beta = (k_B T)^{-1}$ and k_B the Boltzmann constant, and $\eta = 0^+$. In the last line of equation (2) a homogeneous system has been assumed, for which one may simply write $N_p = \mathcal{V}\, n_p$ where $\mathcal{V}$ is the volume occupied by the system and n_p the boson density.

To the extent that the bosonic entities we are considering are made up of fermion pairs, the bosonic operator $\Psi_B(\mathbf{r})$ has to be related to its fermionic counterparts $\psi_\sigma(\mathbf{r})$, where $\sigma = (\uparrow, \downarrow)$ is the spin projection. This can be achieved by setting

$$\Psi_B(\mathbf{r}) = \int \mathrm{d}\boldsymbol{\rho}\, \phi(\boldsymbol{\rho})\, \psi_\downarrow(\mathbf{r} - \boldsymbol{\rho}/2)\, \psi_\uparrow(\mathbf{r} + \boldsymbol{\rho}/2) \tag{3}$$

where $\phi(\boldsymbol{\rho})$ is a suitable function that should itself embody the correlations within a fermion pair we are after.

On physical grounds, at sufficiently low temperature in the BEC regime it is reasonable to take $\phi(\boldsymbol{\rho})$ as the (normalized) bound-state wave function of the fermionic two-body problem *in vacuum*, namely,

$$\phi(\boldsymbol{\rho}) = \frac{1}{\sqrt{2\pi a_F}} \frac{\mathrm{e}^{-\rho/a_F}}{\rho} \tag{4}$$

where $\rho = |\boldsymbol{\rho}|$, whose Fourier transform reads

$$\phi(\mathbf{p}) = \sqrt{\frac{8\pi}{a_F}} \frac{1}{\mathbf{p}^2 + a_F^{-2}}. \tag{5}$$

As already mentioned, the definition (3) together with the expression (4) was originally used in reference [10] to describe condensed composite bosons well below the superfluid transition temperature T_c with fermions treated within the mean-field approximation [14]. The same combination of the expressions (3) and (4) was then utilized in reference [4], aiming to account for the quantity N_p of equation (2) on the BEC side of unitarity in the normal phase above T_c, even up to a few times the Fermi temperature T_F. In addition, in this case fermions were treated within the self-consistent t-matrix approach [7], with a further trap averaging to comply with the experimental procedure of reference [4].

To account for the experimental data of reference [4] in a comprehensive way, however, the function $\phi(\boldsymbol{\rho})$ with which the projection is performed in equation (3) should acquire a more general form than the expression (4), which is expected to be valid only in the BEC regime at low temperature. Accordingly, in what follows (cf section 3.1) we will replace the expression (4) by a more general form obtained from the pair correlation function studied in reference [11], a form which can thus be utilized even past unitarity toward the BCS regime and up to a temperature of even several times T_F.

In addition, we shall see below (cf section 2.2) that in the diagrammatic expansion of the expressions (1) and (3) one should also retain an 'unbound' term that was disregarded in the analysis of reference [4] since it is negligible in the BEC limit.

It turns out (cf section 4.2) that both these refinements (namely, the inclusion of the above unbound term and the improvement of the expression (4) in terms of the pair correlation function) improve the comparison with the experimental data of reference [4], especially just on the BEC side of unitarity. This comparison will also make it possible to distinguish between the pseudo-gap and the molecular regimes mentioned in the Introduction. Specifically, we argue that the molecular regime should be reached when the unbound term contributes in a negligible way to the quantity N_p of equation (2).

2.2. Diagrammatic approach to the pair fraction

We pass now to describe the diagrammatic approach that we have adopted for the calculation of the expressions (1)–(3). Although we are interested in the normal phase above T_c which the experimental data of reference [4] are restricted to, we find it convenient to adopt the Nambu representation of the fermionic field operators

$$\Psi(\mathbf{r}) = \begin{pmatrix} \psi_\uparrow(\mathbf{r}) \\ \psi_\downarrow^\dagger(\mathbf{r}) \end{pmatrix}, \tag{6}$$

in terms of which the diagrammatic approach for the superfluid phase below T_c is usually formulated [15]. This is mainly because the concept of fermion pairing originates from the superfluid phase [14], from which it can be extrapolated to the normal phase in the context of the BCS–BEC crossover [12] under suitable circumstances, like in the present case. In addition, through the Nambu representation (6) one finds it easier to deal with the issue of conserving approximations for a fermionic superfluid [16]. This

proves important when one selects the set of diagrams that would describe at best the physical problem of interest, with the condition that their numerical implementation remains affordable. We shall discuss this issue in appendix A.

In terms of the Nambu representation (6), one writes for the fermionic single-particle Green's function

$$\mathcal{G}(1,2) = -\langle T_\tau[\Psi(1)\Psi^\dagger(2)]\rangle \tag{7}$$

and for the fermionic two-particle Green's function

$$\mathcal{G}_2(1,2;1',2') = \langle T_\tau[\Psi(1)\Psi(2)\Psi^\dagger(2')\Psi^\dagger(1')]\rangle, \tag{8}$$

with the short-hand notation $1 = (\mathbf{r}_1, \tau_1, \ell_1)$ and so on, where the Nambu index $\ell = (1,2)$ refers to the upper or lower component in the expression (6). Here, $\mathcal{G}_2$ is related to the two-particle correlation function

$$L(1,2;1',2') = \mathcal{G}_2(1,2;1',2') - \mathcal{G}(1,1')\,\mathcal{G}(2,2') \tag{9}$$

which satisfies the Bethe–Salpeter equation [10, 16, 17]

$$L(1,2;1',2') = -\mathcal{G}(1,2')\mathcal{G}(2,1') + \int \mathrm{d}3456\; \mathcal{G}(1,3)\mathcal{G}(6,1')\Xi(3,5;6,4)L(4,2;5,2') \tag{10}$$

where

$$\Xi(1,2;1',2') = \frac{\delta\Sigma(1,1')}{\delta\mathcal{G}(2',2)} \tag{11}$$

is an effective two-particle interaction with Σ the fermionic self-energy. Equation (10) can be formally solved in terms of the many-particle T-matrix, defined as the solution to the equation [10, 16, 17]

$$T(1,2;1',2') = \Xi(1,2;1',2') + \int \mathrm{d}3456\; \Xi(1,4;1',3)\mathcal{G}(3,6)\mathcal{G}(5,4)T(6,2;5,2'), \tag{12}$$

by writing

$$-L(1,2;1',2') = \mathcal{G}(1,2')\mathcal{G}(2,1') + \int \mathrm{d}3456\; \mathcal{G}(1,3)\mathcal{G}(6,1')T(3,5;6,4)\mathcal{G}(4,2')\mathcal{G}(2,5). \tag{13}$$

The above equations hold quite generally, regardless of the specific approximation for the kernel Ξ defined in equation (11). In particular, to the BCS approximation Σ_{BCS} for the self-energy there corresponds the kernel:

$$\begin{aligned}\Xi_{\mathrm{BCS}}(1,2;1',2') &= \frac{\delta\Sigma_{\mathrm{BCS}}(1,1')}{\delta\mathcal{G}_{\mathrm{BCS}}(2',2)} \\ &= -\tau^3_{\ell_1\ell_{2'}}\delta(x_1 - x_{2'})v(x_1^+ - x_{1'})\delta(x_{1'} - x_2)\tau^3_{\ell_{1'}\ell_2}(1 - \delta_{\ell_1\ell_{1'}})\end{aligned} \tag{14}$$

where only the off-diagonal terms of the BCS self-energy have been retained following a common practice. In the expression (14), τ^3 is the third Pauli matrix [15], $x_1 = (\mathbf{r}_1, \tau_1)$ and so on, and $v(x_1^+ - x_{1'}) = \delta(\tau_1^+ - \tau_{1'})v(\mathbf{r}_1 - \mathbf{r}_{1'})$ is the attractive fermionic interaction. For the ultra-cold Fermi atoms of interest, one takes $v(\mathbf{r}_1 - \mathbf{r}_{1'}) = v_0\delta(\mathbf{r}_1 - \mathbf{r}_{1'})$ of the contact form, where the (negative) strength v_0 is further eliminated in favor of the scattering length a_{F} through a standard regularization procedure [12].

We return at this point to the expression (1) of the bosonic propagator $\mathcal{G}_{\mathrm{B}}$ with the definition (3) for the bosonic field, which we rewrite in the Nambu representation (6). The following compact form then results for $\mathcal{G}_{\mathrm{B}}$ in terms of the two-particle correlation function (9):

$$\mathcal{G}_{\mathrm{B}}(\mathbf{r}\tau, \mathbf{r}'\tau') = -\int \mathrm{d}\boldsymbol{\rho} \int \mathrm{d}\boldsymbol{\rho}'\, \phi(\boldsymbol{\rho})\phi^*(\boldsymbol{\rho}')\, L(1,2;1',2') \tag{15}$$

with the identification $1 = (\mathbf{r} + \boldsymbol{\rho}/2, \tau, \ell = 1)$, $2 = (\mathbf{r}' - \boldsymbol{\rho}'/2, \tau', \ell = 2)$, $1' = (\mathbf{r} - \boldsymbol{\rho}/2, \tau^+, \ell = 2)$, and $2' = (\mathbf{r}' + \boldsymbol{\rho}'/2, \tau'^+, \ell = 1)$. Hereafter, it will be understood that only the terms that survive once carried over from below to above T_{c} will be retained in the expression (15). Accordingly, in passing from equation (9) to equation (15) we have neglected the second term on the right-hand side of equation (9), which corresponds to the (square magnitude of the) condensate amplitude and thus vanishes above T_{c} [10].

In addition, it will be shown in appendix A that, due to the specific identification of the Nambu indices relevant to equation (15), the many-particle T-matrix of equation (12) which solves the Bethe–Salpeter equation for L can be built *only* in terms of the effective two-particle interaction Ξ of the form (14) [18].

This leaves us with the freedom of endowing the fermionic single-particle Green's function $\mathcal{G}$ of equation (7) with a suitable *additional* self-energy Σ to be selected on physical grounds, without being forced to introduce at the same time related additional terms in the kernel Ξ via equation (11).

With these considerations in mind, we have selected this additional self-energy of the form of the fully self-consistent t-matrix approach, whose performance in the normal phase above T_c has been recently tested against those of the non-self-consistent as well as of other partially self-consistent t-matrix approaches [7], with the result that the fully self-consistent one performs best at least as far as thermodynamic quantities are concerned. To the extent that the quantity N_p given by the expression (2) of interest here is itself a thermodynamic quantity (consistently with the fact that no analytic continuation from Matsubara to real frequencies is required to calculate it), this choice for Σ within the fully self-consistent t-matrix approach appears to be adequate for our purposes. In addition, the BCS self-energy Σ_{BCS}, which has served to obtain the kernel Ξ_{BCS} of equation (14), vanishes identically in the normal phase and no longer needs to be considered in what follows.

For a homogeneous system, we can further make use of the Fourier representation and rewrite equation (15) as:

$$\mathcal{G}_B(\mathbf{q},\Omega_\nu) = -\int\frac{d\mathbf{p}}{(2\pi)^3}\frac{1}{\beta}\sum_n\int\frac{d\mathbf{p}'}{(2\pi)^3}\frac{1}{\beta}\sum_{n'}\phi(\mathbf{p}+\mathbf{q}/2)\phi(\mathbf{p}'+\mathbf{q}/2)\,L_{22}^{11}(\mathbf{p}\omega_n,\mathbf{p}'\omega_{n'};\mathbf{q}\Omega_\nu) \tag{16}$$

where $\omega_n = (2n+1)\pi/\beta$ (n integer) is a fermionic Matsubara frequency (the conventions for the Nambu indices are specified in figure A1 of appendix A). The expression (16) will be utilized in equation (2) to obtain the number of pairs N_p. Solving then for the many-particle T-matrix of equation (12) as described above and entering the result in equation (13) for L, equation (16) reduces eventually to the form:

$$\mathcal{G}_B(\mathbf{q},\Omega_\nu) = -\mathcal{F}_2(\mathbf{q},\Omega_\nu) - \mathcal{F}_1(\mathbf{q},\Omega_\nu)^2\,\Gamma(\mathbf{q},\Omega_\nu). \tag{17}$$

Here,

$$\mathcal{F}_j(\mathbf{q},\Omega_\nu) = \int\frac{d\mathbf{p}}{(2\pi)^3}\,\phi(\mathbf{p}+\mathbf{q}/2)^j\frac{1}{\beta}\sum_n\mathcal{G}(\mathbf{p}+\mathbf{q},\omega_n+\Omega_\nu)\mathcal{G}(-\mathbf{p},-\omega_n) \tag{18}$$

are 'form factors' associated with the particle–particle bubble where $j = (1,2)$, and

$$\Gamma(\mathbf{q},\Omega_\nu) = -\left(\frac{m}{4\pi a_F} + R_{pp}(\mathbf{q},\Omega_\nu)\right)^{-1} \tag{19}$$

is the particle–particle propagator in the normal phase where

$$R_{pp}(\mathbf{q},\Omega_\nu) = \int\frac{d\mathbf{p}}{(2\pi)^3}\frac{1}{\beta}\sum_n\mathcal{G}(\mathbf{p}+\mathbf{q},\omega_n+\Omega_\nu)\mathcal{G}(-\mathbf{p},-\omega_n) - \int\frac{d\mathbf{p}}{(2\pi)^3}\frac{m}{\mathbf{p}^2} \tag{20}$$

is the regularized particle–particle bubble [12]. We emphasize again that the fermionic single-particle Green's functions $\mathcal{G}$ entering the expressions (18) and (20) are meant to be obtained within the self-consistent t-matrix approach in the normal phase [7].

What is still left to be specified is the form of the wave function $\phi(\mathbf{p})$ that enters equation (18). We have already mentioned that, in the theoretical diagrammatic approach to N_p presented in reference [4], $\phi(\mathbf{p})$ was taken of the form (5) corresponding to the fermionic two-body problem. With this choice, however, meaningful results could be obtained only toward the BEC edge of the BEC side of the unitary region. To overcome this limitation, here we adopt a more general form for $\phi(\mathbf{p})$ which will be obtained from the pair correlation function, as discussed in section 3.1 below.

In addition, in reference [4] the first term on the right-hand side of equation (17) was not retained. As anticipated in section 2.1, this term will be referred to as the 'unbound' term as opposed to the 'bound' term discussed below. Here, we are going to keep this 'unbound' term and show that it gives a non-negligible contribution to N_p, through the pairing correlations contained both in the fermionic single-particle Green's function $\mathcal{G}$ and in the wave function $\phi(\mathbf{p})$ that enter the expression (18) with $j = 2$. Accordingly, through this term spin-↑ and spin-↓ fermions correlate with each other *indirectly* via their separate interaction with the environment.

In contrast, the second term on the right-hand side of equation (17) is referred to as the 'bound' term, because in this case spin-↑ and spin-↓ fermions correlate with each other *directly* through their inter-particle attractive interaction. The result for N_p obtained from this term will be shown to reduce to that of the statistical model of atom–molecule equilibrium introduced in references [5, 6], past the BEC side of the unitary region and for not too high temperatures above T_c. The reasons for the success of the statistical atom–molecule model in this sector of the phase diagram will be discussed in appendix B.

2.3. Single-particle Green's function

As discussed in section 2.2, the single-particle Green's function $\mathcal{G}(\mathbf{p},\omega_n)$ that enters the expressions (18) and (20) is taken within the fully self-consistent t-matrix approach. It then reads:

$$\mathcal{G}(\mathbf{p},\omega_n) = \left[\mathcal{G}_0(\mathbf{p},\omega_n)^{-1} - \Sigma(\mathbf{p},\omega_n)\right]^{-1} \tag{21}$$

where $\mathcal{G}_0(\mathbf{p},\omega_n) = [\mathrm{i}\omega_n - \xi(\mathbf{p})]^{-1}$ is the non-interacting counterpart with $\xi(\mathbf{p}) = \mathbf{p}^2/(2m) - \mu$ (m being the fermion mass and μ the chemical potential) and

$$\Sigma(\mathbf{p},\omega_n) = -\int \frac{\mathrm{d}\mathbf{q}}{(2\pi)^3}\frac{1}{\beta}\sum_{\nu}\Gamma(\mathbf{q},\Omega_\nu)\,\mathcal{G}(\mathbf{q}-\mathbf{p},\Omega_\nu-\omega_n) \tag{22}$$

is the self-energy with $\Gamma(\mathbf{q},\Omega_\nu)$ given by equations (19) and (20). The chemical potential is eventually obtained from the fermionic density n_σ via the relation

$$n_\sigma = \int \frac{\mathrm{d}\mathbf{p}}{(2\pi)^3}\frac{1}{\beta}\sum_{n}\mathrm{e}^{\mathrm{i}\omega_n\eta}\,\mathcal{G}(\mathbf{p},\omega_n) \tag{23}$$

where $n_\uparrow = n_\downarrow = n/2$ like in reference [4]. The numerical calculation of the expressions (21)–(23) will be implemented by taking advantage of the detailed procedures recently reported in reference [7].

In addition, the strong-coupling (BEC) limit of the expressions (21)–(23), together with that of the expressions (2) and (17)–(20), will be examined in appendix B, to determine under what circumstances the results for n_p and n_σ obtained by our diagrammatic quantum many-body theory reduce to those of the statistical model of atom–molecule equilibrium developed in references [5, 6].

3. Results for a homogeneous gas

In this section, we implement the calculation of the bosonic density n_p obtained from equations (2) and (17) for a homogeneous gas, as a function of coupling and temperature. The information gathered in this way will be used in section 4 when dealing with a trapped gas, by performing a trap average within a local-density approximation. At that point it will be possible to compare the theoretical results with the experimental data of reference [4].

The main ingredients of the calculation of n_p are the single-particle Green's function $\mathcal{G}(\mathbf{p},\omega_n)$ and the wave function $\phi(\mathbf{p})$ that enter equations (18)–(20). The calculation of $\mathcal{G}(\mathbf{p},\omega_n)$ was already considered in section 2.3. It thus remains to consider the calculation of the wave function $\phi(\mathbf{p})$, as discussed next.

3.1. Pair correlation function

Our interpretation of the experimental data of reference [4] rests on the occurrence of *correlations* between spin-up and spin-down fermions at equilibrium. The preliminary theoretical account of those experimental data presented in reference [4] took the wave function $\phi(\mathbf{p})$ entering equation (18) of the form (5) associated with the fermionic two-body problem. This form, however, proves able to account for the correlations between spin-up and spin-down fermions only in the BEC regime of coupling and at low enough temperature. As anticipated in section 2.2, we now consider a more general form for $\phi(\mathbf{p})$ which is obtained from the pair correlation function

$$g_{\uparrow\downarrow}(\boldsymbol{\rho}) = \left\langle \psi_\uparrow^\dagger\left(\frac{\boldsymbol{\rho}}{2}\right)\psi_\downarrow^\dagger\left(-\frac{\boldsymbol{\rho}}{2}\right)\psi_\downarrow\left(-\frac{\boldsymbol{\rho}}{2}\right)\psi_\uparrow\left(\frac{\boldsymbol{\rho}}{2}\right)\right\rangle - \left(\frac{n}{2}\right)^2. \tag{24}$$

This function contains information about correlations between fermions of opposite spins at a distance $\rho = |\boldsymbol{\rho}|$ apart. This quantity was studied in detail in reference [11] throughout the BCS–BEC crossover, both in the superfluid phase below T_c and in the normal phase above T_c. Here, we consider the formalism of reference [11] above T_c and rephrase it in terms of the fully self-consistent t-matrix approach that was summarized in section 2.3.

Within the fully self-consistent t-matrix approach, the expression (24) for $g_{\uparrow\downarrow}(\boldsymbol{\rho})$ can be cast in the form [11]:

$$g_{\uparrow\downarrow}(\boldsymbol{\rho}) = \int \frac{\mathrm{d}\mathbf{q}}{(2\pi)^3}\frac{1}{\beta}\sum_{\nu}\mathrm{e}^{\mathrm{i}\Omega_\nu\eta}\,\Gamma(\mathbf{q},\Omega_\nu)\int\frac{\mathrm{d}\mathbf{p}}{(2\pi)^3}\,\mathrm{e}^{\mathrm{i}\mathbf{p}\cdot\boldsymbol{\rho}}\,\tilde{\Pi}(\mathbf{p};\mathbf{q},\Omega_\nu)\int\frac{\mathrm{d}\mathbf{p}'}{(2\pi)^3}\,\mathrm{e}^{-\mathrm{i}\mathbf{p}'\cdot\boldsymbol{\rho}}\,\tilde{\Pi}(\mathbf{p}';\mathbf{q},\Omega_\nu) \tag{25}$$

where

$$\tilde{\Pi}(\mathbf{p};\mathbf{q},\Omega_\nu) = \frac{1}{\beta}\sum_{n}\mathcal{G}(\mathbf{p}+\mathbf{q},\omega_n+\Omega_\nu)\,\mathcal{G}(-\mathbf{p},-\omega_n). \tag{26}$$

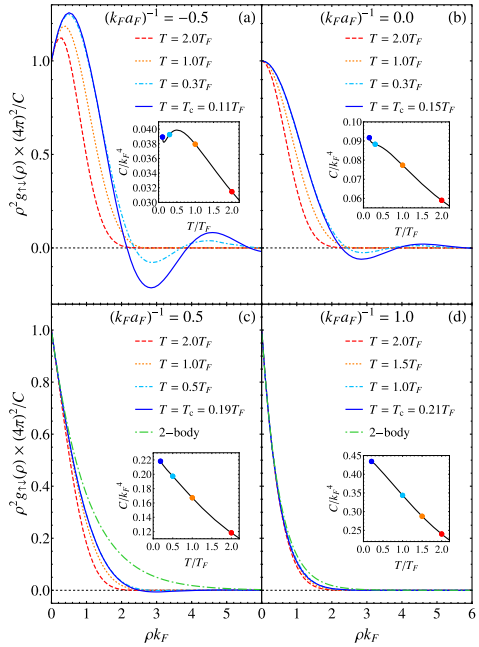

Figure 1. Spatial profiles of $\rho^2 g_{\uparrow\downarrow}(\rho)$ are shown vs ρ (in units of k_F^{-1}), for several couplings about unitarity and different temperatures in the normal phase. In each panel, the inset gives the dependence of the contact C over an extended range of temperature (in units of the Fermi temperature T_F), where the dots correspond to the temperatures reported in the same panel. In panels (c) and (d), the expression $(2\pi a_F)\rho^2|\phi(\rho)|^2 = e^{-2\rho/a_F}$ corresponding to the two-body bound state (4) is reported for comparison (long dash-dotted lines).

Here, the fully self-consistent $\mathcal{G}$'s are considered, while in the original reference [11] non-interacting $\mathcal{G}_0$ corresponding to the non-self-consistent approximation were utilized.

It was also shown in reference [11] that $g_{\uparrow\downarrow}(\boldsymbol{\rho})$ given by the expression (25) recovers the short-range behavior related to Tan's contact C [20–22]

$$g_{\uparrow\downarrow}(\boldsymbol{\rho}) \xrightarrow[(\rho\to 0)]{} \frac{C}{(4\pi)^2}\left(\frac{1}{\rho^2} - \frac{2}{\rho\, a_F} + \cdots\right), \tag{27}$$

such that $\lim_{\rho\to 0} \frac{(4\pi)^2}{C}\rho^2\, g_{\uparrow\downarrow}(\rho) = 1$ irrespective of coupling and temperature. We have reproduced here these analytic results within our fully self-consistent t-matrix approach, with the numerical values of C obtained in agreement with reference [7].

Examples of the spatial profiles of the pair correlation function $g_{\uparrow\downarrow}(\rho)$ are shown in figure 1, for several couplings and temperatures above T_c. Reported in each inset are also the respective values of the contact C [23], from which the numerical values of $g_{\uparrow\downarrow}(\rho)$ can be explicitly reconstructed. Note the oscillatory behavior of $g_{\uparrow\downarrow}(\rho)$, which is present on the BCS side at low temperatures but quickly fades away either by moving toward the BEC side or by increasing temperature. Due to this oscillatory behavior, $g_{\uparrow\downarrow}(\rho)$ may acquire negative values which correspond to a weaker correlation with respect to the uncorrelated value $n_\uparrow n_\downarrow = (n/2)^2$ [11]. This behavior, however, will not affect our argument below, whereby the oscillations about zero (whenever present) will be averaged out.

It can be verified from the expression (25) that, in the BEC limit at sufficiently low temperatures, $g_{\uparrow\downarrow}(\rho)$ reduces to the product of the density $n_\sigma = n/2$ of a single fermionic species times the *square* of the wave function (4) corresponding to the fermionic two-body problem. It can be also verified that, within mean field in the superfluid phase, the square of the pair wave function obtained from the two-particle reduced density matrix [26] corresponds to $g_{\uparrow\downarrow}(\rho)$ [11, 27]. This suggests that the function $\phi(\mathbf{p})$, to be utilized in the form factors (18), can be quite generally extracted from the pair correlation function $g_{\uparrow\downarrow}(\rho)$. To this end, we adopt the following strategy.

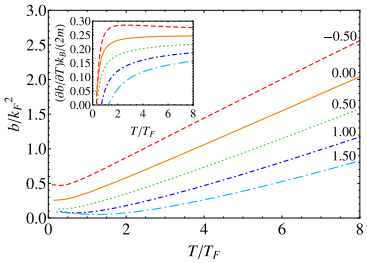

Figure 2. Temperature dependence of the parameter b of the expressions (29)–(31) for several values (reported above each line) of the coupling $(k_F a_F)^{-1}$ across the BCS–BEC crossover. The inset shows the derivative of b with respect to T for the same couplings of the main panel to better evidence the high-temperature behavior.

We begin by fitting the spatial profiles of the function $\frac{(4\pi)^2}{C}\rho^2 g_{\uparrow\downarrow}(\rho)$ of figure 1 with the expression

$$\rho^2\phi(\rho)^2 = \exp(-2\rho/a_F)\,\exp(-2b\rho^2), \tag{28}$$

where b is a parameter that depends on coupling and temperature (note that the function (28), too, has unit value at $\rho = 0$). We then take the square root of the expression (28) to extract $\phi(\rho)$, and multiply the result by a suitable normalization factor $\mathcal{N}$, thus writing:

$$\phi(\rho) = \mathcal{N}(a_F, b)\,\frac{e^{-\rho/a_F}}{\rho}\,\exp(-b\rho^2) \tag{29}$$

with

$$\mathcal{N}(a_F, b) = \frac{1}{\pi^{3/4}}\left(\frac{b}{2}\right)^{1/4}\frac{\exp\left[-\frac{1}{4ba_F^2}\right]}{\sqrt{\mathrm{erfc}\left[\frac{1}{\sqrt{2b}a_F}\right]}} \tag{30}$$

where $\mathrm{erfc}(z)$ is the complementary error function of (complex) argument z [28]. Note that the two-body wave function (4) is recovered for $b \to 0$. Finally, we take the Fourier transform of the expression (29) and obtain the desired result:

$$\phi(\mathbf{p}) = \frac{2\pi^{3/2}\mathcal{N}(a_F, b)}{\sqrt{b}\,p}\;\mathrm{Im}\left\{\exp\left[\frac{(a_F^{-1} - ip)^2}{4b}\right]\mathrm{erfc}\left(\frac{a_F^{-1} - ip}{2\sqrt{b}}\right)\right\} \tag{31}$$

where $p = |\mathbf{p}|$. This expression recovers equation (5) in the limit $b \to 0$.

Figure 2 shows the behavior of the parameter b obtained in this way, over a wide range of coupling and temperature relevant to the experiment of reference [4]. In particular, for sufficiently high temperature and irrespective of coupling, b is expected to become proportional to λ_T^{-2} where $\lambda_T = \sqrt{\frac{2\pi}{mk_BT}}$ is the thermal wavelength. To evidence this linear behavior of b vs T at high temperature, the inset of figure 2 plots the derivative of b with respect to T for the same temperature range and couplings of the main panel. In all cases, we have found that, at high temperature, this derivative is well reproduced by the expression $\frac{k_B}{2}\frac{\partial b}{\partial T} = 0.25 - 0.175(k_F a_F)^{-1}\sqrt{T_F/T}$.

The fitting function $\phi(\rho)$ given by equation (29) focuses on the short-range part of the pair-correlation function $g_{\uparrow\downarrow}(\rho)$ given by equation (24), which is dominated by the intra-pair correlations of relevance here. It thus disregards a possible long-range part of $g_{\uparrow\downarrow}(\rho)$ which may include correlations between spin-↑ and spin-↓ fermions belonging to different pairs (although this long-range part does not occur within the t-matrix approach adopted here).

3.2. Pair fraction

We are now in a position to calculate the pair density n_p given by

$$n_p = -\int\frac{d\mathbf{q}}{(2\pi)^3}\frac{1}{\beta}\sum_\nu e^{i\Omega_\nu\eta}\,\mathcal{G}_B(\mathbf{q}, \Omega_\nu) \tag{32}$$

together with the fermionic density n_σ given by equation (23), for a homogeneous system as a function of coupling and temperature.

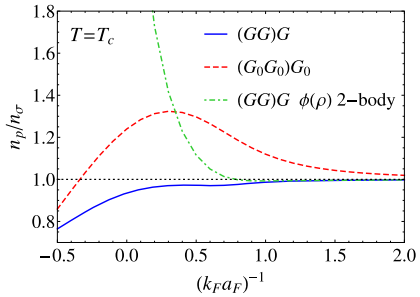

Figure 3. Pair fraction n_p/n_σ at T_c vs $(k_Fa_F)^{-1}$, obtained by the fully self-consistent (full line) and non-self-consistent (dashed line) t-matrix approaches. In both cases, $\phi(\mathbf{p})$ in the form factors (18) is obtained from the expression (31) within the respective approximations for the pair correlation function. Also shown is the result obtained by the fully self-consistent calculation, with $\phi(\mathbf{p})$ approximated instead by the two-body form (5) (dashed-dotted line).

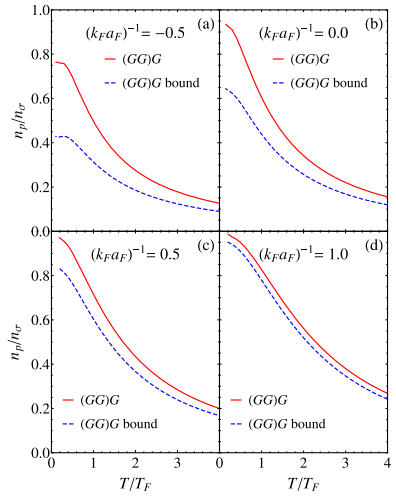

Figure 4. Pair fraction n_p/n_σ vs T/T_F for four couplings, obtained by the fully self-consistent t-matrix approach including (full lines) or neglecting (dashed lines) the 'unbound' term in equation (17). In the latter case, only the 'bound' term is retained in equation (17), as specified in the panels.

To begin with, figure 3 compares the pair fraction n_p/n_σ at T_c over a wide range of the coupling $(k_Fa_F)^{-1}$, as obtained by the fully self-consistent and non-self-consistent t-matrix approaches. As for other thermodynamic quantities [7], also in this case the fully self-consistent approach proves superior to the non-self-consistent one, to the extent that the ratio n_p/n_σ should never exceed unity. Accordingly, from now on results obtained by the fully self-consistent approach will only be presented. In addition, the use of the two-body form (5) for $\phi(\mathbf{p})$ in the form factors (18) is seen to lead to unstable results upon entering the unitary regime with $(k_Fa_F)^{-1} \lesssim +1$. Abandoning the two-body form (5) in favor of the expression (31) associated with the pair correlation function is thus expected to yield a definite improvement over the theoretical analysis made in reference [4] when accounting for the experimental values of the pair fraction for the trapped system (cf section 4.2 below).

In figure 4 the pair fraction n_p/n_σ is shown over a wide range of temperature and a selected number of couplings across unitarity. In particular, this figure compares the results obtained by including (full lines) or neglecting (dashed lines) the 'unbound' term represented by the term $-\mathcal{F}_2$ on the right-hand side of equation (17). One sees that inclusion of this unbound term over and above the bound term (represented by the second term on the right-hand side of equation (17)) leads to substantial differences, especially in the unitary regime at low temperature. The unbound term was not included in the diagrammatic approach to

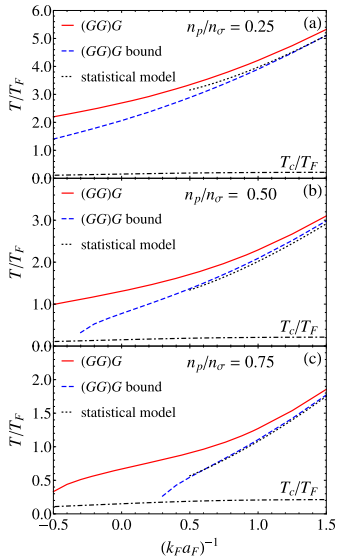

Figure 5. Contour plots of the pair fraction n_p/n_σ in the temperature–coupling phase diagram of the homogeneous system, obtained by the fully self-consistent t-matrix approach by including (full lines) or neglecting (dashed lines) the 'unbound' term in equation (17). Also shown are the results of the statistical model obtained from equation (33) (dotted lines). In each panel, the coupling dependence of the critical temperature T_c (in units of T_F) is reported (dashed-dotted line), which sets the boundary of the normal phase for the homogeneous system. Note that a different vertical scale is used in each of the three panels.

the pair fraction presented in reference [4]. It will be shown in section 4.2 that the agreement with experimental data will be definitively improved by its inclusion.

In preparation for this comparison, figure 5 shows three contour plots where a given value of the pair fraction n_p/n_σ is seen to evolve in the T-vs-$(k_F a_F)^{-1}$ phase diagram. Similarly to what was done in figure 4, for each of the three values of n_p/n_σ here reported the numerical results have been obtained by including (full lines) or neglecting (dashed lines) the unbound term in equation (17). In all cases, the difference between these two sets of results turns out to be substantial as soon as entering the unitary regime with $(k_F a_F)^{-1} \lesssim +1$. This implies that, in this regime of most physical interest, the fermionic character of the constituent particles reveals itself.

To confirm this point of view, figure 5 also shows for comparison the contour plots of n_p/n_σ corresponding to the statistical model (dotted lines), as obtained from the law of mass action

$$\frac{n_f^2}{n_p} = \frac{1}{8}\left(\frac{mk_BT}{\pi}\right)^{3/2} e^{-\varepsilon_0/k_BT} \tag{33}$$

where $\varepsilon_0 = (ma_F^2)^{-1}$ is the two-body binding energy, which results from the integrals in equation (B11) of appendix B by neglecting ± 1 in the denominators therein. It turns out that the results of the statistical model coincides with those of the quantum many-body approach that includes only the bound term, but only at most up to $(k_F a_F)^{-1} \approx 0.6$ after which the molecular regime with the two-body wave function (4) loses its meaning.

From figure 5 one also notes that the pairing fraction is still appreciable on the BCS side of unitarity, especially with the inclusion of the unbound term. This is because the pairing fraction, as obtained in terms of the expression (17), is meant to count correlated fermionic pairs that are present throughout the BCS–BEC crossover, and not only the bosonic dimers that exist in isolation only in the BEC limit at low temperature. The above larger than expected value of the pairing fraction could appear surprising, since other physical quantities, like the single-particle density of states or the single-particle spectral function [7, 29, 30], present less marked effects of pairing correlations on the BCS side of unitarity above T_c. To support our results, it may be remarked that also the pair correlation function of figure 1 shows a similar persistence of pairing like the pairing fraction in the same temperature and coupling region. It may thus be concluded that the pairing fraction, which is defined in terms of a *two-particle* Green's function, is more sensitive to pair correlations than *single-particle* quantities.

4. Results for a trapped gas and comparison with experimental data

The results obtained in section 3 for $n_{\rm p}$ given by equation (32) and for n_σ given by equation (23) refer to a homogeneous system. In order to compare with the experimental data of reference [4], these theoretical results need to be averaged over the trap that contains the Fermi gas.

4.1. Trap average

When considering a Fermi gas trapped in an anisotropic harmonic potential of the type

$$V(\mathbf{r}) = \frac{1}{2} m \left(\omega_x^2 x^2 + \omega_y^2 y^2 + \omega_z^2 z^2\right), \tag{34}$$

one can adopt a *local-density approximation* and obtain the total number $N_{\rm p}$ of pairs and the total number N_σ of fermions in the trap in the following way. One first replaces the fermionic chemical potential μ entering the single-particle Green's function $\mathcal{G}(\mathbf{p}, \omega_n)$ of equation (21) by $\mu \to \mu - V(\mathbf{r})$, thereby obtaining the *local* function $\mathcal{G}(\mathbf{p}, \omega_n; \mathbf{r})$. One then replaces $\mathcal{G}(\mathbf{p}, \omega_n) \to \mathcal{G}(\mathbf{p}, \omega_n; \mathbf{r})$ everywhere this function occurs, namely, in the expressions (17)–(20) for pairs and the expressions (21)–(23) for fermions. Finally, one integrates the expressions of the local densities $n_{\rm p}(\mathbf{r})$ and $n_\sigma(\mathbf{r})$ obtained in this way over the spatial variable $\mathbf{r}$, to get the total number of pairs $N_{\rm p}$ and the total number of fermions N_σ with spin σ. The value of the fermionic chemical potential μ *for the trap* is eventually determined for given coupling and temperature by solving for μ as a function of N_σ. In practice, in the experiment of reference [4] typical values of $\omega_x = \omega_y$ range from $2\pi \times 300$ Hz to $2\pi \times 1.6$ kHz, while $\omega_z = \lambda \omega_x = 2\pi \times 21$ Hz (with $\lambda < 1$).

In the theoretical expressions, it is convenient to map at the outset the anisotropic potential (34) into a spherical one by rescaling the variables from (x, y, z) to $(x' = \lambda^{-1/3} x, y' = \lambda^{-1/3} y, z' = \lambda^{2/3} z)$, such that the trapping potential becomes

$$V(x', y', z') = \frac{1}{2} m \omega_0^2 r'^2 \tag{35}$$

where $r' = \sqrt{x'^2 + y'^2 + z'^2}$ and $\omega_0 = (\omega_x \omega_y \omega_z)^{1/3} = \lambda^{1/3} \omega_x$ is the average trap frequency. Accordingly, the original spatial distribution $n(x, y, z)$ of the fermionic density with an ellipsoidal shape is mapped onto a spherical distribution $n'(x', y', z') = n'(r')$ through the rescaling $n(x, y, z) = n'(\lambda^{-1/3} x, \lambda^{-1/3} y, \lambda^{2/3} z)$ (with both spin components included).

Profiles of the total fermion isotropic density $n'(r') = n'_\uparrow(r') + n'_\downarrow(r')$ obtained from equation (23) in this way are shown in figure 6, for several couplings across unitarity and temperatures in the normal phase. The coupling parameter $(k_{\rm F}^t a_{\rm F})^{-1}$ associated with the trap is expressed in terms of $k_{\rm F}^t = \sqrt{2\, m E_{\rm F}^t}$, where $E_{\rm F}^t = \omega_0 (3N)^{1/3}$ is the Fermi energy in the *trap* and $N = N_\uparrow + N_\downarrow$ is the total number of fermions. (In the experiment of reference [4], typical values of N range from 3×10^4 to 3×10^5).

The values of the critical temperature $T_{\rm c}$ for the trap case, reported in figure 6 only for three specific couplings, can be obtained throughout the whole BCS–BEC crossover. This information is important also to verify whether the experimental values of the pair fraction in the trap of reference [4] were measured in the normal phase. To calculate $T_{\rm c}$ for the trap, we adopt again a local-density approximation and define a local Fermi temperature $T_{\rm F}(\mathbf{r})$ such that $k_{\rm B} T_{\rm F}(\mathbf{r}) = \left[3\pi^2 n(\mathbf{r})\right]^{2/3}/(2\, m)$. This implies that the local Fermi temperature, like the density $n(\mathbf{r})$, has its maximum value at $\mathbf{r} = 0$, to which there corresponds a minimum value of $T/T_{\rm F}(\mathbf{r})$ for given temperature T. Accordingly, the central portion of the cloud density is where superfluidity is first established upon lowering the temperature from the normal phase.

To obtain $T_{\rm c}$ for the trapped system, we then apply the Thouless criterion

$$\Gamma(\mathbf{q} = 0, \Omega_\nu = 0; \mu(\mathbf{r} = 0), T_{\rm c})^{-1} = 0 \tag{36}$$

in terms of the particle–particle propagator (19) in the normal phase, where now $\mu(\mathbf{r} = 0) = \mu - V(\mathbf{r} = 0) = \mu$ is the fermionic chemical potential for the trap calculated at the critical temperature $T_{\rm c}$. Details on how the variables $(T_{\rm c}, \mu_{\rm c})$ have been determined by solving the Thouless criterion in conjunction with the density equation are given in appendix B of reference [7].

Figure 7 shows the results of our calculation for $T_{\rm c}$ in the trap across the BCS–BEC crossover. The results of the fully self-consistent t-matrix approach (full line) are also compared with those of its non-self-consistent counterpart (dashed line). While the two calculations essentially coincide with each other in the BCS regime $(k_{\rm F}^t a_{\rm F})^{-1} \lesssim -1$, they differ considerably on the BEC side of unitarity. We attribute this difference to the occurrence of a residual interaction between composite bosons in the BEC regime $(k_{\rm F}^t a_{\rm F})^{-1} \gtrsim +1$, which is present within the fully self-consistent but absent within the non-self-consistent calculation [7].

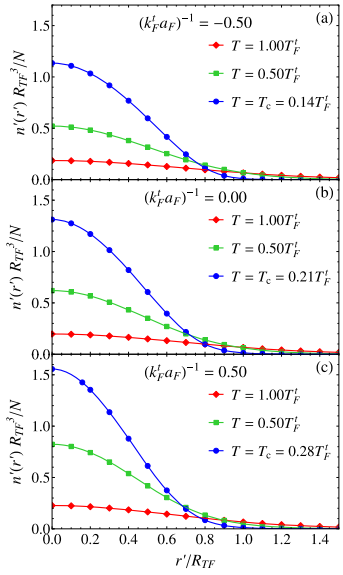

Figure 6. Total fermion isotropic radial density $n'(r')$ vs r' for couplings: (a) $(k_F^t a_F)^{-1} = -0.5$; (b) $(k_F^t a_F)^{-1} = 0.0$; (c) $(k_F^t a_F)^{-1} = +0.5$. In each panel, the results for $T = T_c$ (dots), $T = 0.5T_F^t$ (squares), $T = T_F^t$ (diamonds) are shown. Lengths are in units of the Thomas–Fermi radius R_{TF} given by $\frac{1}{2}m\omega_0^2 R_{TF}^2 = E_F^t$ where $E_F^t = \omega_0(3N)^{1/3}$ is the trap Fermi energy, such that $8N/(\pi^2 R_{TF}^3)$ is the value of $n(r = 0)$ for the non-interacting gas at $T = 0$ within a local-density approximation.

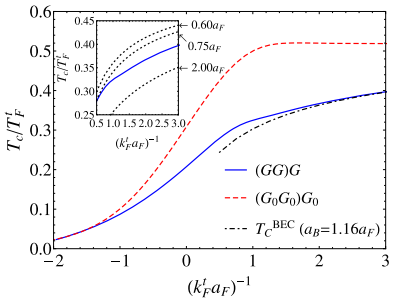

Figure 7. Critical temperature T_c (in units of the Fermi temperature $T_F^t = E_F^t/k_B$) vs $(k_F^t a_F)^{-1}$ for the trapped system. Results are shown for the fully self-consistent (full line) and for the non-self-consistent (dashed line) t-matrix approaches. In the BEC regime, the results of a model calculation for trapped bosons with a mean-field-type interaction (cf appendix C) are also shown with the value $a_B = 1.16a_F$ for the bosonic scattering length (dashed-dotted line). The inset shows the results of additional bosonic calculations with different values of a_B (see text).

To make a check on the results of our numerical calculation, also shown in figure 7 are the results for T_c (dashed-dotted line) obtained for a low-density trapped Bose gas with a residual interaction specified by the scattering length a_B (cf appendix C), where for internal consistency the approximate value $a_B = 1.16a_F$ that results from the fully self-consistent t-matrix approach [7] was considered. In this way, we can confirm quantitatively the effects of a_B on T_c for the trapped system in the BEC regime, which are contained in the fully self-consistent t-matrix approach. For comparison, the inset reports additional bosonic calculations for: (i) $a_B = 2.0a_F$ which corresponds to the residual bosonic interaction being treated at the level of the fermionic exchange diagrams [31]; (ii) $a_B = 0.75a_F$ when the T-matrix for the dimer–dimer scattering built on these exchange diagrams is further considered [31]; (iii) the exact value $a_B = 0.6a_F$ obtained either by a numerical solution of the four-body Schrödinger equation [32] or by a full diagrammatic treatment in the zero-density limit [33].

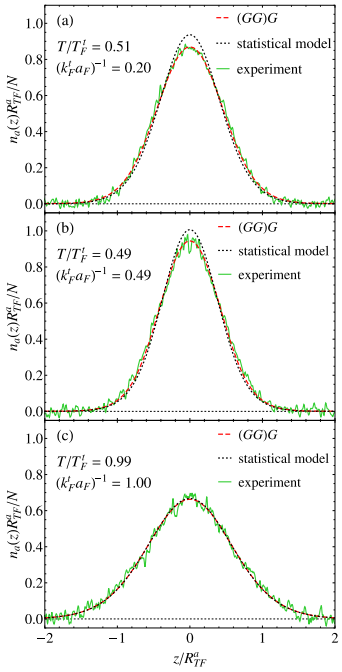

Figure 8. Comparison between the axial densities along the main axis of the trap, as observed experimentally (full lines) and calculated with the self-consistent *t*-matrix approach (dashed lines) and the statistical atom–molecule model (dotted lines), when (a) $T/T_F^t = 0.51(4)$ and $(k_F^t a_F)^{-1} = 0.20(3)$, (b) $T/T_F^t = 0.49(4)$ and $(k_F^t a_F)^{-1} = 0.49(3)$, and (c) $T/T_F^t = 0.99(6)$ and $(k_F^t a_F)^{-1} = 1.00(5)$. The ratio λ between the axial and radial trap frequencies equals 0.0435(8) in (a), 0.0424(7) in (b), and 0.0272(4) in (c). The axial Thomas–Fermi radius $R_{TF}^a = \lambda^{-2/3} R_{TF}$ is used for normalization.

Finally, it should be mentioned that the value $T_c/T_F^t = 0.2074$, which we have obtained at unitarity by the fully self-consistent calculation, coincides with that obtained in reference [9] by the same approach. However, our calculation for T_c is extended to the whole BCS–BEC crossover while that of reference [9] was limited to unitarity only.

4.2. Comparison between theory and experiment

A first quantity to be compared with the experimental data of reference [4] is the *axial* density $n_a(z)$ where z runs along the main axis of the trap, which is obtained by integrating the total fermion density $n(x, y, z)$ over the radial directions x and y. Specifically, the experimental profiles $n_a(z)$ can be compared with their theoretical counterparts $n'_a(z')$, obtained by integrating over x' and y' the isotropic profiles $n'(r') = n'(x', y', z')$ (like those shown in figure 6) and then performing the rescaling

$$n_a(z) \;=\; \lambda^{2/3}\, n'_a(\lambda^{2/3} z). \tag{37}$$

Figure 8 shows this comparison for three sets of values of temperature, coupling, and anisotropy λ. In all cases, excellent agreement results between the experiment and the quantum many-body approach with no adjustable parameter. The figure shows also the comparison with the fermion axial density profiles calculated within the statistical atom–molecule model [34], for which notable deviations from the experiment occur, as expected, for low temperature and close to unitarity.

Note that the comparison shown in figure 8, between the experimental and theoretical fermion axial density profiles, does not provide a test on the validity of the pairing fraction theory described in section 2.2. It is only meant to be an independent check on the fully self-consistent *t*-matrix approach for a thermodynamic property which is an essential ingredient of the trap averaging procedure.

Finally, figure 9 presents the comparison of the pairing fraction N_p/N_σ obtained by our *ab initio* quantum many-body calculation with the experimental data of reference [4] over the temperature–coupling phase diagram (where k_F^t and T_F^t now refer to the trapped system). The comparison is made for three

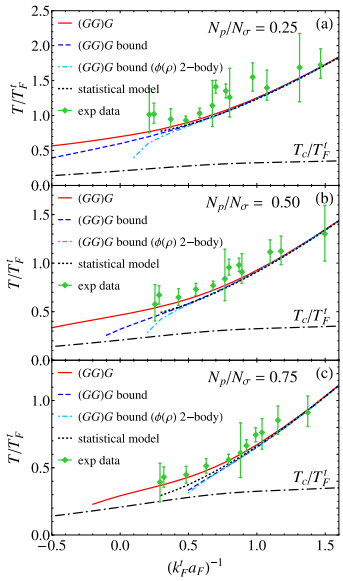

Figure 9. Contour plots of the pair fraction N_p/N_σ in the temperature–coupling phase diagram of the trapped system, obtained by the fully self-consistent t-matrix approach by including in equation (17) (i) both bound and unbound terms (full lines), (ii) only the bound term (dashed lines), and (iii) only the bound term with the two-body form (4) of $\phi(\rho)$ (dashed-dotted lines). The theoretical curves are compared with the experimental data of reference [4] (diamonds with vertical error bars). For $(k_F^t a_F)^{-1} \gtrsim 0.3$ the results of the statistical model obtained from equation (B15) of appendix B are also shown (dotted lines). In each panel, the coupling dependence of the critical temperature T_c (in units of T_F^t) is reported (long dashed-dotted line), which sets the boundary of the normal phase for the trapped system.

characteristic values of N_p/N_σ. In all cases, good agreement is obtained between theory and experiment (we emphasize that the theoretical results have been obtained with no adjustable parameter).

In particular, this comparison shows that *both* the inclusion of the unbound term and the improvement in the description of $\phi(\rho)$ in terms of the pair correlation function (with respect to the preliminary description in terms of the two-body bound state of reference [4]) significantly improve the agreement of our calculations with the experimental data. And this is despite the presence of the trap, which acts to suppress the contribution of the unbound term (as evident by comparing figures 5 and 9). This suggests that the experimental data probe indeed the pairing *correlations* between spin-up and spin-down fermions as defined by our formalism.

From this comparison one can argue that the crossover, between the pseudo-gap regime (where the fermionic character of the constituent particles matters) and the molecular regime (where only the presence of bosonic pairs is relevant), sets in about where the theoretical results for N_p/N_σ, obtained with and without the unbound term, start departing from each other. This argument cannot be made in terms of the statistical atom–molecule model [4], that misses the contribution of the unbound term.

Finally, we have performed a χ^2 test to better quantify the agreement between the experimental data and the theoretical many-body predictions of figure 9. To this end, we have adopted the standard definition

$$\chi^2 = \frac{1}{n_{\rm exp}-1}\sum_{i=1}^{n_{\rm exp}} \frac{(y_i^{\rm th}-y_i^{\rm exp})^2}{(\sigma_i^{\rm exp})^2}, \tag{38}$$

where $y_i^{\rm th}$ is the theoretical prediction corresponding to each of the $n_{\rm exp}$ experimental points $y_i^{\rm exp}$ and $\sigma_i^{\rm exp}$ are the (symmetrized) errors. The results of the test for the three values of N_p/N_σ of figure 9 are reported in table 1. They clearly show that the full bound + unbound calculation better agrees with the experimental data than the bound and bound (ϕ two-body) calculations, since it minimizes the χ^2 test function of equation (38) in each case. (Consistently with figure 9, for $N_p/N_\sigma = 0.75$ the two experimental points closest to unitarity have not been taken into account in the χ^2 test when the unbound term is not included in the theoretical calculation).

Table 1. χ^2 test on the theoretical contour plots of figure 9 with given pairing fraction N_p/N_σ against the corresponding experimental data.

N_p/N_σ	Bound + unbound	Bound	Bound (ϕ two-body)
0.25	2.92	3.75	4.26
0.50	1.33	2.37	2.85
0.75	0.54	1.57	1.74

5. Concluding remarks

In this paper, we have provided a detailed account of a theoretical approach to interpret the experimental data reported in reference [4] in a quantitative way. By this approach, from the data reference [4] we have been able to unravel how the occurrence of pairing correlations between spin-up and spin-down fermions at equilibrium develops, as a function of temperature in the normal phase and of coupling on the BEC side of unitarity. What we claim to have learned from this is how the pseudo-gap regime (where fermions matter) and the molecular regime (where only composite bosons matter) separate from each other. This should be considered rather remarkable, since this result was extracted from experiment [4] where an equilibrium quantity was measured (i.e. the number of fermion pairs) and not a dynamical quantity (the excitation gap).

From the theoretical side, to account for the experimental data we have taken advantage of several favorable circumstances. On the one hand, since the number of fermion pairs in a Fermi gas undergoing the BCS–BEC crossover is an equilibrium quantity, it can be accounted for quite well in terms of the fully self-consistent t-matrix approach [7]. On the other hand, this physical quantity that was measured experimentally by its own nature does not require one to endow the theory with a series of complicated Aslamazov–Larkin and Maki–Thompson diagrams, which should otherwise be included to fulfill conservation criteria when addressing dynamical response functions [16], to the extent that the single-particle self-energy is treated within the fully self-consistent t-matrix approach. In addition, our emphasis here on fermionic correlations has drawn on our previous experience on the pair-correlation function in the normal phase, which was addressed in detail in reference [11] within the non-self-consistent t-matrix approach and here extended to the fully self-consistent one.

Along these lines, future perspectives, that could reinforce our argument about the evidence for the separation between the (fermionic) pseudo-gap and the (bosonic) molecular regimes, may hinge on the possibility of extending the measurements of the ratio N_p/N_σ toward unitarity at temperatures close enough to T_c.

In addition, to highlight experimentally the relevance of the correlations induced indirectly by the environment between spin-↑ and spin-↓ fermions, which are embodied in the 'unbound' term in the expression (17), it could be worth to consider repeating the experiment of reference [4] by replacing the harmonic trap with a box trap along the lines of reference [35]. In this way, one should be able to amplify the difference between the values of the pair fraction obtained with and without the inclusion of the unbound term, as one may anticipate by comparing the results of figure 5 for the homogeneous case with those of figure 9 for the trapped case.

It is, finally, interesting to draw a physical connection between our finding about the indirect correlations established between spin-↑ and spin-↓ fermions through their environment and the recent results of reference [36] about the way the quark-gluon structure of a nucleon bound in an atomic nucleus is modified by the surrounding nucleons. In both cases, it is the environment that plays an important role in modifying the properties of what would be a bound system in isolation.

Acknowledgments

MP, PP, and GCS acknowledge financial support from the Italian MIUR under Projects PRIN2015 (2015C5SEJJ001) and PRIN2017 (CEnTraL 20172H2SC4). MJ and JHD acknowledge financial support from DFG (LI988/6-1), and thank W Limmer, T Paintner and D Hoffmann for discussions.

Appendix A. About the use of conserving approximations for the pair fraction

In section 2.2 we have argued that *only* the form (14) of the effective two-particle interaction Ξ is of relevance for the calculation of the bosonic propagator $\mathcal{G}_B(\mathbf{q}, \Omega_\nu)$ of equation (16) (and thus of the quantity

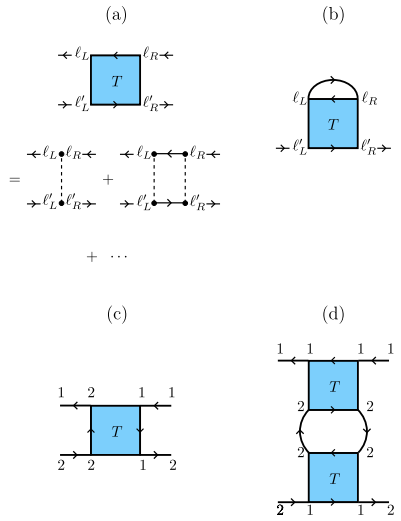

Figure A1. (a) Ladder diagrams for the T-matrix in the superfluid phase, where dots delimiting potential (dashed) lines represent τ^3 Pauli matrices. (b) Corresponding diagram for the t-matrix fermionic self-energy. Examples of (c) MT and (d) AL diagrammatic contributions to the pair propagator $\mathcal{G}_{\rm B}$, which are bound to vanish when carried over to the normal phase owing to the presence of two anomalous fermionic single-particle Green's functions which connect $1 \leftrightarrow 2$. For simplicity, only Nambu spin indices have been explicitly indicated in all diagrams.

$N_{\rm p}$ of experimental interest). We have also anticipated that the reason for this is to be found in the specific sequence of Nambu indices appearing in the expression (15) from which equation (16) is derived. Here, we show specifically how the diagrammatic contributions to Ξ, that would derive from the t-matrix approach for the fermionic self-energy Σ, cannot modify this result. Under different circumstances, like for the calculation of the density and spin response functions, on the other hand, the diagrams for Ξ corresponding to the Aslamazov–Larkin (AL) and Maki–Thomson (MT) contributions would instead result from the t-matrix approach for Σ (see, e.g., figure 3 of reference [37]). In our case, the importance of introducing the t-matrix approach for Σ arises from the need of obtaining an accurate description of the thermodynamic properties of the Fermi gas in the normal phase [7].

Probably the simplest way to convince oneself that the AL-type and MT-type contributions to Ξ, which would result from the t-matrix self-energy taken below $T_{\rm c}$, do not contribute to the expression (15) of the pair propagator $\mathcal{G}_{\rm B}$ once carried over to the normal phase above $T_{\rm c}$, is to draw these contributions in a diagrammatic way. This is done in figure A1. Here, the series of ladder diagrams that approximate the many-particle T-matrix in the broken-symmetry phase is reported in panel (a), while the corresponding t-matrix self-energy is shown in panel (b). For simplicity, in these diagrams only the Nambu indices have been explicitly indicated, while the space and imaginary time variables are not reported since they are not essential to the following argument. The crucial point is that for the T-matrix of panel (b) only combinations with Nambu indices $\ell_{\rm L} \neq \ell'_{\rm L}$ and $\ell_{\rm R} \neq \ell'_{\rm R}$ occur, owing to the inter-particle interaction of the contact form that we have adopted (cf also reference [10]). In addition, only combinations with $\ell_{\rm L} = \ell_{\rm R}$ and $\ell'_{\rm L} = \ell'_{\rm R}$ will survive when these diagrams are extrapolated to the normal phase. As a consequence, a typical example of MT contribution is shown in figure A1(c), while a typical example of AL contribution is shown in figure A1(d). In all cases, it turns out that at least two single-particle Green's functions with off-diagonal Nambu indices would be required to match these contributions to Ξ with the Nambu indices appearing in the expression (15). Since the off-diagonal (anomalous) single-particle Green's functions vanish in the normal phase above $T_{\rm c}$, the MT- and AL-type contributions to Ξ vanish, too, and do not affect the expression (15) which is relevant for the calculation of $N_{\rm p}$ above $T_{\rm c}$. This proves our statement.

Appendix B. Comparison between the quantum many-body approach and the statistical atom–molecule model for the pair fraction

It is interesting to determine under what physical circumstances the expressions for the total number of bosons $N_{\rm p}$ and for the total number of spin-σ fermions N_σ of our fully quantum

many-body approach reduce to those of a statistical model of a fermion–boson mixture at equilibrium [5, 6].

To this end, we consider a homogeneous system, for which $N_\mathrm{p} = \mathcal{V}\, n_\mathrm{p}$ and $N_\sigma = \mathcal{V}\, n_\sigma$ are expressed in terms of the respective densities. By our quantum many-body approach, n_p is given by equation (32) with $\mathcal{G}_\mathrm{B}$ given by the expression (17), while n_σ is given by the expression (23). To recover the physics of a fermion–boson (or atom–molecule) mixture, one requires the fermionic coupling to be sufficiently strong in the BEC regime and the temperature sufficiently low, for the internal structure of the composite bosons (dimers) to become irrelevant.

In this limit, the fermionic chemical potential μ becomes the largest energy scale of the problem and is written in the form $\mu_\mathrm{B} = 2\mu + \varepsilon_0$, where $\varepsilon_0 = (m a_\mathrm{F}^2)^{-1}$ is the dimer binding energy and μ_B the dimer chemical potential [12]. The expression (26) then reduces to

$$\tilde{\Pi}(\mathbf{p}; \mathbf{q}, \Omega_\nu) \simeq \frac{1}{2\xi(\mathbf{p})}, \tag{B1}$$

which, together with the expression (5) for $\phi(\mathbf{p})$ appropriate to this limit, yields the following approximate form for the form factors (18) [10]:

$$\mathcal{F}_1(\mathbf{q}, \Omega_\nu) \simeq \sqrt{\frac{m^2 a_\mathrm{F}}{8\pi}} \quad , \quad \mathcal{F}_2(\mathbf{q}, \Omega_\nu) \simeq \frac{m a_\mathrm{F}^2}{4}. \tag{B2}$$

This implies that, in the BEC limit where $a_\mathrm{F} \to 0^+$, the 'unbound' term $\mathcal{F}_2$ vanishes faster than $\mathcal{F}_1$ and can thus be neglected in the expression (17). In addition, in the same limit the particle–particle propagator $\Gamma(\mathbf{q}, \Omega_\nu)$ of the 'bound' term in the expression (17) acquires the polar form [12]:

$$\Gamma(\mathbf{q}, \Omega_\nu) \simeq -\frac{8\pi}{m^2 a_\mathrm{F}} \frac{1}{\mathrm{i}\Omega_\nu - \frac{\mathbf{q}^2}{4\,m} + \mu_\mathrm{B}}. \tag{B3}$$

Combining these results together, one gets eventually for the bosonic density:

$$\begin{aligned} n_\mathrm{p} &\simeq -\int \frac{\mathrm{d}\mathbf{q}}{(2\pi)^3} \frac{1}{\beta} \sum_\nu \frac{\mathrm{e}^{\mathrm{i}\Omega_\nu \eta}}{\mathrm{i}\Omega_\nu - \frac{\mathbf{q}^2}{4\,m} + \mu_\mathrm{B}} \\ &= \int \frac{\mathrm{d}\mathbf{q}}{(2\pi)^3} \frac{1}{\mathrm{e}^{\beta \xi_\mathrm{B}(\mathbf{q})} - 1} \end{aligned} \tag{B4}$$

in terms of the Bose–Einstein distribution of argument $\xi_\mathrm{B}(\mathbf{q}) = \frac{\mathbf{q}^2}{4\,m} - \mu_\mathrm{B}$.

To determine n_σ in the BEC limit at sufficiently low temperature, we consider the expression (23) where we expand the single-particle Green's function (21) in series of the self-energy Σ

$$\mathcal{G}(\mathbf{p}, \omega_n) \simeq \mathcal{G}_0(\mathbf{p}, \omega_n) + \mathcal{G}_0(\mathbf{p}, \omega_n)\, \Sigma(\mathbf{p}, \omega_n)\, \mathcal{G}_0(\mathbf{p}, \omega_n) \; + \cdots \tag{B5}$$

where $\mathcal{G}_0(\mathbf{p}, \omega_n) = [\mathrm{i}\omega_n - \xi(\mathbf{p})]^{-1}$ is the non-interacting single-particle Green's function, by again relying on the fact that the fermionic chemical potential μ entering $\xi(\mathbf{p}) = \mathbf{p}^2/(2m) - \mu$ is the largest energy scale in the problem. We thus obtain:

$$\begin{aligned} n_\sigma &\simeq \int \frac{\mathrm{d}\mathbf{p}}{(2\pi)^3} \frac{1}{\beta} \sum_n \mathrm{e}^{\mathrm{i}\omega_n \eta}\, \mathcal{G}_0(\mathbf{p}, \omega_n) \\ &\quad + \int \frac{\mathrm{d}\mathbf{p}}{(2\pi)^3} \frac{1}{\beta} \sum_n \mathcal{G}_0(\mathbf{p}, \omega_n)^2\, \Sigma(\mathbf{p}, \omega_n) \; + \cdots \\ &\equiv n_\sigma^{(0)} \; + \; n_\sigma^{(1)}. \end{aligned} \tag{B6}$$

Here,

$$\begin{aligned} n_\sigma^{(0)} &= \int \frac{\mathrm{d}\mathbf{p}}{(2\pi)^3} \frac{1}{\beta} \sum_n \mathrm{e}^{\mathrm{i}\omega_n \eta}\, \mathcal{G}_0(\mathbf{p}, \omega_n) \\ &= \int \frac{\mathrm{d}\mathbf{p}}{(2\pi)^3} \frac{1}{\mathrm{e}^{\beta \xi(\mathbf{p})} + 1} \end{aligned} \tag{B7}$$

coincides with the density n_f of unpaired fermions (atoms) with spin σ and expressed in terms of the Fermi–Dirac distribution of argument $\xi(\mathbf{p})$, and

$$n_\sigma^{(1)} = \int \frac{\mathrm{d}\mathbf{p}}{(2\pi)^3} \frac{1}{\beta} \sum_n \mathcal{G}_0(\mathbf{p}, \omega_n)^2 \, \Sigma(\mathbf{p}, \omega_n)$$
$$\simeq - \int \frac{\mathrm{d}\mathbf{p}}{(2\pi)^3} \frac{1}{\beta} \sum_n \mathcal{G}_0(\mathbf{p}, \omega_n)^2 \, \mathcal{G}_0(-\mathbf{p}, -\omega_n)$$
$$\times \int \frac{\mathrm{d}\mathbf{q}}{(2\pi)^3} \frac{1}{\beta} \sum_\nu \mathrm{e}^{\mathrm{i}\Omega_\nu \eta} \, \Gamma(\mathbf{q}, \Omega_\nu) \tag{B8}$$

owing to the approximate form for the self-energy (22) which is valid in this limit. With the polar approximation (B3) for $\Gamma(\mathbf{q}, \Omega_\nu)$ and the further approximate result (cf, e.g., section 3.1 of reference [12])

$$\int \frac{\mathrm{d}\mathbf{p}}{(2\pi)^3} \frac{1}{\beta} \sum_n \mathcal{G}_0(\mathbf{p}, \omega_n)^2 \, \mathcal{G}_0(-\mathbf{p}, -\omega_n) \simeq - \frac{m^2 \, a_\mathrm{F}}{8\pi}, \tag{B9}$$

the expression (B8) reduces to

$$n_\sigma^{(1)} = \int \frac{\mathrm{d}\mathbf{q}}{(2\pi)^3} \frac{1}{\mathrm{e}^{\beta \xi_\mathrm{B}(\mathbf{q})} - 1} \tag{B10}$$

which coincides with the density n_p of bosons (molecules) given by equation (B4). A combination of equations (B6), (B7), and (B10) yields eventually the result:

$$n_\sigma = n_\mathrm{f} + n_\mathrm{p} = \int \frac{\mathrm{d}\mathbf{p}}{(2\pi)^3} \frac{1}{\mathrm{e}^{\beta \xi(\mathbf{p})} + 1}$$
$$+ \int \frac{\mathrm{d}\mathbf{q}}{(2\pi)^3} \frac{1}{\mathrm{e}^{\beta \xi_\mathrm{B}(\mathbf{q})} - 1}. \tag{B11}$$

At this point, the fermionic chemical potential μ can be eliminated from equation (B11) by fixing the value of n_σ therein, with the bosonic chemical potential $\mu_\mathrm{B} = 2\mu + \varepsilon_0$ following in a consistent way.

There remains to find an explicit connection with the expressions of the fermion–boson (atom–molecule) model, which were obtained in references [5, 6] in the classical limit and used in reference [4] to account for the experimental data in the BEC regime of the phase diagram. To this end, we consider the classical limit of the expressions (B11) by neglecting ± 1 in the denominators, and perform the trap average by replacing $\mu \to \mu - V_\mathrm{f}(\mathbf{r})$ and $\mu_\mathrm{B} \to \mu_\mathrm{B} - V_\mathrm{p}(\mathbf{r})$ and integrating over the space variable $\mathbf{r}$, similarly to what was done in section 4.1. Here,

$$V_{\mathrm{f/p}}(\mathbf{r}) = \frac{1}{2} M_{\mathrm{f/p}} \left(\omega_x^2 x^2 + \omega_y^2 y^2 + \omega_z^2 z^2 \right) \tag{B12}$$

is the (anisotropic) harmonic oscillator potential commonly considered for ultra-cold gases, with $M_\mathrm{f} = m$ for fermions (atoms) and $M_\mathrm{p} = 2m$ for bosons (molecules). The results for the total number of unpaired fermions N_f (per spin component) and the total number of bosons N_p then become:

$$N_\mathrm{f} \simeq \int \mathrm{d}\mathbf{r} \int \frac{\mathrm{d}\mathbf{p}}{(2\pi)^3} \mathrm{e}^{-\beta \left[\frac{\mathbf{p}^2}{2m} + V_\mathrm{f}(\mathbf{r}) - \mu \right]} = \left(\frac{k_\mathrm{B} T}{\omega_0} \right)^3 \mathrm{e}^{\mu / k_\mathrm{B} T} \tag{B13}$$

and

$$N_\mathrm{p} \simeq \int \mathrm{d}\mathbf{r} \int \frac{\mathrm{d}\mathbf{q}}{(2\pi)^3} \mathrm{e}^{-\beta \left[\frac{\mathbf{q}^2}{4m} + V_\mathrm{p}(\mathbf{r}) - \mu_\mathrm{B} \right]} = \left(\frac{k_\mathrm{B} T}{\omega_0} \right)^3 \mathrm{e}^{\mu_\mathrm{B} / k_\mathrm{B} T} \tag{B14}$$

where $\omega_0 = (\omega_x \omega_y \omega_z)^{1/3}$ is the average trap frequency (cf, e.g., references [38, 39]). From these results it follows that

$$\frac{N_\mathrm{f}^2}{N_\mathrm{p}} = \left(\frac{k_\mathrm{B} T}{\omega_0} \right)^3 \mathrm{e}^{(2\mu - \mu_\mathrm{B}) / k_\mathrm{B} T} = \left(\frac{k_\mathrm{B} T}{\omega_0} \right)^3 \mathrm{e}^{-\varepsilon_0 / k_\mathrm{B} T}, \tag{B15}$$

from which, by replacing $\omega_0 = E_\mathrm{F}^t / (6N_\sigma)^{1/3}$ where E_F^t is the Fermi energy for the trap, one recovers the expression reported in appendix A of reference [4]. More generally, N_p and N_f for the trapped case could be obtained in closed form directly from equations (B4) and (B7), in terms of $\mathrm{Li}_3(\mathrm{e}^{\beta \mu_\mathrm{B}})$ for bosons and $\mathrm{Li}_3(-\mathrm{e}^{\beta \mu})$ for fermions (where $\mathrm{Li}_n(z)$ is the poly-logarithmic function of index n and argument z). The expression (B15) generalizes to a harmonically trapped system the *law of mass action* valid for a homogeneous system [40].

Finally, it is worth summarizing what is lost when passing from the fully quantum many-body approach to its simplified version obtained above. To get this simplified version, in equation (17) we have (i)

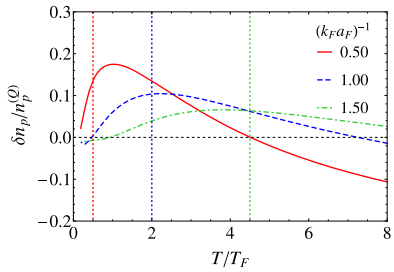

Figure B1. Temperature dependence of the relative difference $\delta n_p/n_p^{(Q)}$ with $\delta n_p = n_p^{(Q)} - n_p^{(C)}$ between the quantum many-body (Q) and classical statistical (C) calculations of the pair density n_p for the homogeneous system at various couplings. The vertical lines indicate the corresponding binding energies ε_0 (in units of E_F), for increasing coupling from left to right.

neglected the 'unbound' term $-\mathcal{F}_2(\mathbf{q}, \Omega_\nu)$, (ii) approximated $\phi(\mathbf{p})$ in the expression (18) for $\mathcal{F}_1(\mathbf{q}, \Omega_\nu)$ by the two-body form (5) and taken $\mu = -\varepsilon_0/2$ therein with $\varepsilon_0 \gg k_B T$, and (iii) approximated $\Gamma(\mathbf{q}, \Omega_\nu)$ by the polar form (B3); while in equation (23) we have performed the expansion (B5) with the typical approximations that apply to the BEC limit at low temperature when μ is the largest energy scale in the problem. None of these approximations, however, is valid either away from the BEC limit when approaching unitarity at any temperature, or in the BEC limit itself for sufficiently high temperature. In both these cases, the fermionic nature of the 'preformed pairs' manifests itself and only fermionic correlations remain physically relevant. On physical grounds, the results of the quantum many-body approach and of the statistical fermion–boson model differ from each other to the extent that the latter bears essentially on the chemical reaction (dimer $\leftrightarrow$ spin-$\uparrow$ + spin-$\downarrow$) for molecules that break up into atom pairs and vice versa, with no regard on the way the molecules are formed by the laws of quantum mechanics and on the effects that the surrounding environment might exert on them through inter-particle collisions.

In this context, it is interesting to explicitly verify to what extent the results of the quantum many-body approach (Q) and of the classical statistical model (C) differ from each other in the BEC limit of the homogeneous system at sufficiently high temperature. To this end, figure B1 shows the temperature dependence of the relative difference $\delta n_p/n_p^{(Q)}$ for the couplings $(k_F a_F)^{-1} = (0.5, 1.0, 1.5)$, where $\delta n_p = n_p^{(Q)} - n_p^{(C)}$. One sees that this relative difference can be substantial in all cases. In particular, for $k_B T \lesssim \varepsilon_0$ the relative difference increases with increasing temperature and decreases with increasing coupling, as expected. The following apparent reduction of the relative difference for $k_B T \gtrsim \varepsilon_0$ then turns into a substantial increase (in absolute value) when $k_B T \gg \varepsilon_0$. Again in favor of the results obtained by the quantum many-body (t-matrix) approach, one should recall that in the high-temperature limit this approach correctly recovers the controlled high-temperature (virial) expansion to second order [41]. Specifically, when this high-temperature expansion is made on the self-energy, keeping both the bound-state (pole) and scattering (continuum) contributions to the particle–particle propagator Γ of equation (19) turns out to be essential to correctly recover the virial expansion. Since the statistical model includes only the bound-state contribution, it unavoidably fails in the high-temperature limit.

Appendix C. Critical temperature of a low-density trapped Bose gas

In this appendix, we calculate the superfluid critical temperature of a low-density Bose gas in a trap, where the interaction is treated at the level of the two-body t-matrix specified by the scattering length a_B. Similarly to what we did in section 4.1 for the trapped Fermi gas, we adopt a local-density approximation whereby the bosonic chemical potential μ_B is replaced by a local chemical potential $\mu_B(\mathbf{r})$. We thus write for the bosonic density

$$n_B(\mathbf{r}) = \int \frac{d\mathbf{q}}{(2\pi)^3} \frac{1}{e^{\beta\left[\frac{q^2}{2m_B} - \mu_B(\mathbf{r})\right]} - 1} \tag{C1}$$

where $\mu_B(\mathbf{r}) = \mu_B - V_B(\mathbf{r}) - 2t_0 n_B(\mathbf{r})$. Here, $V_B(\mathbf{r})$ is the trapping potential of the form (34) with $m \to m_B$ (we also assume $\omega_x = \omega_y = \omega_z = \omega_0$ for simplicity), and $2t_0 n_B(\mathbf{r})$ is the leading approximation to the self-energy of a dilute Bose gas in the normal phase where $t_0 = 4\pi a_B/m_B$ [42]. Note that, owing to the presence of the local self-energy $2t_0 n_B(\mathbf{r})$, equation (C1) is a self-consistent condition for $n_B(\mathbf{r})$. Once $n_B(\mathbf{r})$

is known, the total number of bosons is obtained as follows:

$$N_{\rm B} = \int {\rm d}\mathbf{r}\, n_{\rm B}(\mathbf{r}). \tag{C2}$$

We are interested in determining the dependence on $N_{\rm B}$ of the critical temperature $T_{\rm c}$ for the transition to the superfluid phase. Similarly to what happens for a trapped Fermi gas (cf section 4.1), also for a trapped Bose gas the central portion of the cloud density is where superfluidity first manifests itself upon lowering the temperature from the normal phase. At $\mathbf{r} = 0$, the Hugenholtz–Pines condition [43] for $T_{\rm c}$ then yields

$$\mu_{\rm B} = 2\, t_0\, n_{\rm B}(\mathbf{r} = 0) \tag{C3}$$

for the thermodynamic bosonic potential in the trap. At $T_{\rm c}$, we can then write $\mu_{\rm B}(\mathbf{r}) = -V_{\rm B}(\mathbf{r}) - 2t_0\, \delta n_{\rm B}(\mathbf{r})$ with $\delta n_{\rm B}(\mathbf{r}) = [n_{\rm B}(\mathbf{r}) - n_{\rm B}(\mathbf{r} = 0)]$, such that equation (C1) becomes:

$$n_{\rm B}(\mathbf{r}) = \int \frac{{\rm d}\mathbf{q}}{(2\pi)^3} \frac{1}{{\rm e}^{\beta_{\rm c}\left[\frac{\mathbf{q}^2}{2m_{\rm B}} + V_{\rm B}(\mathbf{r}) + 2t_0 \delta n_{\rm B}(\mathbf{r})\right]} - 1} \tag{C4}$$

where $\beta_{\rm c} = (k_{\rm B} T_{\rm c})^{-1}$. For any given value of $\mathbf{r}$, this equation is solved self-consistently for the variable $n_{\rm B}(\mathbf{r})$ by fixing an arbitrary value of $n_{\rm B}(\mathbf{r} = 0)$ to start with, in such a way that $n_{\rm B}(\mathbf{r})$ never exceeds $n_{\rm B}(\mathbf{r} = 0)$. Once the entire density profile $n_{\rm B}(\mathbf{r})$ is obtained in this way, one calculates $N_{\rm B}$ from equation (C2) so as to obtain $T_{\rm c}$ as a function of $N_{\rm B}$ and $a_{\rm B}$. In addition, upon measuring the values of $T_{\rm c}$ obtained in this way in units of the critical temperature for non-interacting trapped bosons $k_{\rm B} T_{\rm c}^{\rm BEC} = \omega_0 \left[N_{\rm B}/\zeta(3)\right]^{1/3}$ (where $\zeta(z)$ is the Riemann zeta function of argument z), one finds that $T_{\rm c}/T_{\rm c}^{\rm BEC}$ is a function only of the scaling variable $a_{\rm B}\sqrt{k_{\rm B} T_{\rm c}^{\rm BEC}/m_{\rm B}}$. By translating back into the language of the BCS–BEC crossover of the main text, one gets eventually that $T_{\rm c}/T_{\rm F}^t$ is a function of the coupling parameter $(k_{\rm F}^t a_{\rm F})^{-1}$ in the trap since $a_{\rm B}$ is proportional to $a_{\rm F}$ (cf figure 7).

ORCID iDs

P Pieri https://orcid.org/0000-0001-8295-805X
J Hecker Denschlag https://orcid.org/0000-0003-1984-4994
G Calvanese Strinati https://orcid.org/0000-0003-4038-4291

References

[1] Micnas R, Ranninger J and Robaszkiewicz S 1990 Superconductivity in narrow-band systems with local non-retarded attractive interactions *Rev. Mod. Phys.* **62** 113
[2] Tagliavini A, Capone M and Toschi A 2016 Detecting a preformed pair phase: response to a pairing forcing field *Phys. Rev.* B **94** 155114 and references therein
[3] Chen Q, Stajic J, Tan S and Levin K 2005 BCS–BEC crossover: from high temperature superconductors to ultra-cold superfluids *Phys. Rep.* **412** 1 and references therein
[4] Paintner T *et al* 2019 Pair fraction in a finite-temperature Fermi gas on the BEC side of the BCS–BEC crossover *Phys. Rev.* A **99** 053617
[5] Chin C and Grimm R 2004 Thermal equilibrium and efficient evaporation of an ultracold atom–molecule mixture *Phys. Rev.* A **69** 033612
[6] Eagles D M 1969 Possible pairing without superconductivity at low carrier concentrations in bulk and thin-film superconducting semiconductors *Phys. Rev.* **186** 456
[7] Pini M, Pieri P and Strinati G C 2019 Fermi gas throughout the BCS–BEC crossover: comparative study of t-matrix approaches with various degrees of self-consistency *Phys. Rev.* B **99** 094502
[8] Enss T, Haussmann R and Zwerger W 2011 Viscosity and scale invariance in the unitary Fermi gas *Ann. Phys.* **326** 770
[9] Haussmann R and Zwerger W 2008 Thermodynamics of a trapped unitary Fermi gas *Phys. Rev.* A **78** 063602
[10] Andrenacci N, Pieri P and Strinati G C 2003 Evolution from BCS superconductivity to Bose–Einstein condensation: current correlation function in the broken symmetry phase *Phys. Rev.* B **68** 144507
[11] Palestini F and Strinati G C 2014 Temperature dependence of the pair coherence and healing lengths for a fermionic superfluid throughout the BCS–BEC crossover *Phys. Rev.* B **89** 224508
[12] Strinati G C, Pieri P, Röpke G, Schuck P and Urban M 2018 The BCS–BEC crossover: from ultra-cold Fermi gases to nuclear systems *Phys. Rep.* **738** 1
[13] Fetter A L and Walecka J D 1971 *Quantum Theory of Many-Particle Systems* (New York: McGraw-Hill)
[14] Bardeen J, Cooper L N and Schrieffer J R 1957 Theory of superconductivity *Phys. Rev.* **108** 1175
[15] Schrieffer J R 1964 *Theory of Superconductivity* (New York: Benjamin)
[16] Baym G 1962 Self-consistent approximations in many-body systems *Phys. Rev.* **127** 1391
[17] Strinati G 1988 Application of the Green's functions method to the study of the optical properties of semiconductors *La Rivista del Nuovo Cimento* **11** 1
[18] This argument holds barring possible bosonic-like self-energy insertions in the ladder diagrams for the T-matrix of figure A1(a), like that associated with the Gorkov–Melik-Barkhudarov correction as recently discussed in reference [19].

[19] Pisani L, Perali A, Pieri P and Strinati G C 2018 Entanglement between pairing and screening in the Gorkov–Melik-Barkhudarov correction to the critical temperature throughout the BCS–BEC crossover *Phys. Rev.* B **97** 014528
[20] Tan S 2008 Energetics of a strongly correlated Fermi gas *Ann. Phys., NY* **323** 2952
[21] Tan S 2008 Large momentum part of a strongly correlated Fermi gas *Ann. Phys., NY* **323** 2971
[22] Braaten E 2012 Universal relations for fermions with large scattering length *The BCS–BEC Crossover and the Unitary Fermi Gas* (Lecture Notes in Physics vol 836) ed W Zwerger (Berlin: Springer) p 193
[23] The temperature dependence of the contact has recently been measured at unitarity [24, 25] and shown to agree well with the theoretical calculations of reference [8], which are based on the same approach used in the present work. We have verified that our results shown in figure 1(b) coincide with those reported in reference [8].
[24] Carcy C, Hoinka S, Lingham M G, Dyke P, Kuhn C C N, Hu H and Vale C J 2019 Contact and sum rules in a near-uniform Fermi gas at unitarity *Phys. Rev. Lett.* **122** 203401
[25] Mukherjee B, Patel P B, Yan Z, Fletcher R J, Struck J and Zwierlein M W 2019 Spectral response and contact of the unitary Fermi gas *Phys. Rev. Lett.* **122** 203402
[26] Leggett A J 2006 *Quantum Liquids* (Oxford: Oxford University Press)
[27] Pistolesi F and Strinati G C 1994 Evolution from BSC superconductivity to Bose condensation: role of the parameter $k_F\xi$ *Phys. Rev.* B **49** 6356
[28] Abramowitz M and Stegun I A 1972 *Handbook of Mathematical Functions* (New York: Dover)
[29] Tsuchiya S, Watanabe R and Ohashi Y 2009 Single-particle properties and pseudogap effects in the BCS–BEC crossover regime of an ultracold Fermi gas above T_c *Phys. Rev.* A **80** 033613
[30] Haussmann R, Punk M and Zwerger W 2009 Spectral functions and rf response of ultracold fermionic atoms *Phys. Rev.* A **80** 063612
[31] Pieri P and Strinati G C 2000 Strong-coupling limit in the evolution from BCS superconductivity to Bose–Einstein condensation *Phys. Rev.* B **61** 15370
[32] Petrov D S, Salomon C and Shlyapnikov G V 2005 Scattering properties of weakly bound dimers of fermionic atoms *Phys. Rev.* A **71** 012708
[33] Brodsky I V, Kagan M Y, Klaptsov A V, Combescot R and Leyronas X 2006 Exact diagrammatic approach for dimer-dimer scattering and bound states of three and four resonantly interacting particles *Phys. Rev.* A **73** 032724
[34] Within the statistical atom–molecule model, the total fermion density profile $2(\mathrm{nf(r)} + \mathrm{np(r)})$ is obtained in terms of the density profiles of unpaired fermions nf(r) and of bosons np(r). The explicit expressions of nf(r) and np(r) correspond to the integrands of the integrals over r in equations (B13) and (B14).
[35] Mukherjee B, Yan Z, Patel P B, Hadzibabic Z, Yefsah T, Struck J and Zwierlein M W 2017 Homogeneous atomic Fermi gases *Phys. Rev. Lett.* **118** 123401
[36] The CLAS Collaboration 2019 Modified structure of protons and neutrons in correlated pairs *Nature* **566** 354
[37] Strinati G C, Pieri P and Lucheroni C 2002 From superconducting fluctuations to the bosonic limit in the response functions above the critical temperature *Eur. Phys. J.* B **30** 161
[38] Pitaevskii L and Stringari S 2003 *Bose–Einstein Condensation* (Oxford: Clarendon)
[39] Pethick C J and Smith H 2008 *Bose–Einstein Condensation in Dilute Gases* (Cambridge: Cambridge University Press)
[40] Landau L D and Lifshitz E M 1999 *Statistical Physics* (Course of Theoretical Physics vol 5) (Oxford: Butterworth-Heinemann) ch X
[41] Combescot R, Leyronas X and Kagan M Y 2006 Self-consistent theory for molecular instabilities in a normal degenerate Fermi gas in the BEC-BCS crossover *Phys. Rev.* A **73** 023618
[42] Popov V N 1987 *Functional Integrals and Collective Excitations* (Cambridge: Cambridge University Press) ch 6
[43] Hugenholtz N M and Pines D 1959 Ground-state energy and excitation spectrum of a system of interacting bosons *Phys. Rev.* **116** 489

List of Figures

List of Tables

Bibliography

[1] P. Kapitza. "Viscosity of Liquid Helium below the λ-Point". In: Nature **141**, 3558 (1938), pp. 74–74. DOI: 10.1038/141074a0.

[2] J. Bardeen, L. N. Cooper, and J. R. Schrieffer. "Theory of Superconductivity". In: Phys. Rev. **108**, 5 (1957), pp. 1175–1204. DOI: 10.1103/PhysRev.108.1175.

[3] J. Bardeen, L. N. Cooper, and J. R. Schrieffer. "Microscopic Theory of Superconductivity". In: Phys. Rev. **106**, 1 (1957), pp. 162–164. DOI: 10.1103/PhysRev.106.162.

[4] H. Kamerlingh Onnes. "The Resistance of Pure Mercury at Helium Temperatures". In: Commun. Phys. Lab. Univ. Leiden **12**, 1 (1911).

[5] H. Kamerlingh Onnes. "Further Experiments with Liquid Helium. D. On the Change of the Electrical Resistance of Pure Metals at very low Temperatures, etc. V. The Disappearance of the resistance of mercury". In: *Through Measurement to Knowledge: The Selected Papers of Heike Kamerlingh Onnes 1853–1926*. Ed. by Kostas Gavroglu and Yorgos Goudaroulis. Dordrecht: Springer Netherlands, 1991, pp. 264–266. ISBN: 978-94-009-2079-8. DOI: 10.1007/978-94-009-2079-8_16.

[6] Franco Dalfovo et al. "Theory of Bose-Einstein condensation in trapped gases". In: Rev. Mod. Phys. **71**, 3 (1999), pp. 463–512. DOI: 10.1103/RevModPhys.71.463.

[7] Immanuel Bloch, Jean Dalibard, and Wilhelm Zwerger. "Many-body physics with ultracold gases". In: Rev. Mod. Phys. **80**, 3 (2008), pp. 885–964. DOI: 10.1103/RevModPhys.80.885.

[8] Stefano Giorgini, Lev P. Pitaevskii, and Sandro Stringari. "Theory of ultracold atomic Fermi gases". In: Rev. Mod. Phys. **80**, 4 (2008), pp. 1215–1274. DOI: 10.1103/RevModPhys.80.1215.

[9] Cheng Chin et al. "Feshbach resonances in ultracold gases". In: Rev. Mod. Phys. **82**, 2 (2010), pp. 1225–1286. DOI: 10.1103/RevModPhys.82.1225.

[10] Shina Tan. "Energetics of a strongly correlated Fermi gas". In: Annals of Physics **323**, 12 (2008), pp. 2952–2970. DOI: https://doi.org/10.1016/j.aop.2008.03.004.

[11] Shina Tan. "Large momentum part of a strongly correlated Fermi gas". In: Annals of Physics **323**, 12 (2008), pp. 2971–2986. DOI: https://doi.org/10.1016/j.aop.2008.03.005.

[12] Shina Tan. "Generalized virial theorem and pressure relation for a strongly correlated Fermi gas". In: Annals of Physics **323**, 12 (2008), pp. 2987–2990. DOI: https://doi.org/10.1016/j.aop.2008.03.003.

[13] Manuel Jäger and Johannes Hecker Denschlag. "Precise Photoexcitation Measurement of Tan's Contact in the Entire BCS-BEC Crossover". In: Phys. Rev. Lett. **132**, 26 (2024), p. 263401. DOI: 10.1103/PhysRevLett.132.263401.

[14] Manuel Jäger and Johannes Hecker Denschlag. "Methods for studying Tan's contact in the BCS-BEC crossover". In: Phys. Rev. A **109**, 6 (2024), p. 063330. DOI: 10.1103/PhysRevA.109.063330.

[15] Thomas Paintner et al. "Pair fraction in a finite-temperature Fermi gas on the BEC side of the BCS-BEC crossover". In: Phys. Rev. A **99**, 5 (2019), p. 053617. DOI: 10.1103/PhysRevA.99.053617.

[16] M Pini et al. "Pair correlations in the normal phase of an attractive Fermi gas". In: New Journal of Physics **22**, 8 (2020), p. 083008. DOI: 10.1088/1367-2630/ab9ee3.

[17] Sebastian Kölle et al. "Holographic imaging of an array of submicron light scatterers at low photon numbers". In: Applied Physics B **129**, 11 (2023), p. 180. DOI: 10.1007/s00340-023-08105-9.

[18] Mingyuan He et al. "Universal relations for ultracold reactive molecules". In: Science Advances **6**, 51 (2020), eabd4699. DOI: 10.1126/sciadv.abd4699. eprint: https://www.science.org/doi/pdf/10.1126/sciadv.abd4699.

[19] Giancarlo Calvanese Strinati et al. "The BCS–BEC crossover: From ultra-cold Fermi gases to nuclear systems". In: Physics Reports **738** (2018). The BCS–BEC crossover: From ultra-cold Fermi gases to nuclear systems, pp. 1–76. DOI: https://doi.org/10.1016/j.physrep.2018.02.004.

[20] Wilhelm Zwerger, ed. *The BCS-BEC crossover and the unitary Fermi gas*. en. 2012th ed. Lecture notes in physics. Berlin, Germany: Springer, Oct. 2011.

[21] Lev Pitaevskii and Sandro Stringari. *Bose–Einstein Condensation and Superfluidity*. 164. Oxford University Press, 2016.

[22] C. J. Pethick and H. Smith. *Bose–Einstein Condensation in Dilute Gases*. 2nd ed. Cambridge University Press, 2008.

[23] Qijin Chen et al. "BCS–BEC crossover: From high temperature superconductors to ultracold superfluids". In: Physics Reports **412**, 1 (2005), pp. 1–88. DOI: https://doi.org/10.1016/j.physrep.2005.02.005.

[24] Andrew G. Truscott et al. "Observation of Fermi Pressure in a Gas of Trapped Atoms". In: Science **291**, 5513 (2001), pp. 2570–2572. DOI: 10.1126/science.1059318. eprint: https://www.science.org/doi/pdf/10.1126/science.1059318.

[25] W. Pauli. "Über den Zusammenhang des Abschlusses der Elektronengruppen im Atom mit der Komplexstruktur der Spektren". In: Zeitschrift für Physik **31**, 1 (1925), pp. 765–783. DOI: 10.1007/BF02980631.

[26] André Schirotzek et al. "Determination of the Superfluid Gap in Atomic Fermi Gases by Quasiparticle Spectroscopy". In: Phys. Rev. Lett. **101**, 14 (2008), p. 140403. DOI: 10.1103/PhysRevLett.101.140403.

[27] G. Veeravalli et al. "Bragg Spectroscopy of a Strongly Interacting Fermi Gas". In: Phys. Rev. Lett. **101**, 25 (2008), p. 250403. DOI: 10.1103/PhysRevLett.101.250403.

[28] M. Holland et al. "Resonance Superfluidity in a Quantum Degenerate Fermi Gas". In: Phys. Rev. Lett. **87**, 12 (2001), p. 120406. DOI: 10.1103/PhysRevLett.87.120406.

[29] Y. Ohashi and A. Griffin. "BCS-BEC Crossover in a Gas of Fermi Atoms with a Feshbach Resonance". In: Phys. Rev. Lett. **89**, 13 (2002), p. 130402. DOI: 10.1103/PhysRevLett.89.130402.

[30] G. E. Astrakharchik et al. "Equation of State of a Fermi Gas in the BEC-BCS Crossover: A Quantum Monte Carlo Study". In: Phys. Rev. Lett. **93**, 20 (2004), p. 200404. DOI: 10.1103/PhysRevLett.93.200404.

[31] Jia Wang, Xia-Ji Liu, and Hui Hu. "Photoexcitation measurement of Tan's contact for a strongly interacting Fermi gas". In: Phys. Rev. A **104**, 6 (2021), p. 063309. DOI: 10.1103/PhysRevA.104.063309.

[32] Eric Braaten, Daekyoung Kang, and Lucas Platter. "Universal relations for a strongly interacting Fermi gas near a Feshbach resonance". In: Phys. Rev. A **78**, 5 (2008), p. 053606. DOI: 10.1103/PhysRevA.78.053606.

[33] Eric Braaten. "Universal Relations for Fermions with Large Scattering Length". In: *The BCS-BEC Crossover and the Unitary Fermi Gas*. Ed. by Wilhelm Zwerger. Berlin, Heidelberg: Springer Berlin Heidelberg, 2012, pp. 193–231. ISBN: 978-3-642-21978-8. DOI: 10.1007/978-3-642-21978-8_6.

[34] Markus Greiner et al. "Quantum phase transition from a superfluid to a Mott insulator in a gas of ultracold atoms". In: Nature **415**, 6867 (2002), pp. 39–44. DOI: 10.1038/415039a.

[35] Robert Jördens et al. "A Mott insulator of fermionic atoms in an optical lattice". In: Nature **455**, 7210 (2008), pp. 204–207. DOI: 10.1038/nature07244.

[36] Russell A. Hart et al. "Observation of antiferromagnetic correlations in the Hubbard model with ultracold atoms". In: Nature **519**, 7542 (2015), pp. 211–214. DOI: 10.1038/nature14223.

[37] I. M. Georgescu, S. Ashhab, and Franco Nori. "Quantum simulation". In: Rev. Mod. Phys. **86**, 1 (2014), pp. 153–185. DOI: 10.1103/RevModPhys.86.153.

[38] Ruwan Senaratne et al. "Quantum simulation of ultrafast dynamics using trapped ultracold atoms". In: Nature Communications **9**, 1 (2018), p. 2065. DOI: 10.1038/s41467-018-04556-3.

[39] Immanuel Bloch. "Ultracold quantum gases in optical lattices". In: Nature Physics **1**, 1 (2005), pp. 23–30. DOI: 10.1038/nphys138.

[40] Karl D. Nelson, Xiao Li, and David S. Weiss. "Imaging single atoms in a three-dimensional array". In: Nature Physics **3**, 8 (2007), pp. 556–560. DOI: 10.1038/nphys645.

[41] Waseem S. Bakr et al. "A quantum gas microscope for detecting single atoms in a Hubbard-regime optical lattice". In: Nature **462**, 7269 (2009), pp. 74–77. DOI: 10.1038/nature08482.

[42] J. Struck et al. "Quantum Simulation of Frustrated Classical Magnetism in Triangular Optical Lattices". In: Science **333**, 6045 (2011), pp. 996–999. DOI: 10.1126/science.1207239. eprint: https://www.science.org/doi/pdf/10.1126/science.1207239.

[43] W. Ketterle and M. W. Zwierlein. "Making, probing and understanding ultracold Fermi gases". In: La Rivista del Nuovo Cimento **31**, 5 (2008), pp. 247–422. DOI: 10.1393/ncr/i2008-10033-1.

[44] M. R. Andrews et al. "Direct, Nondestructive Observation of a Bose Condensate". In: Science **273**, 5271 (1996), pp. 84–87. DOI: 10.1126/science.273.5271.84. eprint: https://www.science.org/doi/pdf/10.1126/science.273.5271.84.

[45] C. C. Bradley, C. A. Sackett, and R. G. Hulet. "Bose-Einstein Condensation of Lithium: Observation of Limited Condensate Number". In: Phys. Rev. Lett. **78**, 6 (1997), pp. 985–989. DOI: 10.1103/PhysRevLett.78.985.

[46] Lincoln D. Turner et al. "Off-resonant defocus-contrast imaging of cold atoms". In: Opt. Lett. **29**, 3 (2004), pp. 232–234. DOI: 10.1364/OL.29.000232.

[47] L. D. Turner, K. F. E. M. Domen, and R. E. Scholten. "Diffraction-contrast imaging of cold atoms". In: Phys. Rev. A **72**, 3 (2005), p. 031403. DOI: 10.1103/PhysRevA.72.031403.

[48] Miroslav Gajdacz et al. "Non-destructive Faraday imaging of dynamically controlled ultracold atoms". en. In: Rev. Sci. Instrum. **84**, 8 (Aug. 2013), p. 083105.

[49] P. B. Wigley et al. "Non-destructive shadowgraph imaging of ultra-cold atoms". In: Opt. Lett. **41**, 20 (2016), pp. 4795–4798. DOI: 10.1364/OL.41.004795.

[50] Daniel Kai Hoffmann et al. "Holographic method for site-resolved detection of a 2D array of ultracold atoms". In: Applied Physics B **122**, 8 (2016), p. 227. DOI: 10.1007/s00340-016-6501-1.

[51] J. Smits, A. P. Mosk, and P. van der Straten. "Imaging trapped quantum gases by off-axis holography". In: Opt. Lett. **45**, 4 (2020), pp. 981–984. DOI: 10.1364/OL.384120.

[52] T. H. MAIMAN. "Stimulated Optical Radiation in Ruby". In: Nature **187**, 4736 (1960), pp. 493–494. DOI: 10.1038/187493a0.

[53] Steven Chu. "Nobel Lecture: The manipulation of neutral particles". In: Rev. Mod. Phys. **70**, 3 (1998), pp. 685–706. DOI: 10.1103/RevModPhys.70.685.

[54] E. L. Raab et al. "Trapping of Neutral Sodium Atoms with Radiation Pressure". In: Phys. Rev. Lett. **59**, 23 (1987), pp. 2631–2634. DOI: 10.1103/PhysRevLett.59.2631.

[55] A. Ashkin et al. "Observation of a single-beam gradient force optical trap for dielectric particles". In: Opt. Lett. **11**, 5 (1986), pp. 288–290. DOI: 10.1364/OL.11.000288.

[56] M. H. Anderson et al. "Observation of Bose-Einstein Condensation in a Dilute Atomic Vapor". In: Science **269**, 5221 (1995), pp. 198–201. DOI: 10.1126/science.269.5221.198. eprint: https://www.science.org/doi/pdf/10.1126/science.269.5221.198.

[57] B. DeMarco and D. S. Jin. "Onset of Fermi Degeneracy in a Trapped Atomic Gas". In: Science **285**, 5434 (1999), pp. 1703–1706. DOI: 10.1126/science.285.5434.1703. eprint: https://www.science.org/doi/pdf/10.1126/science.285.5434.1703.

[58] Walter Koechner. *Solid-State Laser Engineering*. en. 6th ed. Springer Series in Optical Sciences. New York, NY: Springer, Apr. 2006.

[59] Kireet Semwal and S. C. Bhatt. "Study of Nd3+ ion as a Dopant in YAG and Glass Laser". In: International Journal of Physics **1**, 1 (2013), pp. 15–21. DOI: 10.12691/ijp-1-1-3.

[60] Randall G Hulet, Jason H V Nguyen, and Ruwan Senaratne. "Methods for preparing quantum gases of lithium". en. In: Rev. Sci. Instrum. **91**, 1 (Jan. 2020), p. 011101. DOI: 10.1063/1.5131023.

[61] Ulrich Eismann. "A novel all-solid-state laser source for lithium atoms and three-body recombination in the unitary Bose gas". PhD thesis. Universitó Pierre et Marie Curie, Paris, 2012.

[62] Franz Sievers. "Ultracold Fermi mixtures and simultaneous sub-Doppler laser cooling of fermionic ^{6}Li and ^{40}K". PhD thesis. Universitó Pierre et Marie Curie, Paris, 2014.

[63] Norman Kretzschmar. "Experiments with Ultracold Fermi Gases: Quantum Degeneracy of Potassium-40 and All-solid-state Laser Sources for Lithium". PhD thesis. Ecole Normale Supérieure de Paris, 2015.

[64] Mool C Gupta and John Ballato, eds. *The handbook of photonics*. en. 2nd ed. London, England: CRC Press, Oct. 2019.

[65] Stephan Maier. "Aufbau eines Hochleistungs-Festkörperlasers bei 1342nm". Master's thesis. Universität Ulm, 2016.

[66] Manuel Jäger. "Aufbau eines Hochleistungs- Festkörperlasersystems bei 671 nm". Master's thesis. Universität Ulm, 2018.

[67] W. Ketterle, D. S. Durfee, and D. M. Stamper-Kurn. "Making, probing and understanding Bose-Einstein condensates". In: (Apr. 1999). arXiv: cond-mat/9904034.

[68] W. Kohn and L. J. Sham. "Self-Consistent Equations Including Exchange and Correlation Effects". In: Phys. Rev. **140**, 4A (1965), A1133–A1138. DOI: 10.1103/PhysRev.140.A1133.

[69] M. Houbiers et al. "Superfluid state of atomic ^{6}Li in a magnetic trap". In: Phys. Rev. A **56**, 6 (1997), pp. 4864–4878. DOI: 10.1103/PhysRevA.56.4864.

[70] Hui Hu, Xia-Ji Liu, and Peter D Drummond. "Universal contact of strongly interacting fermions at finite temperatures". In: New Journal of Physics **13**, 3 (2011), p. 035007. DOI: 10.1088/1367-2630/13/3/035007.

[71] S. Giorgini, L. P. Pitaevskii, and S. Stringari. "Condensate fraction and critical temperature of a trapped interacting Bose gas". In: Phys. Rev. A **54**, 6 (1996), R4633–R4636. DOI: 10.1103/PhysRevA.54.R4633.

[72] A J Stone. *The theory of intermolecular forces*. en. International Series of Monographs on Chemistry. Oxford, England: Clarendon Press, July 1996.

[73] Zong-Chao Yan et al. "Variational calculations of dispersion coefficients for interactions among H, He, and Li atoms". In: Phys. Rev. A **54**, 4 (1996), pp. 2824–2833. DOI: 10.1103/PhysRevA.54.2824.

[74] P.S. Julienne, A.M. Smith, and K. Burnett. "Theory of Collisions between Laser Cooled Atoms". In: ed. by David Bates and Benjamin Bederson. Vol. 30. Advances In Atomic, Molecular, and Optical Physics. Academic Press, 1992, pp. 141–198. DOI: https://doi.org/10.1016/S1049-250X(08)60175-5.

[75] J J Sakurai and Jim Napolitano. *Modern quantum mechanics*. en. 3rd ed. Cambridge, England: Cambridge University Press (Virtual Publishing), Oct. 2020.

[76] Rui Li et al. "Absolute Frequency Measurement of ^{6}Li D Lines with khz-Level Uncertainty". In: Phys. Rev. Lett. **124**, 6 (2020), p. 063002. DOI: 10.1103/PhysRevLett.124.063002.

[77] W. I. McAlexander, E. R. I. Abraham, and R. G. Hulet. "Radiative lifetime of the $2P$ state of lithium". In: Phys. Rev. A **54**, 1 (1996), R5–R8. DOI: 10.1103/PhysRevA.54.R5.

[78] G. Zürn et al. "Precise Characterization of ^{6}Li Feshbach Resonances Using Trap-Sideband-Resolved RF Spectroscopy of Weakly Bound Molecules". In: Phys. Rev. Lett. **110**, 13 (2013), p. 135301. DOI: 10.1103/PhysRevLett.110.135301.

[79] P. Jasik and J.E. Sienkiewicz. "Calculation of adiabatic potentials of Li2". In: Chemical Physics **323**, 2 (2006), pp. 563–573. DOI: https://doi.org/10.1016/j.chemphys.2005.10.025.

[80] Paul S. Julienne and Jeremy M. Hutson. "Contrasting the wide Feshbach resonances in ^{6}Li and ^{7}Li". In: Phys. Rev. A **89**, 5 (2014), p. 052715. DOI: 10.1103/PhysRevA.89.052715.

[81] Y. Ohashi, H. Tajima, and P. van Wyk. "BCS–BEC crossover in cold atomic and in nuclear systems". In: Progress in Particle and Nuclear Physics **111** (2020), p. 103739. DOI: https://doi.org/10.1016/j.ppnp.2019.103739.

[82] Daniel K. Hoffmann et al. "Second sound in the crossover from the Bose-Einstein condensate to the Bardeen-Cooper-Schrieffer superfluid". In: Nature Communications **12**, 1 (2021), p. 7074. DOI: 10.1038/s41467-021-27149-z.

[83] A. Perali et al. "BCS-BEC Crossover at Finite Temperature for Superfluid Trapped Fermi Atoms". In: Phys. Rev. Lett. **92**, 22 (2004), p. 220404. DOI: 10.1103/PhysRevLett.92.220404.

[84] L. D. Landau. "The Theory of a Fermi Liquid". In: Sov. Phys. JETP **3**, 6 (1957).

[85] Yoav Sagi et al. "Breakdown of the Fermi Liquid Description for Strongly Interacting Fermions". In: Phys. Rev. Lett. **114**, 7 (2015), p. 075301. DOI: 10.1103/PhysRevLett.114.075301.

[86] Marvin Holten et al. "Observation of Cooper pairs in a mesoscopic two-dimensional Fermi gas". In: Nature **606** (2022), pp. 287–291. DOI: 10.1038/s41586-022-04678-1.

[87] Lev P. Gor'kov and T. K. Melik-Barkhudarov. "Contribution to the theory of superfluidity in an imperfect Fermi gas". In: Sov. Phys. JETP **13**, 5 (1961).

[88] Mark J. H. Ku et al. "Revealing the Superfluid Lambda Transition in the Universal Thermodynamics of a Unitary Fermi Gas". In: Science **335**, 6068 (2012), pp. 563–567. DOI: 10.1126/science.1214987.

[89] M. Bartenstein et al. "Crossover from a Molecular Bose-Einstein Condensate to a Degenerate Fermi Gas". In: Phys. Rev. Lett. **92**, 12 (2004), p. 120401. DOI: 10.1103/PhysRevLett.92.120401.

[90] J. Carlson et al. "Superfluid Fermi Gases with Large Scattering Length". In: Phys. Rev. Lett. **91**, 5 (2003), p. 050401. DOI: 10.1103/PhysRevLett.91.050401.

[91] K. M. O'Hara et al. "Observation of a Strongly Interacting Degenerate Fermi Gas of Atoms". In: Science **298**, 5601 (2002), pp. 2179–2182. DOI: 10.1126/science.1079107.

[92] Xi Li et al. "Second sound attenuation near quantum criticality". In: Science **375**, 6580 (2022), pp. 528–533. DOI: 10.1126/science.abi4480. eprint: https://www.science.org/doi/pdf/10.1126/science.abi4480.

[93] S. Jensen, C. N. Gilbreth, and Y. Alhassid. "Contact in the Unitary Fermi Gas across the Superfluid Phase Transition". In: Phys. Rev. Lett. **125**, 4 (2020), p. 043402. DOI: 10.1103/PhysRevLett.125.043402.

[94] D. S. Petrov, C. Salomon, and G. V. Shlyapnikov. "Weakly Bound Dimers of Fermionic Atoms". In: Phys. Rev. Lett. **93**, 9 (2004), p. 090404. DOI: 10.1103/PhysRevLett.93.090404.

[95] D. S. Petrov, C. Salomon, and G. V. Shlyapnikov. "Scattering properties of weakly bound dimers of fermionic atoms". In: Phys. Rev. A **71**, 1 (2005), p. 012708. DOI: 10.1103/PhysRevA.71.012708.

[96] Bo Gao. "Binding energy and scattering length for diatomic systems". In: Journal of Physics B: Atomic, Molecular and Optical Physics **37**, 21 (2004), p. 4273. DOI: 10.1088/0953-4075/37/21/004.

[97] Cheng Chin and Rudolf Grimm. "Thermal equilibrium and efficient evaporation of an ultracold atom-molecule mixture". In: Phys. Rev. A **69**, 3 (2004), p. 033612. DOI: 10.1103/PhysRevA.69.033612.

[98] S. J. J. M. F. Kokkelmans, G. V. Shlyapnikov, and C. Salomon. "Degenerate atom-molecule mixture in a cold Fermi gas". In: Phys. Rev. A **69**, 3 (2004), p. 031602. DOI: 10.1103/PhysRevA.69.031602.

[99] Daniel Hoffmann. "Dynamics of ultracold Fermi gases in the vicinity of the BEC-BCS crossover". PhD thesis. Universität Ulm, 2020.

[100] J. T. Stewart et al. "Verification of Universal Relations in a Strongly Interacting Fermi Gas". In: Phys. Rev. Lett. **104**, 23 (2010), p. 235301. DOI: 10.1103/PhysRevLett.104.235301.

[101] L. Viverit et al. "Momentum distribution of a trapped Fermi gas with large scattering length". In: Phys. Rev. A **69**, 1 (2004), p. 013607. DOI: 10.1103/PhysRevA.69.013607.

[102] V. V. Flambaum, G. F. Gribakin, and C. Harabati. "Analytical calculation of cold-atom scattering". In: Phys. Rev. A **59**, 3 (1999), pp. 1998–2005. DOI: 10.1103/PhysRevA.59.1998.

[103] William Schneider and Mohit Randeria. "Universal short-distance structure of the single-particle spectral function of dilute Fermi gases". In: Phys. Rev. A **81**, 2 (2010), p. 021601. DOI: 10.1103/PhysRevA.81.021601.

[104] Eric Braaten, Daekyoung Kang, and Lucas Platter. "Short-Time Operator Product Expansion for rf Spectroscopy of a Strongly Interacting Fermi Gas". In: Phys. Rev. Lett. **104**, 22 (2010), p. 223004. DOI: 10.1103/PhysRevLett.104.223004.

[105] E. D. Kuhnle et al. "Studies of the universal contact in a strongly interacting Fermi gas using Bragg spectroscopy". In: New Journal of Physics **13**, 5 (2011), p. 055010. DOI: 10.1088/1367-2630/13/5/055010.

[106] Constantine Shkedrov et al. "Absence of Heating in a Uniform Fermi Gas Created by Periodic Driving". In: Phys. Rev. X **12**, 1 (2022), p. 011041. DOI: 10.1103/PhysRevX.12.011041.

[107] Yoav Sagi et al. "Measurement of the Homogeneous Contact of a Unitary Fermi Gas". In: Phys. Rev. Lett. **109**, 22 (2012), p. 220402. DOI: 10.1103/PhysRevLett.109.220402.

[108] Biswaroop Mukherjee et al. "Spectral Response and Contact of the Unitary Fermi Gas". In: Phys. Rev. Lett. **122**, 20 (2019), p. 203402. DOI: 10.1103/PhysRevLett.122.203402.

[109] Sascha Hoinka et al. "Precise Determination of the Structure Factor and Contact in a Unitary Fermi Gas". In: Phys. Rev. Lett. **110**, 5 (2013), p. 055305. DOI: 10.1103/PhysRevLett.110.055305.

[110] Sébastien Laurent et al. "Connecting Few-Body Inelastic Decay to Quantum Correlations in a Many-Body System: A Weakly Coupled Impurity in a Resonant Fermi Gas". In: Phys. Rev. Lett. **118**, 10 (2017), p. 103403. DOI: 10.1103/PhysRevLett.118.103403.

[111] Olga Goulko and Matthew Wingate. "Numerical study of the unitary Fermi gas across the superfluid transition". In: Phys. Rev. A **93**, 5 (2016), p. 053604. DOI: 10.1103/PhysRevA.93.053604.

[112] R. Rossi et al. "Contact and Momentum Distribution of the Unitary Fermi Gas". In: Phys. Rev. Lett. **121**, 13 (2018), p. 130406. DOI: 10.1103/PhysRevLett.121.130406.

[113] Tilman Enss, Rudolf Haussmann, and Wilhelm Zwerger. "Viscosity and scale invariance in the unitary Fermi gas". In: Annals of Physics **326**, 3 (2011), pp. 770–796. DOI: https://doi.org/10.1016/j.aop.2010.10.002.

[114] Tilman Enss. "Quantum critical transport in the unitary Fermi gas". In: Phys. Rev. A **86**, 1 (2012), p. 013616. DOI: 10.1103/PhysRevA.86.013616.

[115] Selim Jochim. "Bose-Einstein Condensation of Molecules". PhD thesis. University of Innsbruck, 2004.

[116] Timo Ottenstein. "Few-body physics in ultracold Fermi gases". PhD thesis. University of Heidelberg, 2010.

[117] Thomas Paintner. "Aufbau eines Lasersystems zur Kühlung von ^{6}Li". Master's thesis. Universität Ulm, 2012.

[118] Benjamin Vogler. "Design und Aufbau einer Vakuumapparatur zur Laserkühlung von Lithium". Master's thesis. Universität Ulm, 2012.

[119] Daniel Hoffmann. "Abbildung ultrakalter Lithiumatome". Master's thesis. Universität Ulm, 2013.

[120] Michael Griener. "Optical transport and evaporation to a degenerate Fermi gas". Master's thesis. Universität Ulm, 2014.

[121] Tobias Lupfer. "Aufbau einer Dipolfalle zur Erzeugung eines quantenentarteten Fermigases aus Lithiumatomen". Master's thesis. Universität Ulm, 2013.

[122] W. T. Hicks. "Evaluation of Vapor-Pressure Data for Mercury, Lithium, Sodium, and Potassium". In: The Journal of Chemical Physics **38**, 8 (Apr. 1963), 1873–1880. DOI: 10.1063/1.1733889.

[123] Michael Eric Gehm. "Preparation of an optically-trapped degenerate Fermi gas of ^{6}Li: Finding the route to degeneracy". PhD thesis. Duke University, 2003.

[124] U. Schünemann et al. "Simple scheme for tunable frequency offset locking of two lasers". In: Review of Scientific Instruments **70**, 1 (Jan. 1999), pp. 242–243. DOI: 10.1063/1.1149573. eprint: https://pubs.aip.org/aip/rsi/article-pdf/70/1/242/19302402/242_1_online.pdf.

[125] Nikhil Dev K K. "Stabilization of a high-power solid-state laser system at 671 nm". Master's thesis. Universität Ulm, 2023.

[126] Joannis Koepsell et al. "Microscopic evolution of doped Mott insulators from polaronic metal to Fermi liquid". In: Science **374**, 6563 (2021), pp. 82–86. DOI: 10.1126/science.abe7165. eprint: https://www.science.org/doi/pdf/10.1126/science.abe7165.

[127] Jochen Gleiter. "Aufbau eines Lasersystems für eine 2D-Atomfalle". Master's thesis. Universität Ulm, 2015.

[128] Rudolf Grimm, Matthias Weidemüller, and Yurii B. Ovchinnikov. "Optical Dipole Traps for Neutral Atoms". In: ed. by Benjamin Bederson and Herbert Walther. Vol. 42. Advances In Atomic, Molecular, and Optical Physics. Academic Press, 2000, pp. 95–170. DOI: https://doi.org/10.1016/S1049-250X(08)60186-X.

[129] C J Foot. *Atomic Physics*. en. Oxford Master Series in Physics. London, England: Oxford University Press, Nov. 2004.

[130] Daniel K. Hoffmann et al. "Reaction kinetics of ultracold molecule-molecule collisions". In: Nature Communications **9**, 1 (2018), p. 5244. DOI: 10.1038/s41467-018-07576-1.

[131] Biswaroop Mukherjee et al. "Homogeneous Atomic Fermi Gases". In: Phys. Rev. Lett. **118**, 12 (2017), p. 123401. DOI: 10.1103/PhysRevLett.118.123401.

[132] Klaus Hueck et al. "Two-Dimensional Homogeneous Fermi Gases". In: Phys. Rev. Lett. **120**, 6 (2018), p. 060402. DOI: 10.1103/PhysRevLett.120.060402.

[133] Umberto Toniolo et al. "Larkin-Ovchinnikov superfluidity in a two-dimensional imbalanced atomic Fermi gas". In: Phys. Rev. A **95**, 1 (2017), p. 013603. DOI: 10.1103/PhysRevA.95.013603.

[134] Klaus Hueck. "A homogeneous, two-dimensional Fermi gas, Measurements in Position- and Momentum-Space". PhD thesis. University of Hamburg, 2017.

[135] K. M. O'Hara et al. "Scaling laws for evaporative cooling in time-dependent optical traps". In: Phys. Rev. A **64**, 5 (2001), p. 051403. DOI: 10.1103/PhysRevA.64.051403.

[136] Wolfgang Ketterle and N.J. Van Druten. "Evaporative Cooling of Trapped Atoms". In: ed. by Benjamin Bederson and Herbert Walther. Vol. 37. Advances In Atomic, Molecular, and Optical Physics. Academic Press, 1996, pp. 181–236. DOI: https://doi.org/10.1016/S1049-250X(08)60101-9.

[137] C. Chin et al. "Observation of the Pairing Gap in a Strongly Interacting Fermi Gas". In: Science **305**, 5687 (2004), pp. 1128–1130. DOI: 10.1126/science.1100818. eprint: https://www.science.org/doi/pdf/10.1126/science.1100818.

[138] U. Eismann et al. "An all-solid-state laser source at 671 nm for cold-atom experiments with lithium". In: Applied Physics B **106**, 1 (2012), pp. 25–36. DOI: 10.1007/s00340-011-4693-y.

[139] R. Chang et al. "Three-dimensional laser cooling at the Doppler limit". In: Phys. Rev. A **90**, 6 (2014), p. 063407. DOI: 10.1103/PhysRevA.90.063407.

[140] P. M. Duarte et al. "All-optical production of a lithium quantum gas using narrow-line laser cooling". In: Phys. Rev. A **84**, 6 (2011), p. 061406. DOI: 10.1103/PhysRevA.84.061406.

[141] G. Reinaudi et al. “Strong saturation absorption imaging of dense clouds of ultracold atoms”. In: Opt. Lett. **32**, 21 (2007), pp. 3143–3145. DOI: 10.1364/OL.32.003143.

[142] G. B. Partridge et al. “Molecular Probe of Pairing in the BEC-BCS Crossover”. In: Phys. Rev. Lett. **95**, 2 (2005), p. 020404. DOI: 10.1103/PhysRevLett.95.020404.

[143] F. Werner, L. Tarruell, and Y. Castin. “Number of closed-channel molecules in the BEC-BCS crossover”. In: The European Physical Journal B **68**, 3 (2009), pp. 401–415. DOI: 10.1140/epjb/e2009-00040-8.

[144] Stefan Häußler. “Raman Seitenbandkühlen von ^{6}Li Atomen in einem optischen Gitter”. Master’s thesis. Universität Ulm, 2015.

[145] Florian Lenhardt. “Experimentelle Realisierung von neuen Konzepten für Hochleistungs-Nd:YVO_4-Laser bei 1342 nm”. PhD thesis. TU Kaiserslautern, 2012.

[146] Louis McDonagh. “888 nm pumping of Nd:YVO_4 for high-power TEM_{00} lasers”. PhD thesis. TU Kaiserslautern, 2008.

[147] Walter R. Leeb. “Losses introduced by tilting intracavity etalons”. In: Applied physics **6**, 2 (1975), pp. 267–272. DOI: 10.1007/BF00883762.

[148] I. H. Malitson. “Interspecimen Comparison of the Refractive Index of Fused Silica∗,†”. In: J. Opt. Soc. Am. **55**, 10 (1965), pp. 1205–1209. DOI: 10.1364/JOSA.55.001205.

[149] F. Lenhardt et al. “High-power 888-nm-pumped Nd:YVO4 1342-nm oscillator operating in the TEM00 mode”. In: Applied Physics B **96**, 4 (2009), pp. 803–807. DOI: 10.1007/s00340-009-3551-7.

[150] U. Schlarb and B. Sugg. “Refractive Index of Terbium Gallium Garnet”. In: physica status solidi (b) **182**, 2 (1994), K91–K93. DOI: https://doi.org/10.1002/pssb.2221820238.

[151] Ying Shi et al. “Structural evolution of fused silica below the glass-transition temperature revealed by in-situ neutron total scattering”. In: Journal of Non-Crystalline Solids **528** (2020), p. 119760. DOI: https://doi.org/10.1016/j.jnoncrysol.2019.119760.

[152] H. J. Zhang et al. “Thermal and Laser Properties of Nd:YVO4 Crystal”. In: Crystal Research and Technology **34**, 8 (1999), pp. 1011–1016. DOI: https://doi.org/10.1002/(SICI)1521-4079(199909)34:8<1011::AID-CRAT1011>3.0.CO;2-M.

[153] Hiroaki Furuse, Ryo Yasuhara, and Keijiro Hiraga. “Thermo-optic effects of ceramic TGG in the 300–500 K temperature range”. In: Opt. Mater. Express **5**, 6 (2015), pp. 1266–1273. DOI: 10.1364/OME.5.001266.

[154] Gaspar Rego. “Temperature Dependence of the Thermo-Optic Coefficient of SiO2 Glass”. In: Sensors **23**, 13 (2023). DOI: 10.3390/s23136023.

[155] Yoichi Sato and Takunori Taira. “Highly accurate interferometric evaluation of thermal expansion and dn/dT of optical materials”. In: Opt. Mater. Express **4**, 5 (2014), pp. 876–888. DOI: 10.1364/OME.4.000876.

[156] Robert W Boyd. "The nonlinear optical susceptibility". In: *Nonlinear Optics*. Elsevier, 2008, pp. 1–67.

[157] D. A. Kleinman, A. Ashkin, and G. D. Boyd. "Second-Harmonic Generation of Light by Focused Laser Beams". In: Phys. Rev. **145**, 1 (1966), pp. 338–379. DOI: 10.1103/PhysRev.145.338.

[158] R. W. P. Drever et al. "Laser phase and frequency stabilization using an optical resonator". In: Applied Physics B **31**, 2 (1983), pp. 97–105. DOI: 10.1007/BF00702605.

[159] A. Ashkin, G. Boyd, and J. Dziedzic. "Resonant optical second harmonic generation and mixing". In: IEEE Journal of Quantum Electronics **2**, 6 (1966), pp. 109–124. DOI: 10.1109/JQE.1966.1074007.

[160] M. Leidinger et al. "Comparative study on three highly sensitive absorption measurement techniques characterizing lithium niobate over its entire transparent spectral range". In: Opt. Express **23**, 17 (2015), pp. 21690–21705. DOI: 10.1364/OE.23.021690.

[161] Covesion Website: "Material properties of Lithium Niobate". https://covesion.com/en/resource/material-properties-of-lithium-niobate/. Accessed: 06/2024.

[162] Xin-Yuan Gao, D. Blume, and Yangqian Yan. "Temperature-Dependent Contact of Weakly Interacting Single-Component Fermi Gases and Loss Rate of Degenerate Polar Molecules". In: Phys. Rev. Lett. **131**, 4 (2023), p. 043401. DOI: 10.1103/PhysRevLett.131.043401.

[163] Xiang-Pei Liu et al. "Observation of the density dependence of the closed-channel fraction of a 6Li superfluid". In: National Science Review **9**, 10 (Dec. 2021), nwab226. DOI: 10.1093/nsr/nwab226. eprint: https://academic.oup.com/nsr/article-pdf/9/10/nwab226/47070696/nwab226.pdf.

[164] Ionut D. Prodan et al. "Intensity Dependence of Photoassociation in a Quantum Degenerate Atomic Gas". In: Phys. Rev. Lett. **91**, 8 (2003), p. 080402. DOI: 10.1103/PhysRevLett.91.080402.

[165] R. Côté and A. Dalgarno. "Photoassociation intensities and radiative trap loss in lithium". In: Phys. Rev. A **58**, 1 (1998), pp. 498–508. DOI: 10.1103/PhysRevA.58.498.

[166] N. Navon et al. "The Equation of State of a Low-Temperature Fermi Gas with Tunable Interactions". In: Science **328**, 5979 (2010), pp. 729–732. DOI: 10.1126/science.1187582. eprint: https://www.science.org/doi/pdf/10.1126/science.1187582.

[167] E. D. Kuhnle et al. "Universal Behavior of Pair Correlations in a Strongly Interacting Fermi Gas". In: Phys. Rev. Lett. **105**, 7 (2010), p. 070402. DOI: 10.1103/PhysRevLett.105.070402.

[168] Joaquín E. Drut, Timo A. Lähde, and Timour Ten. "Momentum Distribution and Contact of the Unitary Fermi Gas". In: Phys. Rev. Lett. **106**, 20 (2011), p. 205302. DOI: 10.1103/PhysRevLett.106.205302.

[169] George A. Baker. "Neutron matter model". In: Phys. Rev. C **60**, 5 (1999), p. 054311. DOI: 10.1103/PhysRevC.60.054311.

[170] Xia-Ji Liu. "Virial expansion for a strongly correlated Fermi system and its application to ultracold atomic Fermi gases". In: Physics Reports **524**, 2 (2013). Virial expansion for a strongly correlated Fermi system and its application to ultracold atomic Fermi gases, pp. 37–83. DOI: https://doi.org/10.1016/j.physrep.2012.10.004.

[171] F. Palestini et al. "Temperature and coupling dependence of the universal contact intensity for an ultracold Fermi gas". In: Phys. Rev. A **82**, 2 (2010), p. 021605. DOI: 10.1103/PhysRevA.82.021605.

[172] C.A. Regal and D.S. Jin. "Experimental Realization of the BCS-BEC Crossover with a Fermi Gas of Atoms". In: ed. by P.R. Berman, C.C. Lin, and E. Arimondo. Vol. 54. Advances In Atomic, Molecular, and Optical Physics. Academic Press, 2007, pp. 1–79. DOI: https://doi.org/10.1016/S1049-250X(06)54001-7.

[173] T. D. Lee, Kerson Huang, and C. N. Yang. "Eigenvalues and Eigenfunctions of a Bose System of Hard Spheres and Its Low-Temperature Properties". In: Phys. Rev. **106**, 6 (1957), pp. 1135–1145. DOI: 10.1103/PhysRev.106.1135.

[174] Tin-Lun Ho and Erich J. Mueller. "High Temperature Expansion Applied to Fermions near Feshbach Resonance". In: Phys. Rev. Lett. **92**, 16 (2004), p. 160404. DOI: 10.1103/PhysRevLett.92.160404.

[175] Erich Beth and George E. Uhlenbeck. "The quantum theory of the non-ideal gas. II. Behaviour at low temperatures". In: Physica **4**, 10 (1937), pp. 915–924. DOI: https://doi.org/10.1016/S0031-8914(37)80189-5.

[176] X. Leyronas. "Virial expansion with Feynman diagrams". In: Phys. Rev. A **84**, 5 (2011), p. 053633. DOI: 10.1103/PhysRevA.84.053633.

[177] Klaus Hueck et al. "Calibrating high intensity absorption imaging of ultracold atoms". In: Opt. Express **25**, 8 (2017), pp. 8670–8679. DOI: 10.1364/OE.25.008670.

[178] A. Altmeyer et al. "Precision Measurements of Collective Oscillations in the BEC-BCS Crossover". In: Phys. Rev. Lett. **98**, 4 (2007), p. 040401. DOI: 10.1103/PhysRevLett.98.040401.

[179] Qijin Chen and K. Levin. "Population of Closed-Channel Molecules in Trapped Fermi Gases with Broad Feshbach Resonances". In: Phys. Rev. Lett. **95**, 26 (2005), p. 260406. DOI: 10.1103/PhysRevLett.95.260406.

[180] M. W. J. Romans and H. T. C. Stoof. "Dressed Feshbach Molecules in the BEC-BCS Crossover". In: Phys. Rev. Lett. **95**, 26 (2005), p. 260407. DOI: 10.1103/PhysRevLett.95.260407.

[181] Eloisa Cuestas and Ana P Majtey. "A generalized molecule approach capturing the Feshbach-induced pairing physics in the BEC–BCS crossover". In: Journal of Physics: Condensed Matter **33**, 25 (2021), p. 255601. DOI: 10.1088/1361-648X/abf7a2.

[182] Juha Javanainen et al. "Simple Mean-Field Theory for a Zero-Temperature Fermionic Gas at a Feshbach Resonance". In: Phys. Rev. Lett. **95**, 11 (2005), p. 110408. DOI: 10.1103/PhysRevLett.95.110408.

[183] Jacob F. Sherson et al. "Single-atom-resolved fluorescence imaging of an atomic Mott insulator". In: Nature **467**, 7311 (2010), pp. 68–72. DOI: 10.1038/nature09378.

[184] Lawrence W. Cheuk et al. "Quantum-Gas Microscope for Fermionic Atoms". In: Phys. Rev. Lett. **114**, 19 (2015), p. 193001. DOI: 10.1103/PhysRevLett.114.193001.

[185] Elmar Haller et al. "Single-atom imaging of fermions in a quantum-gas microscope". In: Nature Physics **11**, 9 (2015), pp. 738–742. DOI: 10.1038/nphys3403.

[186] Maxwell F. Parsons et al. "Site-Resolved Imaging of Fermionic ^{6}Li in an Optical Lattice". In: Phys. Rev. Lett. **114**, 21 (2015), p. 213002. DOI: 10.1103/PhysRevLett.114.213002.

[187] Ahmed Omran et al. "Microscopic Observation of Pauli Blocking in Degenerate Fermionic Lattice Gases". In: Phys. Rev. Lett. **115**, 26 (2015), p. 263001. DOI: 10.1103/PhysRevLett.115.263001.

[188] Andrea Bergschneider et al. "Spin-resolved single-atom imaging of ^{6}Li in free space". In: Phys. Rev. A **97**, 6 (2018), p. 063613. DOI: 10.1103/PhysRevA.97.063613.

[189] Tatjana Gericke et al. "High-resolution scanning electron microscopy of an ultracold quantum gas". In: Nature Physics **4**, 12 (2008), pp. 949–953. DOI: 10.1038/nphys1102.

[190] C. Veit et al. "Pulsed Ion Microscope to Probe Quantum Gases". In: Phys. Rev. X **11**, 1 (2021), p. 011036. DOI: 10.1103/PhysRevX.11.011036.

[191] Herwig Ott. "Single atom detection in ultracold quantum gases: a review of current progress". In: Reports on Progress in Physics **79**, 5 (2016), p. 054401. DOI: 10.1088/0034-4885/79/5/054401.

[192] S. Kadlecek et al. "Nondestructive spatial heterodyne imaging of cold atoms". In: Opt. Lett. **26**, 3 (2001), pp. 137–139. DOI: 10.1364/OL.26.000137.

[193] L. D. Turner, K. F. E. M. Domen, and R. E. Scholten. "Diffraction-contrast imaging of cold atoms". In: Phys. Rev. A **72**, 3 (2005), p. 031403. DOI: 10.1103/PhysRevA.72.031403.

[194] J P Sobol and Saijun Wu. "Imaging cold atoms with shot-noise and diffraction limited holography". In: New Journal of Physics **16**, 9 (2014), p. 093064. DOI: 10.1088/1367-2630/16/9/093064.

[195] Myung K Kim. *Digital holographic microscopy*. en. 2011th ed. Springer Series in Optical Sciences. New York, NY: Springer, 2013.

[196] N. Verrier et al. "High numerical aperture holographic microscopy reconstruction with extended z range". In: Appl. Opt. **54**, 32 (2015), pp. 9540–9547. DOI: 10.1364/AO.54.009540.

[197] Joseph W Goodman. *Introduction to Fourier Optics*. 3rd ed. New York, NY: W.H. Freeman, Jan. 2005.

[198] Victor V. Goldman, Isaac F. Silvera, and Anthony J. Leggett. "Atomic hydrogen in an inhomogeneous magnetic field: Density profile and Bose-Einstein condensation". In: Phys. Rev. B **24** (5 1981), pp. 2870–2873. DOI: 10.1103/PhysRevB.24.2870.

[199] Bo Huang. "Bose-Einstein condensate immersed in a Fermi sea: Theory of static and dynamic behavior across phase separation". In: Phys. Rev. A **101**, 6 (2020), p. 063618. DOI: 10.1103/PhysRevA.101.063618.

[200] Klaus Mølmer. "Bose Condensates and Fermi Gases at Zero Temperature". In: Phys. Rev. Lett. **80**, 9 (1998), pp. 1804–1807. DOI: 10.1103/PhysRevLett.80.1804.

[201] Francesca M. Marchetti et al. "Phase separation and collapse in Bose-Fermi mixtures with a Feshbach resonance". In: Phys. Rev. B **78**, 13 (2008), p. 134517. DOI: 10.1103/PhysRevB.78.134517.

[202] Sadhan K. Adhikari. "Mean-field description of a dynamical collapse of a fermionic condensate in a trapped boson-fermion mixture". In: Phys. Rev. A **70**, 4 (2004), p. 043617. DOI: 10.1103/PhysRevA.70.043617.

[203] S. Nascimbène et al. "Exploring the thermodynamics of a universal Fermi gas". In: Nature **463**, 7284 (2010), pp. 1057–1060. DOI: 10.1038/nature08814.

[204] R. Haussmann and W. Zwerger. "Thermodynamics of a trapped unitary Fermi gas". In: Phys. Rev. A **78**, 6 (2008), p. 063602. DOI: 10.1103/PhysRevA.78.063602.

[205] L. Landau. "Theory of the Superfluidity of Helium II". In: Phys. Rev. **60**, 4 (1941), pp. 356–358. DOI: 10.1103/PhysRev.60.356.

[206] L. Tisza. "Transport Phenomena in Helium II". In: Nature **141**, 3577 (1938), pp. 913–913. DOI: 10.1038/141913a0.

[207] Russell J. Donnelly. "The two-fluid theory and second sound in liquid helium". In: Physics Today **62**, 10 (Oct. 2009), pp. 34–39. DOI: 10.1063/1.3248499. eprint: https://pubs.aip.org/physicstoday/article-pdf/62/10/34/16655230/34_1_online.pdf.

[208] S. Jochim et al. "Bose-Einstein Condensation of Molecules". In: Science **302**, 5653 (2003), pp. 2101–2103. DOI: 10.1126/science.1093280. eprint: https://www.science.org/doi/pdf/10.1126/science.1093280.

[209] E. Zaremba, T. Nikuni, and A. Griffin. "Dynamics of Trapped Bose Gases at Finite Temperatures". In: Journal of Low Temperature Physics **116**, 3 (1999), pp. 277–345. DOI: 10.1023/A:1021846002995.

[210] Siegfried Grossmann and Martin Holthaus. "On Bose-Einstein condensation in harmonic traps". In: Physics Letters A **208**, 3 (1995), pp. 188–192. DOI: https://doi.org/10.1016/0375-9601(95)00766-V.

[211] J. R. Ensher et al. “Bose-Einstein Condensation in a Dilute Gas: Measurement of Energy and Ground-State Occupation”. In: Phys. Rev. Lett. **77**, 25 (1996), pp. 4984–4987. DOI: 10.1103/PhysRevLett.77.4984.

[212] Y. Castin. “Bose-Einstein Condensates in Atomic Gases: Simple Theoretical Results”. In: *Coherent atomic matter waves*. Ed. by R. Kaiser, C. Westbrook, and F. David. Berlin, Heidelberg: Springer Berlin Heidelberg, 2001, pp. 1–136.

[213] Kerson Huang. *Statistical Mechanics*. Nashville, TN: John Wiley & Sons, Dec. 1963.

[214] Wolfgang Nolting. *Theoretical physics 5*. en. New York, NY: Springer, July 2018.

[215] Tin-Lun Ho and Qi Zhou. “Obtaining the phase diagram and thermodynamic quantities of bulk systems from the densities of trapped gases”. In: Nature Physics **6**, 2 (2010), pp. 131–134. DOI: 10.1038/nphys1477.

[216] Yean-an Liao et al. “Spin-imbalance in a one-dimensional Fermi gas”. In: Nature **467**, 7315 (2010), pp. 567–569. DOI: 10.1038/nature09393.

[217] Michele Pini, Pierbiagio Pieri, and Giancarlo Calvanese Strinati. “Strong Fulde-Ferrell Larkin-Ovchinnikov pairing fluctuations in polarized Fermi systems”. In: Phys. Rev. Res. **3**, 4 (2021), p. 043068. DOI: 10.1103/PhysRevResearch.3.043068.

[218] M. Pini, P. Pieri, and G. Calvanese Strinati. “Evolution of an attractive polarized Fermi gas: From a Fermi liquid of polarons to a non-Fermi liquid at the Fulde-Ferrell-Larkin-Ovchinnikov quantum critical point”. In: Phys. Rev. B **107**, 5 (2023), p. 054505. DOI: 10.1103/PhysRevB.107.054505.

Erklärung

Ich versichere hiermit, dass ich die Arbeit selbständig angefertigt habe und keine anderen als die angegebenen Quellen und Hilfsmittel benutzt sowie die wörtlich oder inhaltlich übernommenen Stellen als solche kenntlich gemacht habe.

Ulm, den

.....

Manuel Jäger

Danksagung

An dieser Stelle möchte ich mich ganz herzlich bei allen Personen bedanken, die mich bei dieser Arbeit unterstützt haben.
In erster Linie gilt mein Dank meinem Doktorvater Johannes Hecker Denschlag, der mir die Arbeit in seinem Institut ermöglicht hat, mir immer mit Rat und Tat zur Seite stand, aber mir dabei dennoch stets den nötigen Freiraum und das Vertrauen gab, selbstverantwortlich zu forschen.
Darüberhinaus danke ich Prof. Dr. Alexander Kubanek für die Übernahme des Zweitgutachters.
Ein weiterer wichtiger Dank gilt meinen ehemaligen und aktuellen wissenschaftlichen Kollegen in der Arbeitsgruppe, die sowohl am Institut als auch bei den vielen freizeitlichen Unternehmungen stets für ein positives und freundschaftliches Klima gesorgt haben. Beim Wandern in den Alpen waren die Höhen der Berge ein wunderbarer Kontrast zu den Höhen und Tiefen im Laboralltag! Namentlich zu nennen sind hierbei Joschka Wolf, Shinsuke Haze und Aleksandr Zaitsev vom BaRbIe-Team, Simon Rupp vom Rubidium Labor und Markus Deiß, der mittlerweile laborübergreifend alle wissenschaftlichen Prozesse tatkräftig unterstützt!
Ein besonderer Dank geht hierbei an Dominik Dorer vom BaRbIE-Team. Auch wenn wir in verschiedenen Laboren zu kämpfen hatten, hatte ich stets das Gefühl einen direkten Laborkollegen zu haben, mit dem man sowohl Fachliches und Außerfachliches ausgiebig diskutieren konnte. Mein Dank gilt auch Daniel Hoffmann und Thomas Paintner, die die großartige Maschine an der ich arbeiten konnte zu großen Teilen aufgebaut haben und mir in meiner Anfangszeit aus der Ferne mit wertvollen Tipps geholfen haben, ihr nach dem Stillstand wieder neues Leben einzuhauchen.
Gerade in dieser Anfangszeit, aber auch im gesamten Verlauf meiner Doktorarbeit, konnte ich mich bei allen Anliegen, im Besonderen mit der Vakuumanlage und dem Kühlwasser, immer auf Wladimir Schoch verlassen. Vielen Dank für alles! Ich hoffe, dass der Lithium Ofen noch viele Jahre funktioniert. Im gleichen Zuge möchte ich auch Holger Schieferdecker und Moritz Biber danken, die sich bei allen elektronischen Problemen und technischen Umsetzungen stets die nötige Zeit genommen haben. Sei es nun beim Aufspüren einen defekten MOSFET-Treibers, die sich vornehmlich Freitag abends für immer in den Feierabend verabschiedet haben; oder beim Anfertigen jeglicher Spezialbauteile, die ein Quantengas-Labor eben so benötigt.
Hierbei ist auch Astrid Sproll zu nennen, für die Unterstützung bei allen administrativen und bürokratischen Vorgängen und dem Organisieren unserer Institutsausflüge und -feiern.
Ein weiterer Dank gilt auch Frederik Koschnick, mit dem ich zeitweise das Labor geteilt habe. Zusammen konnten wir - wenn auch sicher nicht immer beabsichtigt - sehr viele Schwachstellen der Anlage aufdecken und beheben. Ich

wünsche dir alles Gute! Another thanks goes to my successor Abhishek Anand for his company in the last half year and for making me feel that I am leaving the laboratory in capable and caring hands. I wish you all the best for the coming time! I'm sure you'll be able to squeeze some exciting science out of the LiLaLab machine! In the mean time, watch your back and do not cricket too hard!
Ein Dank gilt auch meinen Freunden und vor allem meiner Familie. Ohne euch wäre der Weg von der Schule über mein Studium bis hin zu meiner Promotion nicht möglich und auch nur halb so schön gewesen! Ganz besonders danke ich meiner Freundin Linda, die mich schon seit vielen Jahren geduldig und ermutigend unterstützt und die mir immer wieder die Augen für die wirklich wichtigen Dinge im Leben öffnet.